Growth and Structure of the Organic Molecule PTCDA on Ag(111)

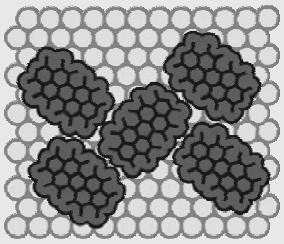

Bärbel Krause
Stuttgart, Mai 2002

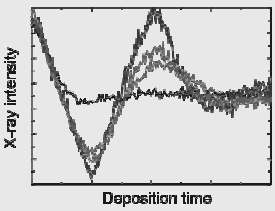

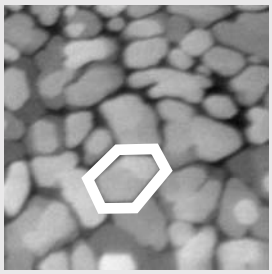

Max-Planck-Institut
für Metallforschung
in Stuttgart

Institut für Theoretische
und Angewandte Physik
der Universität Stuttgart

Growth and Structure of the Organic Molecule PTCDA on Ag(111)

Von der Fakultät für Physik der Universität Stuttgart
zur Erlangung der Würde eines Doktors der
Naturwissenschaften (Dr.rer.nat.) genehmigte Abhandlung

Vorgelegt von Bärbel Krause aus Köln

Hauptberichter: Prof. Dr. H. Dosch
Mitberichter: Prof. Dr. J. Wrachtrup

Eingereicht am 28.5.2002
Tag der mündlichen Prüfung: 24.10.2002

Institut für Theoretische und Angewandte Physik
der Universität Stuttgart

2002

Contents

Zusammenfassung

0.1 Motivation

In den letzten Jahren sind die Grundlagenforschung und die angewandte Forschung im Bereich organischer Halbleiter sehr gefördert worden. Die Ursache dafür sind die charakteristischen Materialeigenschaften organischer Halbleiter: Sie können im Bereich des sichtbaren Lichts durchsichtig sein und sind flexibler als die kovalent gebundenen Halbleiter auf Germanium- oder Siliziumbasis. Dies ermöglicht z.B. die Entwicklung von transparenten elektronischen Bauelementen auf der Basis von Folien.

Organische Halbleiter können aus Polymeren oder leichten Molekülen aufgebaut sein. Die Wechselwirkung zwischen den Molekülen ist in beiden Fällen die Van der Waals-Wechselwirkung. Polymere haben ein großes Molekulargewicht, sind flexibel und bilden ungeordnete Strukturen, während die leichten Moleküle starr sind und kristalline Strukturen bilden können.

Diese Arbeit beschäftigt sich mit aus kleinen, planaren Molekülen aufgebauten Kristallen. Die Kristalle zeigen interessante optische und elektrische Eigenschaften, die starke, mit der Kristallstruktur verbundene, Anisotropien aufweisen. Technische Anwendungen dieser Materialien sind zum Beispiel organische Feldeffekttransistoren (OFETs) [1, 2], organische Leuchtdioden (OLEDs) [3, 4], Photodetektoren [5] und organische Halbleiterlaser [6, 7]. Für das Verständnis der Funktionsweise und für die Optimierung vieler Halbleiterbauelemente ist es notwendig, dünne, hochgeordnete organische Schichten kontrolliert herzustellen [8, 9]. Nur in solchen Schichten können die optischen und elektrischen Eigenschaften direkt mit bestimmten Aspekten der Kristallstruktur in Verbindung gebracht werden. Da Defekte als Rekombinationszentren dienen, wird mit der Verminderung der Defektdichte zudem auch die Zahl der freien Ladungsträger erhöht. Die kontrollierte Herstellung dünner Schichten wird durch die Technik der Molekularstrahlepitaxie ermöglicht, bei der Moleküle thermisch unter UHV-Bedingungen verdampft werden und auf dem Substrat in einer geordneten Struktur kondensieren. Bei der Herstellung von dünnen organischen Schichten ist der Einfluß der

Grenzfläche zwischen Metallen und organischen Materialien von besonderem Interesse [10]. Diese Grenzflächen treten z.B. an den elektrischen Kontakten von OFETs auf.

Die Herstellung der organischen Schichten auf einem metallischen Substrat wirft mehrere Fragen von prinzipieller Bedeutung auf.

- Welche Gesetzmäßigkeiten bestimmen den Wachstumsprozeß der Moleküle auf mikroskopischer Ebene?
- Inwieweit kann man den Wachstumsprozeß mit Modellen beschreiben, die für anorganische Materialien entwickelt wurden? Was sind die charakteristischen Unterschiede zwischen organischen und anorganischen Materialien?
- Welchen Einfluß hat die Bindung zwischen der ersten Molekülllage und dem Substrat auf die Struktur der Schicht?
- Wie wirken sich Verspannungen auf das Wachstum des Films aus und wie werden diese abgebaut?
- Wie wird die Struktur des Volumenkristalls im dünnen Film modifiziert, und welche Polymorphe finden sich unter gegebenen Wachstumsbedingungen im dünnen Film?
- Sind die Filme thermisch stabil?

Die Vielzahl und die Komplexität der organischen Materialien erfordern es, die Forschungsaktivitäten zu ihrem generellen Verständnis auf einige wenige Modellsysteme zu konzentrieren. Das symmetrische, planare Molekül Perylen-Tetracarboxyl-Dianhydrid (PTCDA) ist eines der Modellsysteme für organische Halbleiter. Es hat sich herausgestellt, daß PTCDA interessante optische und elektronische Eigenschaften in sich vereinigt [11–14]. Insbesondere sind die Transporteigenschaften mit der kristallinen Ordnung der Schicht korreliert [9]. Zudem wurde gezeigt, daß es möglich ist, elektronische Bauelemente auf der Basis von PTCDA herzustellen [3, 12]

Das System PTCDA/Ag(111) eignet sich besonders für die Untersuchung epitaktischer organischer Filme auf Metalloberflächen, da die Stapelstruktur der Moleküle ein defektarmes Wachstum verspricht. Zudem wächst die erste Monolage PTCDA kommensurabel auf dem Metallsubstrat [15], und die Moleküle sind zwar chemisch gebunden, aber dissoziieren nicht [16]. In dieser Arbeit werden das Wachstum, die Kristallstruktur und die thermische Stabilität dünner PTCDA Filme untersucht, welche mittels Molekularstrahlepitaxie auf der Ag(111) Oberfläche aufgedampft wurden. Besondere Aufmerksamkeit wird dem Einfluß der

Wachstumsparameter auf diese Eigenschaften gewidmet. Ein weiterer zentraler Teil dieser Arbeit ist die Messung der zeitabhängigen Röntgenstreuintensität während der Deposition von PTCDA, ihre Analyse und die Anwendung verschiedener Wachstumsmodelle auf die experimentellen Beobachtungen.

0.2 Experimentelles

Im Rahmen dieser Arbeit wurden dünne PTCDA-Filme mit Dicken d zwischen 50 und 200 Å, Wachstumsraten zwischen 1 und 10 Å/min und Substrattemperaturen zwischen 135 und 500 K hergestellt. Zu diesem Zweck wurden eine stationäre MBE-Anlage der Firma Omicron und eine transportable MBE-Kammer, die insbesondere für *in situ* Röntgenstreuexperimente ausgestattet ist, verwendet [17].

Es wurden die komplementären Methoden der Rasterkraftmikroskopie und der Röntgenstreuung zur Untersuchung der Schichten verwendet. Die Röntgenexperimente wurden am Meßplatz W1 des *Hamburger Synchrotronstrahlungslabors* (HASYLAB) [18] und am Meßplatz ID10B des *European Synchrotron Radiation Laboratory*'s (ESRF) [19] durchgeführt. Hierfür wurden die Filme in der transportablen UHV-Kammer hergestellt und sowohl während als auch nach dem Wachstum unter UHV-Bedingungen gemessen. Ergänzende Röntgenmessungen wurden an einer Drehanode durchgeführt. Die Proben für die AFM-Messungen wurden in der stationären MBE-Kammer hergestellt und bei Raumtemperatur unter UHV-Bedingungen gemessen.

Die Experimente lassen sich in drei Kategorien einteilen.

- Die Untersuchung der Morphologie und der Kristallstruktur der Schichten direkt nach dem Wachstum (siehe Kapitel 6).
- Die Untersuchung der Morphologie und der Kristallstruktur abhängig von Temperaturveränderungen nach dem Wachstum (siehe Kapitel 7).
- Die *in situ* Beobachtung des Wachstumsprozesses in Echtzeit mittels spekulärer Röntgenstreuung (siehe Kapitel 8).

0.3 Resultate

Die Resultate der Messungen lassen sich wie folgt zusammenfassen.

- Die Struktur und die Morphologie dünner PTCDA-Filme variiert mit der Substrattemperatur T_g während des Wachstums: Für $T_g \lesssim 350$ K sind Filme mit einer vergleichsweise homogenen Dicke beobachtet worden. Die Oberfläche dieser Filme ist im Bereich $320\ \text{K} \lesssim T_g \lesssim 350$ K facettiert. Der Übergang zwischen einer glatten und einer facettierten Oberfläche verschiebt sich mit ansteigender Wachstumsrate zu höheren Temperaturen. Bei $T_g \approx 330$ K wurden zwei Kristallstrukturen beobachtet, die Ähnlichkeiten mit den Volumenstrukturen α und β aufweisen, aber im Vergleich dazu verspannt sind. Für $T_g \gtrsim 350$ K wurden kristalline Inseln beobachtet, die sich auf einer zwei Monolagen dicken Benetzungsschicht befinden. Der Abstand und die Größe der für $T_g \gtrsim 350$ K beobachteten Kristallite wachsen mit T_g an. Es wurde gezeigt, daß die Kristallite bei $T_g \approx 450$ K zwei Kristallstrukturen besitzen, die einer relaxierten α und β Struktur entsprechen. Sowohl die bei $T_g = 330$ K als auch die bei $T_g = 450$ K beobachteten Strukturen sind inkommensurabel zum Substrat und wurden jeweils bei 50 Å und bei 200 Å dicken Schichten beobachtet.

- Die epitaktische Orientierung der bei $T_g \approx 330$ K und der bei $T_g \approx 450$ K gewachsenen Schichten kann mit der Orientierung eines PTCDA-Films auf einer Monolage PTCDA [15] erklärt werden. Bei $T_g \approx 330$ K orientieren sich die Seiten der Einheitszelle der Monolage und des Films parallel (die (01) und die (10)-Ebenen beider Strukturen sind parallel). Bei $T_g \approx 450$ K ordnen sich die Diagonalen zweier Einheitszellen beider Strukturen parallel an, d.h. entweder die (12) oder die $(1\bar{2})$-Ebenen. Es gibt also bei $T_g \approx 330$ K jeweils eine epitaktische Orientierung einer jeden Volumenstruktur, und bei $T_g \approx 450$ K jeweils zwei epitaktische Orientierungen. Zwischen den beiden präferenziellen Orientierungen, die durch die Monolagenstruktur gegeben sind, wurde eine kontinuierliche Verteilung von Rotationsdomänen vorgefunden. In Abhängigkeit von den Wachstumsbedingungen sind zudem Überlagerungen der beiden bei 330 und 450 K beobachteten Strukturen beobachtet worden.

- Es hat sich gezeigt, daß Filme mit einer vergleichsweise homogenen Schichtdicke, die bei $T_g \lesssim 350$ K hergestellt wurden, metastabil sind. Wenn sie auf höhere Temperaturen als etwa 350 K erhitzt werden, ändert sich die Morphologie. Man beobachtet hohe Kristallite mit einer unregelmäßigen Höhenverteilung, die auf einer zwei Monolagen dicken benetzenden Schicht wachsen. Die Morphologie von Filmen, die nach dem Wachstum kristalline Inseln aufweisen, ist thermisch stabil.

- Der lineare thermische Expansionskoeffizient wurde an Schichten, welche die Kristallitstruktur aufweisen, untersucht. Senkrecht zur Molekülebene wurde $\alpha_\perp = 1.05 \pm 0.06 \times 10^{-4}\ \text{K}^{-1}$ gemessen. Der Expansionskoeffizient parallel zur Stapelrichtung wurde zu

$\alpha_{\parallel} = 5 \pm 2 \times 10^{-5}$ K^{-1} abgeschätzt. Diese Anisotropie ist charakteristisch für planare Moleküle mit einer ausgezeichneten Stapelrichtung [20, 21].

- Aus den zeitabhängigen Röntgenmessungen während der Deposition konnten Informationen über die zeitabhängige Bedeckung der Monolagen und somit über den Wachstumsmodus von PTCDA gewonnen werden. In der von uns genutzten Streugeometrie tragen alle Lagen n mit $n = 2m$ (gerade Lagennummer) in gleicher Weise zum Streusignal bei. Gleiches gilt für alle Lagen n mit $n = 2m + 1$ (ungerade Lagennummer). Deshalb konnten aus den gemessenen Intensitäten Informationen über die Materialverteilung zwischen den Lagen mit geradem und ungeradem n gewonnen werden. Je weniger Lagen am Wachstum beteiligt sind, also je mehr der Wachstumsmodus dem Lage-für-Lage Wachstum ähnelt, desto leichter läßt sich dieses Ergebnis hinsichtlich der Bedeckung einzelner Lagen interpretieren. Es kann also direkt mit dem Wachstumsmodus von PTCDA auf Ag(111) in Verbindung gebracht werden.

- PTCDA/Ag(111) wächst im Stransky-Krastanov Wachstumsmodus. Die ersten beiden Monolagen wachsen lagenweise, gefolgt von Inselwachstum auf der zweiten Monolage. Für Wachstumstemperaturen größer als etwa 350 K wurde prefektes Lage-für-Lage Wachstum der ersten beiden Monolagen beobachtet, gefolgt von dreidimensionalem Wachstum. Bei niedrigeren Temperaturen weicht das Wachstumsverhalten der ersten beiden Lagen vom perfekten Lage-für-Lage Wachstum ab und geht mit absteigender Wachstumstemperatur mehr und mehr in dreidimensionales Wachstum über. Diese Abweichungen konnten quantitativ untersucht werden. Ferner zeigten die *in situ* Messungen, daß für $T_g \gtrsim 350$ K auch nach Beenden der Deposition Materialumordnungsprozesse an der Oberfläche des dünnen Films stattfinden. Diese Prozesse wurden dahingehend interpretiert, daß noch nicht festeingebaute Moleküle auf der Oberfläche der benetzenden Schicht zu den Inseln diffundieren und dort eingebaut werden.

- Die *in situ* Röntgenmessungen während der Deposition dünner PTCDA-Filme wurden mit Hilfe von Ratengleichungen und kinetischen Monte Carlo Simulationen simuliert. Die Ratengleichung zeigen die Bedeutung eines lagenabhängigen effektiven Materialtransports zwischen den aufeinanderfolgenden Monolagen während des Wachstums. Dieser Materialtransport wird in den kinetischen Monte Carlo Simulationen einer Diffusionsbarriere für die Diffusion zwischen den Lagen zugeordnet. Eine solche Barriere könnte verschiedene Ursachen haben. Sie könnte zum Beispiel spannungsinduziert sein, da die erste, epitaktisch wachsende, Monolage PTCDA auf Silber verspannt aufwächst und auch bei $T_g = 318$ K eine verspannte Kristallstruktur beobachtet wurde. Es ist auch möglich, daß die Barriere einer Schwöbelbarriere entspricht, die bekanntlich In-

selwachstum hervorruft.

Das epitaktische Wachstum von PTCDA auf Ag(111) zeigt viele Ähnlichkeiten zum heteroepitaktischen Wachstum von Metallen:

- Eine strukturelle und morphologische Veränderung als Funktion der Wachstumstemperatur ähnlich dem für PTCDA beobachteten Verhalten ist für das Wachstum von fcc(111) auf bcc(110) beobachtet worden [22]. Dieses System kann einen strukturellen Übergang zwischen zwei epitaktischen Orientierungen, der Kurdjumov-Sachs und der Nishiyama-Wasserman Orientierung, als Funktion der Wachstumstemperatur durchführen [23].

- Sowohl für PTCDA als auch für die fcc(111)/bcc(110) Epitaxie wurde ein Übergang zwischen kinetisch bestimmten glatten Schichten und Stransky-Krastanov Wachstum für Wachstumstemperaturen, die höher als eine materialabhängige Übergangstemperatur waren, beobachtet [22].

- Die thermische Instabilität der glatten Schichten, die bei PTCDA vorgefunden wurde, ist auch bei anorganischen Schichtsysteme beobachtet worden. Diese schließen das System Mn/Re(001) ein [24], welches, ebenso wie PTCDA, einen schichtdickenabhängigen strukturellen Übergang aufweist und bei höheren Wachstumstemperaturen den Stransky-Krastanov Wachstumsmodus zeigt.

- Die für PTCDA beobachtete Variation der Inseldichte mit der Wachstumstemperatur tritt auch bei anorganischen Systemen auf und wird dort z.B. zur die Herstellung von Quantenpunkten mit einer wohldefinierten Größe genutzt. Es ist möglich, die in diesem Kontext entwickelten Wachstumstheorien auf das System PTCDA/Ag(111) anzuwenden [25–27].

0.4 Schlußfolgerungen

Abschließend kann gesagt werden, daß im Rahmen dieser Arbeit eine umfassende Studie des Wachstums von dünnen PTCDA-Filmen auf Ag(111) durchgeführt wurde, in der sowohl strukturelle und morphologische als auch kinetische Aspekte behandelt wurden. So konnten detaillierte Informationen über das epitaktische Wachstum organischer Filme auf anorganischen Substraten, und insbesondere über den Stranski-Krastanov Wachstumsmodus, gewonnen werden. Es haben sich jedoch einige Nachteile hinsichtlich der technischen Anwendung der Filme gezeigt. Homogene Schichten, die bei $T_g \lesssim 350$ K deponiert wurden, sind schon bei Temperaturen wenig über Raumtemperatur thermisch instabil. Bei höheren Wachstumstemperaturen steigen die Ordnung und die Größe der Kristallite, jedoch haben die Filme

eine inhomogene Schichtdicke. Unter allen Wachstumsbedingungen koexistieren zwei Polymorphe und eine Vielzahl von Domänen.

Die Ergebnisse dieser Arbeit sind insbesondere von Interesse für das Verständnis des Wachstums organischer Schichten. Sowohl die hier berichteten Beobachtungen für das System PTCDA/Ag(111) als auch die Beobachtungen anderer Arbeitsgruppen für eine Vielzahl organische-inorganischer Dünnschichtsysteme (z.B. die in den Referenzen [28–30] dargestellt Ergebnisse) deuten daraufhin, daß sich die Konzepte des inorganischen Schichtwachstums in einem großen Maß auf das Wachstum kleiner organischer Moleküle übertragen lassen. Dies ermöglicht es, auf bereits vorhandene theoretische und experimentelle Ergebnisse zurückzugreifen und diese auf komplexe Molekülschichten zu erweitern.

Chapter 1

Introduction

Over the last few years the properties of organic semiconductors have attracted an increasing industrial interest which is accompanied by a significant progress in the fundamental research related to these materials [2, 12, 31]. In many ways, organic semiconductor devices are complementary to the classical Si or Ge technology. While the inorganic semiconductor devices are rigid due to the covalent bonding between adjacent atoms, the more flexible van der Waals-binding between adjacent molecules allow to develop flexible devices on the basis of foils. Other interesting possibilities arise due to the optical and electronic properties of organic materials. They are useful for the developement of, e.g., wave guides and transparent devices.

There are two types of organic materials used in the semiconductor industry: the polymers and the low molecular weight materials. While polymers form disordered phases, small molecules frequently show ordered, crystalline structures. In this work, we concentrate on molecular crystals consisting of small planar molecules. These materials exhibit a strong anisotropy in their optical and transport properties perpendicular and parallel to the molecular plane. Promising applications include organic field effect transistors (OFETs) [1, 2], organic light-emitting devices (OLEDs) [4], photodetectors [5], organic lasers [6, 7], and photovoltaic cells [32]. These devices have in common that they are based on organic thin films, and that they are very sensitive to the order of these films. Only highly ordered films show the maximum anisotropy of the material properties. The charge carrier density of organic thin films is reduced by the recombination of electrons at defects such as grain boundaries. In this context, the role of the interface between organic and inorganic materials is of special interest [10]. These interfaces occur, e.g., at the metal contacts of OFETs where they influence the charge carrier injection in the organic film. The optimization of the devices relies on the structural properties and the thermal stability of the organic film [8, 9] and requires the controlled deposition of highly ordered thin films by molecular beam epitaxy (MBE).

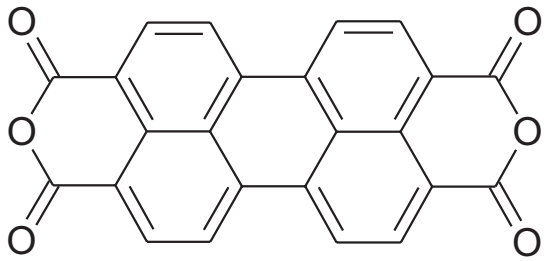

Figure 1.1: Schematic of the molecule 3,4,9,10-perylenetetracarboxylic dianhydride (PTCDA, $C_{24}O_6H_8$).

Several fundamental questions are related to the epitaxial growth of organic thin films, including the following subjects:

- The understanding of the growth process on a microscopic scale
- The relation of the organic-inorganic MBE to the MBE growth of the less complex inorganic materials.
- The influence of the organic-inorganic interface on the growth process and the structure of a thin film.
- The influence of strain on the growth process and the mechanisms of strain relaxation.
- The relation between the bulk structure and the thin film structure.
- The thermal stability of the films.

The number of interesting organic compounds is very large. In order to understand the properties these complex materials have in common, specific model systems are necessary. One of these systems is the aromatic pigment molecule PTCDA (3,4,9,10-perylenetetracarboxylic dianhydride, $C_{24}O_6H_8$) (Fig. 1.1). Its model character is given by the comparatively simple molecular structure. Furthermore, the system shows interesting optical and electronic properties [11–14]. It has been found that these properties are strongly related to the degree of crystalline ordering of the film [9].

In this work, we present a systematic growth study of the system PTCDA/Ag(111) deposited by MBE with various growth parameters. The molecules tend to form stacks on top of the substrate surface. This arrangement is expected to induce a high crystalline quality of the film. Furthermore, the chemical bond of the molecule to the substrate is non-dissociative [16], and the first monolayer has a commensurate structure [15]. We concentrate

on the structure, the morphology, and the thermal stability of the thin films. The questions we try to answer concern the relation between the thin film structure and the growth mechanism, and its theoretical description.

The study combines two complementary methods, atomic force microscopy and X-ray diffraction, in order to observe the structure and the morphology of the films. X-ray scattering is also suitable for *in situ* measurements during the thin film deposition. In contrast to the reflection high-energy electron diffraction (RHEED), which is frequently used for *in situ* growth studies, X-ray diffraction is volume sensitive, non-destructive, and the kinematic scattering theory can be applied to analyze the intensity measurements.

The structure of the thesis is as follows. In the Chapters 2 to 5 we summarize the experimental and theoretical background of the experiments. Chapter 2 introduces shortly the properties of molecular crystals and molecular thin films, Chapter 3 the X-ray scattering methods, and Chapter 4 the theory of thin film growth. The experimental details are shown in Chapter 5. The experimental and theoretical results and their discussion are presented in the Chapters 6 to 8. The results concerning the structure and morphology of PTCDA films directly after the deposition are presented in chapter 6. Chapter 7 focuses on the thermal properties of the films. The *in situ* growth study and the related simulations are found in Chapter 8.

Chapter 2

Molecular crystals and thin films

In this chapter we summarize the properties of organic molecular crystals, with emphasis on the properties of bulk crystals and epitaxial thin films of organic semiconducting materials consisting of small planar molecules. In this context, we introduce the organic molecule PTCDA (3,4,9,10-perylenetetracarboxylic dianhydride, $C_{24}O_6H_8$) which is a model system for organic semiconductors. The properties of thin PTCDA films on Ag(111) will be studied in detail in the Chapters 6, 7, and 8.

2.1 Organic molecular crystals

2.1.1 Building principles of molecular crystals

The structure of molecular crystals depends on several interactions. While the molecular structure is determined by the covalent bonding, the structure of a molecular crystal formed by electrically neutral, nonmagnetic molecules follows from the competition of several interactions including the van der Waals interaction, the electrostatic interaction, and, in some cases, also the hydrogen bonds [33, 34].

The interaction potential of two atoms i and j with the interatomic distance r_{ij} is the Lennard-Jones potential

$$\phi_{ij}(r_{ij}) = -\frac{A}{r_{ij}^6} + \frac{B}{r_{ij}^{12}} \tag{2.1}$$

with the constants A and B. It takes into account the attractive van der Waals interaction between the fluctuating dipole moments (first term), and the repulsion between the overlapping orbitals (second term). A simple approximation of the molecular interaction of a

one-component crystal is the sum of the interactions of the individual atoms,

$$\phi\left(\{r_{ij}\}\right) = \sum_{i,j} \phi_{ij}, \tag{2.2}$$

where $\{r_{ij}\}$ is the set of distances between all atoms i and j of neighboring molecules which interact by the van der Waals interaction. In the case of polar molecules, additional interactions such as the dipole-dipole interaction and the quadrupole-quadrupole interaction have to be taken into account. This can increase the interaction energy between adjacent molecules by a factor 2 – 3. Since the van der Waals-interaction is an interaction between neighboring molecules, the minimization of the intermolecular potential is often accompanied by an increase in the packing density [34].

For large, low-symmetry molecules, $\phi\left(\{r_{ij}\}\right)$ has many local minima. Their energy is similar to the global energy minimum. The difficulties in predicting the crystalline structure of an organic crystal, i.e. in calculating the global energy minimum, increase with the complexity of the molecules.

The low molecular symmetry frequently induces a low-symmetry crystal structure. Most of the organic crystals are monoclinic or triclinic and have more than one molecule in the unit cell, and in many cases several polymorphs exist. The low crystalline symmetry becomes apparent in the optoelectronic and electronic properties of complex organic materials [12, 35, 36].

2.1.2 Planar aromatic molecules

That organic molecules can indeed form crystals is not self-evident. The crystallization may be complicated by the low symmetry of a molecule. This represents a major difficulty in the structure determination of macromolecular crystals such as proteins. Therefore, a considerable effort has been focused on the study of a special class of organic materials, the small planar aromatic molecules (Fig. 2.1). These molecules consist of several carbon rings which ensure the planarity of the molecular core, and may be modified by functional endgroups (e.g. [37]). Representatives of this class of molecules are the perylene- and pentacene-derivatives, the phthalocyanines, and the aromatic hydrocarbons [30, 34, 38, 39]. Their often relatively simple, almost rectangular shape facilitates a dense packing. Hence, the crystallization of these molecules is favored.

Fig. 2.2 shows a schematic of a molecular crystal built from planar molecules. Frequently, the molecules form stacks perpendicular to the molecular plane. This structure increases

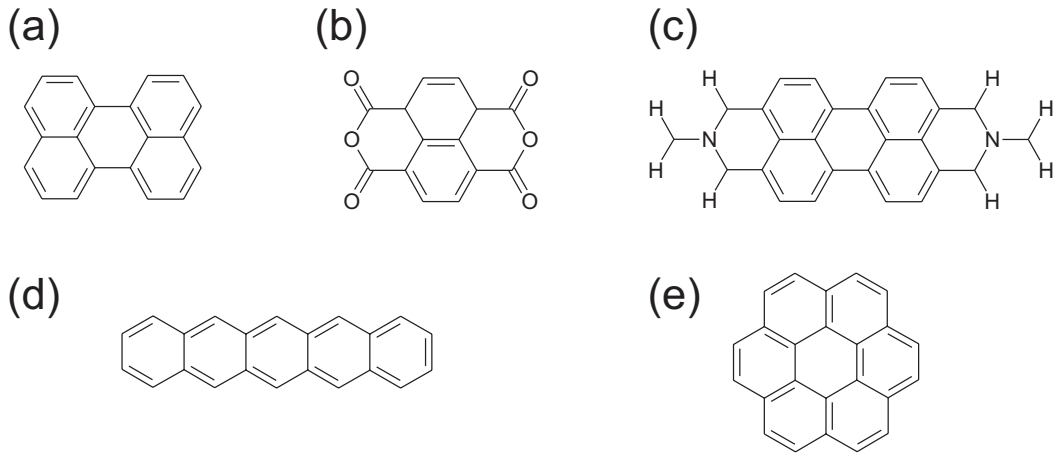

Figure 2.1: Representatives of the class of small, planar molecules. (a) Perylene, (b) 1,4,5,8-naphthalene-tetracarboxylic-dianhydride (NTCDA), (c) N,N'-dimethylperylene-3,4,9,10-bis(dicarboximide) (DM-PBCDI), (d) pentacene, and (e) coronene.

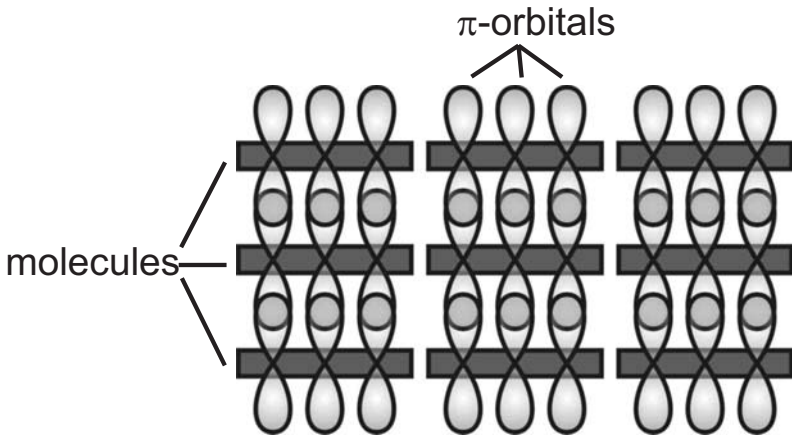

Figure 2.2: Schematic of a molecular crystal of planar aromatic molecules, which form stacks perpendicular to the molecular plane. The overlapping delocalized π-orbitals are indicated.

the packing density and the van der Waals binding energy. The highest occupied molecular orbitals (HOMO) of the planar molecules are delocalized π-orbitals of the carbon rings oriented perpendicular to the molecular plane. If the molecules form stacks, the axis of the π-orbitals is parallel to the stacking direction. The intermolecular distances determine the overlap of the π-orbitals, and by this the formation of a band structure with narrow bands. At room temperature, the charge carrier transport in organic crystals is determined by hopping processes. In the direction of the stacking axis, the charge carrier mobility is enhanced due to the overlap of the π-orbitals.

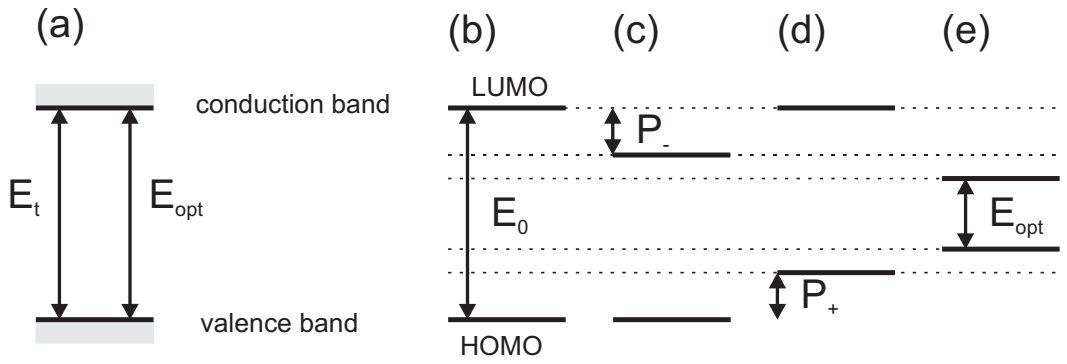

Figure 2.3: (a) Energy diagram of a covalently bonded inorganic semiconductor. E_t is the transport gap, E_{opt} the optical gap. (b)-(e) Energy diagram for organic semiconductors [13]. (a) Highest occupied (HOMO) and lowest unoccupied molecular orbital (LUMO) of a gas-phase molecule with the energy gap, E_0. (b) Energy levels of a negatively charged molecule in a crystal including the polarization, P_-. (c) Energy levels of a positively charged molecule in a crystal with the polarization P_+. (d) Energy levels of a molecule with a localized Frenkel exciton.

2.1.3 Organic and inorganic semiconductors

Fig. 2.3 (a) shows the energy diagram of a covalently bonded inorganic semiconductor with a large band width. Inorganic semiconductors show only small polarization effects if a charge carrier is removed or added to the crystal. The transport gap, E_t, is the energy for the formation of an electron-hole pair. The electron and the hole are delocalized, and their binding energy is negligible. Therefore, E_t equals the optical gap, E_{opt}, which is the lowest absorption energy.

For organic semiconductors, the situation is different. Fig. 2.3 (a) shows the highest occupied (HOMO) and lowest unoccupied molecular orbital (LUMO) of a gas-phase molecule, separated by the energy gap, E_0. Organic crystals have a small bandwidth and a large polarizability. A negatively charged molecule in the crystal induces the polarization P_- in the crystal, a positively charged molecule the polarization P_+. The transport gap is $E_t = E_0 - (P_+ + P_-)$. E_{opt}, the lowest absorption energy, is the energy for the formation of a Frencel exciton. This exciton is localized on the molecule [13, 35], and due to the large exciton binding energy, E_{ex}, we find

$$\begin{aligned} E_{opt} &= E_0 - (P_+ + P_-) - E_{ex} \\ &= E_t - E_{ex}. \end{aligned} \tag{2.3}$$

Typical values for E_t, E_{ex}, and E_{opt} of PTCDA are summarized in Tab. 2.1. Another type

$n_\parallel$	$n_\perp$	μ [cm^2/Vs]	E_t [eV]	E_{opt} [eV]	E_{ex} [eV]
1.36 [12]	2.017 [12]	≈ 1 [12]	3.2 ± 0.4 [13]	2.6 [13]	0.6 ± 0.4 [13]

Table 2.1: Characteristic optical and electronic properties of PTCDA: The refraction indices $n_\parallel$ and $n_\perp$ parallel and perpendicular to the molecular plane, the highest measured charge carrier mobility, μ, the transport gap, E_t, the optical gap, E_{opt}, and the exciton binding energy E_{ex}.

of excitons, the charge-transfer exciton, has been observed for organic crystals. These excitons have a radius of 2-3 molecules. The positive and the negative charge are localized on adjacent molecules and cannot be approximated by the Wannier-Mott exciton (weak interaction between the electron and the hole) or the Frenkel exciton (strong interaction). For covalently inorganic semiconductors, it is often possible to apply these approximations.

2.2 Thin films on inorganic substrates

The growth of an organic molecular thin film on an inorganic substrate is strongly influenced by the characteristics of the interface between both materials, i.e. the structure of the first organic monolayer on the substrate surface [12, 40, 41].

2.2.1 Molecular epitaxy

At the organic / inorganic interface, two systems with different inter-particle interactions, a different size of the particles, a different size of the unit cell, and often a different symmetry group interact with each other. Each molecule interacts with several atoms of the inorganic substrate, and commonly the 2D bulk lattices of the substrate and the organic layer are incommensurate. Nevertheless, in many cases ordered monolayers of planar organic molecules have been observed, sometimes with a domain size of several micrometers. Examples hereof are ordered structures of perylene-derivatives [15, 38, 42], the phthalocyanines [12, 40] and hydrocarbons [38, 43] on various substrates, including semiconductors, metals, and ionic crystals. In the following, the epitaxial relationship between the adsorbate layer and the substrate will be described, following the definitions of Hooks et al. [41].

The unit mesh of the substrate surface is described by two lattice vectors $\mathbf{a}_1$ and $\mathbf{a}_2$, and

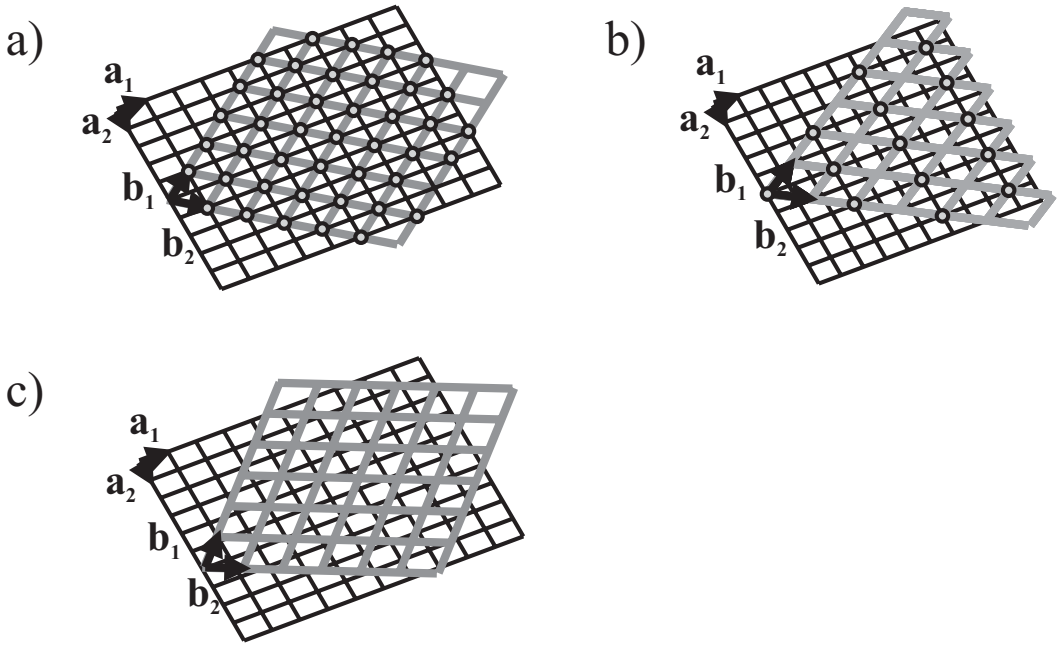

Figure 2.4: Different types of epitaxial relationships between the two-dimensional lattices of the substrate surface (lattice vectors $\mathbf{a}_1$ and $\mathbf{a}_2$) and an adsorbate layer (lattice vectors $\mathbf{b}_1$ and $\mathbf{b}_2$). Overlapping lattice points are marked by a circle. (a) Commensurate structure, (b) coincident structure, and (c) incommensurate structure.

the adsorbate layer by $\mathbf{b}_1$ and $\mathbf{b}_2$. The transformation between the two lattices is given by

$$\begin{bmatrix} \mathbf{b}_1 \\ \mathbf{b}_2 \end{bmatrix} = [C] \begin{bmatrix} \mathbf{a}_1 \\ \mathbf{a}_2 \end{bmatrix} \tag{2.4}$$

with the transformation matrix $[C]$. Fig. 2.4 shows examples for different epitaxial relationships between the substrate and the adsorbate layer. For a socalled *commensurate structure*, every lattice point of the adsorbate coincides with a lattice point of the substrate, and therefore all elements of $[C]$ are integers. In case of *coincident epitaxy*, this condition is relaxed. It is sufficient if the adsorbate lattice points coincide only partially with substrate lattice points, i.e. that the elements of $[C]$ are rational. In case of an *incommensurate structure*, the lattices of the substrate and the adsorbate layer are not related by coincidence, and $[C]$ has at least one irrational element, but no integer. Examples of a commensurate structure are 1,4,5,8-naphthalene-tetracarboxylic-dianhydride (NTCDA) on Ag(111) and Ag(110) [44], of a coincident structure PTCDA on highly-oriented pyrolytic graphite (HOPG) [42, 45], and of an incommensurate structure N,N'-dimethylperylene-3,4,9,10-bis(dicarboximide) (DM-PBCDI) on Ag(111) [15]. The molecules are shown in Fig. 2.1. Further examples can be found in [12, 38, 41].

The epitaxy is determined by the competition between the adsorbate-substrate inter-

action and the adsorbate-adsorbate interaction. The adsorbate-substrate interaction varies between weak interaction (physisorption) and strong interaction (chemisorption) [30], depending on the charge transfer between the adsorbate and the substrate. Several factors favor commensurate or coincident epitaxy:

- The adsorbate-substrate interaction is weak enough to permit surface diffusion, but dominates the intermolecular interaction.
- The existence of a low-index bulk crystalline plane which coincides with the molecular plane.
- The misfit between a low-index plane of the molecular bulk crystal and the substrate lattice is not too large. Organic overlayers tolerate strain up to approximately 10 %, so that this aspect is of minor importance for the epitaxy.

2.2.2 Thin films

In many cases, the monolayer structure of an organic adsorbate is different from the possible bulk structures. We distinguish between two scenarios: a monolayer structure similar to the bulk structure, but slightly distorted, or a monolayer structure wich differs significantly from the bulk structure. In the first case, the structure can relax to the bulk structure, either directly after the first monolayer [46,47], or slowly with increasing film thickness [48]. The film is expected to be highly ordered since the unit cell changes only slightly with the film thickness, and the order of the first monolayer is continued. In the second case, also a transition to the bulk structure is expected with increasing film thickness. Since the monolayer structure differs significantly from the bulk structure, the film is expected to be less ordered. Frequently, organic materials have several bulk polymorphs. In general, the energy differences between the bulk polymorphs are very small, and the structure of the film may change substantially with the growth parameters [49].

2.3 PTCDA as a model system

The planar molecule PTCDA (3,4,9,10-perylenetetracarboxylic dianhydride, $C_{24}O_6H_8$) (see Fig. 2.1 (c)) is a model system for stacked organic layers. Many basic electronic and optoelectronic properties of organic semiconductors can be studied for this system [9,12,13]. In the following, we give a short summary of the results of previous studies of the PTCDA bulk material and thin films on different substrates, as far as they are relevant for the present study.

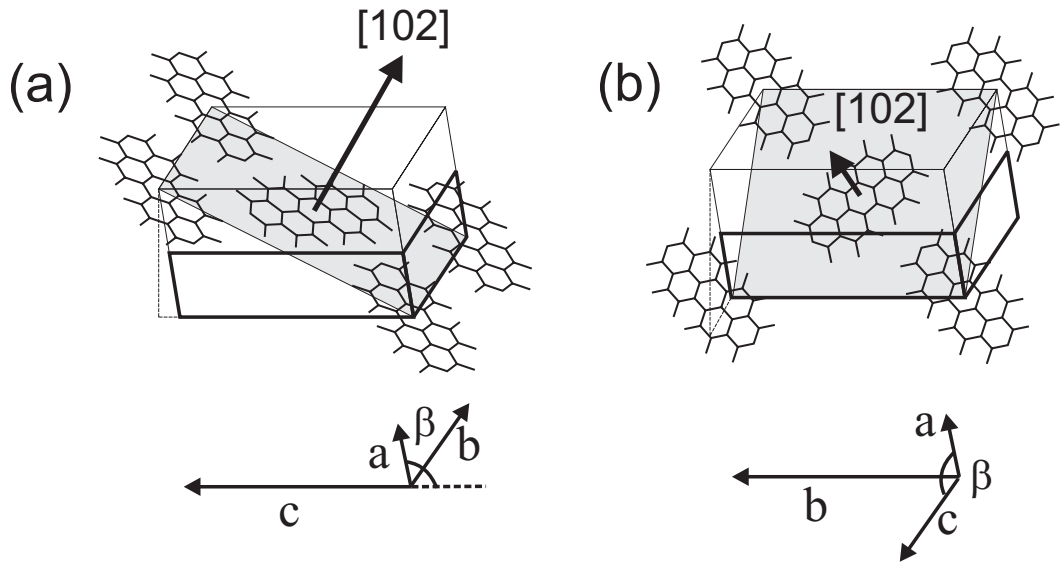

Figure 2.5: (a) Unit cell of the α polymorph, and (b) unit cell of the β polymorph. The (102) plane, which coincides with the molecular plane, is indicated [50].

polymorph	a [Å]	b [Å]	c [Å]	β [Å]	b_1 [Å]	b_2 [Å]	d_{102} [Å]
α [51, 52]	3.74	11.96	17.34	98.8	19.91	11.96	3.22
β [50, 53]	3.87	19.3	10.77	83.5	19.30	12.45	3.25

Table 2.2: Parameters of the monoclinic unit cell of PTCDA [50–53]. a, b, c, and β are the parameters of the three-dimensional bulk unit cell, b_1 and b_2 the parameters of the two-dimensional in-plane unit cell of the PTCDA(102) plane, and d_{102} is the lattice parameter of the (102)-plane.

2.3.1 Bulk properties

Crystalline structure

PTCDA is an electrically neutral pigment and consists of a perylene core with a delocalized π-electron system and two anhydride endgroups. The endgroups give rise to a permanent quadrupole moment with the positive charge situated around the center of the molecule, and the negative charge around the endgroups. Two monoclinic bulk polymorphs, each with two molecules in the unit cell at the positions (000) and (1/2 1/2 1/2), have been found: The more densely packed α phase [51, 52], and the β phase [50, 53], shown in Fig. 2.5. The parameters of the monoclinic unit cells are summarized in Tab. 2.2. In the following, we will always use the α bulk notation for the crystal planes. In both structures, the two molecules of the unit cell are coplanar and order in a herringbone pattern in the (102) plane which is the cleavage plane of the crystal. These molecular sheets are stacked. The two polymorphs mainly differ in the stacking direction of the sheets, as shown in Fig. 2.6. This model has been

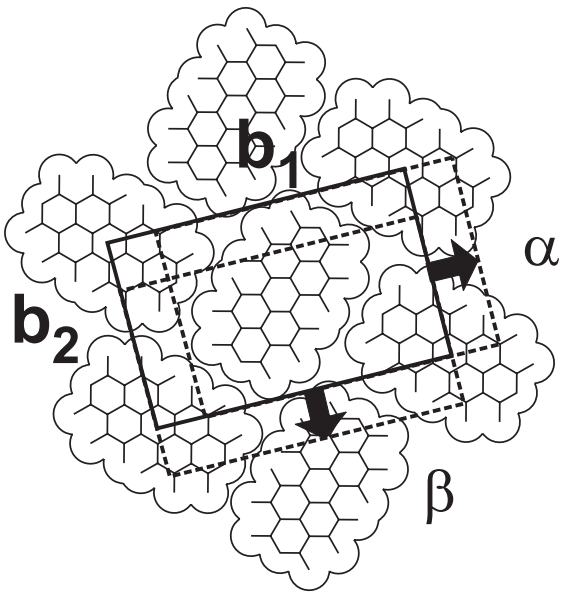

Figure 2.6: Molecular ordering in the (102) plane. The straight lines show the rectangular in-plane unit cell with the unit vectors $\mathbf{b}_1$ and $\mathbf{b}_2$. The dashed lines indicate the projected in-plane unit cell of a second molecular layer translated in the direction characteristic for the α respectively the β phase.

proposed first by Möbus et al. [50]. The rectangular in-plane unit cell of the PTCDA(102) plane has the lattice vectors b_1 and b_2. The distance between adjacent sheets is the lattice parameter of the PTCDA(102) plane, d_{102}. The parameters of the in-plane unit cell of both bulk polymorphs [50] are summarized in Tab. 2.2.

PTCDA is an organic semiconductor. It shows the anisotropic electronic and optoelectronic properties characteristic for planar molecules forming stacks (see Sec. 2.1.3). Tab. 2.1 summarizes some of the electronic and optical parameters of PTCDA.

2.3.2 Structure of a monolayer PTCDA

On most of the substrates studied up to now, PTCDA grows along the [102] direction, i.e. with the molecular plane parallel to the substrate. Commensurate structures of a (sub)-monolayer have been observed by STM or LEED measurements on Ag(111) and Ag(110) [15,54], and on the In-terminated (111)A-(2×2) reconstructed surfaces of InSb and InAs [55]. Coincident structures have been found on reconstructed Au(111) and Au(100) [56], on graphite(0001) [42], and on Ag(110) [47].

Fig. 2.7 shows the commensurate epitaxial relation between the Ag(111) surface and the

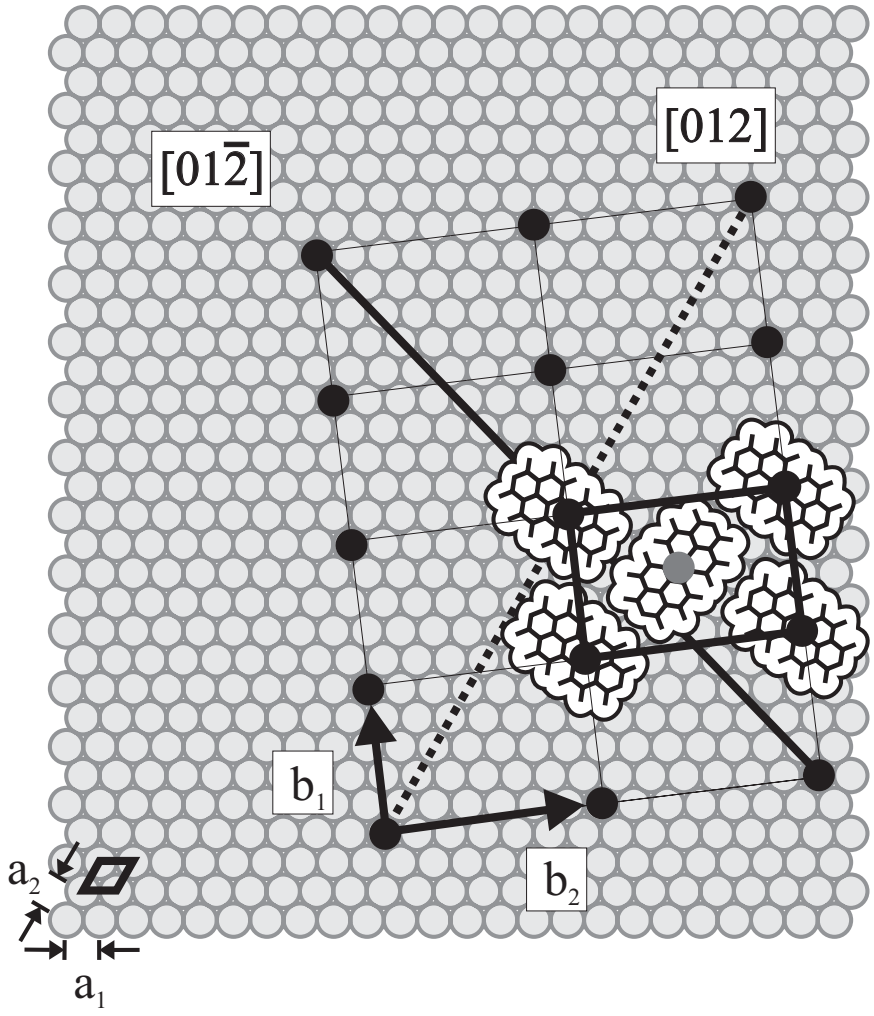

Figure 2.7: Commensurate structure of a monolayer PTCDA on Ag(111) in real-space. The circles represent the hexagonal Ag(111) surface with the in-plane lattice vectors $\mathbf{a}_1$ and $\mathbf{a}_2$. The orientation of the molecules in the in-plane unit mesh of PTCDA with the lattice vectors $\mathbf{b}_1$ and $\mathbf{b}_2$ is indicated.

2D structure of a monolayer of PTCDA. The gray circles represent the Ag surface atoms. The lattice points of the adsorbate lattice which coincide with the substrate lattice are shown in black. The matrix describing the structure is [15]

$$[C] = \begin{bmatrix} 6 & 1 \\ -3 & 5 \end{bmatrix}. \tag{2.5}$$

The monolayer structure of PTCDA/Ag(111) is approximately rectangular with $b_1 = 19.0$ Å, $b_2 = 12.6$ Å, and the angle $\gamma = 89°$ between both lattice vectors [15]. To clarify the relation between adsorbate and substrate, the orientation of the adsorbed molecules in the unit cell is shown. The adsorbate sites of the two molecules in the unit cell, the one aligned along Ag[01] (bulk notation: Ag[22$\bar{4}$]) and the other aligned along Ag[4$\bar{3}$] (bulk notation: Ag[5$\bar{7}$2]), are

phase	ϵ [10] [%]	ϵ [01] [%]	ϵ [12] [%]
α	4.8	-5.1	-1.4
β	1.6	-1.2	-0.2

Table 2.3: Strain of the α and β phase of the PTCDA bulk polymorphs, calculated for b_1, b_2, and for the diagonal of two unit cells relative to the monolayer structure.

inequivalent. Due to the hexagonal symmetry of the Ag(111) surface, the two-dimensional PTCDA unit cell orders in 6 domains (three azimuthal domains and 3 mirror domains) on the substrate.

The adsorbate structure has been explained by the relatively weak, nondissociative bonding of the PTCDA molecules on the Ag(111) surface with covalent contributions [16,57], and by the similarity of the (102) plane of the PTCDA β phase to the monolayer structure [15]. Table 2.3 summarizes the strain ϵ of the bulk polymorphs relative to the monolayer structure. The strain has been calculated for the PTCDA[10], the [01] and the [12] directions, according to

$$\epsilon = \frac{l - l_{ref}}{l_{ref}} \tag{2.6}$$

where l is the bulk value and l_{ref} the corresponding reference value of the monolayer structure. The β-structure is less strained than the α-structure, and the calculated strain for β is less than 2 % for the low-index directions.

2.3.3 Thin epitaxial PTCDA films on different substrates

PTCDA is one of the most thoroughly studied organic materials for crystalline thin film growth. Nevertheless, comparatively few structural studies of epitaxial PTCDA films thicker than a few monolayers have been performed, most of them examining only a limited range of growth parameters. In the following, the results of these studies will be summarized.

For several substrates it has been shown that even for large film thicknesses the molecular plane is parallel to the substrate [16]. In some cases, a transition from the monolayer structure to a different structure as a function of the thickness has been observed. For PTCDA/InAs(001) (4×2)/c(8×2) [46], PTCDA/Au(100) [58], and PTCDA/graphite [42], it has been observed that both structures have a similar molecular arrangement as the PTCDA(102) plane, but slightly different lattice parameters (see Fig. 2.8 (a)). This molecular arrangement is called herringbone structure. For PTCDA/Ag(110) [47], a transition

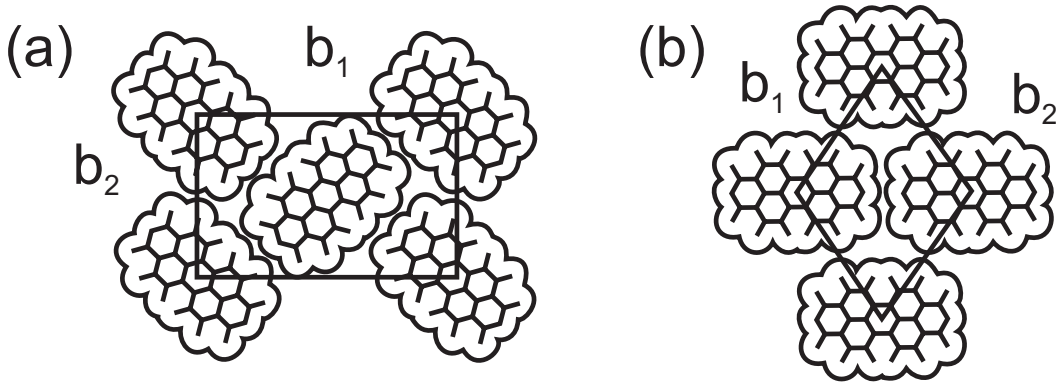

Figure 2.8: In-plane structures of PTCDA. (a) Herringbone structure, similar to PTCDA(102) of the bulk polymorphs. (b) Brick structure.

between the brick structure, shown in Fig. 2.8 (b), and the herringbons structure has been observed.

The morphology of the PTCDA films varies between smooth structures and separate crystallites on a micrometer scale. The crystallite morphology has been observed for PTCDA/Au(111) [59], PTCDA/InAs(001) (4×2)/c(8×2) [46], and PTCDA/NaCl(001), KCl(001) and KBr(001) [60]. Smooth films have been observed on graphite [42, 61], and on Au(111) [59].

PTCDA/Au(111) grows in the herringbone structure. The structure and the morphology of this system have been studied in detail as a function of the growth parameters [48,59,62]. Films grown at 290 K are smooth and show no significant strain relaxation with increasing film thickness. Films grown temperatures higher than 373 K show a significant strain relaxation with increasing film thickness and form three-dimensional islands.

As already mentioned, PTCDA has two bulk polymorphs. The coexistence of the two bulk polymorphs α and β has been observed for PTCDA/NaCl(001), KCl(001) and KBr(001) [50,53,60,63], but also for PTCDA/Ag(111) [64]. The studies indicate that the α-ploymorph is energetically favored.

These examples show that the structure and the morphology of PTCDA are manifold. They vary with the substrate material and the growth parameters. In this study, we will concentrate on the structure and morphology of PTCDA on Ag(111) as a function of the growth parameters, in order to understand the complex structure formation.

Chapter 3

Kinematic theory of X-ray scattering

In this section, we will summarize some aspects of the kinematic theory of X-ray scattering, with special focus on the specular X-ray scattering from thin films. For a more detailed information about the basic principles, the reader is referred to [65–71]. The kinematic scattering theory will be used in the Chapters 6, 7, and 8 to get information about the structure, the morphology and the growth mode of PTCDA. Here, we refer to the aspects relevant for the specular scattering of PTCDA/Ag(111), and to the in-plane reflections of a monolayer PTCDA on Ag(111).

3.1 Introduction

The kinematic scattering theory neglects multiple scattering. It can be applied to small crystals where only single scattering processes occur. The scattering intensity of a fully coherent X-ray beam is $I(\mathbf{q}) = |S(\mathbf{q})|^2$, with the momentum transfer $\mathbf{q} = \mathbf{k}_f - \mathbf{k_i}$ and the wave vectors $\mathbf{k}_i$ and $\mathbf{k}_f$ of the incident and the diffracted beam.

In reality, the X-ray beam is only partially coherent. The illuminated sample volume is much larger than the coherence volume which is the volume in which the X-ray beam can be approximated by a plane wave. The intensity of the scattering with the momentum transfer $\mathbf{q}$ is the ensemble average over the scattered intensity of an arbitrary coherence volume. If the sample consists of several mosaic blocks (see Fig. 3.1) which differ sufficiently in orientation, their scattering adds up incoherently. In this situation, it is sufficient to perform the ensemble average over the scattered intensity of an arbitrary mosaic block with the volume V_{MB}. The average scattering of a mosaic block is

$$I\left(\mathbf{q}\right) = \langle |S\left(\mathbf{q}\right)|^2 \rangle \tag{3.1}$$

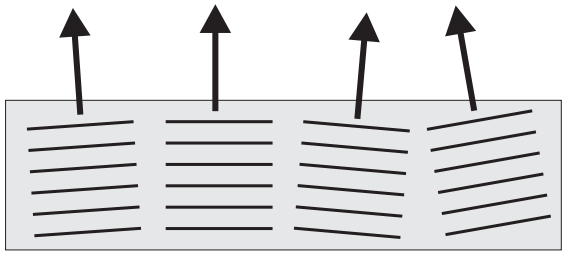

Figure 3.1: Schematic of a mosaic crystal. The orientation of the mosaic blocks is indicated.

with the scattering amplitude

$$S(\mathbf{q}) = \sum_{\mathbf{r}\in V_{MB}} F(\mathbf{q})\, e^{i\mathbf{qr}}. \tag{3.2}$$

$F(\mathbf{q})$ is the structure factor of a unit cell located at the position $\mathbf{r}$. The structure factor of a unit cell with M atoms with the atomic form factors $f_m(\mathbf{q})$ located at the positions $\mathbf{r_m}$ is

$$F(\mathbf{q}) = \sum_{m=1}^{M} f_m(\mathbf{q}) e^{i\mathbf{qr_m}}. \tag{3.3}$$

3.2 Structure factor of PTCDA and Ag

The structure factor of a unit cell depends on the direction of the scattering vector $\mathbf{q}$ relative to the atomic arrangement in the unit cell. If $\mathbf{q} = (0, 0, q_z)$, and if the atoms of the unit cell are situated at the positions $\mathbf{r}_m = (x_m, y_m, 0)$, the exponent $i\mathbf{qr}_m$ equals 0, and Eq. 3.3 reduces to

$$F(q_z) = \sum_{m=1}^{M} f_m(q_z). \tag{3.4}$$

This situation is given for the specular scattering of PTCDA(102) on Ag(111), since the molecular plane of PTCDA coincides with the (102) plane of the bulk crystal, and q_z is perpendicular to the molecular plane. Fig. 3.2 shows the coordinate system relative to the molecular plane used for the calculation of the structure factor. For the calculation of the structure factors of the substrate and of the film, $F_S(q_z)$ and $F_F(q_z)$, we have used the atomic form factors

$$f(q) = f_0(q) + f' + if'' \tag{3.5}$$

where f' and f'' are the dispersion corrections for the used wavelength. They show only a small depencence on q which is neglected here. f_0 has been approximated by

$$f_0(q) = \sum_{i=1}^{4} a_i \exp b_i \left(\frac{q}{4\pi}\right)^2 + c. \tag{3.6}$$

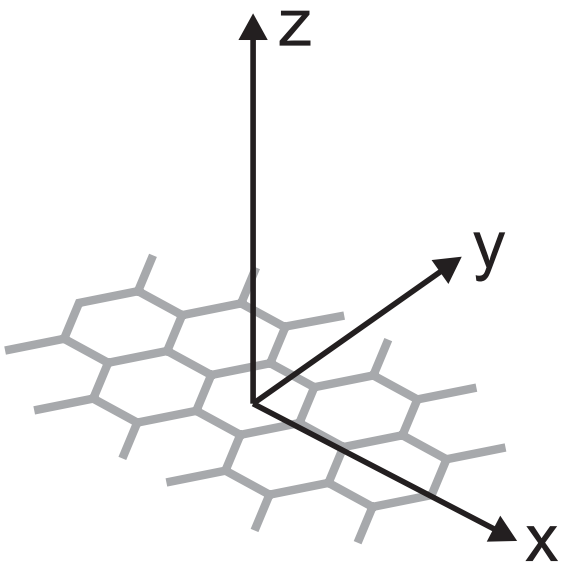

Figure 3.2: For the calculation of the structure factor of PTCDA(102) with $\mathbf{q} = (0, 0, q_z)$.

The scattering amplitude of the film has been calculated from the scattering amplitudes of two molecules,

$$F_F(q_z) = 2\left(24 f_C(q_z) + 6 f_O(q_z)\right), \tag{3.7}$$

each with 24 carbon atoms with the atomic form factor $f_C(q_z)$ and 6 oxygen atoms with the atomic form factor $f_O(q_z)$. The hydrogen atoms have been neglected. The scattering amlitude of the substrate is the sum of the atomic form factors $f_{Ag}(q_z)$ of the 4 atoms in

Parameter	C	O	Ag
a_1	2.31	3.0485	19.2808
a_2	1.02	2.2861	16.6885
a_3	1.5886	1.5463	4.0845
a_4	1.865	0.867	1.0463
b_1	20.8439	13.2771	0.6446
b_2	10.2075	5.7011	7.4726
b_3	0.5687	0.3239	24.6605
b_4	51.12	32.9089	99.8156
c	0.2156	0.2508	5.176
f'	0.017	0.047	-0.06
f''	0.009	0.032	4.284

Table 3.1: Parameters used for the calculation of the atomic scattering factor [69]

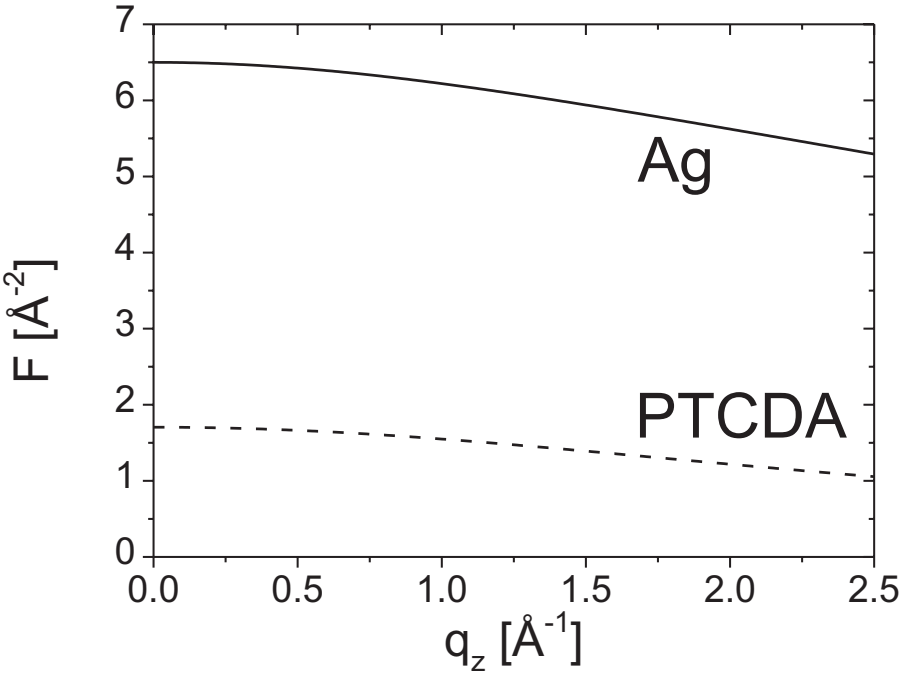

Figure 3.3: Scattering factor per unit area for the specular scattering of PTCDA and Ag.

the fcc unit cell,

$$F_F(q_z) = 4 f_{Ag}(q_z). \tag{3.8}$$

Tab. 3.1 summarizes the parameters used for the calculation of $F_F(q_z)$ and $F_S(q_z)$, taken from reference [69]. In general, a mosaic block consisting of a substrate covered by a film contains a different number of substrate and film scatterers. Therefore, the scattering factor per unit area shown in Fig. 3.3 is an appropriate measure for the scattering of the substrate and the film.

3.3 Specular and diffuse scattering

3.3.1 Introduction

The scattered intensity of a mosaic block, $I(\mathbf{q}) = \langle |S(\mathbf{q})|^2 \rangle$, is the sum of the diffuse intensity, I_{diff}, and the Bragg intensity, I_B. We can write

$$\begin{aligned} I(\mathbf{q}) &= \left(\langle |S(\mathbf{q})|^2 \rangle - |\langle S(\mathbf{q}) \rangle|^2 \right) + |\langle S(\mathbf{q}) \rangle|^2 \\ &= I_{diff}(\mathbf{q}) + I_B(\mathbf{q}), \end{aligned} \tag{3.9}$$

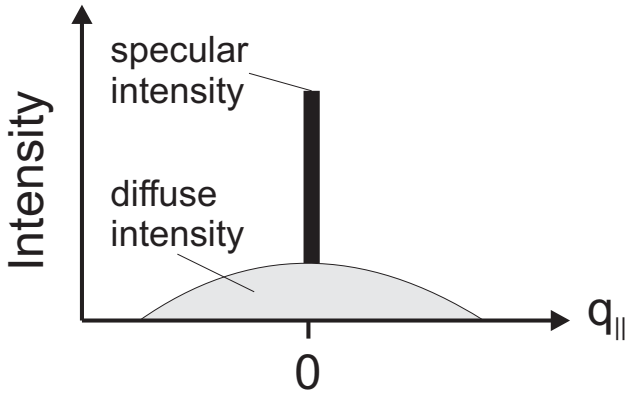

Figure 3.4: Schematic of the specular and diffuse component of the scattered intensity.

with $I_{diff}(\mathbf{q}) = (\langle|S(\mathbf{q})|^2\rangle - |\langle S(\mathbf{q})\rangle|^2)$ and $I_B(\mathbf{q}) = |\langle S(\mathbf{q})\rangle|^2$. In Sec. 3.3.2, we will show this equation explicitly for a rough substrate.

The Bragg intensity is the part of the scattered intensity which is a δ-function at $\mathbf{q}_\parallel = \mathbf{G}_\parallel$. $\mathbf{q}_\parallel$ is the component of $\mathbf{q}$ parallel to the substrate surface, and $\mathbf{G}_\parallel$ the respective component of a reciprocal lattice vector, $\mathbf{G}$. The specular scattering, $I_{spc}(\mathbf{q})$, is the Bragg scattering for $\mathbf{q}_\parallel = 0$. The specular scattering of a (multi-) layer on a substrate contains information on the average sample structure. The diffuse scattering contains information on the roughness correlation of surfaces and interfaces. Fig. 3.4 shows a schematic of the specular and the diffuse scattering as a function of $\mathbf{q}_\parallel$ at a fixed q_z. Experimentally, the specular and the diffuse scattering can be separated by measuring the scattered intensity at $\mathbf{q}_\parallel = 0$ and at a position $\mathbf{q}_\parallel = \delta\mathbf{q}_\parallel$ near the specular position since the diffuse scattering varies on a larger length scale than the specular scattering.

3.3.2 Rough substrate

In the following, we will show Eq. 3.9 for a mosaic crystal with the lattice constants d_x, d_y and $d_z = d_S$. Each mosaic block covers the area $A_{MB} = N_x d_x N_y d_y$ of the sample surface, where N_x and N_y are the number of unit cells in x and y direction, and has an infinite number of layers in z-direction. The surface of the mosaic block is described by the local height, $\tilde{z}(\mathbf{r}_\parallel) = \tilde{n}_z(\mathbf{r}_\parallel)d_S$, with the local number of layers, $\tilde{n}_z(\mathbf{r}_\parallel)$, and the average height, $z_0 = 0$. The position of each unit cell is given by the lattice vector $\mathbf{r} = \mathbf{r}_\parallel + \mathbf{r}_\perp$ (see Fig. 3.5). The scattering amplitude of a rough substrate is

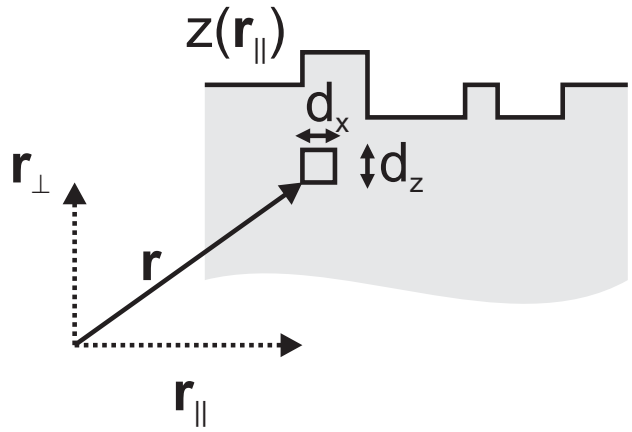

Figure 3.5: The local surface height of a rough substrate is $z(\mathbf{r}_\parallel)$. The position of each unit cell of the with the lattice parameters d_x, d_y, and d_z is given by the lattice vector $\mathbf{r}$ with the components $\mathbf{r}_\parallel$ and $\mathbf{r}_\perp$ parallel and perpendicular to the surface.

$$\begin{aligned} S(\mathbf{q}) &= F(\mathbf{q}) \sum_{\mathbf{r}\in V_{MB}} e^{i\mathbf{q}\mathbf{r}} \\ &= F(\mathbf{q}) \sum_{\mathbf{r}_\parallel \in A_{MB}} e^{i\mathbf{q}_\perp \mathbf{r}_\parallel} \sum_{r_\perp=-\infty}^{\tilde{z}(\mathbf{r}_\parallel)} e^{iq_z r_\perp} \\ &= F_S(\mathbf{q}) \frac{1}{1-e^{-iq_z d_S}} \sum_{\mathbf{r}_\parallel \in A_{MB}} e^{iq_z \tilde{z}(\mathbf{r}_\parallel)} e^{i\mathbf{q}_\parallel \mathbf{r}_\parallel}. \end{aligned} \tag{3.10}$$

For a smooth substrate with $\tilde{z}(\mathbf{r}_\parallel) = z_0 = 0$, this is

$$S_S(\mathbf{q}) = N_x N_y F(\mathbf{q}) \frac{1}{1-e^{-iq_z d_S}}. \tag{3.11}$$

Calculation of $\langle |S(\mathbf{q})|^2 \rangle$

The scattered intensity of a rough substrate is

$$\begin{aligned} \langle |S(\mathbf{q})|^2 \rangle &= \left| \frac{S_S(\mathbf{q})}{N_x N_y} \right|^2 \left\langle \sum_{\mathbf{r}_\parallel, \mathbf{r}'_\parallel} e^{iq_z\left(\tilde{z}(\mathbf{r}_\parallel) - \tilde{z}(\mathbf{r}'_\parallel)\right)} e^{i\mathbf{q}_\parallel\left(\mathbf{r}_\parallel - \mathbf{r}'_\parallel\right)} \right\rangle \\ &= \left| \frac{S_S(\mathbf{q})}{N_x N_y} \right|^2 \sum_{\mathbf{r}_\parallel, \mathbf{r}'_\parallel} e^{-\frac{\Delta q^2}{2} g\left(\mathbf{r}_\parallel - \mathbf{r}'_\parallel\right)} e^{i\mathbf{q}_\parallel\left(\mathbf{r}_\parallel - \mathbf{r}'_\parallel\right)} \end{aligned} \tag{3.12}$$

with $g\left(\mathbf{r}_\parallel - \mathbf{r}'_\parallel\right) = \left\langle \left(\tilde{z}\left(\mathbf{r}_\parallel\right) - \tilde{z}\left(\mathbf{r}'_\parallel\right)\right)^2 \right\rangle$ and the deviation Δq from the nearest specular Bragg reflection. Here we assume that $\tilde{z}\left(\mathbf{r}_\parallel\right) - \tilde{z}\left(\mathbf{r}'_\parallel\right)$ is a Gaussian random variable with the standard deviation σ.

In order to separate the part of Eq. 3.12 which is a δ-function in $\mathbf{q}_\parallel$, we write $e^{-\frac{\Delta q^2}{2}g\left(\mathbf{r}_\parallel-\mathbf{r'}_\parallel\right)}$ as the sum of the constant $e^{-(\Delta q\sigma)^2}$ and the function

$$H\left(\mathbf{r}_\parallel-\mathbf{r'}_\parallel\right)=e^{-\frac{\Delta q^2}{2}g\left(\mathbf{r}_\parallel-\mathbf{r'}_\parallel\right)}-e^{-(\Delta q\sigma)^2}. \tag{3.13}$$

The limiting values of $g\left(\mathbf{r}_\parallel-\mathbf{r'}_\parallel\right)$ are $g\left(0\right)=0$ and $g\left(|\mathbf{r}_\parallel-\mathbf{r'}_\parallel|\rightarrow\infty\right)=2\sigma^2$. Therefore,

$$e^{-\frac{\Delta q^2}{2}g\left(\mathbf{r}_\parallel-\mathbf{r'}_\parallel\right)}\rightarrow e^{-(\Delta q\sigma)^2}\quad\text{for}\quad|\mathbf{r}_\parallel-\mathbf{r'}_\parallel|\rightarrow\infty,$$

and $H\left(|\mathbf{r}_\parallel-\mathbf{r'}_\parallel|\rightarrow\infty\right)=0$. In contrast to $g\left(\mathbf{r}_\parallel-\mathbf{r'}_\parallel\right)$, the function $H\left(\mathbf{r}_\parallel-\mathbf{r'}_\parallel\right)$ has no constant part. With this, we write Eq. 3.12 as

$$\begin{aligned}\langle|S\left(\mathbf{q}\right)|^2\rangle &= \left|\frac{S_S\left(\mathbf{q}\right)}{N_xN_y}\right|^2\sum_{\mathbf{r}_\parallel,\mathbf{r'}_\parallel}\left[\left(H\left(\mathbf{r}_\parallel-\mathbf{r'}_\parallel\right)-e^{-(\Delta q\sigma)^2}\right)+e^{-(\Delta q\sigma)^2}\right]e^{i\mathbf{q}_\parallel\left(\mathbf{r}_\parallel-\mathbf{r'}_\parallel\right)}\\ &= \left|\frac{S_S\left(\mathbf{q}\right)}{N_xN_y}\right|^2\sum_{\mathbf{r}_\parallel,\mathbf{r'}_\parallel}\left(H\left(\mathbf{r}_\parallel-\mathbf{r'}_\parallel\right)-e^{-(\Delta q\sigma)^2}\right)e^{i\mathbf{q}_\parallel\left(\mathbf{r}_\parallel-\mathbf{r'}_\parallel\right)}+\\ &\quad\left|S_S\left(\mathbf{q}\right)\right|^2\ \delta\left(\mathbf{q}_\parallel-\mathbf{G}_\parallel\right)e^{-(\Delta q\sigma)^2}.\end{aligned} \tag{3.14}$$

The first term of equation 3.14 contains no δ-component in $\mathbf{q}_\parallel$ and is the intensity of the diffuse scattering, $I_{diff}(\mathbf{q})$. The second term, the δ-component of the scattered intensity, is the Bragg scattering, $I_B(\mathbf{q})$, which differs from 0 at $\mathbf{q}_\parallel=\mathbf{G}_\parallel$.

Calculation of $|\langle S(\mathbf{q})\rangle|^2$

In this section we show that the Bragg scattering equals $|\langle S\left(\mathbf{q}\right)\rangle|^2$. The average scattering amplitude of the substrate is

$$\begin{aligned}\langle S\left(\mathbf{q}\right)\rangle &= \frac{S_S\left(\mathbf{q}\right)}{N_xN_y}\left\langle\sum_{\mathbf{r}_\parallel\in A_{MB}}e^{iq_z\tilde{z}\left(\mathbf{r}_\parallel\right)}e^{i\mathbf{q}_\parallel\mathbf{r}_\parallel}\right\rangle\\ &= \delta\left(\mathbf{q}_\parallel-\mathbf{G}_\parallel\right)S_S\left(\mathbf{q}\right)\sum_z P(z)e^{iq_zz}.\end{aligned} \tag{3.15}$$

Here we have used the assumption that $\tilde{z}(\mathbf{r}_\parallel)$ is a random variable with the probability P(z) to find the surface height z at a arbitrary position $\mathbf{r}_\parallel$. For the specific situation of a Gaussian distribution of z with the standard deviation σ, the average scattering amplitude is

$$\langle S\left(\mathbf{q}\right)\rangle=\delta\left(\mathbf{q}_\parallel-\mathbf{G}_\parallel\right)S_S\left(\mathbf{q}\right)\frac{\sum_z\exp\left(-\frac{z^2}{2\sigma^2}\right)e^{iq_zz}}{\sum_z\exp\left(-\frac{z^2}{2\sigma^2}\right)}. \tag{3.16}$$

Eq. 3.16 can be solved analytically if we approximate the sum over z by an integral. With $q_z=q_l+\Delta q$ where Δq is the deviation from the nearest specular Bragg reflection at the

position $q_l = l2\pi/d_z$, Eq. 3.16 reduces to

$$\begin{aligned}\langle S(\mathbf{q})\rangle &= \delta\left(\mathbf{q}_\parallel - \mathbf{G}_\parallel\right) S_S(\mathbf{q}) \frac{\sum_{\Delta z} e^{iq_l z} e^{i\Delta q z} \exp\left(-\frac{z^2}{2\sigma^2}\right)}{\sum_z \exp\left(-\frac{z^2}{2\sigma^2}\right)} \\ &= \delta\left(\mathbf{q}_\parallel - \mathbf{G}_\parallel\right) S_S(\mathbf{q}) \frac{\int_{-\infty}^{\infty} \exp\left(-\frac{z^2}{2\sigma^2}\right) e^{i\Delta q z} dz}{\int_{-\infty}^{\infty} \exp\left(-\frac{z^2}{2\sigma^2}\right) dz} \\ &= \delta\left(\mathbf{q}_\parallel - \mathbf{G}_\parallel\right) S_S(\mathbf{q}) \exp\left(-\frac{(\Delta q\sigma)^2}{2}\right). \end{aligned} \tag{3.17}$$

The intensity of the average scattering amplitude is

$$|\langle S(\mathbf{q})\rangle|^2 = \delta\left(\mathbf{q}_\parallel - \mathbf{G}_\parallel\right) |S_S(\mathbf{q})|^2 \exp\left(-(\Delta q\sigma)^2\right). \tag{3.18}$$

This is equivalent to the expression for the Bragg scattering derived in the last section, and with this we have shown Eq. 3.9 for the scattering of a rough substrate. We will discuss the features of the specular intensity in Sec. 3.5.

3.4 Bragg scattering of a thin film on a substrate

Now we discuss the scattering amplitude of the Bragg scattering of a rough film on a rough substrate. This will be used later for the analysis of the measured specular intensity of the system PTCDA/Ag.

The important parameters of the film/substrate system are shown in Fig. 3.6. d_S and d_F are the lattice parameters of the film and the substrate in z-direction. The distance between the first monolayer of the film and the topmost monolayer of the substrate, d_0, differs from the lattice spacing of the subsequent layers. In Chapter 6, we will see that this is the situation observed for the system PTCDA/Ag(111). The structure factor of the substrate is $F_S(q_z)$, the structure factor of the film is $F_F(q_z)$. We assume that each mosaic block of the substrate is continued by the film with the average layer number N_F. The size of the substrate and the film unit cell are different. The area of the mosaic block corresponds to $N_{xS}N_{yS}$ unit cells of the substrate and $N_{xF}N_{yF}$ unit cells of the film, respectively, where N_{xF} and N_{yF} are the number of unit cells in x- and y-direction.

Fig. 3.7 (a) shows a schematic of a rough film with the local surface height $\tilde{z}_F(\mathbf{r}_\parallel)$, and the local interface height $\tilde{z}_S(\mathbf{r}_\parallel)$. We define the interface height as the height of the first monolayer of the film. The scattering amplitude of a film on a substrate is the scattering

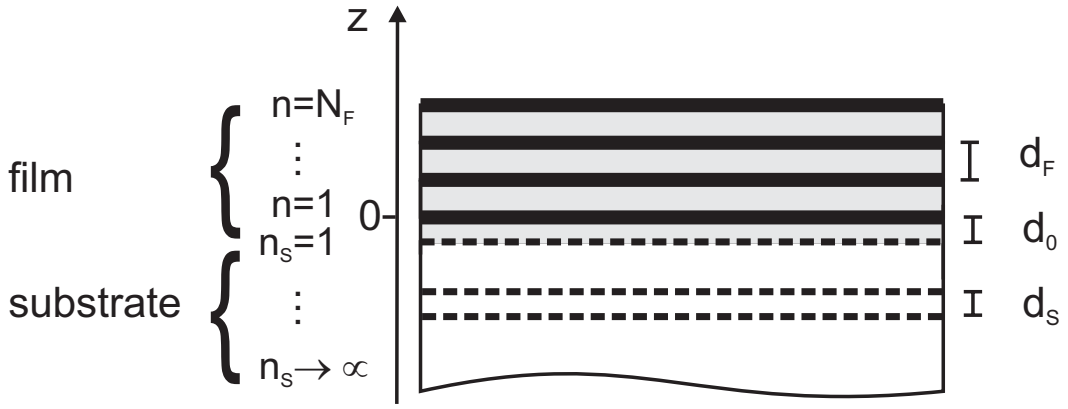

Figure 3.6: Schematic of the a smooth film on a smooth substrate. The lattice parameters of the substrate and the film are indicated.

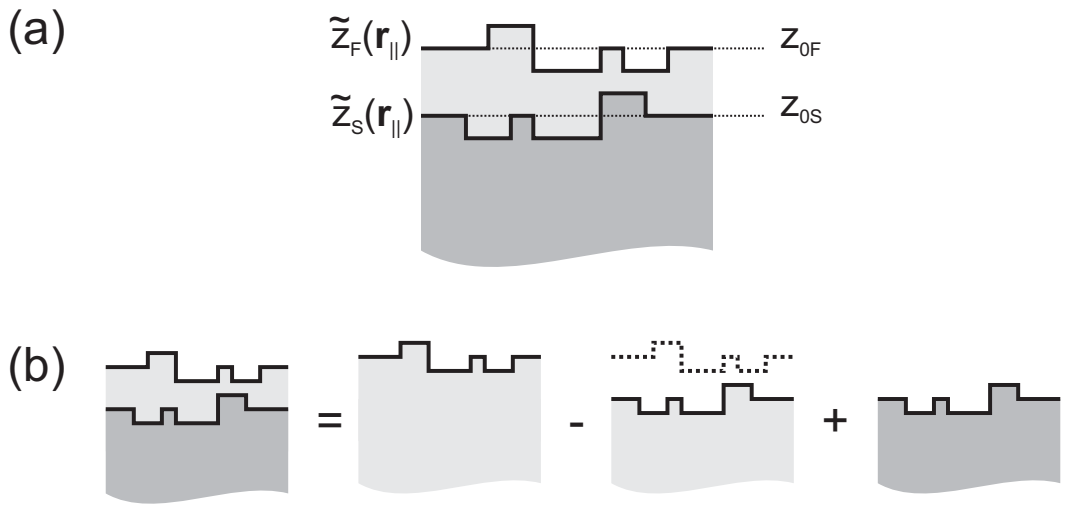

Figure 3.7: (a) Schematic of the a rough film on a rough substrate. The interface height, $\tilde{z}_S(\mathbf{r}_\parallel)$, is the height of the first monolayer of the film and has the average value $z_{0S} = 0$. The film surface, $\tilde{z}_F(\mathbf{r}_\parallel)$, has the average value $z_0F = (N_F - 1)d_F$. (b) Illustration of the relation between the scattering of a rough film on a substrate and the scattering of a substrate.

amplitude of a film with an infinite number of layers and the surface $\tilde{z}_F(\mathbf{r}_\parallel)$, minus the scattering amplitude of a film with an infinite number of layers and the surface $\tilde{z}_S(\mathbf{r}_\parallel) - d_0$, plus the scattering amplitude of the substrate with the surface $\tilde{z}_S(\mathbf{r}_\parallel) - d_0$. Therefore, the separation of the diffuse and the specular scattering of a film on a substrate follows essentially the same calculation as discussed in the last section, and we use directly the expression

$I_{spc}(\mathbf{q}) = |\langle S(\mathbf{q})\rangle|^2$. The average structure factor of the system is

$$\begin{aligned}\langle S(\mathbf{q})\rangle &= \left\langle F_S(\mathbf{q}) \sum_{\mathbf{r}_S \in V_{MB}} e^{i\mathbf{q}\mathbf{r}_S} + F_F(\mathbf{q}) \sum_{\mathbf{r}_F \in V_{MB}} e^{i\mathbf{q}\mathbf{r}_F} \right\rangle \\ &= \left\langle F_S(\mathbf{q}) \sum_{\mathbf{r}_{\parallel S} \in A_{MB}} e^{i\mathbf{q}_\parallel \mathbf{r}_{\parallel S}} \sum_{r_{\perp S}=-\infty}^{\tilde{z}(r_{\parallel S})-d_0} e^{iq_z r_{\perp S}} \right. \\ &\quad \left. + F_F(\mathbf{q}) \sum_{\mathbf{r}_{\parallel F} \in A_{MB}} e^{i\mathbf{q}_\parallel \mathbf{r}_{\parallel F}} \sum_{r_{\perp_F}=\tilde{z}_S(\mathbf{r}_\parallel)}^{\tilde{z}(r_{\parallel F})} e^{iq_z r_{\perp F}} \right\rangle. \end{aligned} \tag{3.19}$$

$\mathbf{r}_S$ and $\mathbf{r}_S$ are the lattice vectors of the substrate and the film unit cells. Their components parallel and perpendicular to the surface are denoted by the subscript $\parallel$ and $\perp$. In the last section, we calculated the first part of this sum (without the phase shift due to d_0). The average of the second part is

$$\begin{aligned}\langle S'_F(\mathbf{q})\rangle &= F_F(\mathbf{q}) \left\langle \sum_{\mathbf{r}_{\parallel F} \in A_{MB}} e^{i\mathbf{q}_\parallel \mathbf{r}_{\parallel F}} \sum_{r_{\perp_F}=\tilde{z}_S(\mathbf{r}_\parallel)}^{\tilde{z}(\mathbf{r}_{\parallel F})} e^{iq_z r_{\perp F}} \right\rangle \\ &= F_F(\mathbf{q}) \left\langle \sum_{\mathbf{r}_{\parallel F} \in A_{MB}} e^{i\mathbf{q}_\parallel \mathbf{r}_{\parallel F}}\, e^{\tilde{z}_S(\mathbf{r}_{\parallel F})} \sum_{r'_{\perp_F}=0}^{\tilde{z}_F(\mathbf{r}_{\parallel F})-\tilde{z}_S(r_{\parallel F})} e^{iq_z r'_{\perp F}} \right\rangle \\ &= F_F(\mathbf{q}) \left\langle \sum_{\mathbf{r}_{\parallel F} \in A_{MB}} e^{i\mathbf{q}_\parallel \mathbf{r}_{\parallel F}}\, e^{\tilde{z}_S(r_{\parallel F})} \sum_{n=1}^{\tilde{N}(\mathbf{r}_{\parallel F})} e^{iq_z(n-1)d_F} \right\rangle \end{aligned} \tag{3.20}$$

where $\tilde{N}(\mathbf{r}_{\parallel F})$ is the local number of layers of the film. In Sec. 3.6, we will discuss the specular scattering of a growing film. For this, it is convenient to divide the scattering amplitude of the film into the sum of the average scattering amplitudes of the individual monolayers n. If the interface height is a Gaussian variable, we can write

$$\langle S'_F(\mathbf{q})\rangle = \delta(\mathbf{q}_{\parallel F} - \mathbf{G}_{\parallel F}) N_{xF} N_{yF} F_F(\mathbf{q}) e^{\frac{\Delta q^2 \sigma_S^2}{2}} \sum_{n=1}^{\infty} \theta_n(q_z) F_F(q_z) e^{i(n-1)q_z d_F} \tag{3.21}$$

with the coverage θ_n of each monolayer, and the parallel component $\mathbf{G}_{\parallel F}$ of a reciprocal lattice vector of the film. A Gaussian height distribution of the film thickness with the standard deviation σ_F corresponds to

$$\theta_n = \frac{1}{2}\left(1 - \mathrm{erf}\left(\frac{n d_F - N_F d_F}{\sqrt{2}\sigma_F}\right)\right). \tag{3.22}$$

With the contribution of the film to the scattering amplitude,

$$S_F(\mathbf{q}) = N_{xF} N_{yF} F_F(\mathbf{q}) \sum_{n=1}^{\infty} \theta_n F_F(q_z) e^{i(n-1)q_z d_F}, \tag{3.23}$$

the average scattering amplitude of the substrate/film system is

$$\langle S(\mathbf{q})\rangle = \delta\left(\mathbf{q}_{\parallel} - \mathbf{G}_{\parallel}\right) \exp\left(-\frac{\Delta q^2 \sigma_S^2}{2}\right) \left(S_S(\mathbf{q}) e^{-iq_z d_0} + S_F(\mathbf{q})\right), \tag{3.24}$$

where σ_S is the roughness of the substrate and $\Delta q = q_z - l2\pi/d_S$ is the distance to the nearest substrate Bragg peak.

3.5 Discussion of the specular scattering

The specular intensity scattered by one mosaic block of a film on a substrate is

$$\begin{aligned} I_{spc}(\mathbf{q}) &= \delta\left(\mathbf{q}_{\parallel}\right) \exp\left(-\Delta q^2 \sigma_S^2\right) \\ &\quad \left[|S_S(\mathbf{q})|^2 + |S_F(\mathbf{q})|^2 + 2Re\left(S_S(\mathbf{q}) S_F(\mathbf{q})^* e^{-iq_z d_0}\right)\right]. \end{aligned} \tag{3.25}$$

The brackets contain the specular intensity of a smooth substrate, the specular intensity of a rough film, and a term due to the interference of the waves scattered from the substrate and from the film. The total intensity is multiplied by a Debye-Waller factor $\exp\left(-\Delta q^2 \sigma_S^2\right)$ which damps the intensity exponentially as a function of Δq_z. Δq_z is the distance to the nearest substrate Bragg peak. The damping increases with increasing substrate roughness. We will discuss the characteristic features of the intensity scattered by a smooth substrate, by a smooth film, and finally, by a rough film on a rough substrate.

The specular intensity of a smooth substrate at $\mathbf{q} = q_z \mathbf{e}_z$ is

$$I_{spc}(q_z) = N_{xS}^2 N_{yS}^2 |F_S(q_z)|^2 \frac{1}{\sin^2(\frac{1}{2} q_z d_S)} \tag{3.26}$$

with the lattice constant of the substrate, d_S, perpendicular to the surface, and the in-plane number of substrate unit cells in the mosaic block, $N_{xS} N_{yS}$. The specular intensity is distributed along the specular rod with $\mathbf{q}_{\parallel} = 0$, and peaks at the specular Bragg reflections with $q_z = l2\pi/d_S$. For Ag(111), these are the $(l\ l\ l)$ reflections. The specular intensity of a smooth film with $\theta_n = 1$ for $1 \leq n \leq N_F$, and $\theta_n = 0$ for $n > N_F$, is

$$I_{spc}(q_z) = N_{xF}^2 N_{yF}^2 |F_F(q_z)|^2 \frac{\sin^2\left(N_F q_z d_F/2\right)}{\sin^2\left(q_z d_F/2\right)}. \tag{3.27}$$

Maximum intensity is found at the position of the Bragg reflections where q_z is a reciprocal lattice vector of the film with $q_z = l2\pi/d_F$. For PTCDA(102), these are the $(l\ 0\ 2l)$ reflections. The intensity oscillates with q_z due to the finite size of the film. These oscillations are called Laue oscillations. The distance between subsequent minima is $\Delta q_z = 2\pi/N_F d_F$.

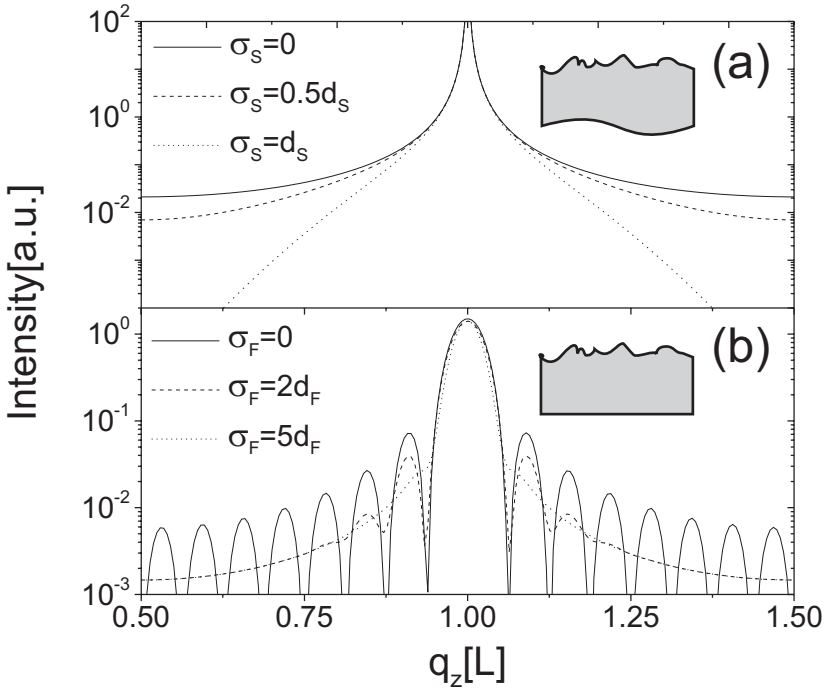

Figure 3.8: (a) Intensity of the specular rod of a rough substrate (see inset), calculated for the substrate roughness $\sigma_S = 0$, $\sigma_S = 0.5d_S$, and $\sigma_S = d_S$. (b) Intensity of the specular rod of a rough film (see inset), calculated for the film roughness $\sigma_F = 0$, $\sigma_F = 2d_F$, and $\sigma_F = 5d_F$.

Fig. 3.8 (a) shows some examples of the damping of specular intensity of a substrate with a Gaussian roughness, and Fig. 3.8 (b) shows examples for the damping of the specular intensity of a freestanding film with one smooth and one rough surface and the average layer number $N_F = 16$. The intensity has been calculated with Eq. 3.25.

Two examples of a rough film with $N_F = 16$ on a rough substrate, caculated with Eq. 3.25, are shown in Fig. 3.9 (black lines). This film thickness has been used for most of our experiments. The typical lattice parameters and electron densities of the system PTCDA/Ag(111) at room temperature have been used, and all parameters except the substrate roughness are kept constant for the two calculations. The grey line corresponds to the scattering of a clean substrate. The scattered intensity of the film/substrate system is dominated by the scattering of the substrate. The characteristic features of the intensity scattered by the film are still visible (the Bragg peak and the Laue oscillations). Due to the interference with the substrate, the Laue oscillations are asymmetric around the film Bragg peak.

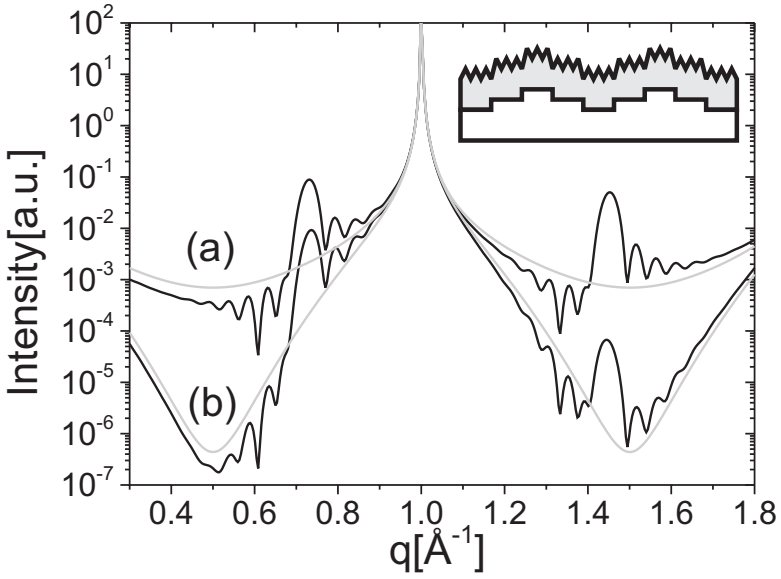

Figure 3.9: Calculated intensity of the specular crystal truncation rod of a rough sample (black lines) and the clean substrate (grey lines), calculated for (a) $\sigma_{film} = d_{film}$ and $\sigma_{sub} = 0.5 d_{sub}$, respectively (b) $\sigma_{sub} = d_{sub}$. The inset shows the model for the roughness of the sample.

3.6 *In situ* measurements at the anti-Bragg point

In the last section, we have shown that the specular X-ray intensity is sensitive to the average material distribution of a film on a substrate. Now we discuss the specular scattering of a film during its growth. In this situation, the material distribution changes as a function of the deposition time. We show how to deduce information on the time-dependent material distribution from the specular X-ray scattering. In Sec. 8.1, we will present experimental results of measurements of the specular X-ray intensity. The quantitative description of the process introduced in this section will be applied to our data in Sec. 8.2.

Within the kinematic scattering theory, the scattering amplitude of the Bragg scattering during the deposition of a film on a substrate is

$$\begin{aligned} \langle S(\mathbf{q},t)\rangle &= \delta\left(\mathbf{q}_{\parallel}-\mathbf{G}_{\parallel}\right)\exp\left(-\frac{\Delta q^2\sigma_S^2}{2}\right) \\ &\quad \left(S_S(\mathbf{q})e^{-iq_z d_0}+N_{xF}N_{yF}F_F(\mathbf{q})\sum_{n=1}^{\infty}\theta_n(t)e^{i(n-1)q_z d_F}\right). \end{aligned} \tag{3.28}$$

with the time-dependent coverages, $\theta_n(t)$. In the following, the Debye-Waller factor is ne-

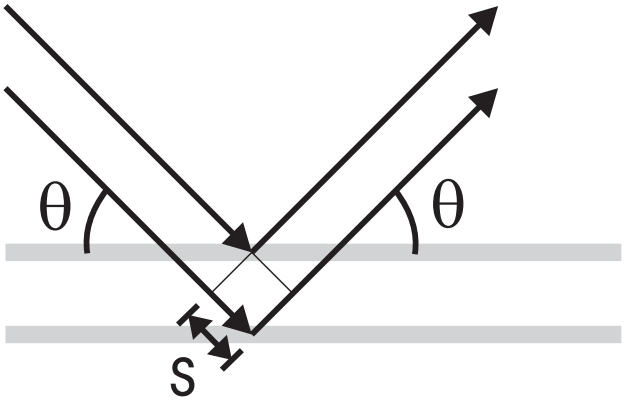

Figure 3.10: Two plane waves scattered by subsequent layers have a path length difference $2s$. At the anti-Bragg point, the path length difference is $\lambda/2$, and the waves interfere destructively.

glected since constant prefactors will be canceled by the intensity normalization we perform later. At $q = q_z^{anti} = \pi/d_F$, the path length difference $2s$ between the waves scattered by subsequent layers is $\lambda/2$ (see Fig. 3.10). The phase $q_z^{anti}(n-1)d_F$ of the X-rays scattered by subsequent layers is shifted by π, corresponding to destructive interference. Therefore, the momentum transfer q_z^{anti} is called anti-Bragg point. The scattering amplitude for the specular scattering at q_z^{anti} is

$$\langle S(t)\rangle = S_S\left(\frac{\pi}{d_{film}}\right)e^{-iq_z d_0} + N_{xF}N_{yF}F_F\left(\frac{\pi}{d_{film}}\right)\sum_{n=1}^{\infty}\theta_n(t)(-1)^{n-1}. \tag{3.29}$$

This we rewrite as

$$\langle S(t)\rangle = |R_{sub}|\,e^{i\varphi_{sub}} + |R_{film}|\,e^{i\varphi_{film}}\sum_{n=1}^{\infty}\theta_n(t)(-1)^{n-1} \tag{3.30}$$

where all growth-independent parameters of the substrate and of the film are included in the respective amplitude R and the phase φ. Assuming that the scattering amplitudes of the layers, and the lattice spacings between them, do not change during the deposition, the intensity $I(t) = |\langle S(t)\rangle|^2$ depends only on the coverage. The factor $(-1)^{n-1}$ contains the destructive interference of subsequent layers (see Fig. 3.10). All layers with odd numbers n scatter with the same phase shift modulus 2π and cannot be distinguished in the experiment at q_z^{anti}, as well as all layers with even n. Mathematically, this shows in

$$\sum_{n=1}^{\infty}\theta_n(t)(-1)^{n-1} = \sum_{n=1}^{\infty}\theta_{2n-1}(t) - \sum_{n=1}^{\infty}\theta_{2n}(t) = \theta_{odd}(t) - \theta_{even}(t) = \Delta\theta(t). \tag{3.31}$$

The intensity measurement yields direct information on the difference between the sum of the coverages of all odd and all even layers. To compare calculated and measured intensities,

it is convenient to normalize the specular intensities to the specular intensity scattered by the substrate,

$$\tilde{I}(t) = \frac{I(t)}{|R_{sub}|^2}. \tag{3.32}$$

With this normalization, $\tilde{I}(t) = 1$ before the deposition starts. From Eq. (3.30) and (3.31), we finally obtain a quadratic equation,

$$\tilde{I}(t) = 1 + 2\left[\frac{|R_{film}|}{|R_{sub}|}[\Delta\theta(t)]\right]\cos\phi + \left[\frac{|R_{film}|}{|R_{sub}|}[\Delta\theta(t)]\right]^2. \tag{3.33}$$

All phases are contained in

$$\phi = \varphi_{sub} - \varphi_{film}. \tag{3.34}$$

We now assume that each layer has a lower coverage than the respective previous one, i.e. that there are no voids in the film. From this follows $\Delta\theta \leq 1$. The solution of Eq. 3.33 with $\Delta\theta \leq 1$ is

$$\Delta\theta(t) = \frac{|R_{sub}|}{|R_{film}|}\left[-\sqrt{\tilde{I}(t) - (1-\cos^2\phi)} - \cos\phi\right]. \tag{3.35}$$

If the deposition rate, F, and the sticking coefficient are constant during growth, the total amount of deposited material at the time t is Ft. With $\theta_{even}(t) + \theta_{odd}(t) = Ft$ we write the coverage of even and odd layers as

$$\theta_{odd}(t) = \frac{1}{2}\left[\frac{|R_{sub}|}{|R_{film}|}\left[-\sqrt{\tilde{I}(t) - (1-\cos^2\phi)} - \cos\phi\right] + Ft\right] \tag{3.36}$$

$$\text{and} \qquad \theta_{even}(t) = Ft - \theta_{odd}(t). \tag{3.37}$$

In this section, we have shown how to calculate $\Delta\theta(t)$ from the specular intensity at the anti-Bragg point. For a constant deposition rate and a constant sticking coefficient, we can also calculate θ_{even} and θ_{odd}, but not the individual θ_n.

3.7 Measured intensity

The experimentally determined intensity of the specular scattering, $I_{exp}(q_z)$, deviates from the calculated intensity $I(q_z) = \langle|S(q_z)|^2\rangle$. This is due to geometric aspects (the size of the illuminated area of the sample), the scattering process itself (the polarization of the beam), and the resolution of the experiment (the energy distribution and the divergence of the incident and the diffracted beam). In the following, we will summarize the correction factors which are necessary to calculate $I_{exp}(q_z)$ from $\langle|S(q_z)|^2\rangle$. For a detailed treatment of

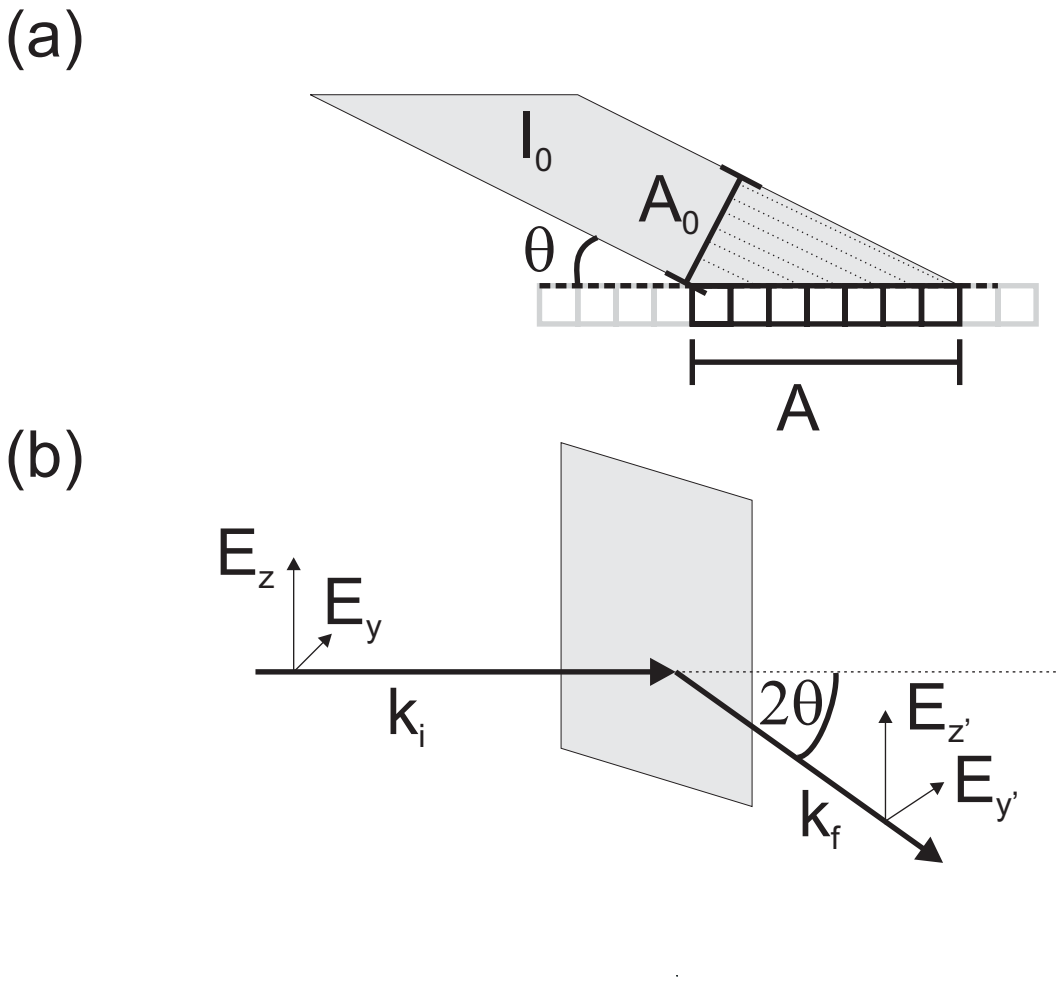

Figure 3.11: (a) Active area A, illuminated by a beam with the cross-section A_0. (b) Schematic of the scattering of a polarized incident beam with the electric field components E_z and E_y perpendicular and parallel to the scattering plane.

the corrections we refer to [65, 72, 73].

(I) Influence of the illuminated area. The active area, A, illuminated by a beam with the cross-section A_0 and the incident angle θ, is shown in Fig. 3.11 (a). The scatterer density projected on A_0 is proportional to $A = A_0/\sin\theta$. Therefore, the number of mosaic blocks projected on A_0 increases with

$$C^{area}(\theta) = \frac{1}{\sin\theta} \tag{3.38}$$

which is the area correction factor, and the scattered intensity is proportional to $C^{area}(\theta)$.

(II) Influence of the polarization. Fig. 3.11 (b) shows a schematic of the scattering of a polarized incident beam with the electric field $\mathbf{E}$ and its components E_z and E_y perpendicular

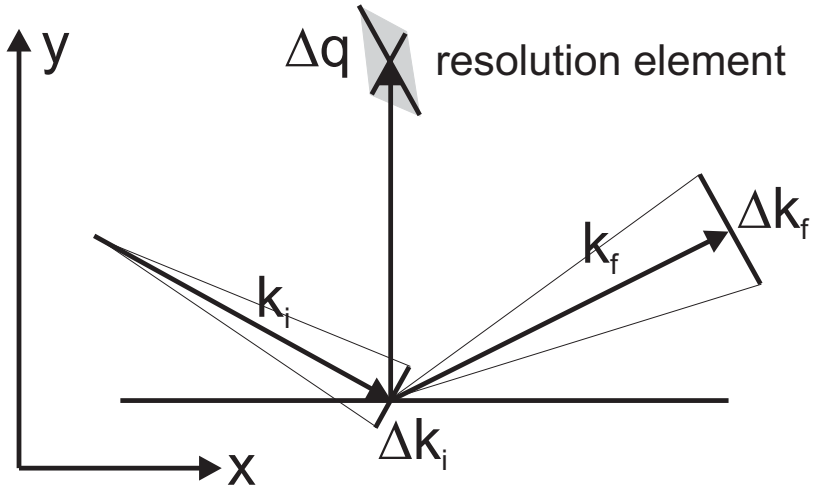

Figure 3.12: Geometric construction of the resolution element in reciprocal space. $\mathbf{k}_i$ and $\mathbf{k}_f$ are the wave vectors of the incident and the diffracted beam. Δk_i and Δk_f are the uncertainties due to the divergence of the incident and the diffracted beam. Δq is the resolution element due to the uncertainty of the momentum transfer during the scattering process.

and parallel to the scattering plane. The polarization factor is

$$C^{pol}(\theta) = \begin{cases} \cos^2(2\theta) & \text{for} \quad E = E_z \\ 1 & \text{for} \quad E = E_y. \end{cases} \tag{3.39}$$

In our case, the incident synchrotron beam is polarized perpendicular to the scattering plane of the sample, and $C^{pol} = 1$.

(III) Influence of the resolution element. Due to the divergence $\Delta\alpha_i$ and $\Delta\alpha_f$ of the incident and the diffracted beam, and due to the wave length distribution, $\Delta\lambda$, of the incident wave length, λ, the intensity measured by a detector with an infinitesimal angular acceptance integrates over an area Δq in reciprocal space. This area is called the resolution element. Its geometric construction, assuming a monochromatic incident beam ($\Delta\lambda = 0$), is shown in Fig. 3.12. The wave vectors $\mathbf{k}_i$ and $\mathbf{k}_f$ have an uncertainty $\Delta k_i = \Delta\alpha_i k$ and $\Delta k_f = \Delta\alpha_f k$ perpendicular to their direction. For the specular scattering, we find

$$\begin{aligned} \Delta q &= [(\Delta\mathbf{k}_f - \Delta\mathbf{k}_i)\cdot\mathbf{e}_x]\,[(\Delta\mathbf{k}_f - \Delta\mathbf{k}_i)\cdot\mathbf{e}_y] \\ &= \frac{1}{2}(\Delta k_f - \Delta k_i)\sin(2\theta) \\ &= \frac{1}{2}k\Delta\theta\sin(2\theta) \end{aligned} \tag{3.40}$$

with $\Delta\theta = \Delta\alpha_i - \Delta\alpha_f$. The detector integrates $I(q_z)$ over a range of θ. The transformation between the angular resolution element, $\Delta\theta$, and the resolution element in reciprocal space,

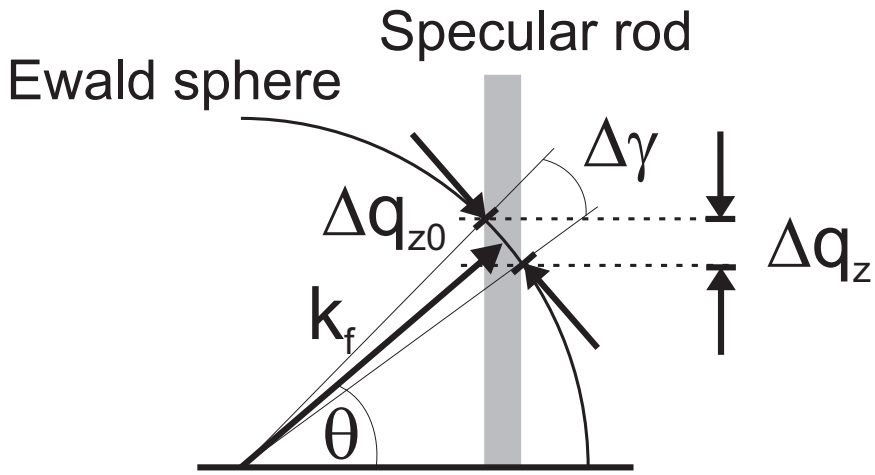

Figure 3.13: Schematic of the integration of the detector with the angular acceptance $\Delta\gamma$ over a section of the specular rod.

Δq, is taken into account by the Lorentz factor

$$C^{Lorentz}(\theta) = \frac{1}{\sin(2\theta)}. \tag{3.41}$$

(IV) Integration over the crystal truncation rod. The specular rod of a mosaic crystal has a finite size in q_x and q_y corresponding to the average lateral size of the mosaic blocks. The interception of the rod and the Ewald sphere depends on the scattering angle, as shown in Fig. 3.13. The detector with the angular acceptance $\Delta\gamma$ integrates over $\Delta q_z = \Delta q_{z0} \cos\theta$ with the integration range Δq_{z0} for $\theta = 0$. If $I(q_z)$ is approximately constant in the integration range, the measured specular intensity is proportional to the integration range. This is taken into account by

$$C^{rod}(\theta) = \cos\theta. \tag{3.42}$$

Summarizing all correction factors, the measured and the calculated intensity are related by

$$I_{exp}(q_z, \theta) = C^{area}(\theta) C^{Lorentz}(\theta) C^{rod}(\theta) C^{pol}(\theta) I(q_z). \tag{3.43}$$

3.8 In-plane reflections of PTCDA/Ag(111)

In the previous sections, we have discussed the specular scattering, referring to the system PTCDA/Ag(111). The epitaxy and the in-plane order of the thin films shows in the in-plane reflections. In Sec. 2.3.2, we have discussed the in-plane structure of a monolayer PTCDA on Ag(111) in real-space. The in-plane unit cell is nearly rectangular and similar to the in-plane unit cell of the PTCDA(102) plane. In the following, we discuss the positions of

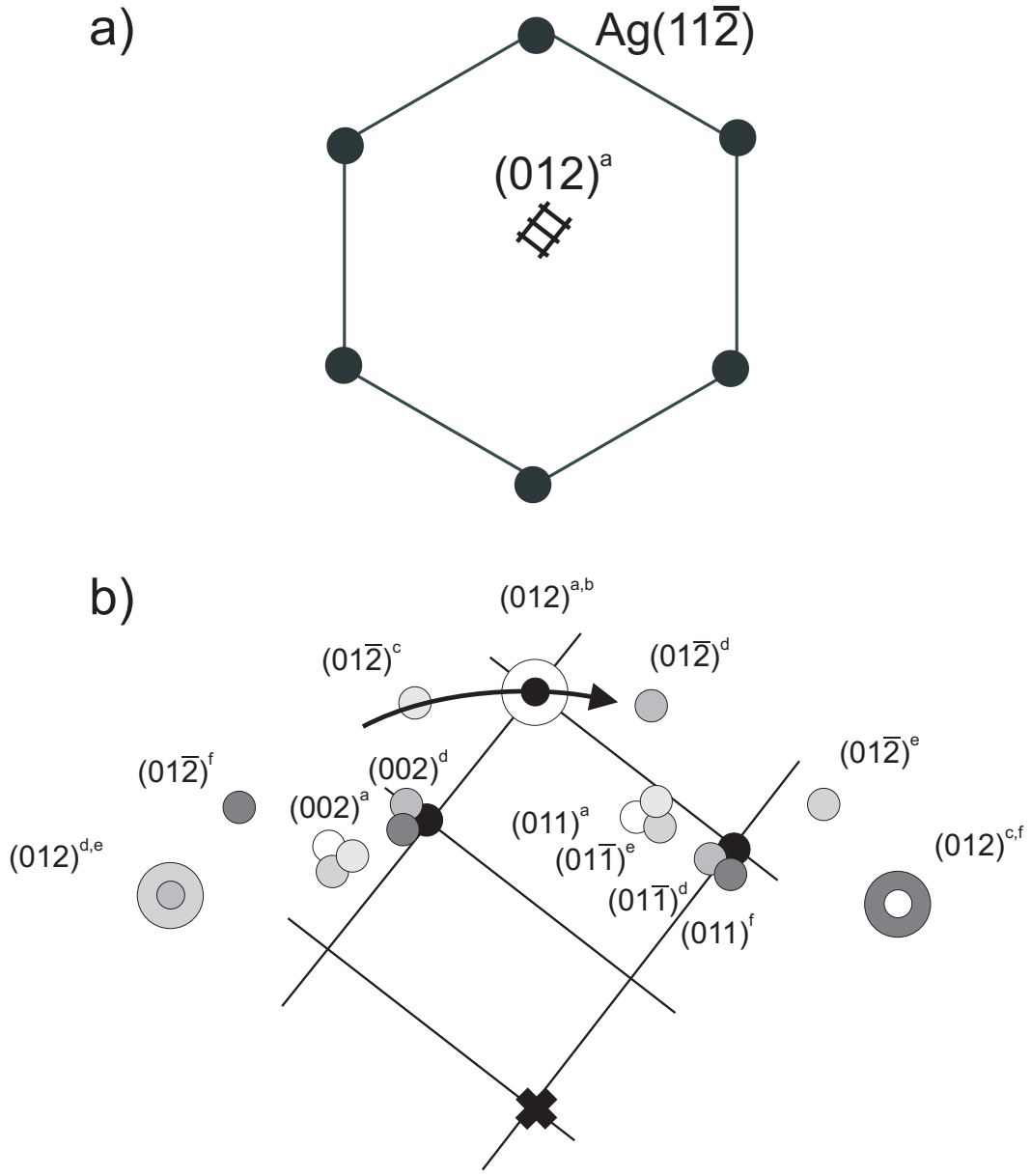

Figure 3.14: Reciprocal space map of PTCDA/Ag(111). (a) Orientation of one of the PTCDA domains relatively to the Ag unit cell. (b) PTCDA(012) and (011) type reflections of the 6 domains. The reflections of each domain are shown in different shade of gray and labeled a,b,c,d,e and f.

the in-plane reflections of a two-dimensional rectangular unit cell oriented similar to the monolayer structure.

The rectangular in-plane unit cell has the dimensions $b_1^* = 2\pi/b_1$ and $b_2^* = 2\pi/b_2$, where b_1 and b_2 define the unit cell in real-space. Fig. 3.14 (a) shows the orientation of one of the PTCDA domains (represented by two in-plane unit cells) relatively to the Ag(11$\bar{2}$) reflection. Due to the fcc structure of Ag, this reflection is forbidden. PTCDA[012], the direction of

the diagonal of two in-plane unit cells, is oriented parallel to Ag[11$\bar{2}$]. In Fig. 3.14 (b), the unit cells of this domain are shown again. The (012), the (011), and the (002) reflections of the domain are marked in black. These are the reflections we will use later on to determine the in-plane structure of our films. The reflections of the other domains, marked in different shades of gray, arise from rotational domains and mirror domains of the highlighted domain. The reflections marked in white are the reflections of the mirror domain of the highlighted domain (mirror axis: Ag[11$\bar{2}$]). All other reflections are derived from these two domains by rotations in 60° steps due to the substrate symmetry.

Chapter 4

Theory of thin film growth

4.1 Introduction

In this section, a short overview of the atomic processes during the thin film growth and of the related growth models is given. For further information, we refer to the literature, e.g. to introductory textbooks [74–78] and review articles [26], and the references therein.

Epitaxial thin film growth can be classified as homoepitaxial (substrate material = film material) and heteroepitaxial growth (substrate material $\neq$ film material). Homoepitaxial growth depends on the interaction between one type of atoms, while for heteroepitaxial growth the interaction between the substrate atoms, the interaction between the film atoms, and the interaction between substrate and film atoms has to be taken into account. These different interactions can induce strain and defects in the system. Examples for elementary growth processes are the adsorption, the surface diffusion of monomers or dimers, the island nucleation, the attachment to and detachment from step edges, the diffusion along steps, and the desorption (Fig. 4.1).

Every atomic configuration of the sample corresponds to an energy state, E. If a surface changes, e.g. by diffusion of an adatom from a lattice site a with the energy E_a to a lattice site b with the energy E_b, the adatom has to occupy energetically unfavored intermediate states, as shown in Fig. 4.2. The most unfavored excited state with the energy E^+ determines the enery barrier between initial and final state. For the diffusion of monomers on a surface, this is the surface diffusion barrier, E_D. The Ehrlich-Schwoebel barrier is a barrier for monomers jumping over a step edge, additional to the surface diffusion barrier. A phenomenological explanation for its existence is that such an atom has to assume an energetically unfavored position during the diffusion process, as shown in Fig. 4.3 (a). The asymmetric incorporation probability from atoms diffusing from the upper or lower level

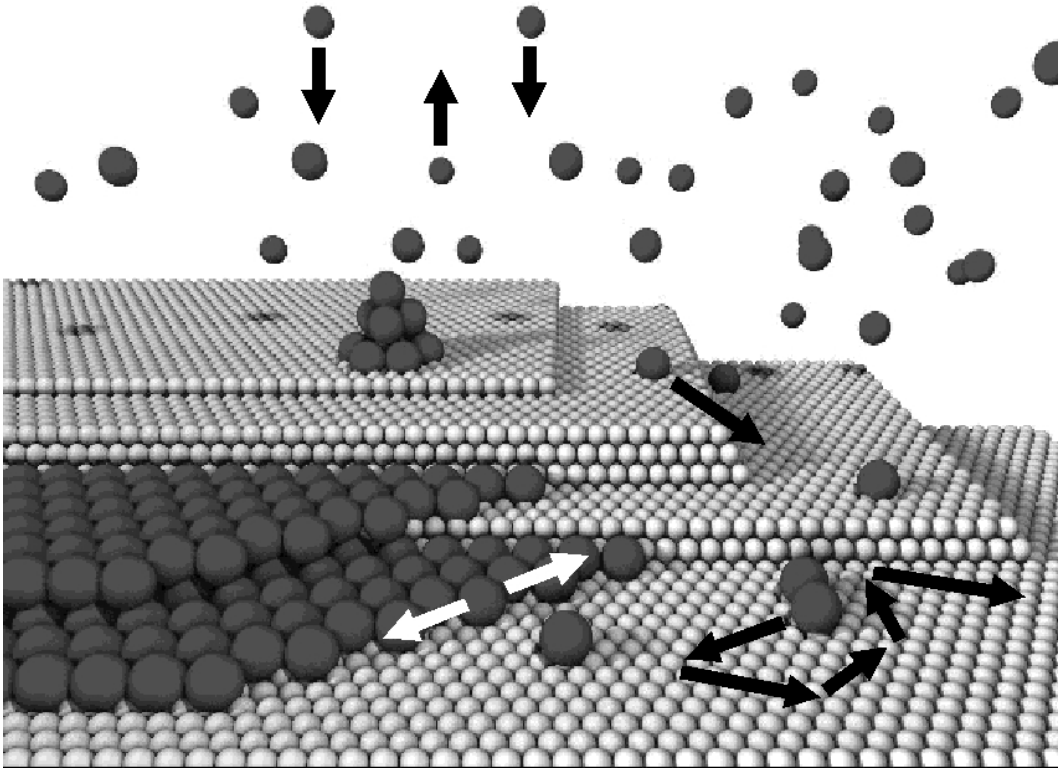

Figure 4.1: Elementary processes during MBE growth. Atoms from the gas phase adsorb on the surface. There, the monomers diffuse on terraces, incorporate in step edges, form two-dimensonal and three-dimensional clusters or desorb again into the gas phase. The arrows indicate a selection of possible processes during the deposition.

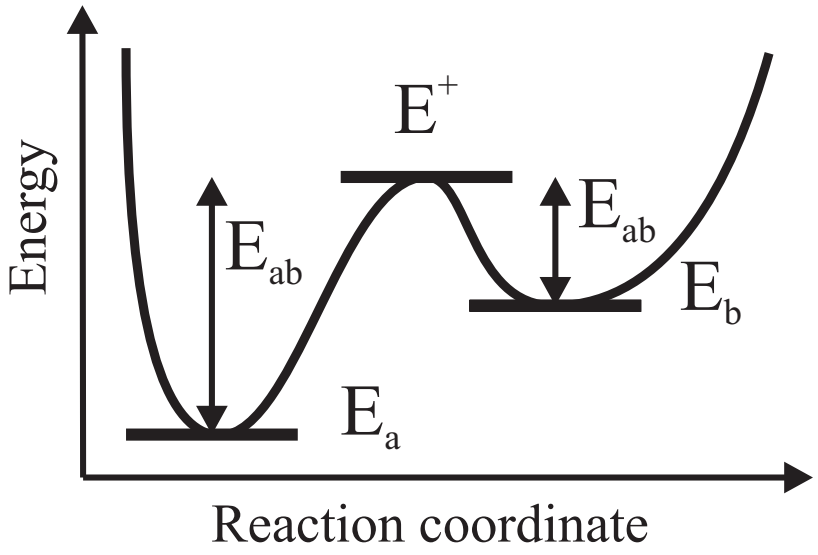

Figure 4.2: Energy of a system which changes trom state a to state b. The energy barriers E_{ab} for the transition $a \rightarrow b$ and E_b for the transition $b \rightarrow a$ are indicated, together with the energy E^+ of the most unfavored transition state.

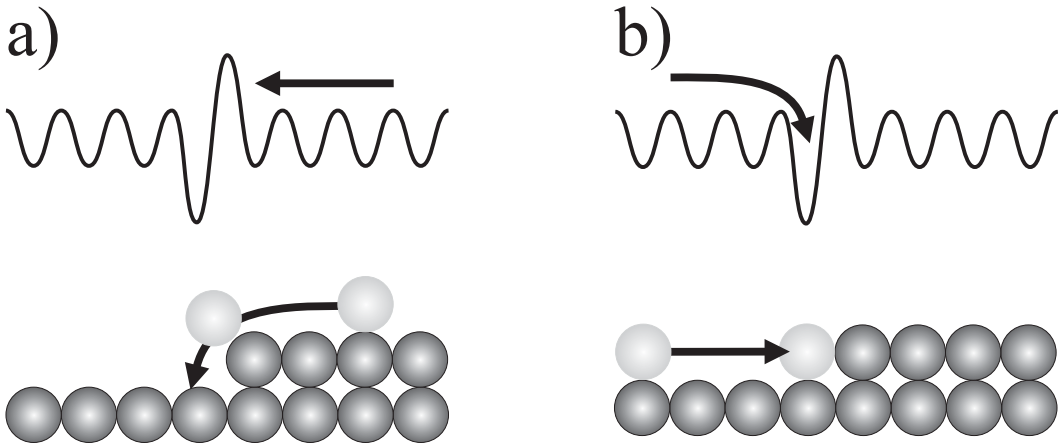

Figure 4.3: Schematic of the Ehrlich-Schwoebel barrier. (a) Monomers diffusing from the upper level to the step edge. (b) Monomers diffusing from the lower level to the step edge.

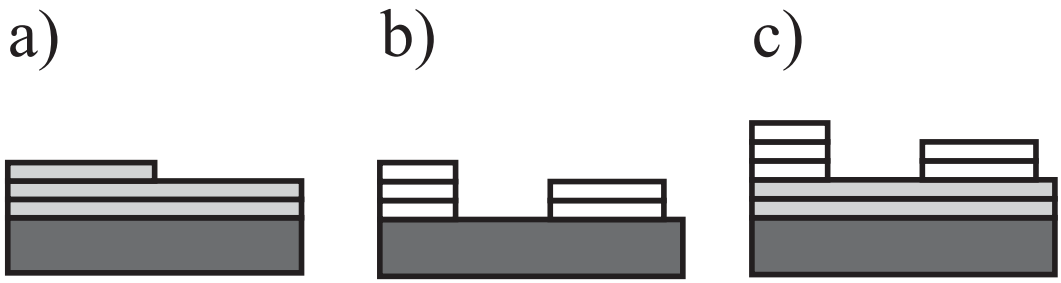

Figure 4.4: Schematic of the basic growth modes: (a) layer-by-layer growth, (b) island growth, and (c) Stransky-Krastanov growth.

to a step edge contributes to step bunching and islanding. The influence of the Ehrlich-Schwoebel barrier on the MBE growth is discussed. e.g., in the references [74, 79–81].

The microscopic growth processes discussed above lead to several epitaxial growth modes relevant on a larger scale (see Fig. 4.4). These include (a) layer-by-layer growth, also called Frank-van der Merve growth, where one monolayer grows after the other, (b) island growth (Vollmer-Weber growth), where separate islands with several monolayers height develop, and (c) Stransky-Krastanov growth, where the initial layer-by-layer growth is followed by island growth (for details see, e.g., the references [74, 76]).

For the thin film growth, in general a large range of time and length scales is important. The samples have macroscopic dimensions of the order of 10^{-2} m, while the diffusion processes take place on the atomic scale (10^{-10} m). The deposition time of a thin film is typically of the order of 10^3 s or even higher, while at room temperature the typical time scale for processes on atomic scale is of the order of the inverse Debye frequency, i.e. 10^{-10}–10^{-13} s.

The AFM and X-ray methods used in this work limit the experimentally accessible time scales and length scales. The experimental time resolution is of the order of seconds, the typical length scales are of the order of the molecular dimensions up to several micrometers.

Several theoretical methods can be applied to the growth simulation, including *ab initio* methods [82, 83], molecular dynamics simulations (MD) [84], kinetic Monte Carlo methods (MC) [81,85], and continuum methods such as the rate equation approach [26,86]. A review about different simulation methods can be found in [87]. At present, MD simulations are generally applied on a time scale of nanoseconds. For longer time scales (which applies for our data), the rate equation approach and kinetic Monte Carlo methods are appropriate. In the following, the basic ideas of Monte Carlo simulations and the rate equation approach will be presented, together with their application to the thin film growth.

4.2 Rate equations

4.2.1 Basic principles of the rate equation theory

Rate equations are used to characterize the time-dependence of a chemical reaction. If the material AB with the concentration $[AB]$ decomposes to the material A and the material B with the reaction constant k (first order reaction), the time-dependence of the concentrations is expressed by

$$\frac{d[A]}{dt} = \frac{d[B]}{dt} = -\frac{d[AB]}{dt} = k[AB]. \tag{4.1}$$

However, this effective description can be applied to any process which can be described by an initial state A with the concentration (or occurency) $[A]$, a final state B with a concentration $[B]$, and a reaction constant k determining the velocity of the transition between the initial and the final state. The problem may also be expanded to the more complex situation of several initial and final states. Depending on the complexity of the process, k can be a constant, a function of the time, the concentrations, and other parameters.

Rate equations have been introduced as a classical dynamic model for the non-equilibrium processes occuring during molecular beam epitaxy [26, 27]. The basic idea is to define a set of deterministic differential equations describing the rates of the fundamental growth processes. The rate equation model is a mean field model, i.e. the behavior of all islands of a typical size is averaged, and their lateral distribution is neglected. The rates determining the growth process are effective quantities including effects such as strain, material properties,

the influence of surface defects, etc. [86].

Rate equations have been successfully used to describe important aspects of several growth modes including layer-by-layer growth [88], island growth with and without coalescence [26,89–91], and Stransky-Krastanov growth [86,92,93]. Island densities determined from AFM images or electron micrographs [89,93], but also time-dependent RHEED and X-ray intensity measurements at the anti-Bragg condition can be explained by models based on rate equations [85,94–96]. Nevertheless, some restrictions to the application of rate equations occur. As a consequence of the oversimplified treatment, it is difficult to deduce microscopic parameters from a comparison between the simulations and the experiment. For the exact modelling of a growth scenario, the rate equation systems become very complex. It is still a challenge to develope more sophisticated rate equation models to simulate, e.g., coalescence if many layers contribute to the growth process.

4.2.2 Rate equations and X-ray diffraction experiments

In Sec. 3.6 we showed that the specular X-ray intensity measured at the anti-Bragg point is sensitive to the coverages, θ_n, of the layers, n. Cohen et al. have developed a simple rate equation model for the time-dependent coverages, $\theta_n(t)$ [88]. After solving the rate equation system, it is possible to calculate the X-ray intensity at the anti-Bragg point as a function of the coverage. This calculated intensity can be compared with the experimental data, and the observations can be related to the effective interlayer diffusion constant. In the following, the results of Cohen et al. [88] are briefly summarized.

The basic assumptions of the model are (I) that the effective flux from the layer $n+1$ to the layer n is always positive and stabilizes the film, and (II) that $\theta_n \geq \theta_{n+1}$, i.e. the film has no voids. θ_n increases due to the adsorption and the interlayer diffusion from $n+1$ to n , and decreases due to the interlayer diffusion from n to $n-1$. The adsorption rate is $F = 1/t_{ML}$ where t_{ML} is the deposition time for one monolayer. The interlayer diffusion from $n+1$ to n is assumed to be proportional to the concentration of monomers in the layer $n+1$ which, in turn, is assumed to be proportional to $\theta_n - \theta_{n+1}$. This leads to a set of coupled differential equations

$$\begin{aligned} \frac{\mathrm{d}\theta_n}{\mathrm{d}t} &= \frac{1}{t_{ML}}(\theta_{n-1}-\theta_n) + \frac{k_n}{t_{ML}}(\theta_n-\theta_{n+1}) - \frac{k_{n-1}}{t_{ML}}(\theta_{n-1}-\theta_n) \\ &= \text{deposition} + \text{flux from } n+1 \text{ to } n - \text{flux from } n \text{ to } n-1 \end{aligned} \tag{4.2}$$

with the effective diffusion constants k_n corresponding to the situation shown in Fig. 4.5 (a). The starting values for the coverages are $\theta_0(t) = 1$ and $\theta_n(0) = 0$. k_n determines the

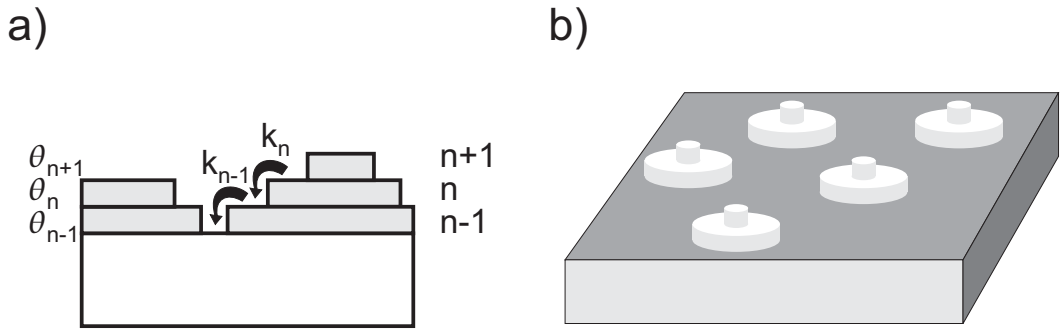

Figure 4.5: (a) Illustration of the coverages θ_n and the layers n. The arrows indicate the inter-layer diffusion to and from the layer n controlled by the effective diffusion constants k_n and k_{n-1}. (b) Island distribution assumed in the rate equation model [88].

time dependence of θ_n. For $k_n \to 0$, the solution of Eq. 4.2 approaches non-diffusive growth, for $k_n \to \infty$ it approaches layer-by-layer growth.

4.2.3 Rate equations and AFM measurements

In the previous section, rate equations for the time dependent coverage have been introduced. Another observable is the island density, which can be determined by microscopy methods. In the following, we will summarize a set of rate equations developed for island nucleation [25–27]. This rate equation approach has been used, e.g., in the references [26,97,98]. In Sec. 6.2.2, we will apply an extended version of this model to our measurements.

The basic assumptions of the model are that only single atoms are mobile and that there exists no desorption. i is the critical cluster size. All clusters with $j > i$ are more likely to grow than to decrease. They are assumed to be stable. For all clusters with $j \leq i$, local equilibrium is assumed. This leads to the differential quation set

$$\begin{aligned} \frac{dn_1}{dt} &= F - \frac{d(n_x w_x)}{dt} \\ \frac{dn_j}{dt} &= 0 \\ \frac{dn_x}{dt} &= U_i \end{aligned} \tag{4.3}$$

where n_1 is the number of monomers, n_x the number of stable clusters, w_x the average number of atoms in a stable cluster, and U_i the nucleation rate of stable clusters with

$$U_i = \sigma_i D n_1 n_i. \tag{4.4}$$

σ_i is the capture number which takes into account that the islands act as an effective sink for monomers, and D is the diffusion constant

$$D = \nu \exp(-E_D/k_B T). \tag{4.5}$$

with the attempt frequency ν, and the energy barrier for surface diffusion E_D. n_x increases by nucleation processes, and decreases by the coalescence. The solution of Eq. 4.3 for the maximum cluster density ρ (the maximum number of clusters n_x normalized to the number of nucleation sites, N_0) for 3D islands, assuming that the island density is independent of the area covered by the clusters, is

$$\rho = \frac{n_x}{N_0} \sim (F\nu)^p \, e^{\frac{E}{k_B T}} \tag{4.6}$$

with the temperature T, the Boltzmann constant k_B, $p = 1/(i{+}2.5)$, $E = (E_i{+}iE_D)/(i{+}2.5)$, and the nucleation energy for the critical cluster E_i. Eq. 4.6 is equivalent to

$$\rho \sim \left(\frac{F}{D_{eff}}\right)^p \tag{4.7}$$

where D_{eff} is an effective diffusion constant with the effective diffusion energy $E_{eff} = E_D + E_i/i$. If the attempt frequency ν can be treated as temperature independent, we can write

$$\ln \rho = const + p\frac{E_{eff}}{k_B T}. \tag{4.8}$$

One possibility to use Eq. 4.7 in the analysis of experimental data is to plot the logarithm of $\rho(T)$ over $1/T$, and to determine pE_{eff} from the slope. E_{eff} depends on the critical cluster size, and only for large i we find $E_{eff} \approx E_D$.

4.3 Monte Carlo simulations

In chapter 8.4 we present kinetic Monte Carlo simulations of the MBE growth, based on a modified bond-counting model. For the better understanding of our model and our results, in this section we give a short introduction in the principles of Monte Carlo simulations, following the book of Newman et al. [99] where a comprehensive description of the different Monte Carlo methods and their applications can be found.

4.3.1 Equilibrium Monte Carlo simulation

Classical thermodynamics applied to an n particle system in thermodynamic equilibrium predict that the system can assume every state r with the probability p_r according to the

Boltzmann distribution. Every observable quantity $\langle f \rangle$ of the system can be calculated by

$$\langle f \rangle = \frac{\sum_r f_r e^{-\beta E_r}}{\sum_r e^{-\beta E_r}} = \sum_r f_r p_r. \tag{4.9}$$

For large n, it is difficult to calculate the probabilities p_r of all states r. The idea of a Monte Carlo simulation is to sample a number of states which the equilibrated model system assumes during the time t and to estimate from this the probabilities p_r. In thermal equilibrium, the total energy of the system fluctuates and induces transitions from the state r to the state r'. An ergodic system will eventually assume every state r. If the system is monitored for an appropriate time, a statistically significant estimate of the probability distribution can be achieved.

The computer time of a MC simulation depends on the method to generate new states r' of the model system. (1) We can chose an arbitrary state r' and accept it with the probability $e^{-\beta E_{r'}}$. This method is very ineffective since most of the transitions will be rejected. (2) A more efficient way to chose a new state is the Markov process. By definition, a Markov process is a process which always accepts the arbitrarily chosen state r' (which can also be the initial state). The probability for a transition from a state r to a state r' is given by $P(r \to r')$ with

$$\sum P(r \to r') = 1. \tag{4.10}$$

The additional condition of detailed balance

$$p_r P(r \to r') = p_{r'} P(r' \to r). \tag{4.11}$$

ensures that the equilibrium distribution represented by an infinite number of successive states will be identical with the Boltzmann distribution. Since p_r and $p_{r'}$ follow the Boltzmann distribution,

$$\frac{P(r \to r')}{P(r' \to r)} = e^{-\beta(E_{r'} - E_r)}. \tag{4.12}$$

This is the only restriction on the choice of the transition probabilities $P(r \to r')$.

4.3.2 Monte Carlo simulation and thin film growth

Non-equilibrium Monte Carlo simulations are used to describe the kinetics of a system. In contrast to the equilibrium Monte Carlo simulation, where only the final equilibrium state is of interest, now the result of the simulation is time-dependent. The time-dependence is

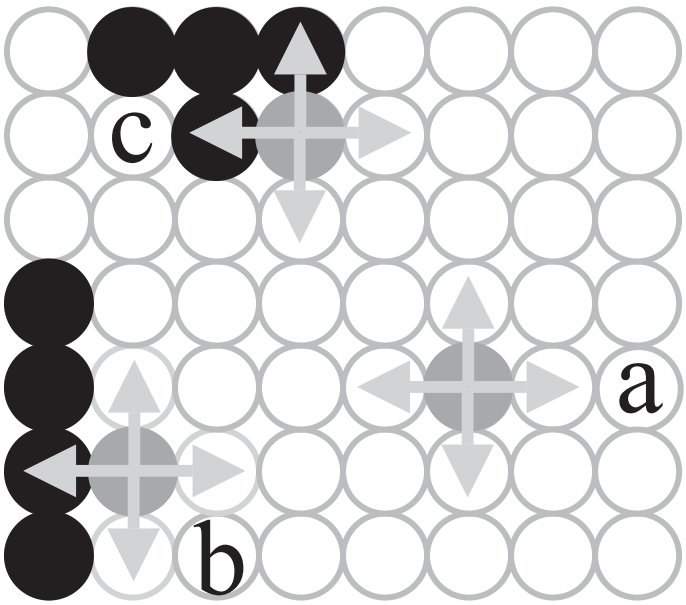

Figure 4.6: Representation of a thin film in a Monte Carlo simulation. The atoms can occupy lattice sites on a square lattice. Different adatom positions and their possible diffusion directions have to be taken into account, e.g. (a) an adatom can have no nearest neighbors, (b) an adatom is situated at a step edge, and (c) an adatom is situated in a kink.

determined by the choice of the transition probabilities. Kinetic Monte Carlo simulations of the non-equilibrium MBE growth process are a special case of non-equilibrium Monte Carlo simulations and will be discussed in this section.

A thin film can be treated as an ensemble of particles $\{x_i\}$ at discrete lattice sites (x, y, z). Fig. 4.6 shows an example of a cubic lattice. All models developed for a cubic lattice can be transferred to other crystal lattices by changing the definition of the nearest neighbor sites. The state r of the thin film is defined by the number of particles and their position. Transitions between different states can be performed by the change of one particle position (diffusion), and an increase in the particle number (deposition). Examples for several possible diffusion processes can be found in Fig. 4.6.

We assume that the possible processes of the model system are single-particle diffusion and adsorption. It has been shown experimentally and theoretically that the diffusion rate r_{ij} of a molecule or atom from the site i to the site j is described by the Arrhenius law

$$r_{ij} = r_0 e^{-\frac{E_{ij}}{k_B T}} \tag{4.13}$$

where E_{ij} ist the diffusion barrier and r_0 is the attempt frequency. The probability for the

transition $i \rightarrow j$ and for a deposition process with the deposition rate F are

$$p_{ij} = \frac{r_{ij}}{F + \sum_{kl} r_{kl}} \qquad \text{and} \qquad p_F = \frac{F}{F + \sum_{kl} r_{kl}}. \tag{4.14}$$

A simple model for the diffusion barrier is the bond-counting method. In this model, the energy barrier for the diffusion of the atom at the site i depends on the configuration of the nearest neighbors of the initial site. It is defined by

$$E_{ij} = E_D + n_i E_B \tag{4.15}$$

where E_D is the barrier for surface diffusion, n_i is the number of nearest neighbors of the initial site of the particle and E_B is the binding energy to the nearest in-plane neighbors. In this model it is assumed that the binding energy increases linearly with the number of nearest neighbors.

The bond-counting model is restricted to short-range interactions, i.e. pair-pair interaction potentials. Cooperative interactions cannot be described by this model. For systems where the long-range interaction is essential, e.g. for the system Ag/Pt(111) [82], the model has to be modified. The diffusion barriers for every possible process have to be detemined by *ab initio* calculations. The results of *ab initio* calculations can be fed into a Monte Carlo simulation. Then, the evolution of the system under different growth conditions can be studied.

Chapter 5

Experimental details

In this section, we will present a short outline of the experimental setups and the different techniques exploited for this study, namely X-ray diffraction and the atomic force microscopy (AFM). During the past few decades, the scientific effort to understand and improve these methods has been very large. For a detailed description of molecular beem epitaxy (MBE) we refer to [75], for the principles of the generation of Synchrotron radiation to the text books [66, 69, 100], and for an introduction of scanning microscopy methods to [101]. All experiments have been performed at six-circle diffractometers. For the angle calculations and the corrections of the integrated intensities we refer to [73, 102].

5.1 Apparatus for MBE growth

Two MBE systems have been used for the sample preparation and the *in situ* analysis: (1) a stationary Omicron MBE system (in the following called OMBE for *organic* MBE), and (2) a portable MBE chamber optimized for *in situ* X-ray diffraction experiments [17].

The OMBE chamber consists of the load lock, the deposition chamber and the analysis chamber, as shown in Fig. 5.1. The base pressure of the deposition and analysis chamber is in the 10^{-11} mbar range. The growth chamber is equipped with a quadrupole mass spectrometer (QMS), a quartz crystal microbalance (QCM) and several evaporation cells for organic materials and metals. PTCDA has been evaporated from a commercial Knudsen cell. For the *in situ* analysis of the samples, LEED, Auger electron spectroscopy (AES), and a combined room temperature AFM and STM are available. The system has two heating stages, located in the deposition chamber and in the analysis chamber, respectively. Additionally, the sample can be cooled by liquid nitrogen in the deposition chamber.

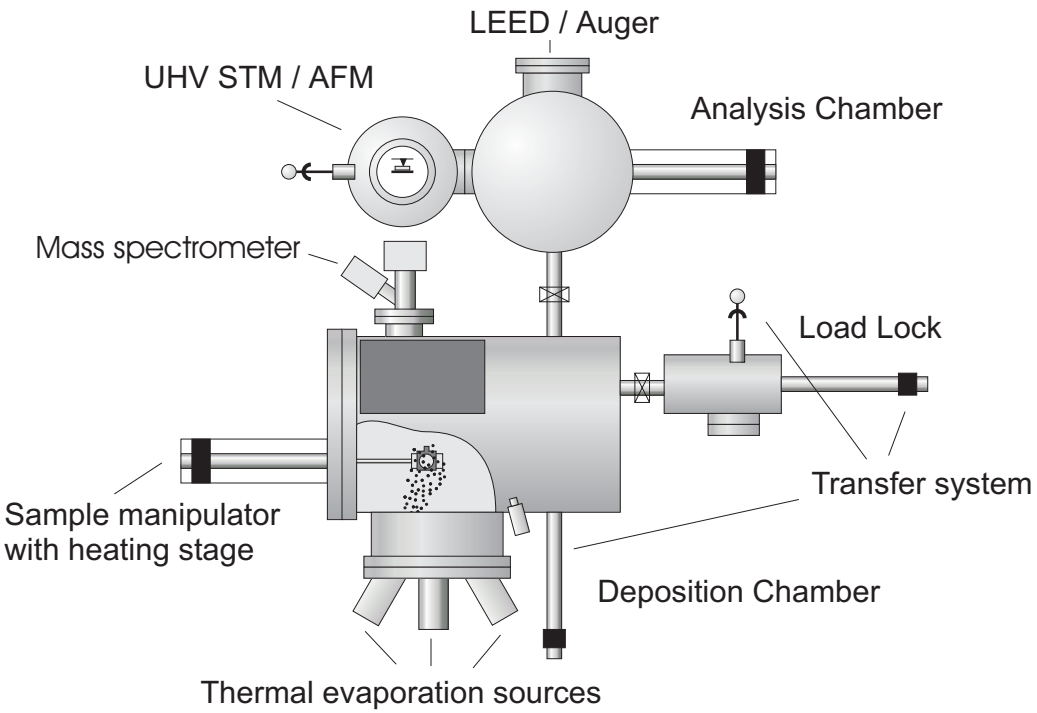

Figure 5.1: Schematic top view of the stationary Omicron MBE system.

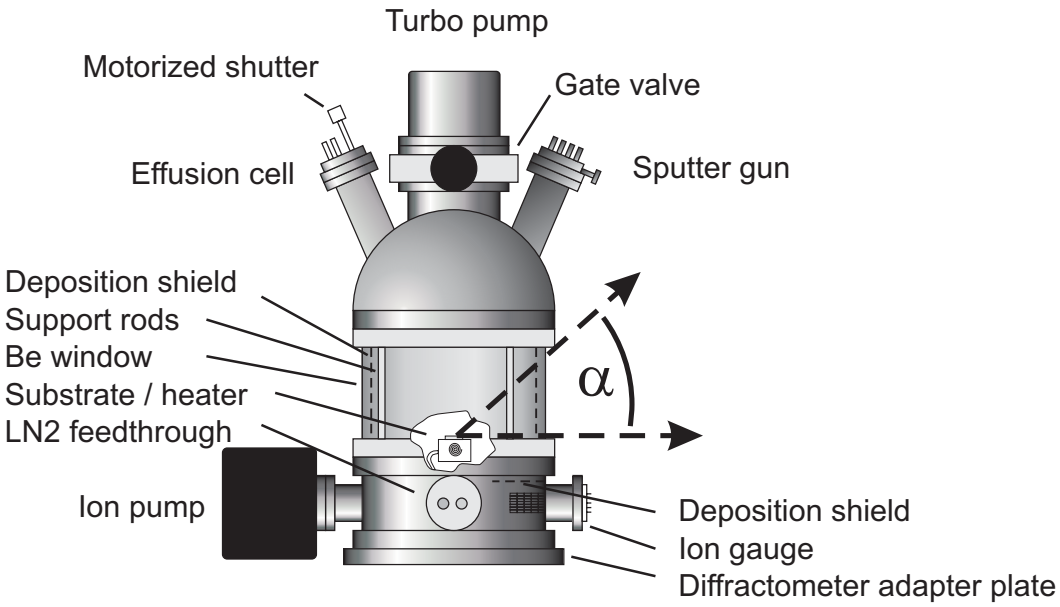

Figure 5.2: Schematic side-view of the portable MBE chamber which is optimized for *in situ* X-ray diffraction.

The base pressure of the portable MBE system (Fig. 5.2) is in the 10^{-10} mbar range. The system can be mounted directly on a X-ray diffractometer. In the configuration used for the PTCDA experiments, it contains a sample heater, a sputter gun, a custom evaporation source for PTCDA, a QCM, and an installation for sample cooling. A 360° beryllium

window permits *in situ*, real-time X-ray diffraction measurements to be carried out during growth. The system is pumped by a top-mounted turbomolecular pump and a side-mounted battery-powered ion pump, which can maintain the vacuum during the transport to a synchrotron beamline. A detailed description of the portable MBE chamber can be found in [17].

In both MBE systems, K-type thermocouples are used for the temperature measurement, and the heating current is regulated by Eurotherm PID controllers. In the portable MBE chamber, the thermocouple touches directly the substrate. In the OMBE system, the thermocouples are mounted at some distance of the sample position. The temperature measurement in the deposition chamber has been calibrated by a reference measurement with a second thermocouple, mounted directly at the sample position. The absolute temperature in the analysis chamber has been estimated by a comparison of the desorption temperature of a thin film in the analysis chamber and in the portable MBE chamber. The error of the relative temperature measurement is ± 1 K, and the absolute error is around ± 10 K.

The deposition rate of the Knudsen cells is monitored by a QCM which has been calibrated by reflectivity measurements of a thin film deposited on quartz glass. In the portable MBE, a motorized shutter controls the deposition time; in the OMBE system the shutter is opened and closed manually.

5.2 Synchrotron beamlines

5.2.1 Beamline ID10B at the ESRF

The beamline ID10B is an undulator beamline at the European Synchrotron Radiation Facility (ESRF) in Grenoble, France [19]. The source has a divergence of 0.017 mrad perpendicular to the ring plane, and of 0.028 mrad parallel to the plane. Fig. 5.3 (a) shows a schematic of the beamline. Behind the primary slit, the beam is monochromized by a diamond(111) double crystal monochromator with an energy resolution of $\Delta E \approx 1$ eV at an energy $E = 13$ keV. A double mirror is used for the suppression of higher harmonics, and the intensity ratio of the first harmonic and the selected wavelength is

$$\frac{I(\lambda/3)}{I(\lambda)} < 10^{-4}. \tag{5.1}$$

Prior to the experimental hutch, it further be adjusted by a deflector. The beam size at the sample is smaller than 1×0.5 mm^2, and the typical flux at the sample is 10^{11} photons/s/mm^2 at a ring current of 100 mA and at a beam energy of 8 keV. For our experiments, a position

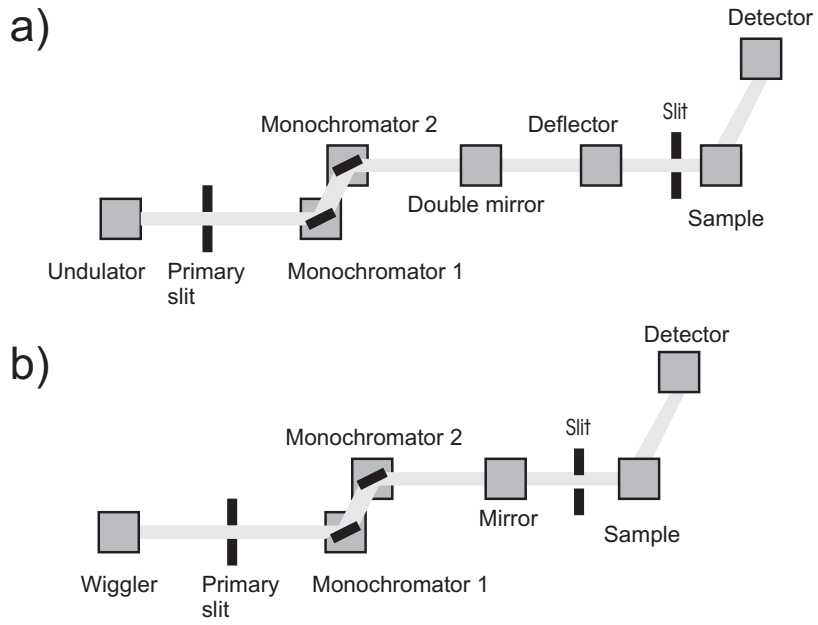

Figure 5.3: Schematic beamline layout of (a) the beamline ID10B at the ESRF (Grenoble), and of (b) the beamline W1 at the HASYLAB (Hamburg)

sensitive detector (PSD) has been used. The detector is a wire detector with 1000 channels. The width of each channel is 50 – 80 μm, and the spacial resolution of the detector is 140 – 300 μm. The angular resolution in our experiments is 256 channels/1°. The detector has been operated with an argon/methane mixture. The diffractometer at ID10B is a Huber z-axis diffractometer in the vertical scattering geometry.

5.2.2 Beamline W1 at the HASYLAB

The beamline W1 is a wiggler beamline at the Hamburger Synchrotronstrahlungslabor (HASYLAB) [18]. The source has a divergence of 0.08 mrad perpendicular to the plane of the storage ring, and of 1.7 mrad parallel to the plane. Fig. 5.3 (b) shows a schematic of the beamline. Behind the primary slit, the beam is monochromized by a Si(111) double crystal monochromator with an energy resolution of $\Delta E = 2$ eV at an energy $E = 9$ keV. The beam is focused by an Au-coated mirror to 4×2 mm^2 (horizontal size $\times$ vertical size) at the sample position. At $E = 9$ keV, the typical flux at the sample position is 5×10^{10} photons/s/mm^2. The intensity has been detected by a NaI(Tl) scintillation detector combined with a photomultiplier. The diffractometer at $W1$, a six-circle diffractometer with a horizontal instrument axis, has been used in the vertical scattering geometry.

5.3 Sample preparation

The commercially available organic compound PTCDA contains other molecules, including water. Therefore, it has been purified 2–3 times by gradient sublimation [12]. The purified material has been inserted in the Knudsen cells, and has been outgassed for several days at ≈ 430 K under UHV conditions.

As substrate, a commercial Ag(111) single crystal (MATECK) with the diameter 10 mm and the height 2 mm has been used. The crystal has been oriented by X-ray diffraction and polished with minimum force on one side using diamond particles down to 0.05 μm diameter and a mixture of soap and glycerine on the polishing cloth PolySat 2 (Fa. Struers). The substrate has been fixed on an Omicron sample holder. For the experiments in the portable UHV chamber, this sample holder has been mounted on a Riber sample holder by spot-welding with thin tantalum stripes.

After polishing, the sample was treated with repeated sputtering cycles (30 min at room temperature, Ar^+ energy 500–600 eV, Ar pressure $\approx 6 \times 10^{-5}$ mbar) and annealing cycles (at 700–900 K, for more than 15 min) in the OMBE system to remove impurities and surface defects induced by the polishing. The surface quality has been checked with by LEED, by AES, and by AFM in the contact mode, where large terraces up to the micrometer scale could be observed with sufficient quality as to attain atomic resolution.

5.4 Thin film growth procedure

The general procedure for the deposition of PTCDA films on the Ag(111) substrate is as follows. After thermal desorption of the film, typically three sputtering and annealing cycles as described above are performed to remove possible remains of the previous film and to generate a smooth substrate surface. The surface quality is then verified with Auger and LEED in the stationary MBE system, and with X-ray measurements of the specular rod in the portable MBE chamber. The typical growth parameters are deposition rates between 1 and 10 Å/min at the Knudsen cell temperature between 540 and 600 K, substrate temperatures between 140 and 470 K and film thicknesses between 30 and 200 Å. A detailed list of the samples under investigation can be found in Appendix D.

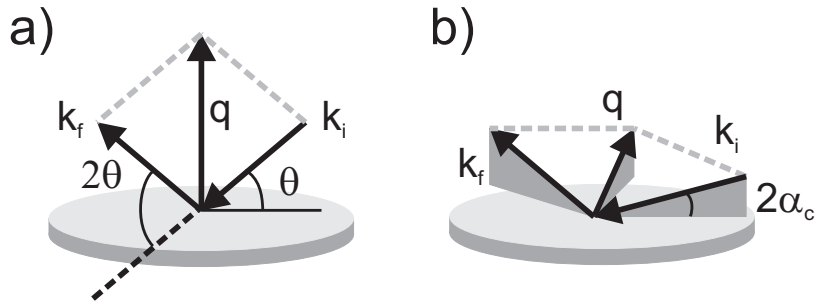

Figure 5.4: Scattering geometries used for the X-ray experiments. (a) specular rod measurement, (b) measurement of an asymmetric Bragg reflection with a large in-plane component.

5.5 Measurements

5.5.1 X-ray experiments

All samples studied by X-ray diffraction were deposited in the portable UHV chamber and measured *in situ* under UHV conditions. Depending on the experiment, the samples have been measured at the temperature at which they were grown, or else at various annealing temperatures set following the deposition.

The crystal structures at different growth temperatures (see Sec. 6.1.2) has been studied at the beamline ID10B (ESRF) at an energy $E = 13.3$ keV. The sample has been horizontally mounted, and two types of scattering experiments have been performed. The specular rod has been measured as shown in Fig. 5.4 (a). The momentum transfer q is oriented perpendicular to the substrate plane, and the incident wavevector k_i and the wavevector k_f of the reflected wave have the angle θ to the substrate. The scattering geometry shown in Fig. 5.4 (b) has been used for the measurements of asymmetric Bragg reflections with dominant in-plane components. For this study, the six-circle diffractometer has been used with a fixed incident angle $\alpha_i \approx 2\alpha_c$, where α_c is the critical angle for Ag at this energy. Supplementary measurements of the in-plane crystal structure have been performed with a laboratory source, a rotating anode with Molybdenum K-alpha radiation ($E = 17.4$ keV), and equipped with a NaI scintillation detector.

The *in situ* growth experiments (see Sec. 8.1) and the systematic specular rod measurements (see Sec. 6.1.3 and 7.1.2) have been performed at the beamline W1 (HASYLAB), at an energy $E = 10$ keV. The sample has been mounted horizontally, and the momentum transfer q is oriented perpendicular to the sample surface. In this geometry, the less divergent beam direction determines the experimental resolution.

5.5.2 AFM experiments

All samples studied by AFM (see Sec. 6.1.1 and 7.1.1) have been deposited in the stationary OMBE system and subsequently transferred to the AFM stage of this chamber, where they were measured under UHV conditions with the maximum scanning area of 5×5 μm^2. The measurements have been performed at room temperature. The organic films have been studied by non-contact AFM to prevent possible damages of the sample. The experiments separate into the study of as-grown samples and of annealed samples. The annealing has been performed in the analysis chamber.

5.5.3 Additional experiments

In some cases, the observed morphology was macroscopic, and neither X-ray diffraction nor AFM were suitable for the study of the morphology. Therefore, additional studies with an optical microscope have been performed under ambient conditions using polarization filters. The polarization filters are necessary to enhance the contrast between the features of the substrate and the film. By this method, length scales down to approximately 1 μm and areas up to 0.5×0.5 mm have been accessible.

Chapter 6

As-grown thin PTCDA films

6.1 Experimental results

6.1.1 AFM experiments

Several samples with an average film thickness $d = 50$ Å, deposited at growth temperatures T_g between 135 K and 474 K and with the deposition rate $F = 1.3 \pm 0.5$ Å/min, have been grown in the stationary OMBE system. After the growth, they were studied by non-contact AFM in the UHV.

Fig. 6.1 shows examples of the morphology of PTCDA films as a function of T_g. All AFM images show structures which are representative of the respective sample as has been ensured by measuring several spots on each sample, separated by up to several millimeters. For better comparison, the images presented have an identical size of 2.5×2.5 μm^2. At least four separate morphological regions can be identified, depending on the growth temperature: (I) a low-temperature morphology observed at 135 K showing a mesa-like structure (Fig. 6.1 (a)), (II) a region characterized by a relatively smooth surface around room temperature (Fig. 6.1 (b)), (III) a transition region at 333 ± 5 K exhibiting facets (Fig. 6.1 (c)) and (IV) a region characterized by small crystallites for $T_g \geq 343$ K (Fig. 6.1 (d)–(f)). The AFM experiments are summarized in Fig. 6.2 and classified according to the different observed morphologies. The transitions between the different regions are smooth. Therefore it is not possible to identify well-defined phase transition temperature. The dashed lines separating the different regions in Fig. 6.2 are a guide to the eye.

Region (I) is characterized by small islands which are arranged along the steps of the silver substrate. This can be concluded from the characteristic undulation of the island chains, which reflects the typical step morphology of the substrate. The typical island size

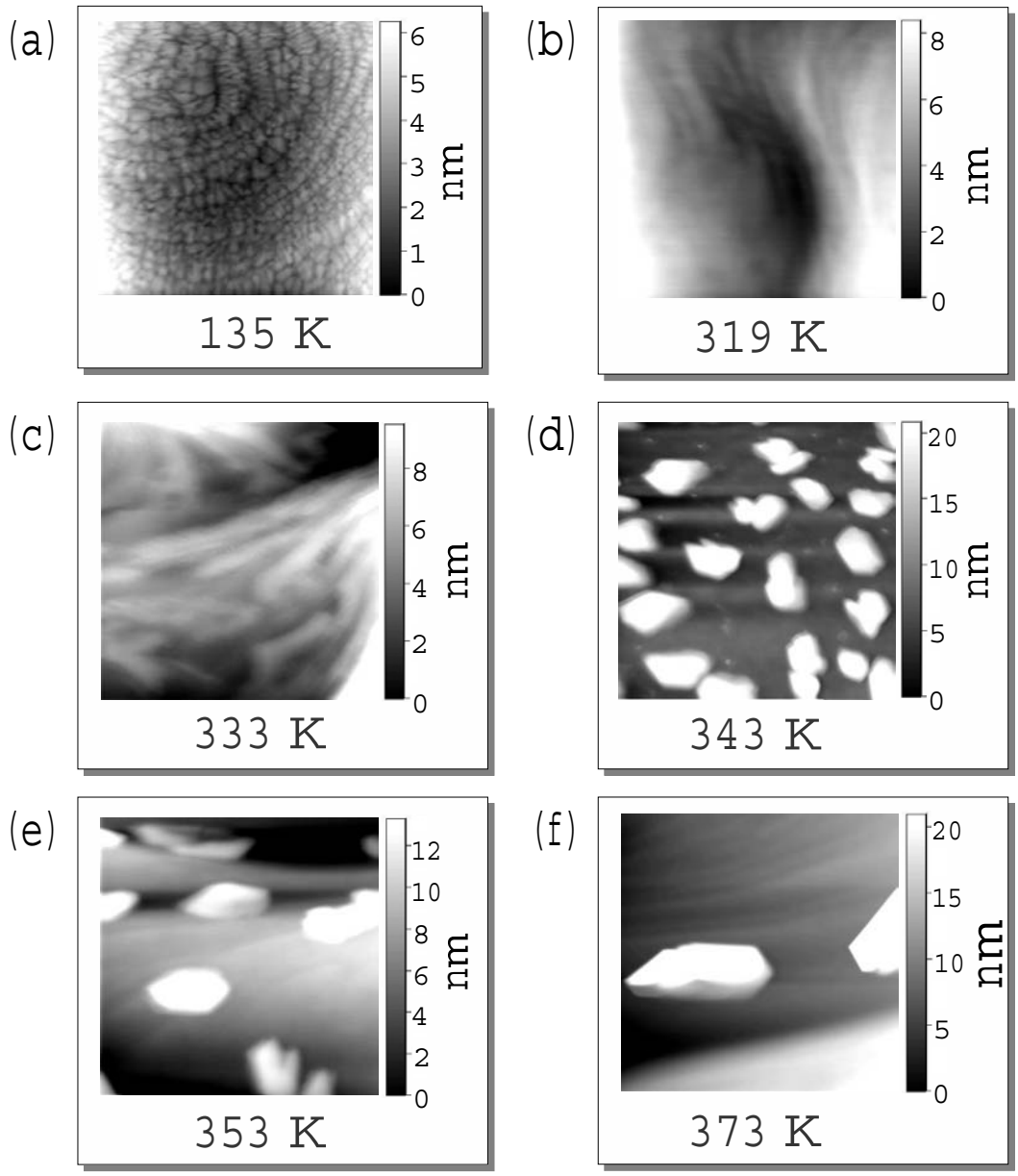

Figure 6.1: Morphology of a 50 Å PTCDA film (area 2.5×2.5 μm^2) as a fuctcion of T_g.

is $(150 \pm 50) \times (75 \pm 25)$ nm^2. The islands are elongated perpendicular to the substrate steps. The approximately vertical island sides do not correspond to well-defined crystallographic planes. The smooth, slightly curved, surface on top of the islands is dominated by the PTCDA(102) plane, as determined from X-ray scattering (see Sec. 6.1.3). The root mean square roughness observed for this morphology region is $\sigma = 8 \pm 2$ Å, corresponding to 2 – 4 ML.

Region (II) is characterized by a relatively smooth surface. Lateral ripples on a micrometer scale indicate the buried substrate steps. The smooth ripples show a height variation of about 2 nm. For some areas of the samples a tendency to form more facet-like structures

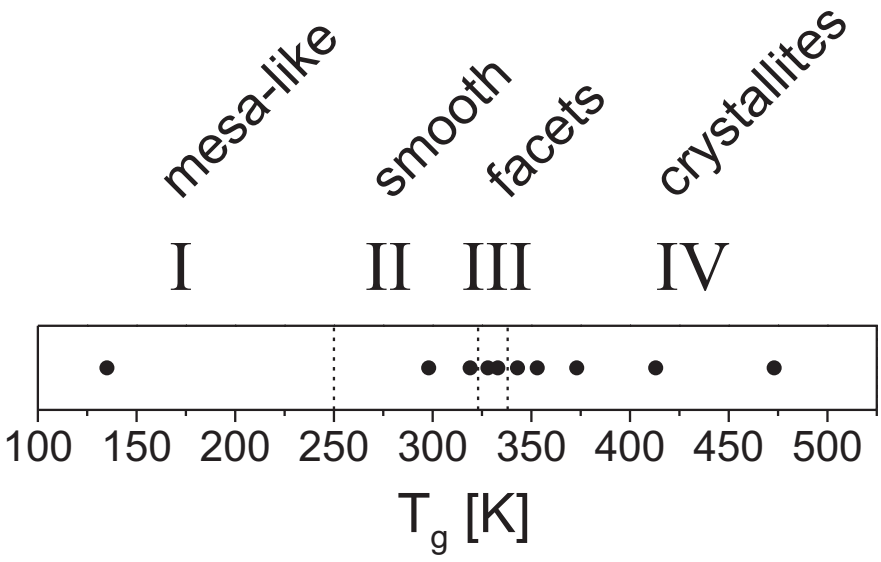

Figure 6.2: AFM measurements of samples with $d = 50$ Å and $F = 1.3 \pm 0.5$ Å/min, and their assignment to different morphological regions. The dashed lines indicate the approximate transition between the different growth regions.

has been observed. The overall roughness is comparable to the one observed for region (I), and the average surface is PTCDA(102).

In the faceted region (III) the main facet axis is preferentially aligned parallel to the silver steps. The length of the facets is in the micrometer range. The facets are $100 - 200$ nm wide, and their surfaces are only slightly, i.e. $1 - 5°$, inclined to the substrate surface. Most likely, the dominant facet surface is the (102) plane. In some cases, the facets change to elongated islands with steep sides and the (102) plane on top. Therefore, this region can be regarded as a "transition" region which shows already evidence of the crystallite morphology even if the film is not partially dewetted.

Region (IV) is characterized by separate crystallites. Fig. 6.3 shows a typical crystallite, grown at $T_g = 373$ K, $F = 1.3$ Å/min, and $d = 50$ Å. The in-plane angles between the facets correspond to the three planes of the two-dimensional lattice determining the in-plane shape of the crystallite: the $(\bar{1}2)$, the (10) and the (11) plane. The surface of the crystallite is the (102) plane. Fig. 6.4 relates the in-plane orientation of the facets to the molecular arrangement in the (102) plane. For the individual islands, the angles between the facets vary by up to several degrees. The islands show many different orientations with respect to the substrate. For the island shown in Fig. 6.3, the (10) plane is rotated by approximately

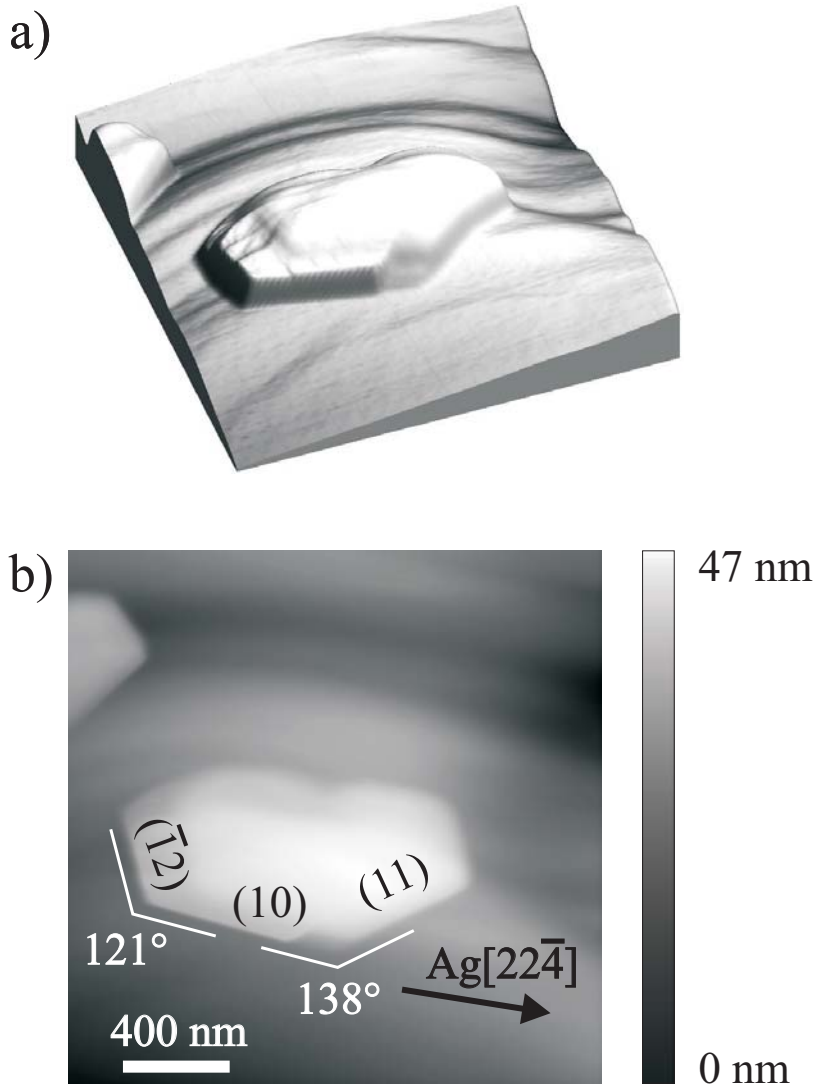

Figure 6.3: Example for the characteristic island shape. (a) 3d-plot showing the influence of the substrate steps on the island, (b) 2d-plot of the same island ($T_g = 373$ K, $F = 1.3$ Å/min, $d = 50$ Å). The characteristic PTCDA planes and angles are indicated.

5° relative to Ag[22$\bar{4}$], as has been determined by comparison with atomic resolution AFM images of the Ag substrate. The symmetry of the observed island orientations is consistent with the substrate orientation. The island orientation has been analyzed in detail for a sample with $T_g = 478$ K, $F = 6.3$ Å/min, and $d = 126$ Å. Fig. 6.5 shows the in-plane orientation of the (10) plane as a function of the azimuthal separation from Ag[22$\bar{4}$]. The data have been derived from large scale optical microscopy images of crystallites with a length of up to 10 μm. Symmetry-equivalent orientations due to the substrate symmetry have been summarized. A broad distribution of preferred orientations has been found, concentrated in 2 peaks at $\phi = \pm 7°$, with the width 4°. The two maxima can be attributed to mirror domains.

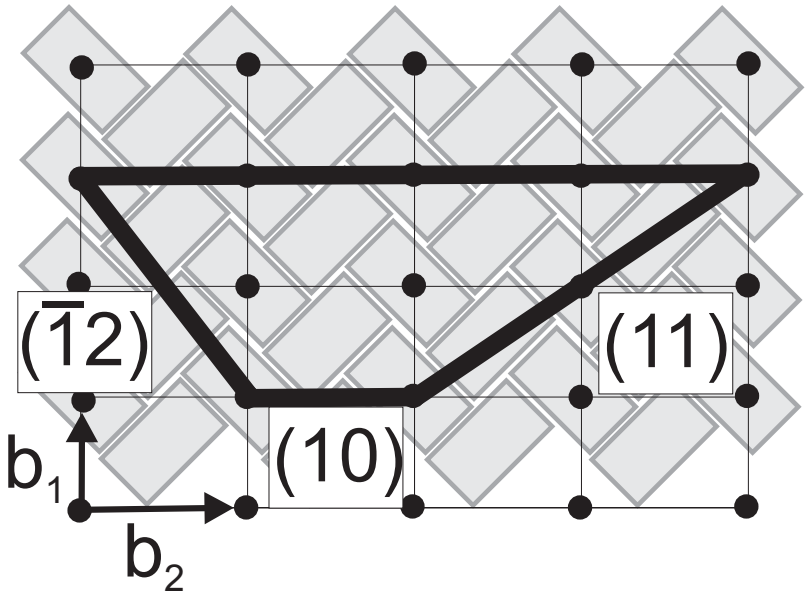

Figure 6.4: In-plane orientation of the PTCDA facets superimposed on the molecular crystallography of the (102) plane. The unit cell dimensions are indicated.

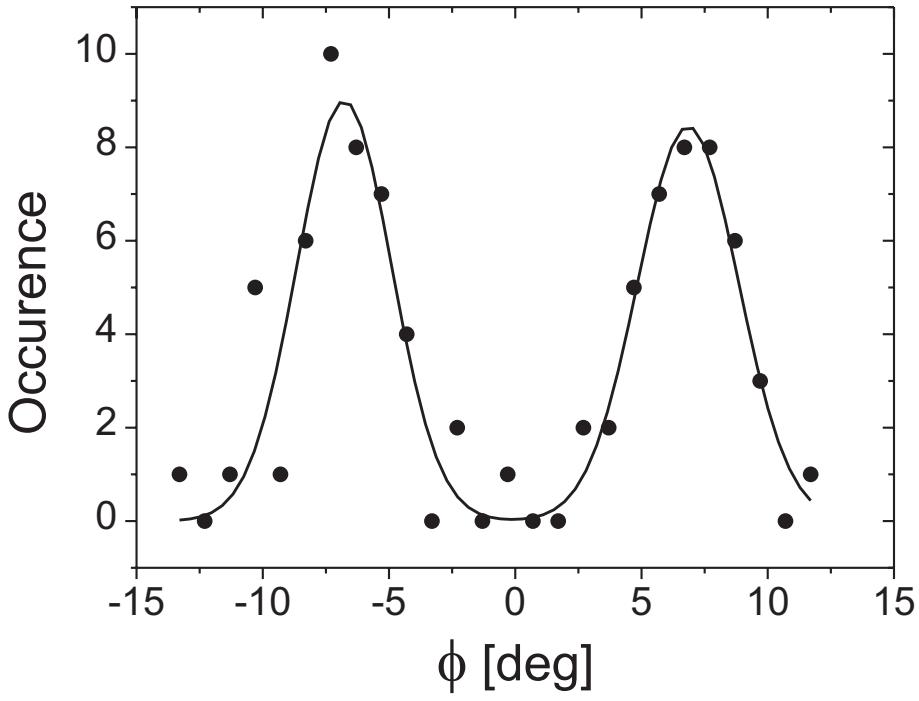

Figure 6.5: Azimuthal distribution of the (10) facet, relative to Ag[22$\bar{4}$], as determined by optical microscopy for a sample with $T_g = 478$ K, $F = 6.3$ Å/min, and $d = 126$ Å.

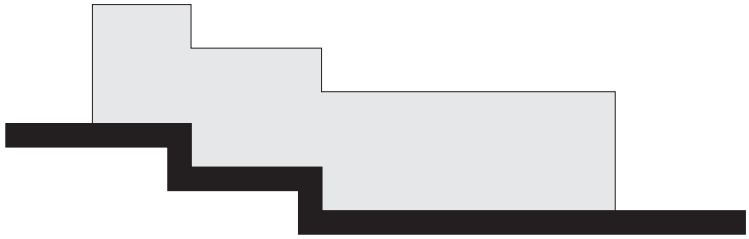

Figure 6.6: Schematic of a "coherent" island which covers several Ag steps.

A typical crystallite is defined by between three and six facet edges. Frequently, three smooth sides are connected by a fourth, not so well-defined surface. For large crystallites, e.g. the crystallite shown in Fig. 6.3, it has been observed that the islands align along bunched substrate steps and even extend over several substrate steps with a height of $2-5$ ML. These steps are projected on the island surface. The islands are not perturbed by the substrate steps and seem to be of constant height. This is indicated in the schematic of a large island which overgrows several steps (Fig. 6.6).

The island distribution, their lateral extent, and their height change as a function of T_g. The AFM pictures show that the island size (area covered by the islands) increases with T_g from approximately 0.1 μm^2 at 343 K to 5 μm^2 at 413 K, while the island density decreases from approximately 12 μm^{-2} at 343 K to 0.001 μm^{-2} at 413 K. The combined analysis of images taken with the optical microscope and the AFM images makes it possible to measure the temperature-dependent changes with sufficient statistical certainty. For all samples (except the one grown at $T_g = 343$ K) only one island size distribution has been found; for $T_g = 343$ K small clusters between the crystallites have been observed.

6.1.2 Grazing-incidence X-ray experiments

In order to establish the PTCDA in-plane structure, a large number of Bragg reflections has been measured at T_g. Superscripts denote reflections of the α- or β-type structure, but for consistency the Miller indices are always given in the α-nomenclature [50,64], as introduced in Sec. 3.8.

High temperature GIXD experiments

Fig. 6.7 (a) shows the average in-plane intensity distribution of a sample grown at high temperatures with $d = 50$ Å, $T_g = 448$ K and $F = 0.9$ Å/min, and its relation to the crystal orientation of the substrate. Table 6.1 summarizes the average q-values of equivalent

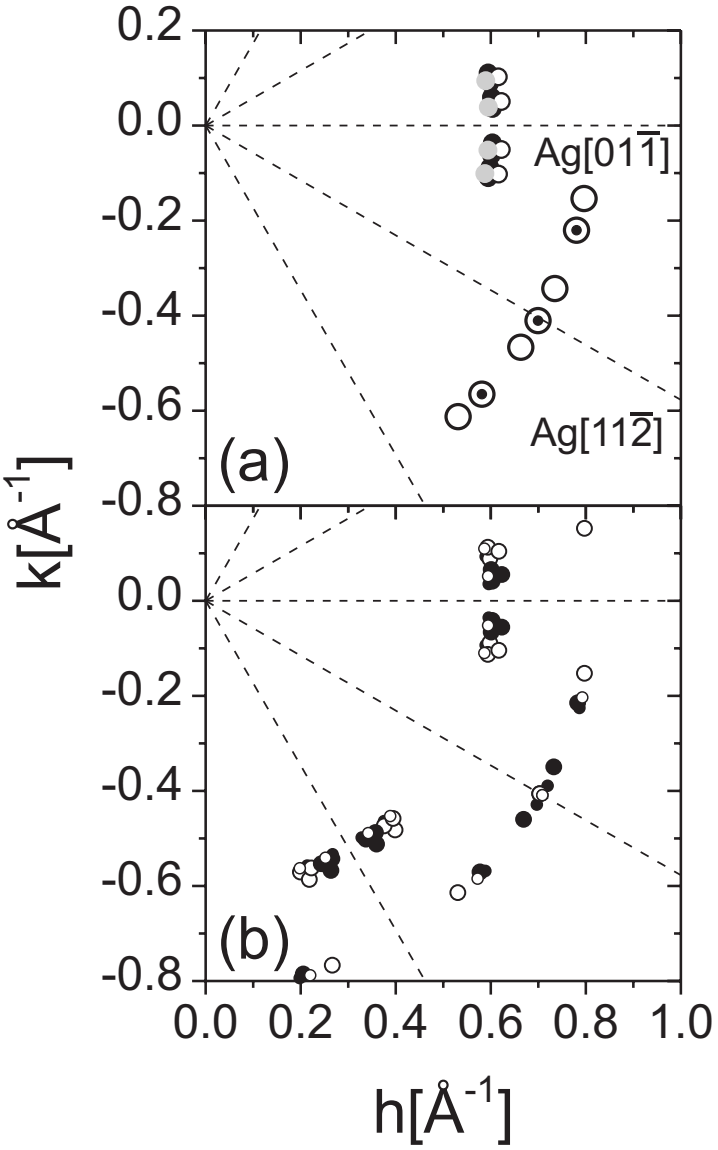

Figure 6.7: (a) Position of the measured in-plane intensity distribution of a sample with $d = 50$ Å, $T_g = 448$ K and $F = 0.9$ Å/min. The crystallographic orientation of the Ag substrate indicates the epitaxial relation of film and substrate. The reflections have been categorized according to the nearest bulk polymorph and the reflection type; $(012)^{\alpha}$ is represented by large open circles, $(012)^{\beta}$ by small black circles, $(011)^{\alpha}$ by large black circles, $(011)^{\beta}$ by grey circles, and $(002)^{\alpha}$ by small open circles (see text). (b) Expected positions of the (012), (011) and (002) reflections (parameters of the unit cell: see text). α_1 is represented by large filled circles, α_2 by small filled circles, β_1 by large open circles, and β_2 by small open circles.

Reflection	q_z [Å^{-1}]		$q_\parallel$ [Å^{-1}]		q [Å^{-1}]	
$(012)^\alpha$	0.363	(0.373)	0.911	(0.822)	0.888	(0.902)
$(012)^\beta$	0.309	(0.334)	0.818	(0.824)	0.875	(0.889)
$(011)^\alpha$	0.181	(0.111)	0.605	(0.614)	0.631	(0.641)
$(011)^\beta$	0.298	(0.300)	0.596	(0.601)	0.667	(0.671)
$(002)^\alpha$	0.364	(0.373)	0.624	(0.631)	0.723	(0.733)
$(002)^\beta$		(0.000)		(0.651)		(0.651)

Table 6.1: Average q-values of the reflections of the sample grown at high temperature. The reflections have been assigned to the related bulk reflections of the α and the β structure. In brackets: calculated bulk values from the unit cell dimensions of Ref. [50].

reflections in reciprocal space in comparison with the calculated bulk values. The nomenclature of the measured peaks (Fig. 6.7 (a)) follows from the bulk reflections with the least positional deviations. Since no significant difference in the q-values of (012) and $(01\bar{2})$ has been observed, these reflections are treated as equivalent.

The azimuthal intensity distribution of the (012) reflections, which is split in q_z, is shown in Fig. 6.8 (a). While the azimuthal intensity distribution is rather broad, the radial in-plane measurements show narrow peaks with an in-plane coherence length of 550 ± 100 Å for all reflections. As an example for the out-of-plane peak width, the raw data of the peaks associated with the α-like phases around $\phi = 0$ is shown in Fig. 6.9. The out-of-plane coherence for all measured peaks is 470 ± 30 Å, i.e. larger than d. This is consistent with the island morphology seen in Fig. 6.1 (d)–(f).

A thicker but otherwise similar sample has been grown with $d = 200$ Å, $T_g = 453$ K, and $F = 3.4$ Å/min. In particular, both samples have a similar azimuthal intensity distribution (shown for the (012) reflections in Fig. 6.8), and no difference between the q values of the reflections from both samples could be resolved. Compared to the thin sample, the in-plane intensity distribution of the thick sample is more focused on specific positions. This shows in particular for the β-like reflections where the 50 Å film shows a broad intensity distribution, which for the thick film splits into several reflections. Measurements of the 200 Å sample at room temperature indicate no significant changes of the azimuthal intensity distribution.

For a thorough analysis of the intensity distribution, the number of contributing domains and their orientation relative to the substrate have to be established. In the following discussion, we refer mainly to the number of (012) peaks observed for the thick structure since

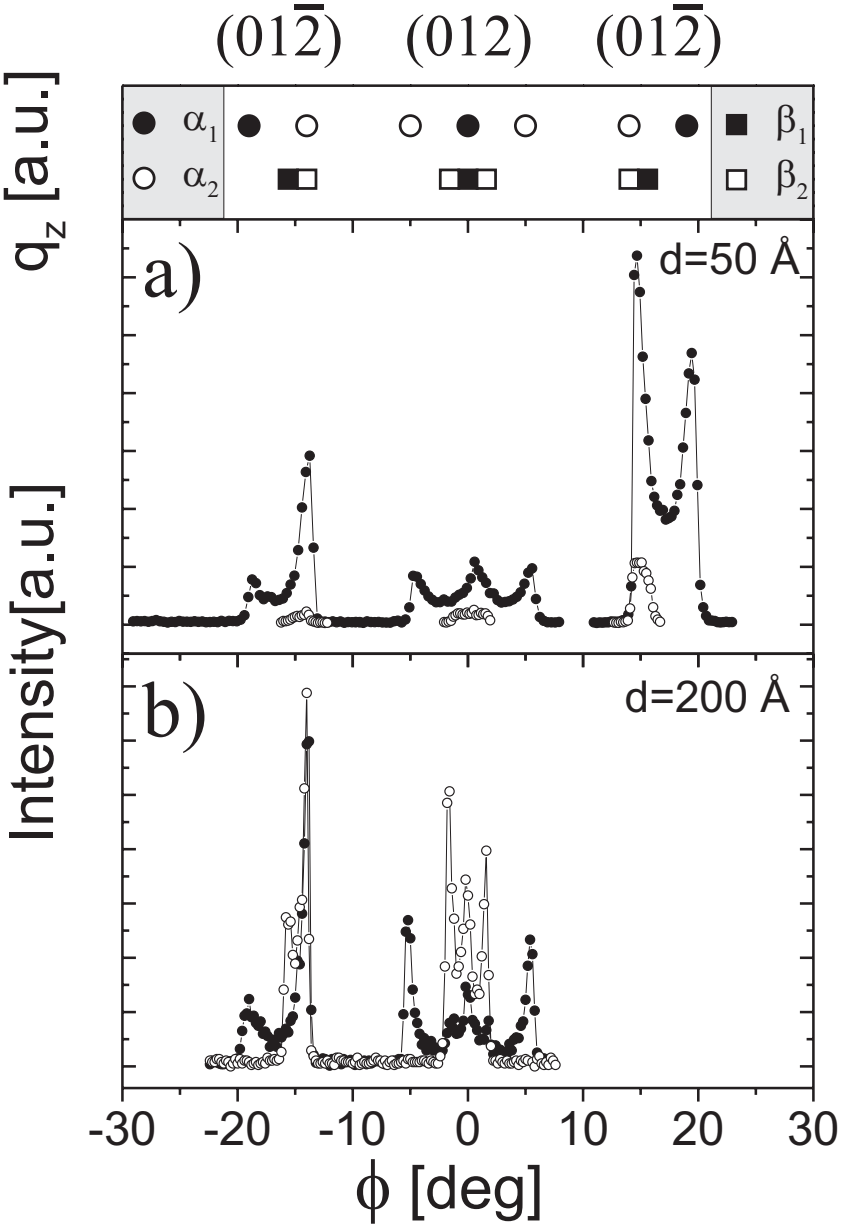

Figure 6.8: Azimuthal intensity distribution of the (012) reflections (the angle ϕ denotes the azimuthal separation to Ag[22$\bar{4}$]). On top: schematic of the preferential azimuthal positions and their assignment to 4 structures. The intensity distributions are attributed to (01$\bar{2}$) and (012) reflections. Filled circles denote the α-like structure with higher q_z, open circles the β-like structure with lower q_z. (a) Azimuthal intensity distribution of the 50 Å sample. (b) Intensity distribution of the 200 Å sample. The open circles represent the β-like structure, the filled circles the α-like structure. Most likely, the asymmetry between the (01$\bar{2}$) intensities is due to the substrate miscut.

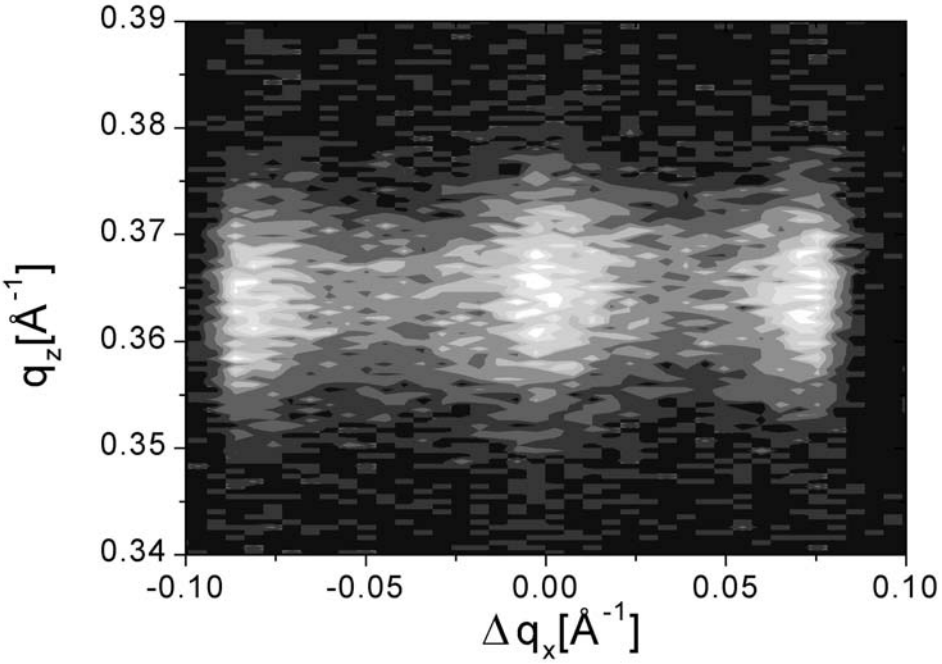

Figure 6.9: PSD measurement of the $(012)^{\alpha}$ reflections near Ag[22$\bar{4}$] for the sample with $T_g = 448$ K and $d = 50$ Å.

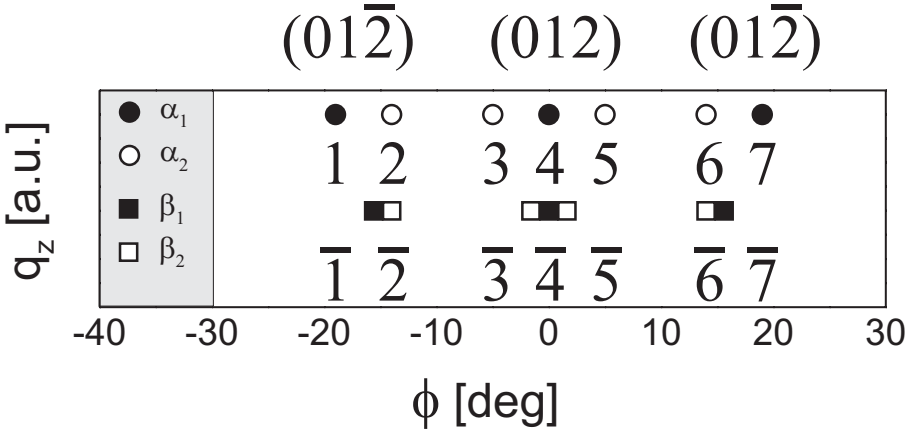

Figure 6.10: The labels indicated are used for the discussion of the peaks observed for the samples grown at 448 K (i.e. high T_g) .

for these the azimuthal splitting of the β reflections is clearly visible while it is seen only in the peak width for the thin sample. The (012) reflections have been chosen since there are no other reflections with similar q in this region of the reciprocal space.

structure	domains	$\Delta\phi$ [deg]	alignment
ML	6	13.9	(012) ‖ Ag($22\bar{4}$)
			($01\bar{2}$) ‖ Ag($5\bar{7}2$)
α_1	12	19.15 ± 0.3	(012) ‖ Ag($22\bar{4}$)
α_2	12	19.15 ± 0.3	($01\bar{2}$) ‖ Ag($5\bar{7}2$)
β_1	12	13.9 ± 0.3	(012) ‖ Ag($22\bar{4}$)
β_2	12	13.9 ± 0.3	($01\bar{2}$) ‖ Ag($5\bar{7}2$)

Table 6.2: Number of domains, azimuthal separation of the (012) and the ($01\bar{2}$) reflection, and orientation to the substrate for the PTCDA monolayer [15, 103] and the structures observed at $T_g = 448$ K (i.e. high T_g).

In the studied azimuthal range, 14 (012)-type reflections have been identified as schematically shown in Fig. 6.10. The reflections 1 – 7 have a slightly higher q_z than the reflection $\bar{1}$ – $\bar{7}$. The reflection pairs (1,7), (2,6), (3,5), and the respective reflections with low q_z are related by mirror operations, i.e. only 8 independent reflections, 1 – 4 and $\bar{1}$ – $\bar{4}$, have been observed. Since every domain has a (012) and a ($01\bar{2}$) reflection, at least 4 domain sets are necessary to explain the pattern, 2 with high and 2 with low q_z.

The observed intensity distribution has been attributed to the α and the β structure, respectively, both with two inequivalent orientations with the subscripts 1 and 2. In the upper part of Fig. 6.8, a schematic of the azimuthal distribution of the peaks and their assignment to the different domains is shown. Tab. 6.2 summarizes the number of domains, the azimuthal separation $\Delta\phi$ of the (012) and of the ($01\bar{2}$) reflections, and the epitaxial orientation of the different structures. All in-plane reflections of the high T_g sample exhibit a characteristic azimuthal asymmetry. Mirror domains, e.g. the reflections (1,7) and (2,6), show the same distortion, but in the opposite rotational direction [64]. Reflections belonging to equivalent domains according to the substrate symmetry, e.g. the reflections (1,4) and (2,5), are distorted in the same rotational direction. The asymmetry of the peaks can be attributed to a rotation of the entire in-plane unit mesh (see Sec. 6.2.3).

For α_1 and β_1, the full-width at half maximum (FWHM) of the (102) reflection is approximately two times the FWHM of the ($01\bar{2}$) reflection since the (012) reflection is a superposition of two asymmetric reflections, while the ($01\bar{2}$) reflections belong only to one domain. All reflections of α_2 and β_2 show a similar width.

With the assignment of the reflections, and with the model of the rotated domains,

structure	domains	$\Delta\phi$ [deg]	alignment
α	12	18.1 ± 0.5	$(01\bar{2})$ rotated by $2.2 \pm 0.5°$
			from Ag$(25\bar{7}2)$ to Ag$(22\bar{4})$
β	12	13.9 ± 0.3	$(012) \parallel$ Ag$(22\bar{4})$
			$(01\bar{2}) \parallel$ Ag$(5\bar{7}2)$

Table 6.3: Number of domains, azimuthal separation of the (012) and the $(01\bar{2})$ reflection, and orientation to the substrate for $T_g = 318$ K (i.e. low T_g).

the in-plane unit mesh of the preferential α and β domains has been calculated assuming a rectangular unit mesh, similar to the (102) plane of the bulk polymorphs. For α, $b_1 = 20.11 \pm 0.05$ Å, $b_2 = 12.16 \pm 0.05$ Å and the angle $\gamma = 90.0 \pm 0.2°$ between b_1 and b_2 have been found, the unit mesh of β has the dimensions $b_1 = 19.44 \pm 0.05$ Å, $b_2 = 12.53 \pm 0.05$ Å and $\gamma = 90 \pm 0.2°$. With these values, the (011), (012) and (002) reflections have been calculated (see Fig. 6.7 (b)). All measured reflections, i.e. also the $(011)^\alpha$, the $(011)^\beta$ and the $(002)^\alpha$ reflections, can be explained consistently. This supports the assumption of a rectangular unit cell. We note that the lattice parameters correspond to the preferred unit cell. A certain distribution of lattice parameters around the calculated values cannot be excluded.

Low temperature GIXD experiments

Similar data have been taken for a film with $d = 50$ Å, $T_g = 318$ K and $F = 0.9$ Å/min (i.e. low T_g). Fig. 6.11 (a) shows the measured (012) reflections in a ϕ-range of 30°. The (011) reflections have been found at $q_z = 0.18$ Å^{-1}, the (012) reflections at $q_z = 0.36$ Å^{-1}. No q_z splitting of the (012) intensity distribution could be observed. A scan of the azimuthal intensity distribution of the (012) type reflections is shown in Fig. 6.12 (a). While all (012) peaks are well-separated, the (011) intensity consist of two sharp peaks, between which a broad intensity distribution is found. For all reflections, an in-plane coherence length of 650 ± 100 Å and an out-of-plane coherence length of 50 ± 5 Å have been determined.

A thicker ($d = 200$ Å), but otherwise similar film has been grown at $T_g = 336$ K and $F = 3.5$ Å/min. Qualitatively, this film shows the same structure as the 50 Å film, as can be seen in Fig. 6.12 (b).

For the films grown at low temperature, four symmetric (012)-type reflections not related by mirror operations have been observed. Therefore, at least two structures are expected. The measured (012)-type reflections can be divided into two groups, according to the intensi-

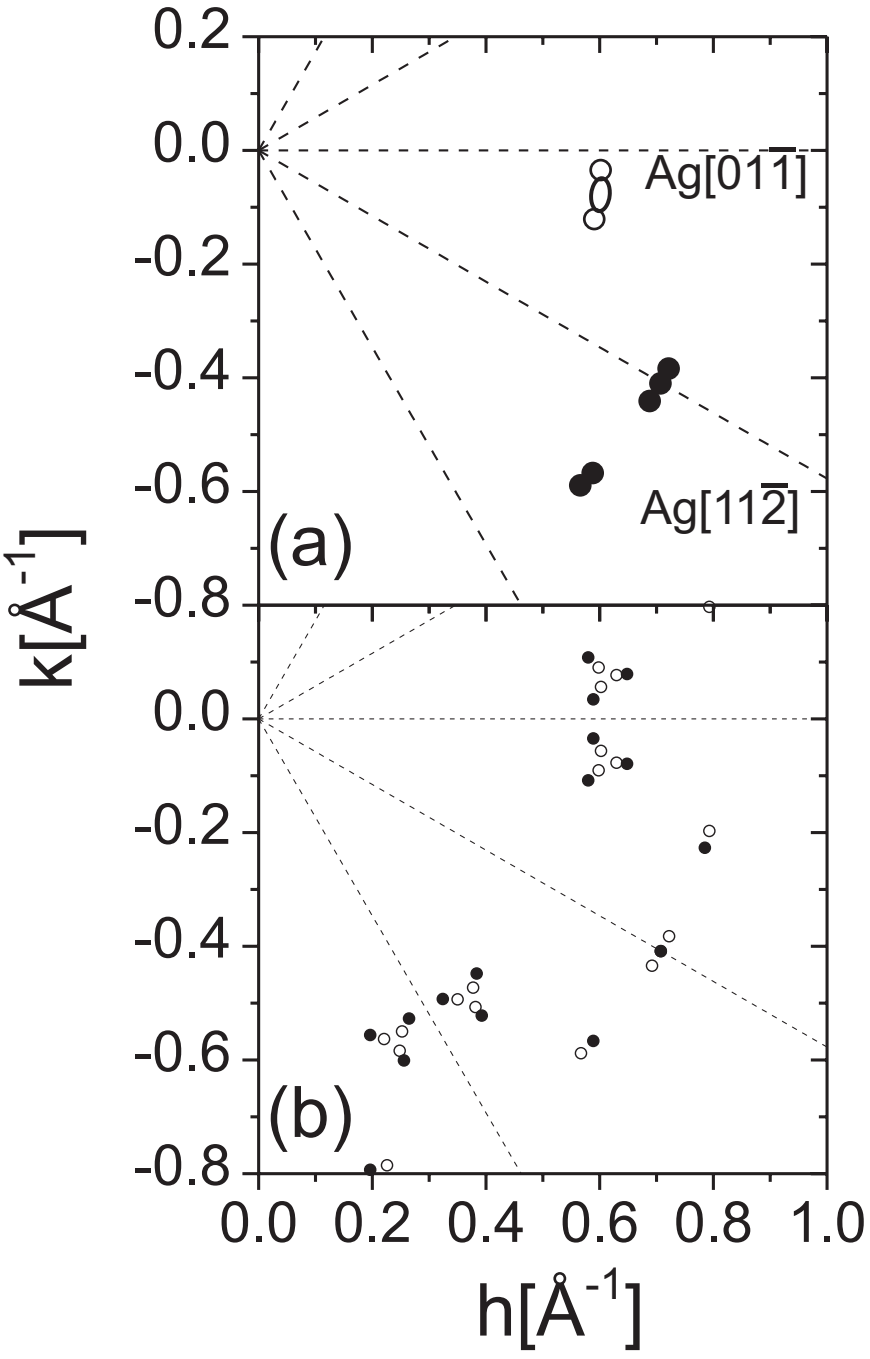

Figure 6.11: (a) Positions of the measured in-plane intensity distribution of the sample grown with the parameters $d = 50$ Å, $T_g = 318$ K and $F = 3.5$ Å/min. The open symbols denote the (011) peaks, the filled symbols the (012) peaks. (b) Calculated positions of the (011) and (012) reflections of the α (open circles) and the β structure (filled circles) (unit cell dimensions see text).

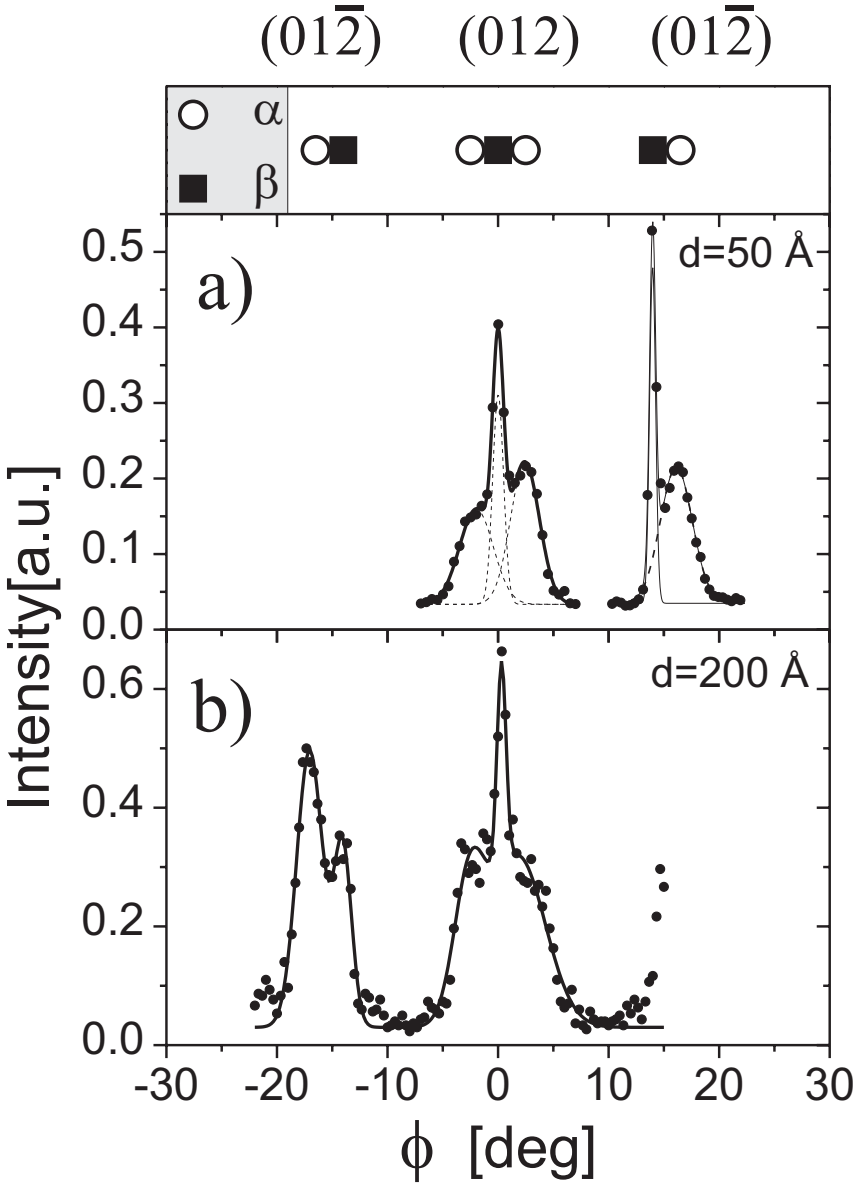

Figure 6.12: Azimuthal intensity distribution of the (012) type reflections. On top: schematic of the preferred azimuthal positions and their assignment to 2 structures. The intensity distributions are attributed to (01$\bar{2}$) and (012) reflections. (a) Azimuthal intensity distribution of the 50 Å sample. (b) Intensity distibution of the 200 Å sample.

ties and peak widths, i.e. sharp and broad reflections. The sharp peaks have been attributed to a β-like structure, the broad peaks to a α-like structure. The number of domains, the azimuthal separation of the (012) and the (01$\bar{2}$) reflection, and the orientation of the domains to the substrate are summarized in Tab. 6.3.

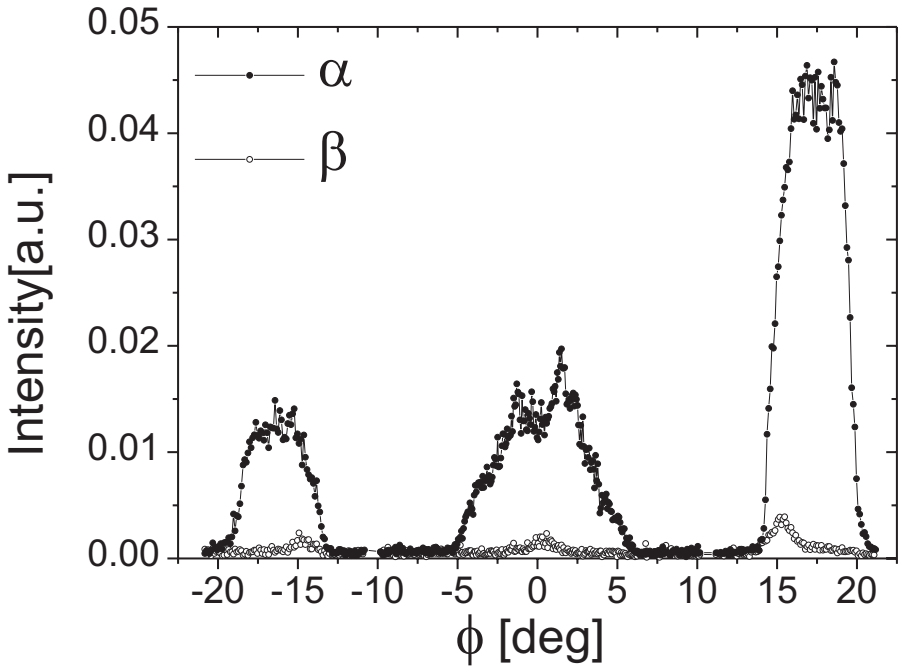

Figure 6.13: In-plane intensity distribution of the (012)-type reflections of a sample with the growth parameters $d = 32$ Å, $T_g = 473$ K, and $F = 6.3$ Å/min.

Assuming a rectangular unit mesh for both structures (as observed for the (102) plane of the bulk polymorphs), the lattice parameters of α have been calculated as $b_1 = 19.8 \pm 0.1$ Å and $b_2 = 12.2 \pm 0.1$ Å. For β, $b_1 = 19.25 \pm 0.05$ Å and $b_2 = 12.79 \pm 0.05$ Å have been determined. From this, the positions of the (011), (012) and (002) reflections have been calculated (see Fig. 6.11 (b)). All measured peaks can be explained with the aligned α- and the rotated β-like domain set, yet the positions of the (011) reflections of the β-like structure deviate slightly from the measured value. This may be an indication that either the unit mesh is actually not rectangular for the β-like structure, or the $q_{\|}$-values of the (011) or (012)-type reflections of α and β differ slightly.

Additional GIXD experiments

Several samples have been grown at temperatures between 388 K and 473 K, and at various deposition rates and film thicknesses. In all cases a broad intensity distribution has been observed. As an example, Fig. 6.13 shows the (012) reflections of a 32 Å sample grown

T_g [K]	d [Å]	F [Å/min]	α [%]	α_1/α_2	β [%]	β_1/β_2
318	50	0.9	75		25	
336	200	3.5	90		10	
388	180	7	90		10	
448	50	0.9	90	0.5–1	10	1
453	200	3.5	45	0.5	55	0.5
473	32	6.3	93		7	

Table 6.4: Estimated ratio of the α and the β structure. The estimates are made on the basis of the peak intensities of the measured domains. Note, however, that the ratio of α to β is most likely determined by a very delicate balance of various factors including the morphology and the miscut of the substrate.

at 473 K. For all samples, a q_z splitting of the (012) type reflections has been found. The intensity distribution around $\phi = 0$ has been attributed to (012), the one around $\phi = \pm 17°$ to $(01\bar{2})$. While the $(01\bar{2})$ intensity shows a steep increase at $\phi = \pm 19°$ and $\phi = \pm 14°$, and a constant intensity distribution inbetween, the (012) intensity distribution is more irregularly distributed in the range of $\phi = \pm 5°$ and consists of two tips and two shoulders. Most likely, the asymmetric intensity distribution between the peaks at $\phi = 17°$ and $\phi = -17°$ is due to the substrate miscut. The steep decrease of the $(01\bar{2})$ intensity is found at positions related to the high temperature structure, while the intensity distribution inbetween is related to the low temperature structure. These features, together with the irregular shape of the central peak, can be explained by a superposition of both structures.

Coexistence of the bulk polymorphs

The intensity distribution of the in-plane Bragg reflections can be used to determine the ratio of the α- and the β-like structure. Tab. 6.4 summarizes the growth conditions and the estimated ratio of the α and the β structure for several samples. Without exception, for all samples both structures have been observed. For all samples except one the α structure, which is also the preferred bulk structure, dominates. With one exception the α contribution seems to increase with T_g. In many cases, the structures aligned to Ag[$5\bar{7}2$], i.e. α_2 and β_2, are preferred.

6.1.3 Out-of-plane measurements

Specular rod measurements have been performed for samples grown at different T_g in the range of 197 – 473 K in order to determine the structure of the PTCDA film perpendicular to

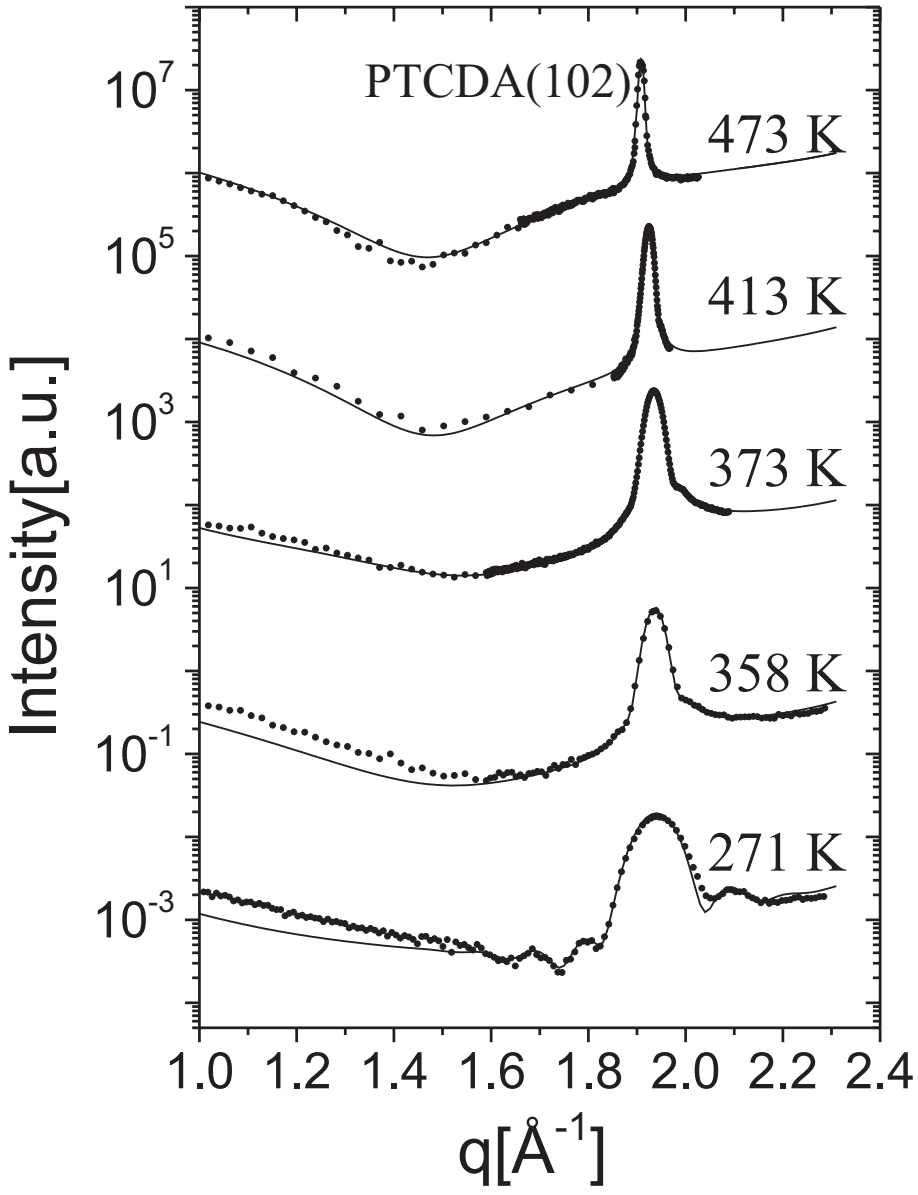

Figure 6.14: Measured (circles) and calculated (lines) specular rod intensity as a function of T_g for samples with $F = 0.8 - 2$ Å/min and $d = 50$ Å.

the substrate surface. Two sets of samples have been studied, one with $F = 0.8 - 2.0$ Å/min (low F), the other with $F = 12 - 14$ Å/min (high F).

Fig. 6.14 shows examples of the specular rod measurements including the PTCDA(102) reflection for the samples grown at low deposition rate. It has been found that PTCDA(102)

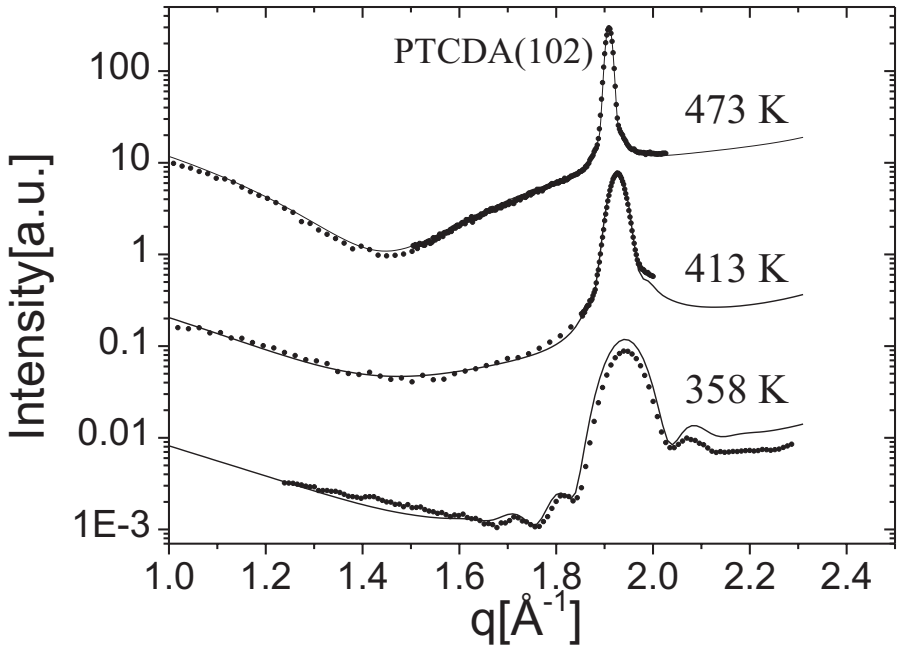

Figure 6.15: Measured (symbols) and calculated (lines) specular rod intensity as a function of T_g for samples with $F = 12 - 14$ Å/min and $d = 50$ Å.

is parallel to Ag(111). Rocking scans through PTCDA(102) show in all cases the same peak width of $0.13 \pm 0.02°$ which corresponds to the mosaicity of the substrate. The radial scans show no reflectivity oscillations, independent of the growth conditions. Up to 358 K, 1–3 Laue oscillations around PTCDA(102) have been observed. The oscillations are reduced to two shoulders for $T_g \geq 413$ K, for 473 K no oscillations are measured. The rod shape changes as a function of T_g. For $T_g \lesssim 323$ K, it is rather straight (on the logarithmic scale) for $q \leq 1.6$ Å^{-1}. The peak width corresponds to the average film thickness and is independent of T_g. For $T_g \gtrsim 358$ K, the rod developes a pronounced minimum at $q_z \approx 1.4$ Å^{-1}, and the peak width decreases with increasing T_g.

The corresponding measurements for the high deposition rate samples show a similar behavior. The Laue oscillations are visible for $T_g \leq 358$ K, while for $T_g \geq 473$ K only two shoulders near the Bragg reflection are detected. For $T_g \leq 358$ K, the rod is straight on a logarithmic scale, while for higher T_g a minimum at 1.4 Å^{-1} evolves. The peak width decreases for $T_g > 358$ K.

6.2 Discussion

6.2.1 Modelling of the rod measurements

According to the AFM data, a morphology change of the PTCDA film as a function of T_g has been observed for low F. For $T_g < 343$ K, relatively smooth or faceted films have been observed (growth regions (I) – (III)), and for $T_g \geq 343$ K large crystallites have been found. The characteristic changes in the shape of the truncation rod occur at a similar temperature as the morphology transition to region (IV). The films of relatively homogenous thickness result in a broad PTCDA(102) peak, distinct Laue oscillations and a straight rod on a logarithmic scale. The island morphology gives rise to very weak Laue oscillations (or none), a narrow Bragg peak and a pronounced minimum of the rod at $q_z \approx 1.4$ Å^{-1}. A similar narrowing of the PTCDA(102) reflection as a function of T_g has been observed for PTCDA on H-passivated Si(100) [104]. In this section, we show that the qualitative features of the rod measurements can be understood by a model based on the morphological features observed with the AFM.

The substrate has an in-plane mosaic block size of approximately 500 Å, and an out-of-plane mosaicity of about $0.13 \pm 0.02°$. For several films grown at $T_g \gtrsim 323$ K, the in-plane mosaic block size of the film and the substrate were found to be similar. The out-of-plane mosaicity of the film and the substrate are the same for all studied samples with $T_g \gtrsim 197$ K. We conclude that the PTCDA film adopts the out-of-plane orientation of the substrate and continues the substrate mosaic blocks (see Fig. 6.16 (a) and (b)).

For the specular intensity, $|\langle S(q_z)\rangle|^2$, of each mosaic block, Eq. 3.25 applies. The specular intensity of the illuminated area is the average specular intensity of the different mosaic block types. In what follows, the specular intensity will be discussed explicitly for the different morphology regions of PTCDA (see Sec. 6.1.1).

Low T_g model

The films grown in region (I), (II), and (III) are relatively smooth and homogenous, with a roughness which saturates on a lateral scale much smaller than the mosaic block size. Nevertheless, in region (I) and (III), narrow valleys between the islands or depleted areas between the facets,respectively, have been observed. To approximate this morphology, we introduce two types of mosaic blocks: (1) mosaic blocks with n_F film layers and the roughness σ_F representing the homogenous areas of the film, and (2) mosaic blocks covered by a film of

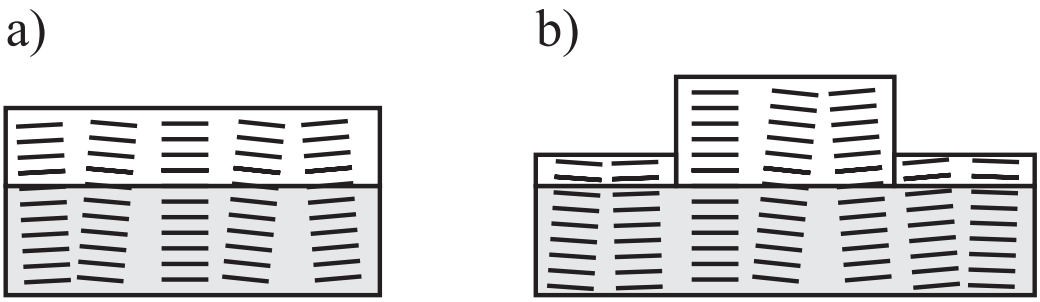

Figure 6.16: Model for the mosaic block distribution of the substrate and the film. (a) Relatively smooth, homogenous film. (b) Inhomogenous film with large islands and nearly depleated areas.

only a few monolayers with coverages θ_n, representing the valleys respectively the depleted areas. The total intensity of the illuminated area is

$$I(q_z) = (1 - A_{ML}) \left|\langle S_1(q_z)\rangle\right|^2 + A_{ML} \left|\langle S_2(q_z)\rangle\right|^2, \tag{6.1}$$

where $S_1(q_z)$ and $S_2(q_z)$ are the scattering functions of the different types of mosaic blocks, and A_{ML} is the fraction of the substrate surface covered by the type (2) mosaic blocks. Fig. 6.16 (a) shows a schematic of how the mosaic block structure of a relatively smooth film is related to the substrate.

High T_g model

Region (IV) is characterized by large crystallites separated by macroscopic distances. The typical lateral island size and the distance separating the islands are much larger than the in-plane mosaic block size. On this scale the islands, and also the area between the islands, are almost molecularly flat. AFM experiments imply that the film roughness is correlated with the substrate roughness. Two types of mosaic blocks are necessary to describe region (IV), as indicated in Fig. 6.16 (b). Type (1) is a substrate mosaic block covered by a molecularly smooth film with a thickness n_F corresponding to the island height. Type (2) is a substrate mosaic block covered by a thin film with the monolayer coverages θ_n. For the type (1), the intrinsic roughness of a PTCDA island is assumed to be 0, and the mosaic blocks follow a Gaussian distribution of the number of layers, n, with the average value, n_F, and the

ρ_S [e$^-$/Å^3]	ρ_F [e$^-$/Å^3]	d_S [Å]	d_S^1 [Å]	σ_S [Å]
2.7751	0.5247	2.36	2.34	0.9

Table 6.5: Parameters which remain unchanged for all simulations. ρ_S and ρ_F are the electron densities of the substrate and the film, d_S is the substrate lattice constant in z direction, d_S^1 is the lattice parameter of the topmost substrate layer, and σ_S is the substrate roughness.

standard deviation σ_F. The intensity of the illuminated area is therefore

$$I(q_z) = (1 - A_{ML}) \frac{\sum_n \left(e^{-\frac{(n-n_F)^2}{2\sigma_F^2}} |S_1(q_z, n)|^2 \right)}{\sum_n \left(e^{-\frac{(n_F-n)^2}{2\sigma_F^2}} \right)} + A_{ML} |S_2(q_z)|^2 . \quad (6.2)$$

Here, $S_1(q_z, n)$ is the scattering amplitude of a smooth mosaic block with n PTCDA layers, and $S_2(q_z)$ is the scattering amplitude of the mosaic blocks with only a few monolayers coverage.

Fitting the model to the data

Tab. 6.5 contains the parameters which are kept constant for all simulations. The Ag parameters have been determined by fitting the specular rod of the clean substrate. The observed relaxation of the first ML corresponds to the results of studies using LEED [105] and medium energy ion scattering (MEIS) [106]. Within the experimental uncertainty, no variation of these parameters has been observed after depositing a thin PTCDA film. For the simulations, the geometrical parameters of the film have been varied. These include the lattice parameter d_F, the lattice parameter d_0 of the first monolayer PTCDA on the substrate, the area, A_{ML}, the number of layers of the type (1) mosaic blocks, n_F, the roughness of the type (1) mosaic blocks, σ_F, and the coverages of the type (2) mosaic blocks, θ_n.

Fig. 6.14 shows examples of the fitting of the specular rod for samples deposited at low F. For the comparison of the model and the experiment, the geometric corrections mentioned in Sec. 3.7 have been taken into account. The model and the empirical parameters used for the low F data are summarized in Tab. 6.6.

For $T_g \leq 323$ K, the low T_g model appears reasonable, for $T_g > 323$ K the high T_g model. For all samples it has been found that $d_0 = 2.8 \pm 0.1$ Å$\ll d_F$. For $T_g \leq 323$ K, the height of the type (1) mosaic blocks equals the average film thickness. The roughness is approximately

T_g [k]	271	303	323	358	373	393	413	473
Model	low T	low T	low T	high T	high T	high T	high T	high T
A_{ML} [%]	35	0	15	70	65	91	94	97.5
d_0 [Å]	2.90	2.80	2.80	2.70	2.90	2.77	2.90	2.87
d_F [Å]	3.26	3.25	3.24	3.249	3.251	3.261	3.266	3.29
n_F [ML]	17	15	19	35	39	72	85	120
σ_F [ML]	2	2.6	2.5	10	10	20	27	42
θ_1	1	0	1	1	1	1	1	1
θ_2	0	0	1	0.6	0 5	0.6	0.8	0.8
θ_3	0	0	0	0.1	0.2	0.1	0	0.1

Table 6.6: Fit parameters for the low deposition rate data.

T_g [k]	303	358	413	473
Model	low T	low T	high T	high T
A_{ML} [%]	20	30	60	93
d_0 [Å]	2.85	2.90	3.00	2.85
d_F [Å]	3.245	3.253	3.263	3.29
n_F [ML]	15	18	36	75
σ_F [ML]	1.7	2.8	12	30
θ_1	1	1	1	1
θ_2	1	0.9	0.7	0.93
θ_3	0.1	0.1	0.3	0
θ_4	0	0	0.1	0

Table 6.7: Fit parameters for the high deposition rate data.

2 ML, independent of T_g. For $T_g \geq 358$ K the height if the type (1) mosaic blocks increases with T_g up to $8d$, and their height distribution is comparatively wide (about 30 %). The type (2) mosaic blocks have a coverage of about 2 ML. For $T_g \leq 323$ K, they cover at most 35 % of the sample, for $T_g \geq 358$ K, this area increases up to nearly the entire sample surface at $T_g = 473$ K.

Fig. 6.15 shows examples for the simulations for the high F data. The parameters of the model are summarized in Tab. 6.7. For $T_g \leq 385$ K, the low T_g model has been applied, and for $T_g \geq 413$ K the high T_g model. The parameters change in a similar way as observed for the low F data.

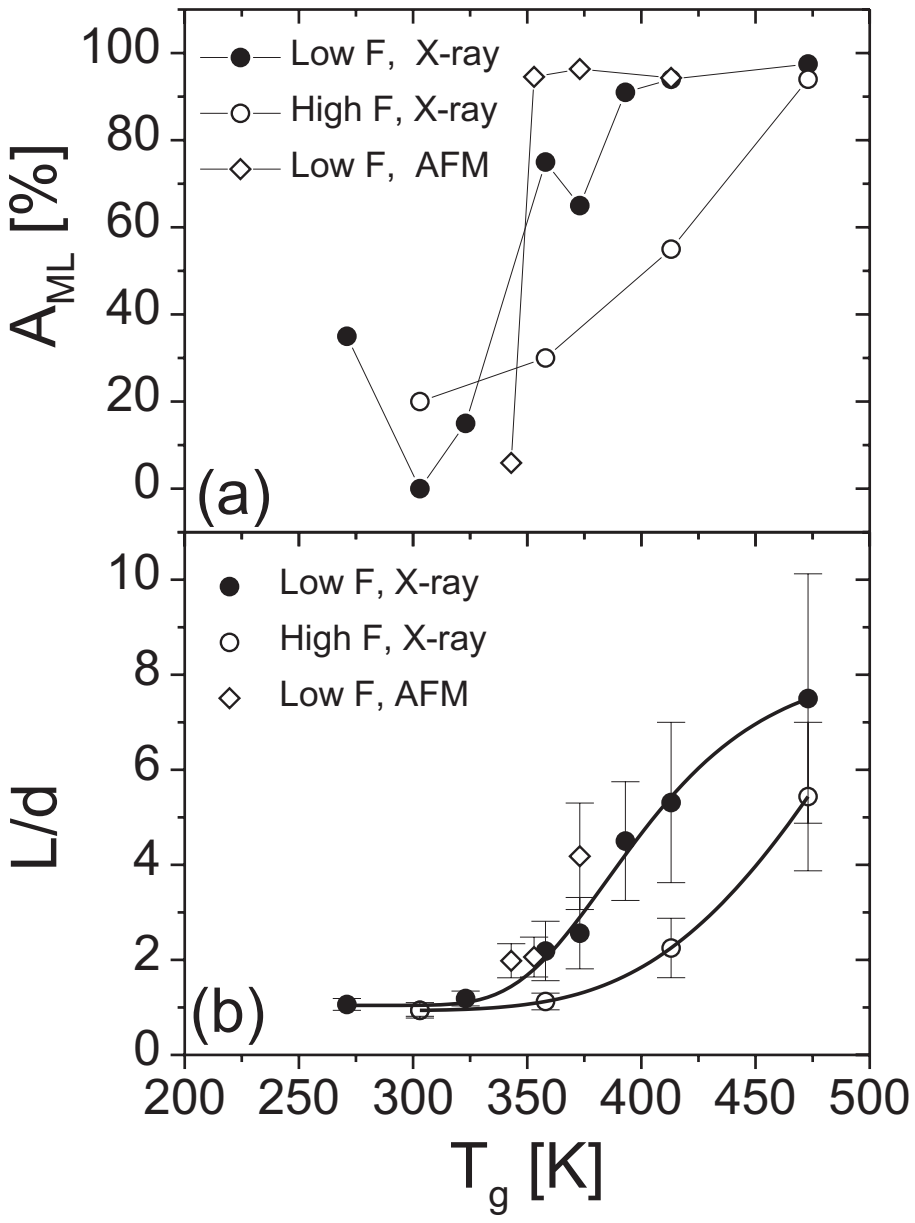

Figure 6.17: Comparison of the results of the modelling of the X-ray data for high (open circles) and low F (filled circles) with the AFM data (open diamonds). (a) Area occupied by type (2) mosaic blocks and area between the islands. (b) Height of the type (1) mosaic blocks and island height.

Results

Fig. 6.17 (a) compares the variation of the area between the islands as a function of T_g observed by AFM measurements and derived from the rod measurements. Fig. 6.17 (b)

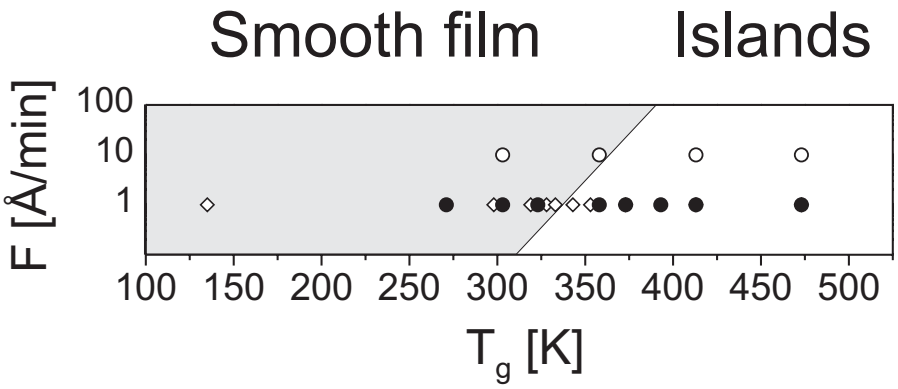

Figure 6.18: Schematic of the transition between smooth films and crystallites. The circles denote the X-ray data taken at different F, the diamonds denote the AFM data.

shows the island height and height of the type (1) mosaic blocks. For the low F data, the islands behave like the type (2) mosaic blocs with respect to their height and area. The morphology derived from the X-ray data and from the AFM data is equivalent. This allows us to extend the morphological interpretation of the X-ray data to the T_g and F range which is not accessible by AFM measurements or which has only be studied by X-ray diffraction. For low F, we find that the island height increases up to 8 times the average film thickness. For the same T_g, the islands grown with high F are thinner and cover a larger area than the islands grown at low F. The temperature range for the crystallite growth changes from $T_g \gtrsim 343$ K at $F = 1$ Å/min to $T_g > 358$ K for $F = 10$ Å/min. This is shown schematically in Fig. 6.18.

Compared to the AFM measurements, the X-ray experiments provide additional structural information: The distance of the first monolayer of PTCDA to the topmost substrate layer is independent of T_g. The charge transfer between the film and the substrate has little or no influence on the relaxation of the topmost substrate layers. For the areas between the islands, the model provides the additional information that they are covered by a 2 ML PTCDA film. The scattering of this film can be calculated using the same lattice spacings as for the islands.

6.2.2 Analysis of the island distribution

The island morphology depends on the growth temperature. Specifically, the AFM measurements show that in region (IV), the island density ρ and the island size, e.g. represented by the island height L or the area covered by the island, A, vary as a function of T_g. There

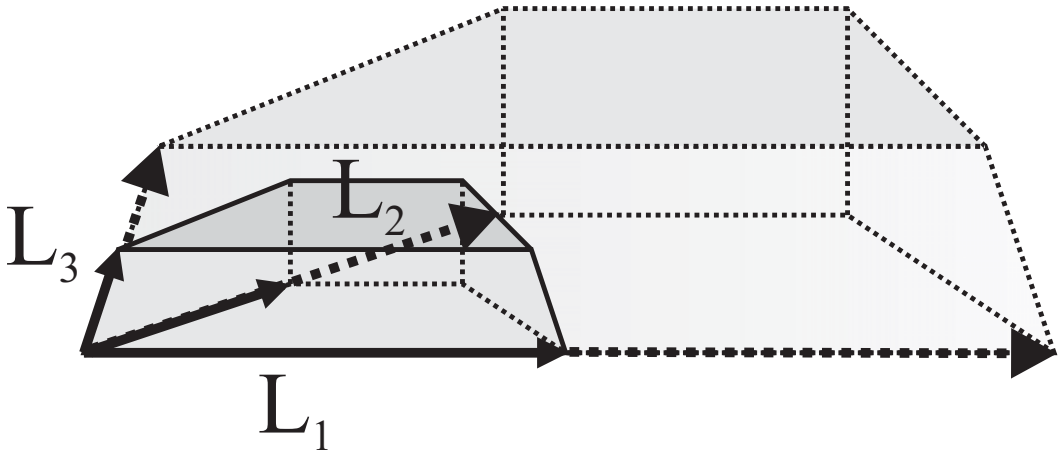

Figure 6.19: Schematic of the scaling of the islands with T_g. The typical island shape is shown in two sizes. For each size, three characteristic vectors are indicated.

exists an inverse relation between ρ and L. For a constant amount of deposited material an increase of the island density is accompanied by a decrease in the island size. A similar change of the island size and density with temperature as observed here has been observed for metal clusters and semiconductor quantum dots [26,97,107]. A rate-equation based model developed for these systems has been summarized in Sec. 4.2.3. Before applying this model to the PTCDA measurements we must extend it to incorporate not only ρ, but also A and L.

Extension of the model

The island density is defined as

$$\rho = \frac{N}{A_{tot}} = \frac{Nd}{V_{tot}} \tag{6.3}$$

with the number of the islands N and the total area A_{tot} of the sample. The total volume $V_{tot} = A_{tot}d$ of deposited material is identical for all samples. For PTCDA, the X-ray data imply two wetting monolayers on top of the substrate surface. Therefore, the effective volume contributing to the islands is $V^* = V_{tot} - n_{wet}A_{tot}d_F$. V^* is related to the average volume of an island by $V^* = NV$, and we receive

$$\rho \sim \frac{1}{V}. \tag{6.4}$$

Since the islands are small crystallites of a characteristic shape, their volume is directly related to the island height and the island area. If the geometrical relationship between all facets and edges of the island shape is known, the volume of an island can be calculated from three independent vectors with the lengths L_1, L_2 and L_3. An example of three arbitrary,

independent vectors is shown in Fig. 6.19. The scaling of the islands as a function of T_g permits application of the theorem of intersecting lines: The ratio $L_1 : L_2 : L_3$ is constant, as a consequence of the geometry, and if $L_1 \sim L$ is assumed, $V \sim L^3$. With this, Eq. (6.4) changes to

$$\rho \sim \frac{1}{L^3}. \tag{6.5}$$

Inserting Eq. 6.5 in Eq. 4.7, we obtain

$$\ln\left(\frac{1}{L^3}\right) \sim const + \frac{pE_{eff}}{k_B T_g}. \tag{6.6}$$

The same analysis, applied to the island area $A \sim L^2$, can be used when plotting $\ln(A^{-3/2})$ against the inverse temperature. For PTCDA, not only one island size and shape but a distribution around an average size and shape has been observed. For this system, Eq. 6.5 refers to the average values.

We now apply the above model to the experimentally determined PTCDA island density, coherence length and island area. The respective plots of the logarithm vs. the inverse substrate temperature are presented in Fig. 6.20. All plots show a linear behavior for growth temperatures larger than $T_g \approx 350$ K below which the morphology is smooth films. For the island density (excluding the data point at 343 K with two island distributions), and also for the two coherence length datasets, an effective diffusion energy barrier $pE_{eff} = 0.6 \pm 0.2$ eV has been determined. The slope of both coherence length datasets is similar in the crystallite growth temperature range, the variation of the offset can be explained by the change in the deposition rate. The energy barrier determined from the island area is $pE_{eff} = 1.1 \pm 0.3$ eV.

Clearly, pE_{eff} determined by the island area is much larger than the energy barrier derived by the other two methods. In the following, we discuss the significance of these different values. The model used here has been developed for the island density. The basic assumption for the translation of the island density into the island size is that the islands grown at different T_g have the same average shape. Since the shape of islands can vary to some extent during the MBE deposition [108], this assumption is not generally fulfilled. Furthermore, it has been observed that the shape of the coexisting α and the β-type crystals is different [50]. For our experiments the coexistence of the bulk polymorphs causes only minor problems since the α phase dominates in most films. This is supported by the fact that the island height and the island density give the same pE_{eff}. However, it is difficult to determine the island area from the microscopy images. The optical microscopy images give the best statistics, but due do their optical properties the circumference of the islands

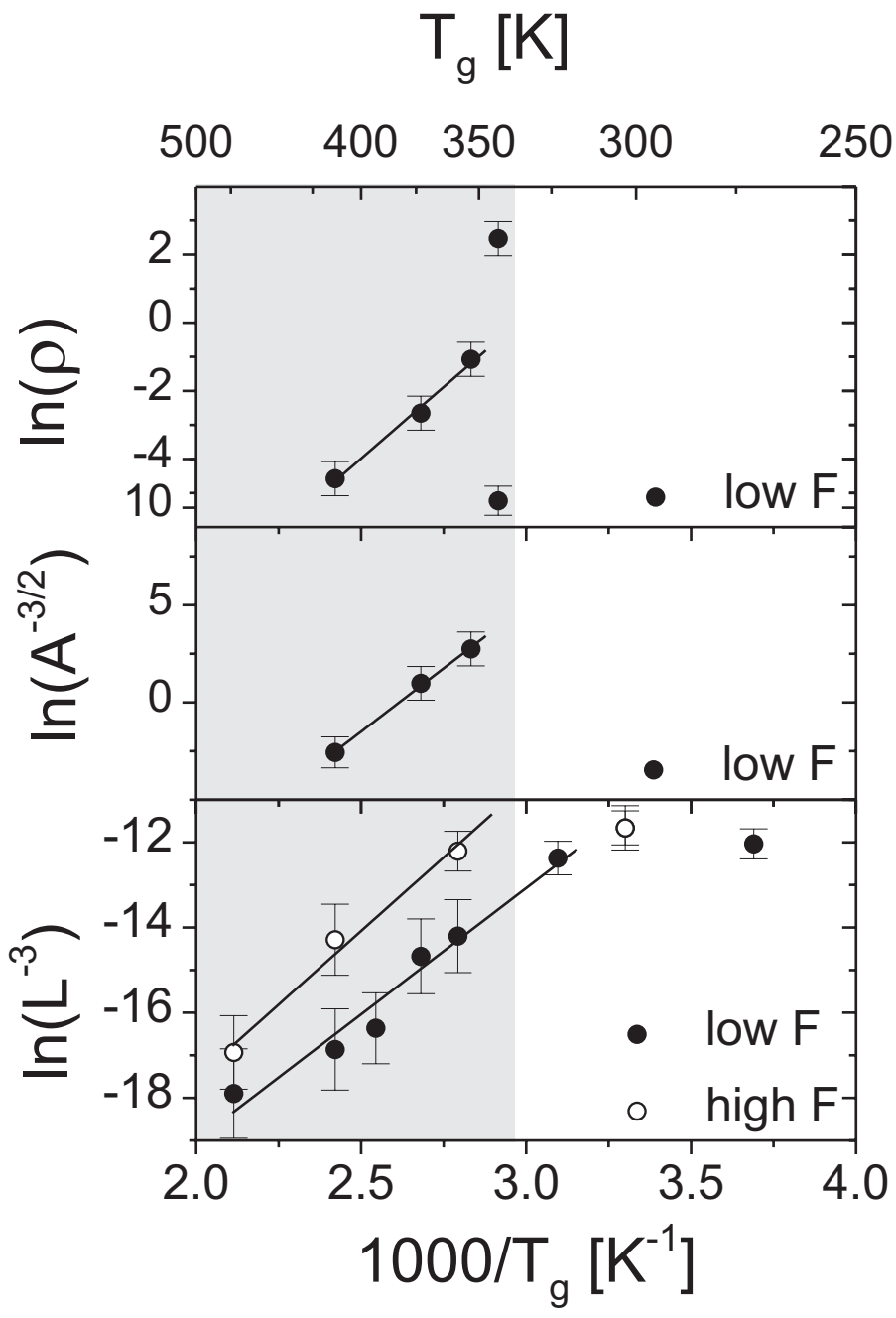

Figure 6.20: $\ln(\rho)$, $\ln(L^{-3})$, and $\ln(A^{-2/3})$, plotted against the inverse growth temperature, using the island density and area determined by microscopic methods, and the island height determined by X-ray diffraction. The shaded area indicates the crystallite growth regime.

is not clearly visible. Therefore, the reason for the deviation of the value determined by the island area might be a systematic error in determining the island area.

The island morphology on top of two wetting monolayers corresponds to the Stransky-Krastanov growth mode. The observed energy barrier which refers to the later stages of the growth (i.e. $d \approx 6...50$ Å) as opposed to the first few monolayers is an effective energy barrier for surface self-diffusion of PTCDA on PTCDA. This effective energy barrier includes the island nucleation process, i.e. the critical cluster size, of PTCDA. Since the islands seem to nucleate preferentially at steps, the island density, and with this also pE_{eff}, are influenced by the substrate step density. It is important to note that the diffusion between the islands takes place on the strained wetting layer of PTCDA which covers the substrate. Therefore we expect to obtain a slightly different pE_{eff} for the growth of PTCDA on a relaxed PTCDA layer with bulk properties.

We emphasize that the energy barriers presented here should be considered only as estimates. Nevertheless, the true value for pE_{eff} will probably fit to the range obtained in our studies. For a more detailed analysis several of the simplifications made here would have to be abandoned and a thickness-dependent strain profile should be taken into account. In addition, for the system under study, the anisotropy of the interactions would have to be considered at a certain level of refinement.

The most remarkable conclusion of this analysis is the following: The application of classical growth models developed for metals and semiconductors to comparatively complex organic molecules such as PTCDA works quite well, at least in the framework of our simple analysis.

6.2.3 Epitaxy and strain

Two different morphologies of epitaxially grown PTCDA films have been observed, one for high temperature and one for low temperature deposition. In Tab. 6.8, the in-plane lattice parameters and the angle between the neighboring (012) and (01$\bar{2}$) reflections of the bulk phases, the monolayer PTCDA/Ag(111) and the measured high and low temperature phases are summarized. In addition, the ratio $\xi = b_1/b_2$ is shown which is a measure for the distortion of the in-plane unit cell. In the following sections, we will discuss these observed structures in detail.

phase	b_1 [Å]	b_2 [Å]	$\lvert\phi(012) - \phi(01\bar{2})\rvert$ [deg]	ξ
bulk α [50]	19.91	12.6	19.5	1.665
bulk β [50]	19.3	12.45	15.8	1.550
monolayer [15]	19.0	12.6	13.9	1.508
α_1, α_2 (high T_g)	20.11 ± 0.05	12.16 ± 0.05	19.15 ± 0.3	1.65 ± 0.01
β_1, β_2	19.44 ± 0.05	12.53 ± 0.05	15.6 ± 0.3	1.55 ± 0.01
α (low T_g)	19.8 ± 0.1	12.2 ± 0.1	18.1 ± 0.5	1.62 ± 0.02
β	19.25 ± 0.05	12.79 ± 0.05	13.9 ± 0.3	1.50 ± 0.01

Table 6.8: Dimensions of the in-plane unit mesh for the bulk structure, the monolayer structure, and the experimentally determined values for the different phases of the low and the high temperature structure.

High temperature growth

The unit mesh of all high T_g structures is rectangular, as expected from the bulk PTCDA phases. Furthermore, ξ_α^{exp} deviates only by 0.5 ± 0.6 ∀ from the bulk ratio, and ξ_β^{exp} corresponds to the bulk ratio within 0 ± 0.6 ∀. We conclude that both phases correspond to a relaxed, but thermally expanded, bulk structure. The high T_g structure consists of 2 α-like and 2 β-like phases. All structures are incommensurate with the substrate. The β_1 and the α_1 phase are preferentially aligned to Ag($22\bar{4}$), the β_2, and the α_2 structures to Ag($5\bar{7}2$). We note that, integrated over the film thickness, these are the dominating structures.

Low temperature growth

The unit mesh of the α-like phase is rectangular, as observed for the bulk, whereas the unit cell of the β phase most likely is not rectangular. A deviation from the rectangular unit cell has also been observed for the commensurate monolayer structure investigated in detail in Ref. [15]. ξ_β^{exp} deviates by at most -0.25 ± 0.6 ∀ from ξ observed for the monolayer, but by 3.0 ± 0.6 ∀ from the value of the bulk β phase. ξ_α^{exp} is between the α and the β bulk values, but more similar to the α bulk value with a deviation of 2.5 ± 1.2 ∀. We conclude that both phases are distorted relative to the respective bulk structures. The β-like structure is similar to the monolayer structure of PTCDA/Ag(111), whereas the α-like structure is similar to a distorted α bulk structure.

Both structures observed at low T_g are incommensurate with the substrate. The α-like structure is oriented parallel to the monolayer structure, the β-like structure is aligned to Ag($22\bar{4}$) and Ag($5\bar{7}2$), as observed for the monolayer structure. Again we note that these

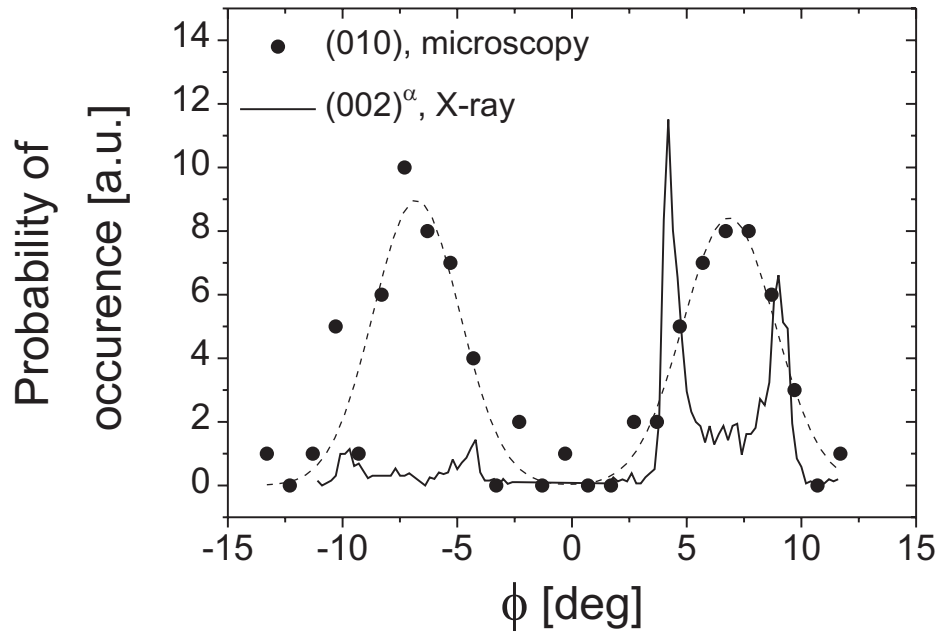

Figure 6.21: Comparison of the azimuthal orientation of the PTCDA(10) facet of the islands and the azimuthal orientation of the unit mesh of the α-phase. The X-ray data are plotted with an offset of 90° since [010] is perpendicular to [002] $\phi = 0$ corresponds to Ag[22$\bar{4}$].

are the structures dominating by volume.

Rotational order

We now address the rotational order in the high temperature structure. The X-ray intensity distribution inbetween the preferential orientations of α_1 and α_2, respectively β_1 and β_2, indicates a rotational distribution of the respective α-like and the β-like domains between the preferential orientations. A similar azimuthal distribution has been observed by microscopy methods for the (010) plane of the crystallites. For simplicity, in the following we will use the bulk nomenclature of the directions even if the AFM data are only sensitive to their in-plane projection.

Fig. 6.21 compares the orientation of PTCDA[010] relative to Ag[22$\bar{4}$], determined for a sample with $T_g = 478$ K, $F = 6.3$ Å/min and $d = 126$ Å, with the PTCDA[002] direction pf the α-phase of a sample with $T_g = 348$ K, $F = 6.3$ Å/min and $d = 50$ Å. Both samples are grown in the high T_g regime and characterized by large, well-separated islands. The X-ray

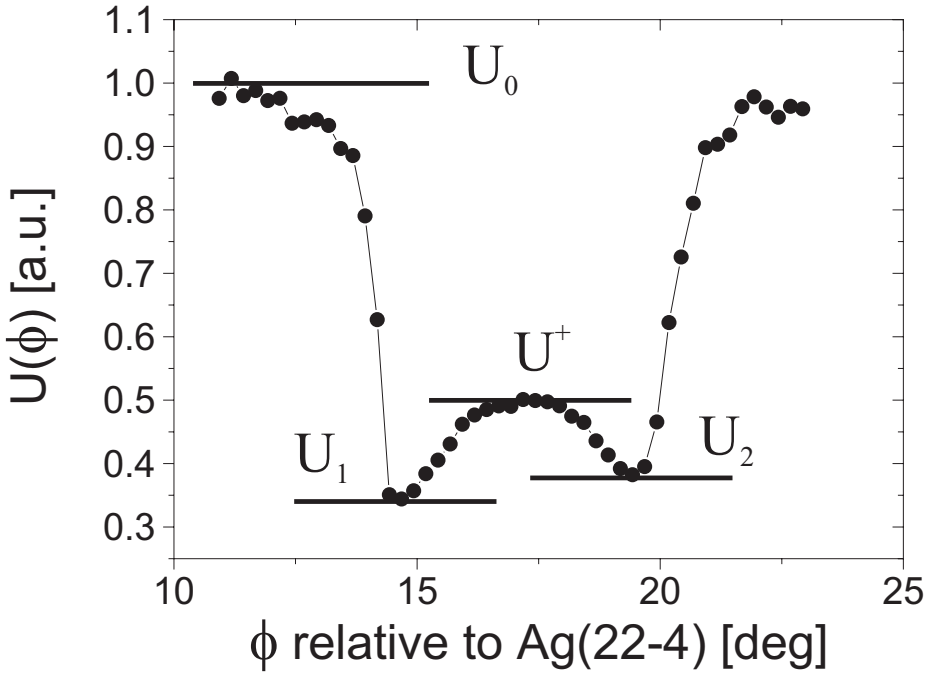

Figure 6.22: Azimuthal potential energy, calculated for the $(01\bar{2})$ intensity distribution between α_1 and α_2 for the sample grown with the parameters $d = 50$ Å, $T_g = 448$ K. U_1 and U_2 are the potential minima, U^+ a local maximum and U_0 the absolute potential maximum.

data are plotted with an offset of 90° since PTCDA(010) is perpendicular to PTCDA(002). The PTCDA(002) α reflections are found at $\phi \approx \pm 9°$ and $\phi \approx \pm 5°$. Their separation of $\approx 4°$ equals the FWHM of the PTCDA(010) facet distribution. The PTCDA(002) β reflections are expected at the position of the maximum of the microscopy data. Most likely, the in-plane rotation of the unit mesh corresponds to a rotation of the mesoscopic crystallites on top of the wetting layer.

The azimuthal X-ray intensity I at every azimuthal orientation of the sample, ϕ, is proportional to the number of domains or crystallites, respectively, oriented along this direction. This can be related to a potential $U(\phi)$ via

$$I \sim e^{-\frac{U(\phi)}{k_B T}}. \tag{6.7}$$

In Fig. 6.22, the azimuthal potential, calculated for the $(01\bar{2})$ intensity distribution between α_1 and α_2, for the sample grown with the parameters $d = 50$ Å and $T_g = 448$ K,

is shown. The two minimum potentials U_1 and U_2 at the preferred orientations are nearly equivalent. At $\phi \approx 14°$ and $\phi \approx 19°$, a steep potential increase is found. Inbetween these orientations, the potential changes only slightly, assuming a local maximum U^+ at $\phi \approx 17°$. U^+ is located at the position of the α-like structure at low T_g.

The azimuthal intensity distribution shows a marked difference between the high T_g and the low T_g samples (see Fig. 6.8 and 6.12). Therefore, the azimuthal potential depends cleary on the growth parameters. It does not simply reflect the surface potential of the wetting layer, but rather the reaction potential of the growth process itself.

Model for the epitaxy

Based on STM and LEED measurements it was reported that a monolayer of PTCDA is commensurate to the substrate and aligned such that Ag[22$\bar{4}$] and Ag[5$\bar{7}$2] grow parallel with the PTCDA[012] and [01$\bar{2}$] directions, respectively [15]. Due to the strong binding of the monolayer to the substrate [16, 57], in contrast to the weak binding between subsequent layers, we do not expect that the commensurate monolayer structure is continued during further growth. However, both reported multilayer structures, the low temperature and the high temperature one, nevertheless show characteristic orientations with respect to the monolayer structure.

Therefore, we propose a model for the epitaxial growth of a PTCDA film (for high and low T_g) on top of an initial layer with monolayer structure. For the low temperature structure, a strained epitaxial film grows on top of the monolayer structure *without changing the orientation of the unit cell*, as shown in Fig. 6.23 (a). The (10) and (02) planes of the monolayer and the film are parallel. The orientation of α- and β-like structure are similar. For the high temperature structure, a relaxed epitaxial film grows on top of the monolayer structure in two orientations for each polymorph, which are *both different from the monolayer orientation*, as shown in Fig. 6.23 (b). For one orientation, the [12] directions of the monolayer and the film are parallel, for the other orientation the [1$\bar{2}$] directions are parallel.

Interestingly, a similar orientational relationship has been observed for the metal-on-metal epitaxy of fcc(111)/bcc(110). The bcc surface structure is rectangular (as the PTCDA unit mesh), the fcc surface structure hexagonal, but can also be described by rectangular unit mesh with the ratio $\sqrt{3} : 1$ between the long and the short side. In the Nishiyama-Wassermann (NW) orientation, the sides of the rectangular unit cells of fcc and bcc are

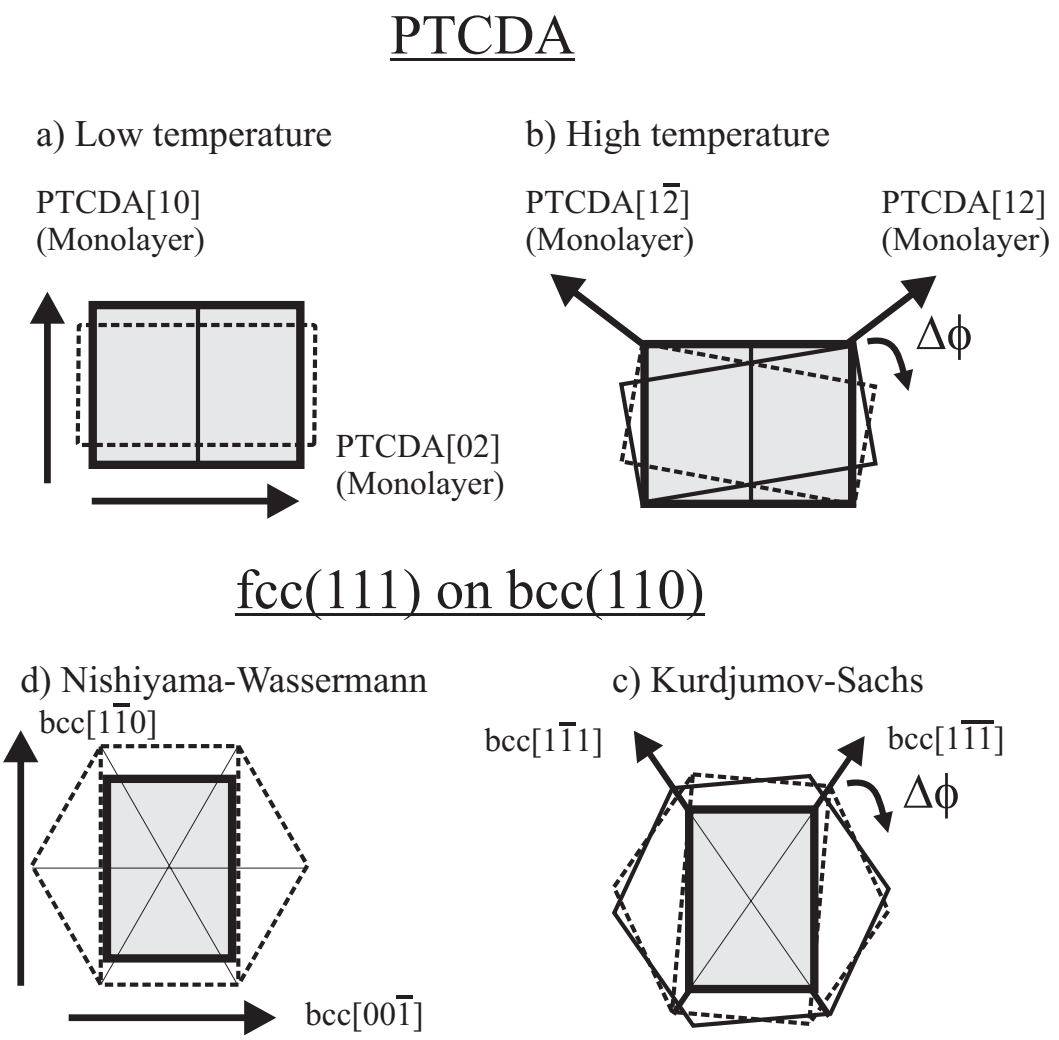

Figure 6.23: Orientation of the thin film unit mesh relative to the template structure (shaded in gray). (a) Orientation of the PTCDA film grown at low T_g (dashed line) relative to the PTCDA monolayer. The (10) and (02) planes of the monolayer and film align parallel. (b) Two possible orientations of the PTCDA film grown at high T_g (dashed and straight thin lines). Either the (12) or the (1$\bar{2}$) planes of the monolayer and the film are parallel. (c) Nishiyama-Wassermann orientation, observed for the growth of fcc(111)/bcc(110) with fcc(1$\bar{1}$0) ∥ bcc(001). (d) Kurdjumov-Sachs orientation, observed for the growth of fcc(111)/bcc(110), with fcc(1$\bar{1}$0) ∥ bcc(1$\bar{1}$1) or bcc(1$\bar{1}\bar{1}$).

parallel, i.e. fcc(1$\bar{1}$0) ∥ bcc(001), similar to the observed low temperature structure of PTCDA/Ag(111). In the Kurdjumov-Sachs (KS) orientation, the rectangular unit meshes are aligned along one of the diagonals, i.e. either fcc(1$\bar{1}$0) ∥ bcc(1$\bar{1}$1) or bcc(1$\bar{1}\bar{1}$), similar to the high temperature orientation of PTCDA/Ag(111). [22, 23]

One important difference between the NW/KS orientations of fcc(111)/bcc(110) metal

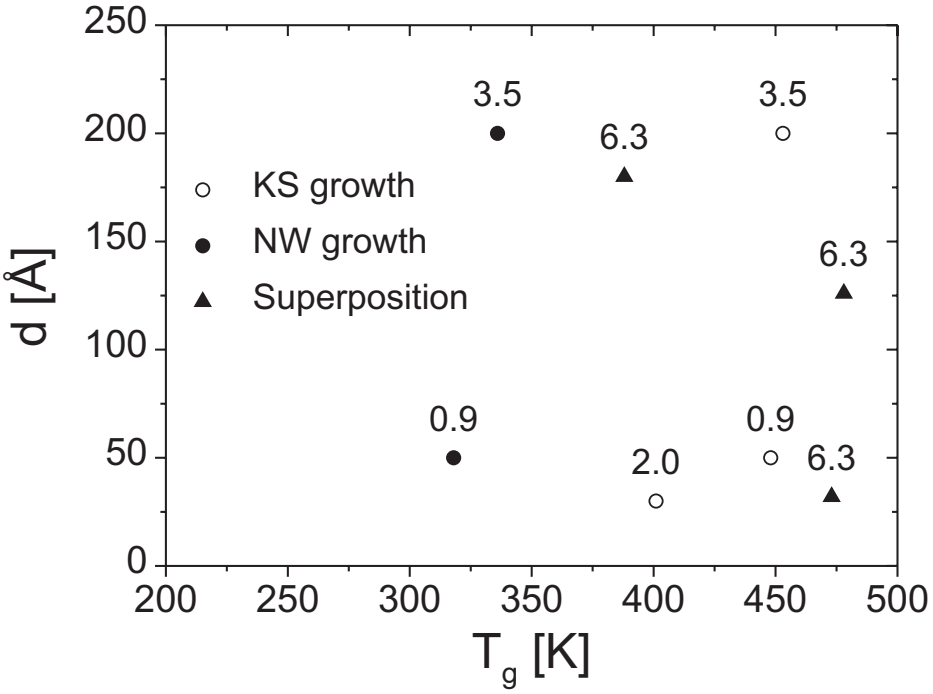

Figure 6.24: Overview of the sample structure as a function of the growth parameters. The labels indicate the deposition rate F. The KS-structure is represented by open circles, the NW structure by filled circles, and the superposition of both structures by triangles. The gray shading indicates the growth temperature range in which relatively smooth films are observed.

systems and the similar orientations observed for PTCDA is that the orientation of the metals is determined by one unit cell, while the orientation of PTCDA is determined by two unit cells.

Fig. 6.24 summarizes the in-plane structures of PTCDA/Ag(111) as a function of the growth parameters. The labels indicate the deposition rate F. The KS structure is represented by open circles, the NW structure by filled circles, and the superposition of both structures by triangles. The gray shading indicates the growth temperature range in which relatively smooth films are observed. Relatively smooth films correspond to the NW structure, while the island morphology observed at high T_g corresponds to either a superposition of NW and KS structure or to the KS structure. While for $F \leq 3.5$ Å/min only one structure (NW or KS) has been found, for $F = 6.3$ Å/min a superposition of the structures has been observed. It seems that the island morphology favors the KS orientation, but that kinetic

considerations are also important, since higher growth rates can induce a coexistence of both epitaxial orientations.

For most fcc(111)/bcc(110) systems, only one of the orientations, either KS or NW, has been found to exist at one time, since the strain between the unit meshes depends on their size (and therefore also on the ratio of the atomic radii of the substrate and the film) [22]. One exception has been Pd(111)/Cr(110), where the relative fractions of both structures are a function of the temperature [23]. The coexistence of NW and KS is similar to the superposition of the low and the high temperature structure of PTCDA/Ag(111), observed for a variation of growth parameters. As observed for Pd/Cr, the azimuthal orientations of α_1 and β_1 are shifted by 5°, which implies that such a large azimuthal shift can be expected.

For all growth parameters studied, a well-ordered out-of-plane crystal structure has been observed. This is consistent with the observation of Taborski et al. that even for large film thicknesses the molecules are aligned parallel to the substrate [16]. Despite of the similar lattice parameters of the substrates, the here reported in-plane structures of PTCDA films on Ag(111) deviate from the structures observed on Au(111) [48,59,62]. This is not surprising since even the monolayer structure on both substrates is different [15, 56, 109]

Origin of the morphology and the structure transition

The PTCDA films undergo two transitions as a function of the growth temperature: A structure and a morphology transition. The transion of the structure, from the NW to the KS orientation, can be explained with the strain of the phases relative to the distorted monolayer structure (see Sec. 2.3.2). For both bulk polymorphs, especially for the preferred α phase, the NW-type alignment is unfavorable due to the large misfit strain in the directions [10] and [01], while the alignment in a KS-type structure along [12] is clearly more favorable (see Tab. 2.3). This is the orientation observed for $T_g \gtrsim 350$ K.

The structural transition is accompanied by a morphology transition from smooth films for $T_g \lesssim 350$ K to islands on a wetting layer for $T_g \gtrsim 350$ K (Stransky-Krastanov growth). For metals, the strain-induced transition from a strained commensurate structure of fcc(111)/bcc(110) to either the NW or the KS structure is often accompanied by Stransky-Krastanov growth [22, 110, 111]. The criterion for layer-by-layer growth in equilibrium thermodynamics is

$$\gamma_{film} + \gamma_{substate} - \gamma_{inter} \leq 0. \tag{6.8}$$

Here, γ_{film} is the interfacial energy of the film surface, $\gamma_{substrate}$ of the substrate surface, and γ_{inter} of the substrate-film interface. γ_{inter} contains the chemical interaction with the

substrate (which decreases after a few ML's) and the strain energy of every monolayer. The second contribution increases with increasing film thickness, and for a critical layer number n_c, the criterion for layer-by-layer growth will not be fulfilled anymore, and islanding occurs for near-equilibrium growth conditions. Nevertheless, it is possible to induce a quasi layer-by-layer growth by limiting the surface diffusion length, i.e. using low T_g and high F.

The above criteria seem to apply also for PTCDA/Ag(111). It can be assumed that the morphology and the structure of the film results from a competition between kinetic constraints due to the non-equilibrium growth conditions and the structure favored by the equilibrium thermodynamics. The total energy of the film is minimized by several mechanisms. (1) The structural transition away from the strained monolayer structure, (2) the development of energetically favored facets and separate crystallites, and (3) the increase of the volume ratio of the preferred bulk polymorph. Especially the last aspect is difficult to control since free energy of both polymorphs is similar. It has been observed that the ratio α/β increases with T_g. Our observations, and the observations of other groups [63, 104, 112], indicate that α is energetically favored.

The SK growth is a typical growth mode of PTCDA on several substrates, including Au(111) [59] and In-terminated InAs(001) $(4 \times 2)/c(8 \times 2)$ [46]. In both cases a difference between the structure of the wetting layer and the islands has been found. Furthermore, for Au(111) a transition between relatively smooth films and separate islands has been observed as a function of T_g, similar to the results of this study.

Chapter 7

Temperature-dependent effects

In this chapter, we study the effect of temperature changes on thin PTCDA films grown under various conditions. The relevance of understanding the thermal behavior of organic thin films lies in the effect of thermally-induced changes on the performance of organic electronic devices. From a fundamental point of view, however, it is interesting to understand the metastable and stable structures organic films can form, and especially the mechanism of the transition between different structures.

This chapter is organized as follows. First, we show results concerning the effect of annealing on PTCDA films with different morphologies. Then, the thermal expansion of the film is discussed in a separate section, followed by the report of cooling-induced structural changes of the film.

7.1 The effects of annealing

In this section, we present the results of AFM and X-ray experiments during the annealing and the desorption of thin PTCDA films from the Ag substrate. The AFM data are analyzed qualitatively. The X-ray data are modelled (similar to the data taken from as-grown films, see Sec. 6.2.1) to derive quantitative information about the influence of the annealing on the structure and the morphology.

7.1.1 AFM experiments

The effect of annealing on the morphology of PTCDA/Ag(111) has been studied on a sample with T_g = 135 K, F = 0.8 Å/min, and d = 50 Å. The annealing has been performed in several 30 – 40 K steps, up to the temperature at which desorption of the PTCDA film

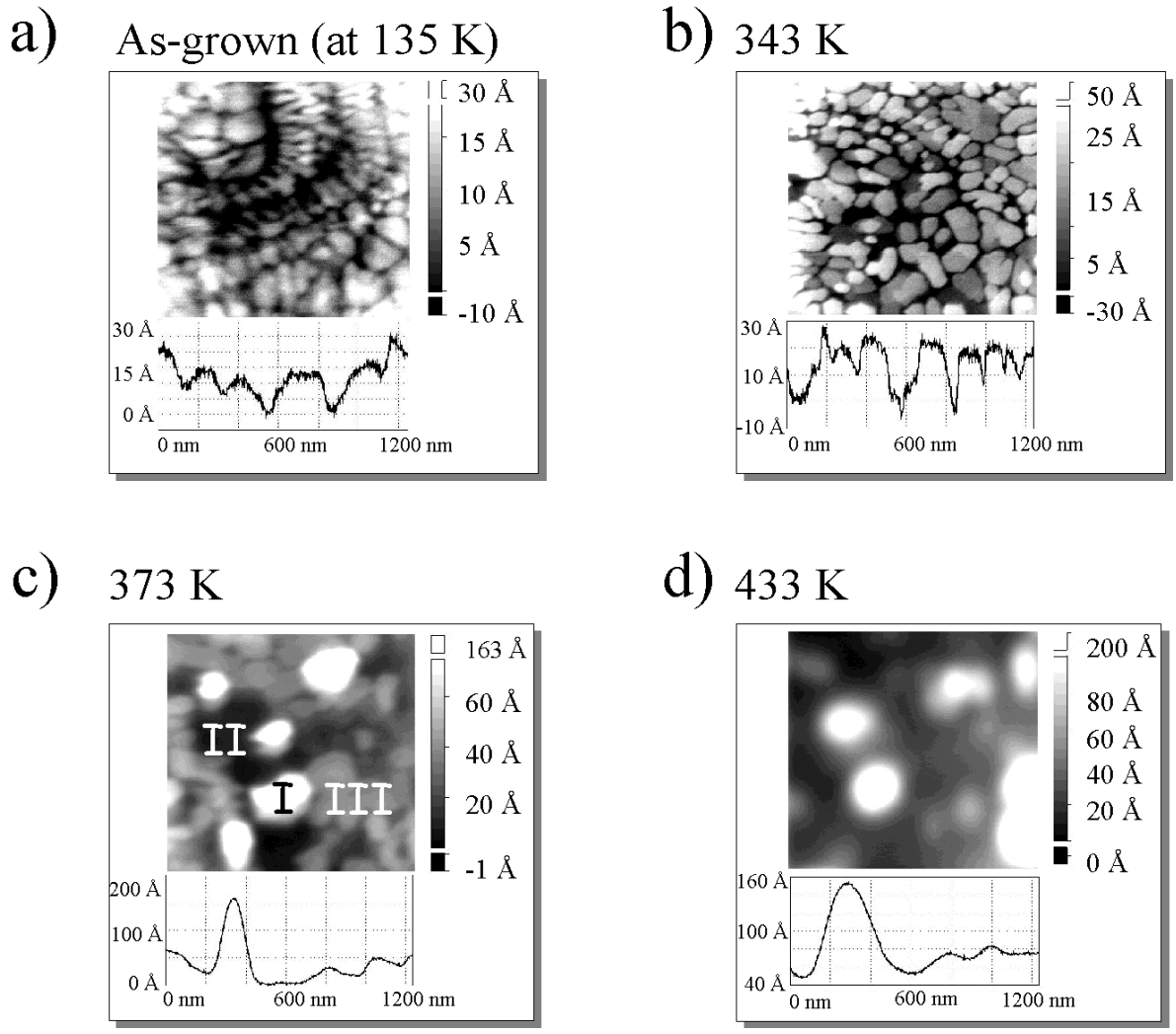

Figure 7.1: Non-contact AFM measurements of the morphology of a PTCDA film with the growth parameters $T_g = 135$ K, $F = 0.82$ Å/min, and $d = 50$ Å as a function of T_a. All AFM pictures have an area of 1.25×1.25 μm^2.

occurs. Each measurement cycle consists of annealing the sample at the annealing temperature, T_a, for typically 2 h, followed by a slow cooling respectively heating of the sample to room temperature. The subsequent non-contact AFM measurements have been performed at room temperature. Fig. 7.1 presents non-contact AFM measurements of the PTCDA film as a function of T_a. Three morphology regions can be distinguished: (1) the as-grown morphology at $T_g = 135$ K (Fig. 7.1 (a)), (2) a similar, but smoother morphology at $T_a = 343$ K (Fig. 7.1 (b)), and (3) irregular islands for $T_a \geq 373$ K (Fig. 7.1 (c) and (d)).

Region (1) is characterized by islands separated by narrow valleys. The arrangement of the islands reflects the substrate steps. For a detailed description of the as-grown morphology we refer to Sec. 6.1.1. The more compact islands observed in region (2) are molecularly flat

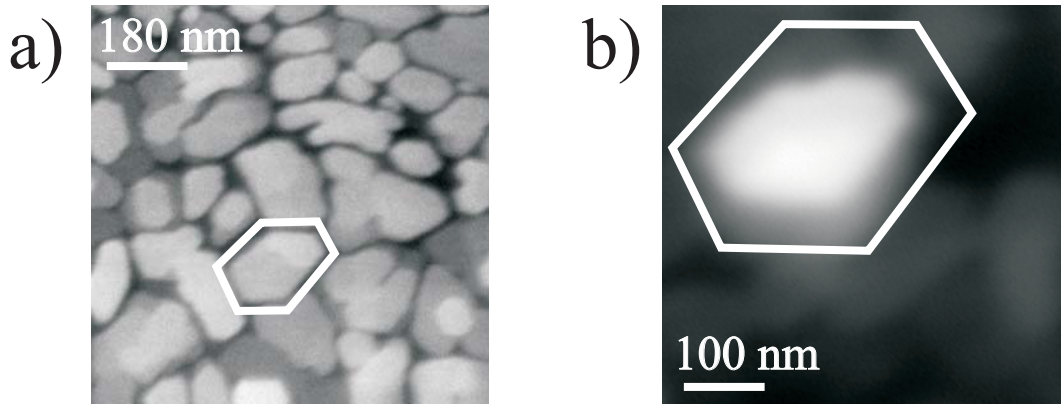

Figure 7.2: Faceted islands observed at different annealing temperatures. (a) Close-up of Fig. 7.1 (b), $T_a = 343$ K, (b) close-up of Fig. 7.1 (c), $T_a = 373$ K.

and show characteristic facets (see Fig. 7.2 (a)), similar to the as-grown films for $T_g \geq 343$ K (see Sec. 6.1.1). All islands have the height $h \approx d$ and the lateral size 50 – 200 nm, similar to the as-grown sample. The arrangement of the islands follows the substrate morphology. Region (3) ($T_a \geq 373$ K) separates in 3 areas with a different morphology: (I) faceted islands with $h \approx 3d$, (II) depleted areas, and (III) islands with $h \approx d$. Fig. 7.2 (b) shows a close-up of a high island at $T_a = 373$ K. The influence of the substrate morphology is not anymore visible. The lateral sizes of the high islands are 200 – 500 nm, and of the low islands 50 – 200 nm. The depleted area seems to increase for $T_a > 373$ K, while the area of the small islands decreases.

7.1.2 X-ray experiments

Stepwise annealing / smooth films

Several samples with $d = 50$ Å, deposited at various growth parameters, have been grown and annealed in the portable UHV chamber. The dewetting process has been monitored with *in situ* measurements of a large section of the specular rod including the (102) PTCDA peak.

The sample with $T_g = 235$ K, $F = 0.8$ Å/min, and $d = 50$ Å has been annealed in several steps. The growth conditions of the sample correspond to a relatively smooth film (see Sec. 6.2). After three annealing steps up to 308 K, T_a has been increased in steps of 5 K, typically every 15 – 45 min. Prior to the rod measurements at T_a, it has been ensured that the shape of the PTCDA(102) Bragg peak does not change on a time scale of at least 10 min.

Fig. 7.3 shows examples of the specular rod measurements performed at different T_a. The

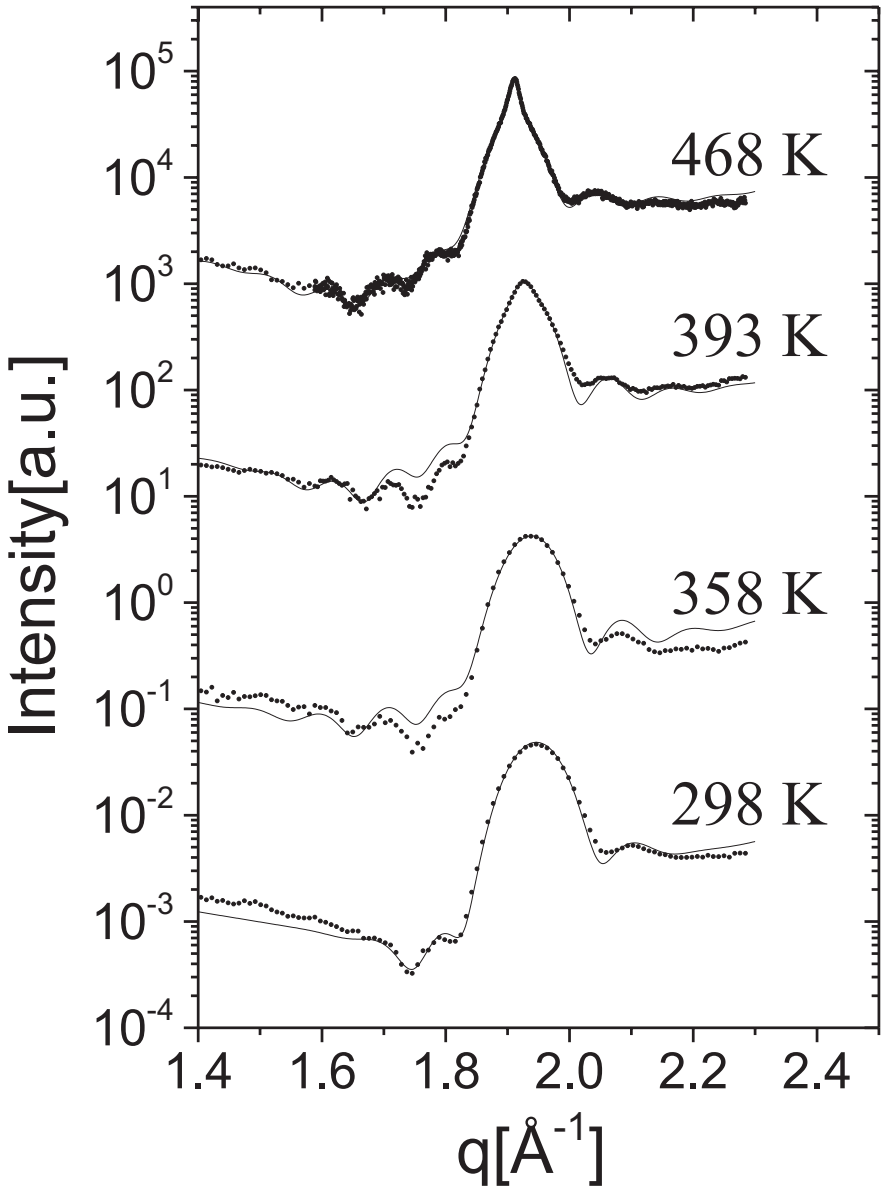

Figure 7.3: Measured (circles) and calculated (lines) specular rod intensity as a function of T_a measured at a sample $T_g = 235$ K, $F = 0.8$ Å/min, and $d = 50$ Å.

measurements show several characteristic features: an asymmetric rod shape, the shape of the Bragg peak, and the Laue oscillations around the Bragg peak. For $T_a < 358$ K, the number of Laue oscillations per side increases with the temperature from one to three. For $T_a \geq 358$ K, the number and periodicity of the Laue oscillations is independent of T_a. The Bragg peak observed for $T_a \geq 358$ K is Gaussian in shape, and it develops a second, nar-

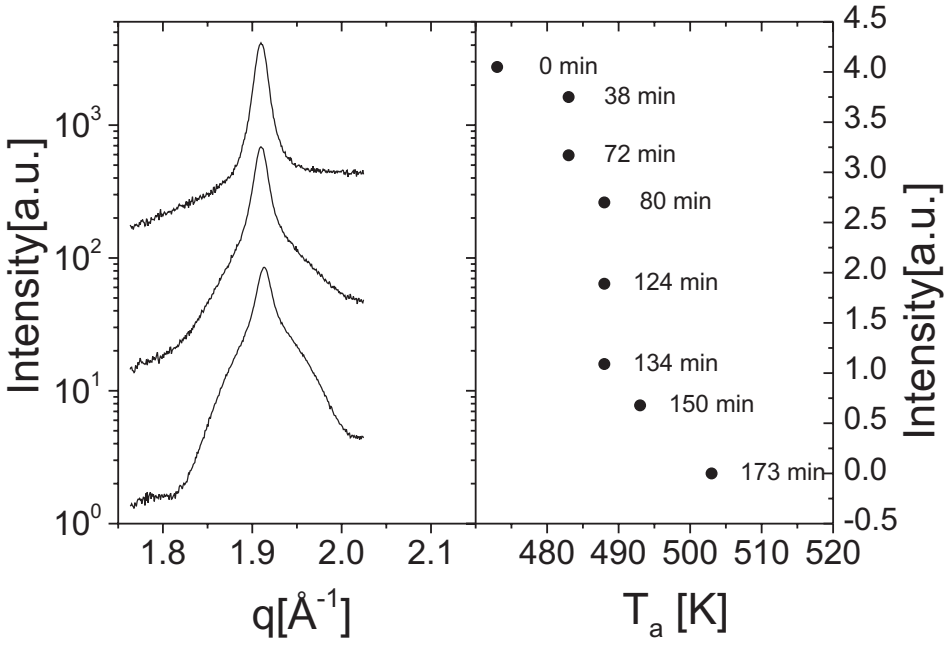

Figure 7.4: Shape and integrated intensity of the PTCDA(102) reflection near the desorption temperature as a function of t and T_a. $t = 0$ has been chosen as the last data point before the integrated intensity starts to decrease.

rower component for $T_a > 358$ K. The peak width of the narrow component decreases with increasing T_a.

Stepwise annealing / island morphology

Additionally, several samples grown in the island regime (large separate islands on a 2 ML thick wetting layer) with the parameters $F = 6.3$ Å, $d = 30 - 180$ Å, and $T_g = 381 - 473$ K have been annealed stepwise. The annealing induced no qualitative change of the crystal truncation rod and the Bragg peak. Only the position of the Bragg peak changed due to the thermal expansion. This will be discussed in Sec. 7.2.

Desorption

The thermal desorption has been studied in detail for a sample with $T_g = 271$ K, $F = 0.8$ Å/min and $d = 50$ Å. Fig. 7.4 shows the shape and the integrated intensity of the

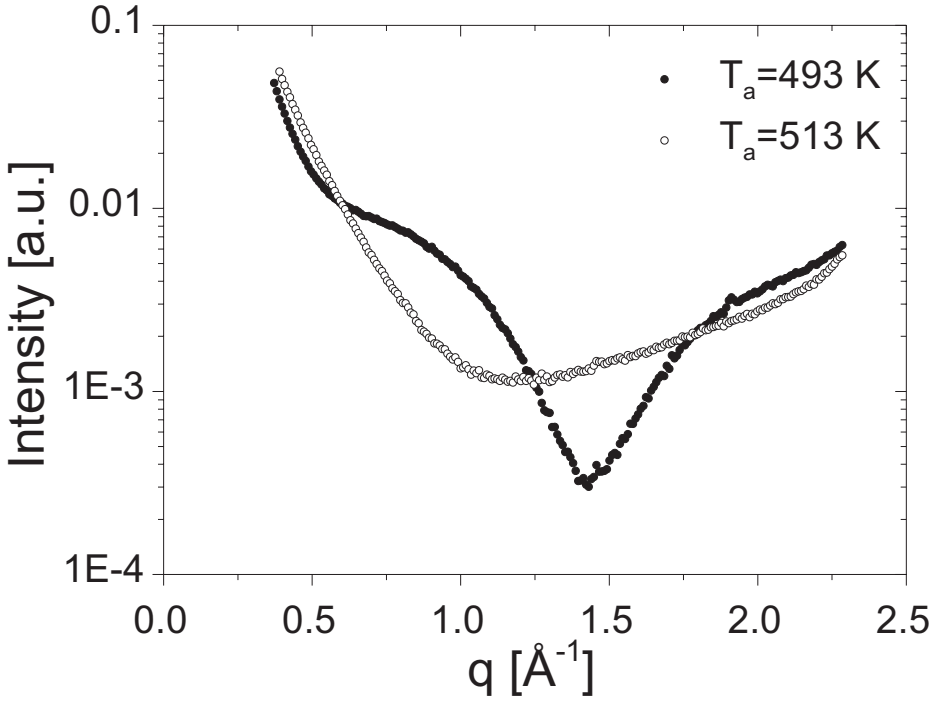

Figure 7.5: Stable shapes of the specular rod for $T_a = 493$ K (filled circles) and $T_a = 513$ K (open circles).

PTCDA(102) reflection near the desorption temperature as a function of the time, t, and T_a. At 483 K, the two-component Bragg peak and the Laue oscillations are still observed. During the further annealing, both components decrease up to zero intensity at $T_a \leq 493$ K. First, the Laue oscillations vanish, then the broad component vanishes, followed thereafter by the narrow component.

Fig. 7.5 shows the rod measured at $T_a = 493$ K and $T_a = 513$ K. The rod measured at $T_a = 493$ K has a minimum at $q \approx 1.4$ Å^{-1}, the rod measured at $T_a = 513$ K has a minimum at ≈ 1.0 Å^{-1}. This intensity distribution has been observed for $T_a \leq 673$ K.

7.1.3 Modelling the rod measurements

Three morphology regions have been observed as a function of T_a during the post-growth annealing of a relatively smooth film. As already observed for the as-grown morphology of thin PTCDA films, the Bragg intensity yields information about the morphology. In analogy to Sec. 6.2.1, we now develop a model for the simulation of the rods at different T_a, based

on the AFM measurements.

Model

As we have previously done to model the as-grown samples, we now postulate that the film is comprised of several types of mosaic blocks:

1. Substrate mosaic blocks covered by a thin film with n_{thin} monolayers and the roughness σ_{thin},

2. Substrate mosaic blocks covered by a thick film with n_{thick} monolayers and a height distribution of different mosaic blocks, and

3. Substrate mosaic blocks with residual coverages, θ_n, of the individual layers.

The thin film mosaic blocks have the average height, $h \approx d$, and a roughness, σ_{thin}, on a smaller lateral scale than the in-plane mosaic block size. The thick film mosaic blocks are molecularly smooth. The height of the film on different mosaic blocks, n, follows a Gaussian distribution with the average value, n_{thick}, and the standard deviation, σ_{thick}. The thin film covers the fraction A_{thin} of the total substrate surface, the thick film the fraction A_{thick}, and the residual film the fraction A_{res}. 100 % of the sample surface correspond to the sum of A_{thin}, A_{thick} and A_{res}. The scattering functions $S^{thin}(q_z)$, $S^{thick}(q_z, n_{thick})$, and $S^{res}(q_z)$ of the different mosaic block types are calculated with Eq. 3.25, and the diffracted intensity is

$$\begin{aligned} I(q_z) &= A_{thick} \frac{\sum_n \left(e^{-\frac{(n-n_{thick})^2}{2\sigma^2_{thick}}} \left| S^{thick}(q_z, n_{thick}) \right|^2 \right)}{\sum_n \left(e^{-\frac{(n-n_{thick})^2}{2\sigma^2_{thick}}} \right)} \\ &\quad + A_{thin} \left| S^{thin}(q_z) \right|^2 + A_{res} \left| S^{res}(q_z) \right|^2 . \end{aligned} \tag{7.1}$$

7.1.4 Results of the model

For the model results presented in this section, the substrate parameters and electron densities shown in Sec. 6.2.1 have been used. The local film thicknesses (n_{thick}, n_{thin}), the lattice parameters (d_0, d_{thick}, and d_{thin}), the coverages, θ_n, of the depleted area, the roughnesses (σ_{thin} and σ_{thick}), and the fractional areas (A_{thin}, A_{thick}, and A_{res}) covered by different mosaic blocks have been varied. The lattice spacing, d_0, between the substrate and the first monolayer of the film is assumed to be the same for all mosaic block types, the lattice parameters of the thin film , d_{thin}, and the lattice spacing of the thick film, d_{thick}, are allowed

Parameters					
T_a [K]	298	358	393	413	468
A_{thin} [%]	98	60	33.9	37.1	32.6
A_{thick} [%]	0	0	5.1	2.9	5.4
A_{res} [%]	2	40	55	60	72
d_0 [Å]	2.85	2.95	2.85	2.80	2.85
d_{thin} [Å]	3.252	3.258	3.273	3.281	3.302
d_{thick} [Å]			3.267	3.270	3.289
n_{thin} [ML]	16	17.5	19.7	19.5	20
σ_{thin} [ML]	2.7	2.0	1.5	1.5	1.2
n_{thick} [ML]	0	0	26	45	40
σ_{thick} [ML]	0	0	26	45	40
θ_1	0	1	1	1	1
θ_2	0	0.6	0.4	0.4	0.4
θ_3	0	0.5	0.4	0.3	0.4
θ_4	0	01	0.15	0.2	0.15

Table 7.1: Fit parameters for simulations of measurements of the specular rod at selected steps of T_a.

to be different.

The fits of measurements at selected T_a are shown in Fig. 7.3. Tab. 7.1 summarizes the parameters used for the calculations. For the measurements with $T_a \leq 358$ K, two types of mosaic blocks are necessary: The thin film and the residual coverage mosaic blocks. For $T_a > 358$ K, three types of mosaic block (thin film, thick film, and depleted areas) have been taken into account.

With increasing T_a, the ratio of the thin film mosaic blocks decreases from nearly 100 % to approximately 30 %, their thickness increases slightly from 16 to 20 ML, and their roughness decreases from 3 to 1.5 ML. The thick film mosaic blocks develop for $T_a > 358$ K. They cover approximately 5 % of the sample, their average height increases with T_a up to $3d$, and they have a broad height distribution. The residual area is covered with approximately 2 ML PTCDA coverage. The total amount of the coherently scattered material decreases during the annealing at $T_a \leq 358$ K and stablizes at approximately 65 % of the initial value. We always find $d_0 \approx 2.85$ Å which is less than both d_{thin} and d_{thick}. The lattice constants d_{thin} and d_{thick}, with $d_{thin} > d_{thick}$, increase with T_a, as shown in Fig. 7.6.

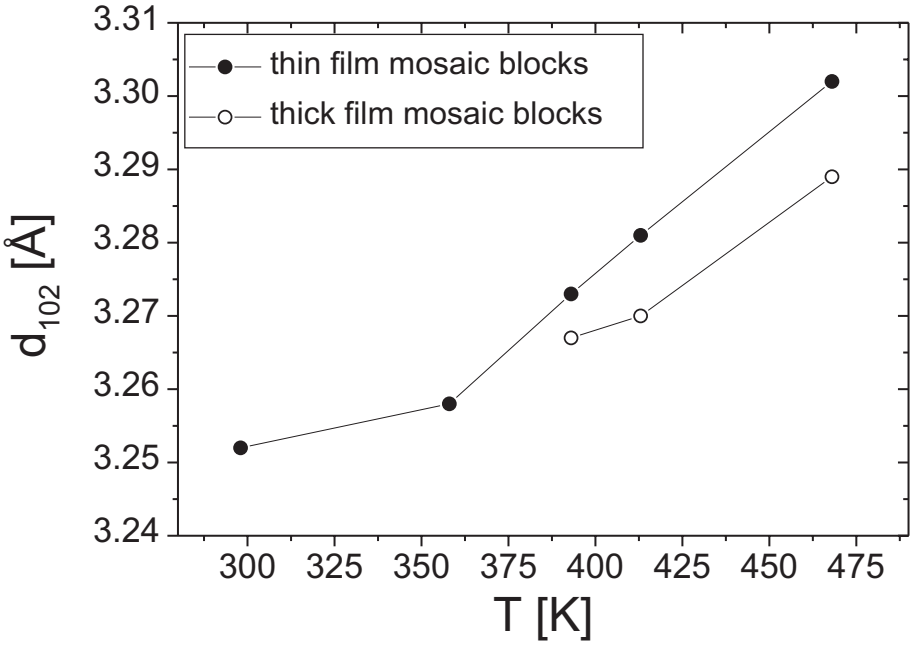

Figure 7.6: d_{102} of the thin film and thick film mosaic blocks at selected steps of T_a. The filled circles represent d_{102} of the thin film mosaic blocks, the open circles d_{102} of the thick film mosaic blocks.

The three types of mosaic blocks correspond to the different island sizes and the depleted regions observed by AFM. The initial smoothing of the thin islands, and the growth of thick islands and depleted areas for $T_a \gtrsim 343$ K has already been observed by AFM. The additional information derived from the X-ray scattering is the distribution of the lattice constants in the various mosaic blocks, the island height relative to the substrate, and statistically significant values for the island height distribution and the average area covered by the islands.

7.1.5 Discussion of the thermal stability

The annealing experiments show that a smooth PTCDA film is thermally unstable. It has been observed by AFM and X-ray diffraction that the initial relatively flat film smoothens further for $T_a \lesssim 358$ K and develops facets. For $T_a > 358$ K, the film undergoes a transition to an island morphology with two characteristic island size distributions. The crystallite morphology seems to be stable upon annealing even if the island distribution might change during a long-time annealing.

First, we discuss the thermal instability of smooth films in terms of the equilibrium thermodynamics. The surface free energy γ is a function of the crystallographic surface orientation. For a given amount of material, γ can be minimized by developing the equilibrium shape of the crystal [113]. Since the annealed PTCDA film develops faceted islands, this mechanism for the energy minimization seems to be important for this material. The bulk lattice sites are energetically favored compared to the surface lattice sites due to the increased number of nearest neighbors. The observed increase in the island size for $T_a > 358$ K might be related to the minimization of the surface contribution in favor of the bulk.

A second possibility to reduce the free energy of a film is strain relaxation. As discussed in Sec. 6.2.3, the in-plane unit cell of a smooth film is strained. Although not studied in detail for the system PTCDA/Ag(111), it is expected that this strain relaxes with increasing film thickness, as observed, e.g., for PTCDA/Au(111) [48]. The positions on top of large islands have less strain energy than the positions on top of small islands and are thus energetically favored. Therefore, the transition from a smooth film to high islands during annealing can indeed be driven by the strain relaxation.

Not only morphological changes, but also structural changes may contribute to the energy minimization. The lattice spacing of the PTCDA(102) plane with $d_{102} \approx 3.25$ Å at 300 K is similar to d_{102} of the β-phase. During annealing, the d-spacing of the thick and the thin film domain blocks splits into two values separated by ≈ 0.1 Å. The higher, more β-like, value has been observed for the thin film mosaic blocks; the lower, more α-like, value has been observed for the thick film mosaic blocks. This supports the assumption that the α-phase is energetically favored compared to the β-phase, as already discussed for the as-grown samples. Unfortunately, no in-plane diffraction experiments have been performed during the annealing process which could unambigously decide if the ratio of the two polymorphs changes during the annealing or if the peak shift is only due to strain relaxation.

The aforementioned aspects of equilibrium thermodynamics (strain relaxation, the ratio of the volume energy vs. the surface energy, and the voulme ratio of the two polymorphs) might explain why islands are energetically favored, and why a smooth film is metastable. Now we discuss how the transition between the metastable and the stable configuration takes place.

The transition temperature from a smooth film to a partially dewetted surface is comparable to the transition temperature deduced from the transition of as-grown smooth films

to crystallites on a wetting layer. This implies that both processes are determined by the same energy barrier, E. Based on this, we develop the following model. The initially smooth, metastable film is a consequence of the non-equilibrium growth conditions. For $T_a \lesssim 358$ K, the surface mobility is limited by E, and the only possible route for the energy minimization is the generation of facets similar to the as-grown crystallites. For $T_a > 358$ K, the barrier can be overcome and high islands grow.

Similar to the system PTCDA/Ag(111), the epitaxial system Mn/Fe(001) prefers the Stransky-Krastanov growth mode for substrate temperatures higher than the transition temperature. For these films, it has also been observed that smooth, metastable films grown at temperatures less than the transition temperature partially dewet upon annealing [24]. The growth- and the dewetting mechanisms of the PTCDA and the Mn films seem to be related.

While some of the PTCDA islands grow with increasing T_a, others degrade. We assume that the degradation is controlled by surface diffusion. Most likely the molecules from the top (102) surface diffuse to other islands since, at this surface, the molecules do not overlap. It has been experimentally observed that the morphology is inhomogenous at high T_a. This indicates that not all of the low islands degrade with the same probability. The degradation could be influenced by local effects including the substrate morphology, the influence of the island shape, and the energy difference between the two bulk polymorphs.

7.1.6 Discussion of the thermal desorption

The X-ray diffraction experiments show that the thin film mosaic blocks (represented by the broad component of the Bragg reflection) desorb faster than the thick film mosaic blocks (narrow component). The desorption temperature of bulk PTCDA is around 493 K. The AFM experiments have confirmed that we can interpret the mosaic block height as the island height. Due to the constant desorption rate, the low islands are already desorbed when the high islands have only decreased in height. The Laue oscillations vanish while the broad component is still visible. Therefore, we assume that the height distribution of the low islands increases during desorption, i.e. that the desorption rate varies locally. Modelling the specular rod after the decrease of the Bragg peak shows that the measurement at $T_a = 493$ K corresponds to a coverage of 2 ML, the measurement at $T_a = 513$ K to 1 ML PTCDA. This indicates that the second and first monolayer near the interface are more strongly bound than the bulk material. The first monolayer ist stable up to at least 673 K. The binding

energy of the first monolayer to the substrate, E_{ML1}, the binding energy of the second ML, E_{ML2}, and the binding energy of the subsequent monolayer, $E_{ML>2}$, behave like

$$E_{ML1} \gg E_{ML2} > E_{ML>2}. \tag{7.2}$$

The layer-dependent binding energy has been used for the discussion of the epitaxy and the Stransky-Krastanov growth of PTCDA in Chapter 6.

Our result is consistent with the the observation of other groups that the first monolayer is covalently bound to Ag(111) and cannot be desorbed before the dissociation upon annealing. A strong binding of the first monolayer in contrast to the binding between the subsequent layers has also been observed for copper-phthalocyanine on Ag(111) [114].

7.2 Thermal expansion

In this section, we present measurements and the analysis of the linear thermal expansion coefficients of PTCDA parallel and perpendicular to the (102) plane. The thermal expansion is of special interest for future applications of organic thin films, since differences in the thermal expansion of different materials combined in one heterogenous stack might cause strain, cracks, and therefore the eventual failure of a device based on organic materials.

7.2.1 Experimental results

Fig. 7.7 shows the out-of-plane lattice parameter d_F as a function of T_a determined for a sample with $T_g = 388$ K, $F = 6.3$ Å/min, and $d = 180$ Å, i.e. with the crystallite morphology. The inset shows a radial scan of the PTCDA(102) reflection measured at $T_a = 373$ K, and a Gaussian fit of the peak. Due to the sharpness of the Bragg reflection, interference effects involving the substrate induce no significant peak shift and can be neglected. For every temperature step, the peak position has been determined by a Gaussian fit of the maximum.

Within the experimental uncertainty, the lattice parameter varies linearly with T_a. The linear thermal expansion coefficient $\alpha_\perp$, averaged over several samples grown in the island regime, is $\alpha_\perp = 1.05 \pm 0.06 \times 10^{-4}$ K^{-1}. For the in-plane linear thermal expansion coefficient $\alpha_\parallel$, we can only make an estimate. In Sec. 6.1.2, we have determined the in-plane unit mesh of the small crystallites grown at high T_g. We have attributed their structure to a thermally expanded, relaxed bulk structure of PTCDA. From the comparison of the unit cell dimensions measured at high T_g with the room temperature structure of the bulk phases,we derive

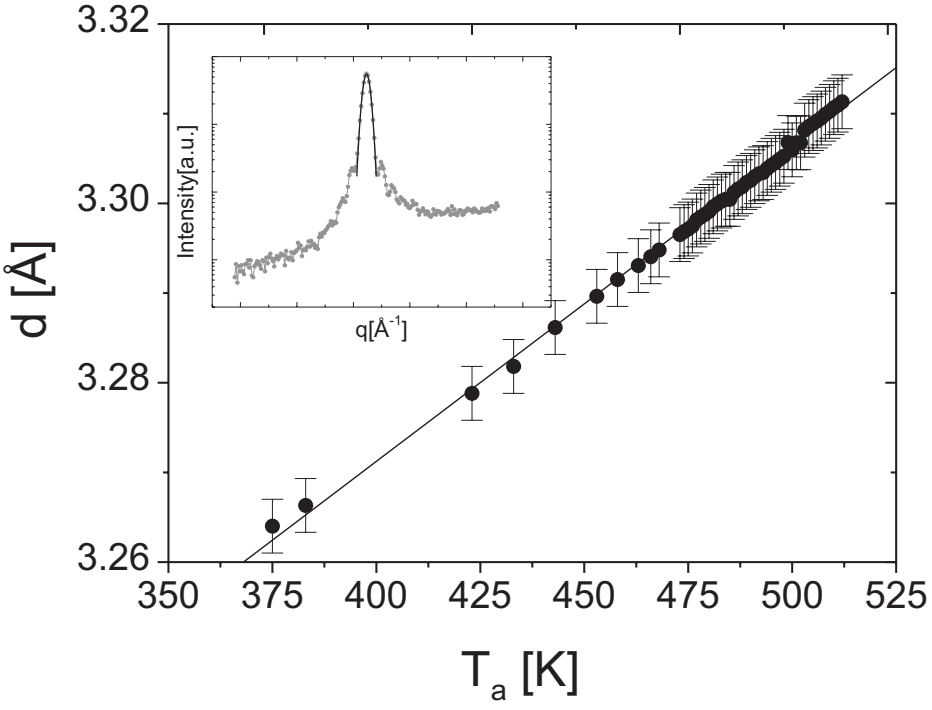

Figure 7.7: Thermal expansion, measured in out-of-plane direction for a sample with T_g = 388 K, $F = 6.3$ Å/min, and $d = 180$ Å. The inset shows a radial scan of the PTCDA(102) reflection measured at $T_a = 373$ K, and a Gaussian fit to the peak.

the linear thermal expansion $\alpha_{\parallel} = 5 \pm 2 \times 10^{-5}$ K^{-1}. To their experimental uncertainty, the thermal expansion of both polymorphs is indistinguishable.

7.2.2 Discussion of the anisotropic thermal expansion

The thermal expansion of PTCDA seems to be anisotropic with the ratio $\alpha_{\perp} : \alpha_{\parallel} = 2.1 \pm 0.8$. A similar anisotropy of the linear thermal expansion coefficient has been previously observed for several molecular crystals consisting of planar molecules [20]. These materials include several TCNQ salts [21], oligothiophenes [115] and also the compound benzene:hexafluorobenzene [116]. Even highly oriented pyrolytic graphite (HOPG, which can be regarded as stacked molecules with a very large size) shows an anisotropic thermal expansion coefficient (at room temperature $\alpha_{\perp} = 2.3 \times 10^{-5}$ K^{-1} and $\alpha_{\parallel} = -0.6 \times 10^{-5}$ K^{-1}) [117].

Every molecule has three rotational and three translational degrees of freedom. In the

high temperature limit, all vibrational and librational modes are excited according to the Boltzmann distribution. Due to the geometry of a planar, rectangular molecule, only a selection of the oscillatory modes contributes significantly to the thermal expansion. In the stacking direction, one translational and two rotational modes contribute to the expansion, while in the molecular plane only one translational mode contributes significantly in every direction. For a simplified van der Waaly crystal, Smaalen et al. [21] predict the ratio $\alpha_{\parallel}$:$\alpha_{\perp}$ of 3:1 for the directions parallel and perpendicular to the stack axis. Our own calculations for a similar system imply that the ratio depends on the molecular size (see Appendix A).

Within the uncertainty of the measured thermal expansion, we cannot exclude any of the models for the anisotropy of the thermal expansion. One reason for this is the more complicated stacking of PTCDA than is assumed for model crystals (see Appendix A), as well as the permanent quadrupole moment which is not included in the models. A further complication in comparing the experimental data with the theory may be related to a possible phase transition. Since the expansion of the bulk polymorphs cannot be distinguished, a transition between the α and the β polymorphs should not influence the results. Furthermore, the bulk polymorphs are structurally quite similar and thus they are expected the have a similar anisotropy of the thermal expansion. No other phase transition has been found in the temperature range studied.

7.3 Cooling-induced changes

In this section, we examine the effects of cooling the as-grown films. Similar to the annealing, this may induce changes in the crystal and defect structures.

7.3.1 Stepwise cooling

The growth conditions of the sample used for this experiment are T_g = 473 K, F = 13.5 Å/min, and d = 50 Å, i.e. in the crystallite regime. After the growth, the heating current has been reduced in three steps. The time-dependent temperature determined by the current reduction and the heat loss of the sample holder is shown in Fig. 7.8. The maximum cooling rate is approximately 0.2 K/s. Before and during the cooling process, radial scans of PTCDA(102) have been performed. After the first cooling, the sample is again annealed to T_g and cooled down within one step. The time-dependent temperature is shown in Fig. 7.8. The maximum cooling rate for the second cooling is approximately 0.4 K/s.

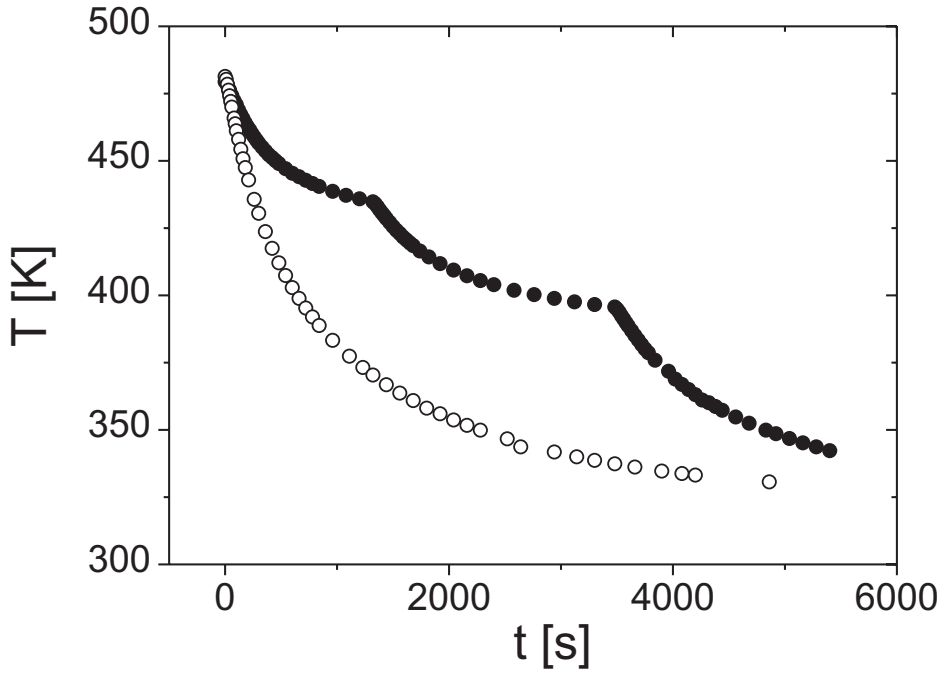

Figure 7.8: Comparison of stepwise cooling (filled circles) and cooling in one step from 473°C to room temperature (open circles).

cooling cycle	T_1 [K]	Δq_1 [Å^{-1}]	T_2 [K]	Δq_2 [Å^{-1}]
1	473	0.034	323	0.040
2	473	0.036	323	0.042

Table 7.2: Width Δq of the PTCDA(102) peak before and after the cooling cycles.

Tab. 7.2 summarizes the width Δq of the PTCDA(102) peak before and after the cooling cycles. The peak width increases during the cooling by approximately 15 %. This increase is larger than expected from the thermal expansion, and not fully reversible.

7.3.2 Cooling in one step

Two samples grown in the crystallite regime at similar T_g have been cooled down in one step after the deposition, as shown in Fig. 7.8. The thin sample has the growth parameters T_g = 473 K, F = 0.9 Å/min, and d = 50 Å/min, the thick sample T_g = 453 K, F = 3.5 Å/min, and d = 200 Å. The thin film has been studied during the cooling process, the thick film at T_g and at room temperature.

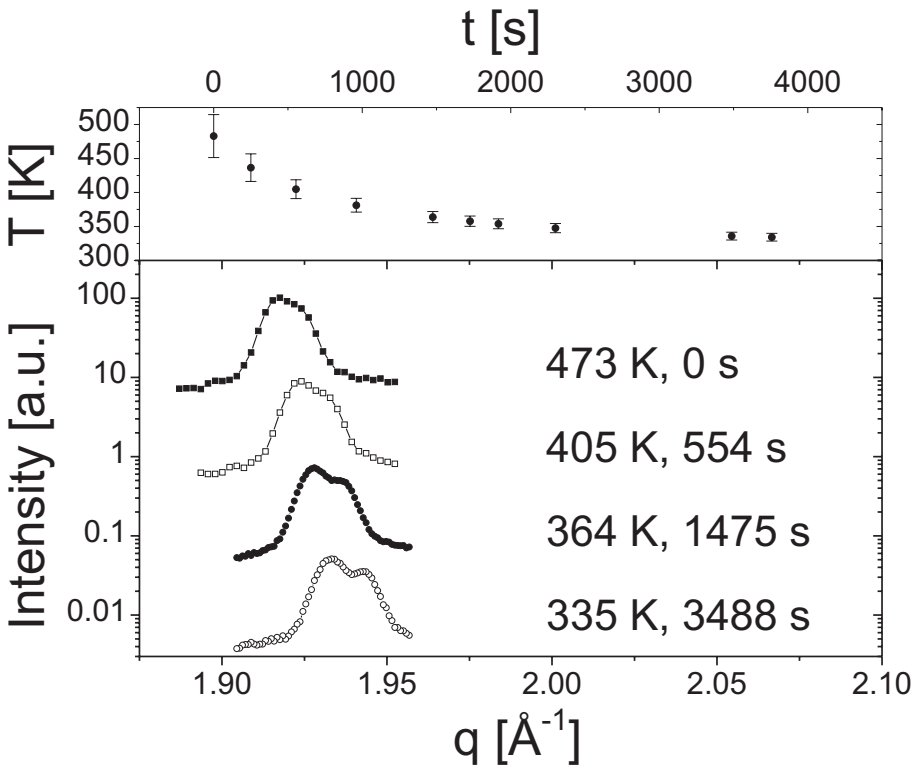

Figure 7.9: Peak splitting during sudden cooling down, observed for a sample with d = 50 Å, T_g = 473 K and F = 0.9 Å/min, as a function of the time and T_a. The time-dependent temperature change is indicated in the upper part of the figure, the lower part shows snapshots of the peak splitting.

Fig. 7.9 shows the peak splitting, observed for the thin film as a function of time and annealing temperature. The change as a function of time is indicated in the upper part of the figure, and the lower part shows snapshots of the peak splitting. The uncertainty of the temperature is mainly due to the temperature change during the measurement of the (102) peak. The slight asymmetry of the Bragg peak at T_g becomes more and more pronounced during the cooling process. After approximately 600 s, the peak has developed a shoulder which in turn evolves to a second maximum after 1900 s. The q-range of the intensity distribution corresponds to the initial peak width $\Delta q = 0.15 \pm 0.01$ Å. The final width of the peaks, fitted with a Gaussian, is $\Delta q = 0.1 \pm 0.01$ Å. For the thick sample, both peaks have the same intensity, for the thin film the peak at higher q has only half of the intensity of the other peak.

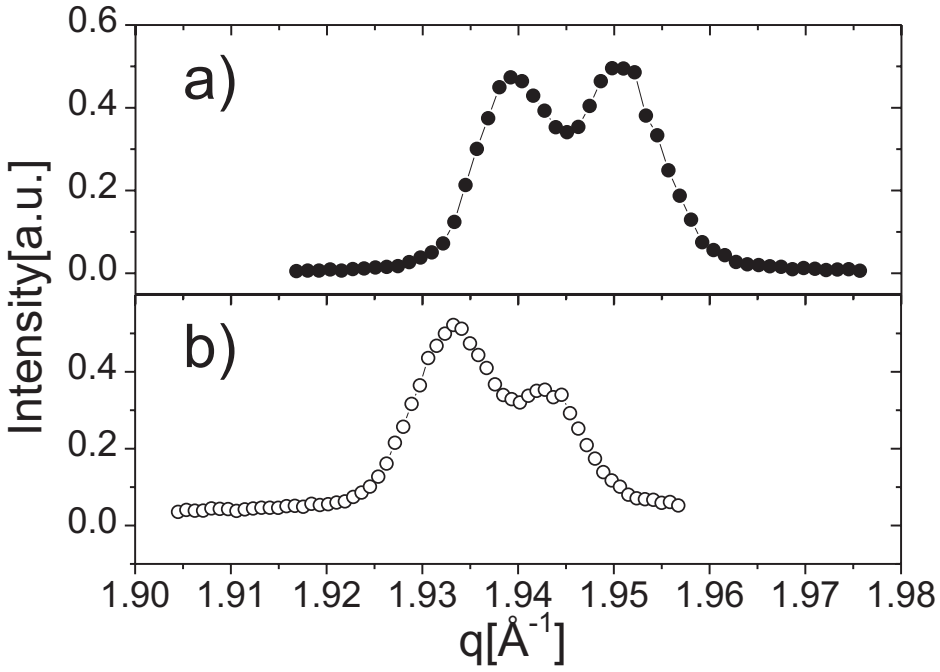

Figure 7.10: Splitted PTCDA(102) peak observed for (a) the thick sample with $d = 200$ Å, $T_g = 453$ K and $F = 3.5$ Å/min, and (b) the thin sample with $d = 50$ Å, $T_g = 473$ K and $F = 0.9$ Å/min.

7.3.3 Discussion of the splitting

While for most samples with different growth parameters no peak splitting during the cooling process is observed, for two samples grown near the desorption temperature, but at different F and d, a splitting similar to the separation of the (102) peak of the α and the β polymorph is found. For the 200 Å sample, the intensity ratio of both peaks corresponds to the ratio of the α and the β phase as determined from in-plane measurements.

The (102) Bragg reflection is an incoherent superposition of the scattering of mosaic blocks of different domains and different phases. Since at high T_g the material orders in separate islands with a relaxed in-plane structure, the peak position is expected to be mainly influenced by the ratio between the bulk polymorphs, and not by the strain.

We propose that the two peaks after the cooling correspond to the (102) reflections of both phases, since these have different room temperature lattice constants. This model also explains why the peak splitting is found only for selected samples. For most samples studied,

the α phase dominates and no peak splitting is observed. Additionally, for samples with a smaller film thickness respectively island height, the (102) peak width increases, and it is more difficult to separate the two components.

According to our model, we assume that the film composition, and not the cooling rate itself, determines the peak splitting. The fact that at T_g only one asymmetric peak is observed implies that the thermal expansion coefficient of both phases may be slightly different. To confirm this model, further systematic studies of the ratio of the polymorphs α and β in samples grown under various growth conditions are necessary.

Chapter 8

In situ growth studies

In this chapter we present the results of the *in situ* growth study of PTCDA/Ag(111) using time-dependent X-ray intensity measurements at the anti-Bragg point. In Sec. 8.1, the experimental observations of various growth conditions are reported. The data are analyzed quantitatively in Sec. 8.2, and the results are interpreted in terms of the growth mode. In addition to the experimental results, we present simulations of the growth process. In order to identify the parameters determining the growth mode, we apply two methods: a rate equation approach (Sec. 8.3) and kinetic Monte Carlo simulations (Sec. 8.4).

8.1 Experiment

In this section, we first describe the procedure of the experiment. After discussing a representative measurement, we present measurements performed at two growth rates and various growth temperatures.

8.1.1 Overview of the typical measurement

The growth process of most of the samples discussed in Chapter 6 has been studied *in situ* and in real-time by X-ray diffraction at the anti-Bragg point of the PTCDA film with $q_z^{anti} = \pi/d_F$, where d_F is the lattice constant of PTCDA(102). The position of the anti-Bragg point on the specular rod, relative to PTCDA(102) and Ag(111), is indicated in Fig. 8.1. The experiments divide into low F ($d = 50$ Å, $F = 0.8 - 2$ Å/min) and high F measurements ($d = 50$ Å, $F = 12 - 14$ Å/min) at substrate temperatures between 197 K and 473 K. All samples discussed here have been grown in the portable MBE chamber and measured with a point detector. Some additional samples have been monitored by a position-sensitive

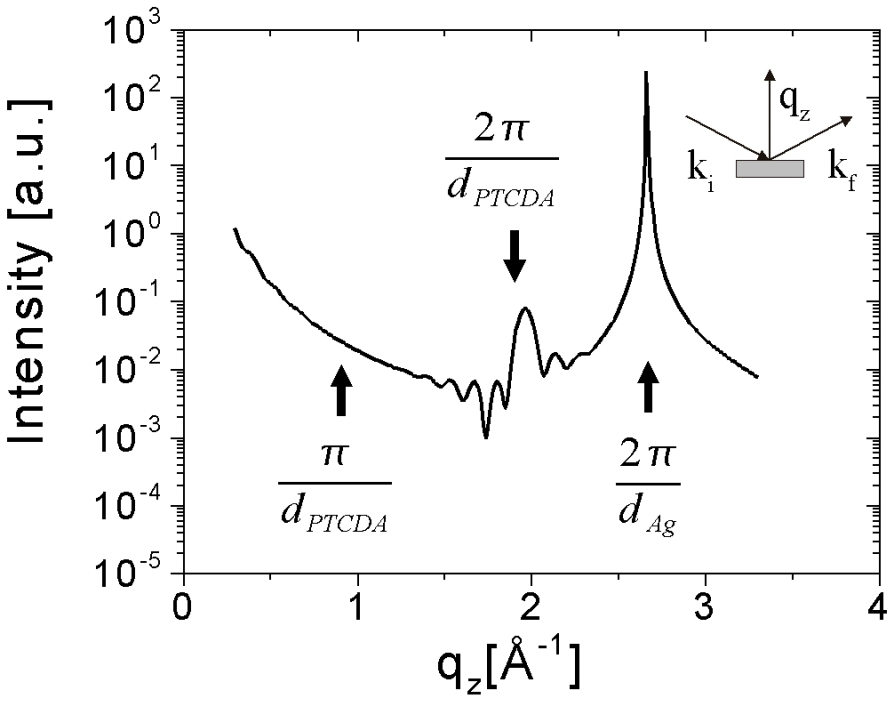

Figure 8.1: Simulated intensity of the specular rod of a smooth PTCDA film with $d = 50$ Å. The anti-Bragg condition with $q_z = \pi/d_{PTCDA}$ is indicated. The inset shows the scattering geometry.

detector (PSD).

A typical intensity measurement at q_z^{anti} as a function of time (as shown in Fig. 8.2) consists of three steps. (I) After cleaning the substrate, the intensity of the specular rod of the substrate at q_z^{anti} is measured as a function of time to verify surface purity and for reasons of intensity normalization. (II) The motorized shutter of the Knudsen cell is opened from outside the experimental hutch, without interrupting the X-ray measurement, and the intensity measurement is continued during the deposition of the PTCDA film. (III) After the deposition of 50 Å PTCDA (controlled by the QCM), the shutter is closed. The intensity measurement is continued to monitor possible intensity changes after the deposition.

Now we discuss the principal characteristics of the observed intensity as a function of time. By way of example, Fig. 8.2 shows the normalized intensity, $\tilde{I}(t)$, observed during deposition of a sample with $T_g = 293$ K and $F \approx 1$ Å/min. $t = 0$ indicates the time when the deposition commences. The intensity is normalized to the substrate rod intensity

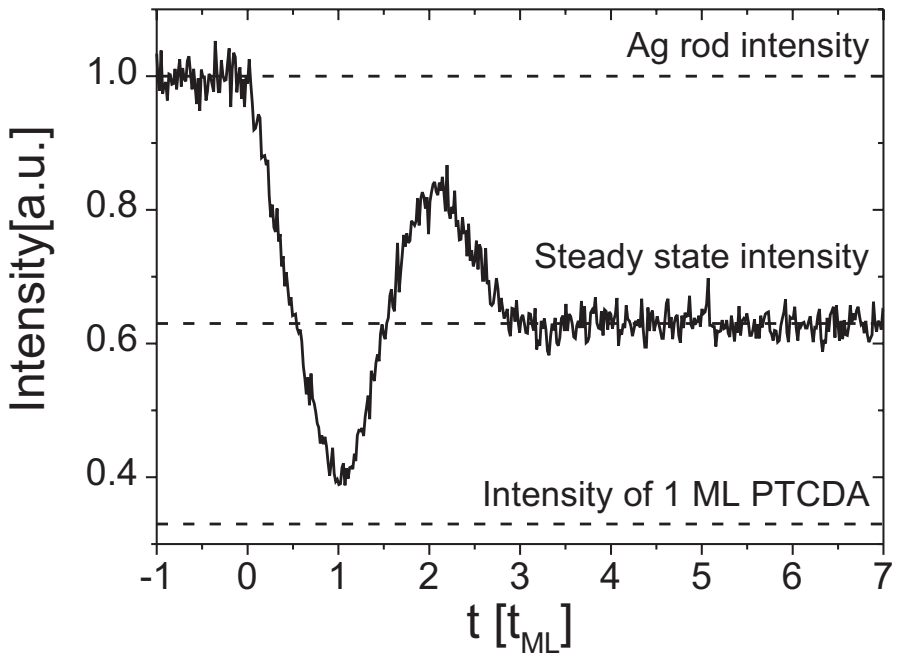

Figure 8.2: Typical intensity measurement at q_z^{anti} during growth, after the time and intensity normalization. The lines indicate the maximum intensity of the first oscillation minimum and maximum, and the steady state intensity.

(measured before deposition). The time is normalized to the deposition time t_{ML} of one monolayer, which corresponds (in the limits of the experimental uncertainties) to the first intensity minimum. A typical intensity measurement consists of intensity oscillations for $t \lesssim 3 - 5t_{ML}$, followed by the constant steady state intensity. A measure for the damping of the oscillations are the normalized intensity I_{Min} of the first intensity minimum, and the normalized intensity I_{Max} of the first intensity maximum.

The time normalization assumes a constant growth rate for PTCDA/Ag(111). Experimentally, no indication of a layer-dependent sticking coefficient has been found. The observed regular oscillations indicate that at least the first monolayers have a constant growth rate. The deposition rate determined by the intensity oscillations and the deposition rate based on QCM measurements differ by up to 25 % for low deposition rates, and by up to 50 % for high deposition rates. The unsystematic deviations are mostly due to stabilization problems of the evaporation rate on a long time scale compared to t_{ML}, caused by recrystallization on the aperture of the evaporation cell.

Most measurements have been normalized as mentioned above. Additional measurements complicated by minor experimental problems (such as a partially closed shutter before deposition) could be included in the analysis, after establishing that the initial submonolayer growth is mostly restricted to the first monolayer for all studied growth conditions, i.e. the slope of $\tilde{I}(t)$ for $t << 1\ t_{ML}$ is the same for all measurements.

Measurements with a PSD detector performed at various growth conditions have shown that the diffuse scattering due to steps of the PTCDA layers is very weak. The normalized background is of the order of 10^{-3} and therefore negligible compared to the statistical uncertainties of the intensity measurement.

8.1.2 Low deposition rate

Fig. 8.3 shows representative intensity measurements during deposition performed at different substrate temperatures and low deposition rates, $F = 0.8$–2 ML/s. The intensity measurements show the characteristic change between the oscillatory behavior and a constant intensity as reported in the previous section. With increasing T_g the first oscillation period is more and more pronounced, while the second oscillation period is always strongly damped (if it is detectable at all). For all datasets the constant intensity observed for $t \gtrsim 3-5\ t_{ML}$ equals 0.65 ± 0.03.

The damping of the oscillations as a function of T_g is characterized by the intensity of the first maximum, I_{Max}, and the first minimum, I_{min}, as shown in Fig. 8.4. The lines following the data points serve as a guide to the eye. At 197 K, no oscillations, but a monotonical intensity decrease up to the steady state intensity is observed. For increasing T_g, the oscillations become distinguishable. I_{min} decreases with increasing temperature and saturates for $T_g \gtrsim 358$ K at the intensity expected for one closed monolayer PTCDA. Starting from the steady state intensity, I_{Max} increases with T_g, and for $T_g \gtrsim 385$ K it assumes the intensity of the specular rod prior to the deposition. The observed change in I_{Min} and I_{Max} corresponds to a transition from damped to undamped oscillations at $T_g \approx 385$ K. The transition is continuous, therefore it is difficult to define a transition temperature. The temperature range over which the damping occurs is approximately 150 K wide. The lowest intensity minimum observed is 0.33 ± 0.02, the highest maximum is 1.00 ± 0.02. With decreasing T_g and increasing damping, the position of the maximum shifts from $t = 2t_{ML}$ to slightly higher values.

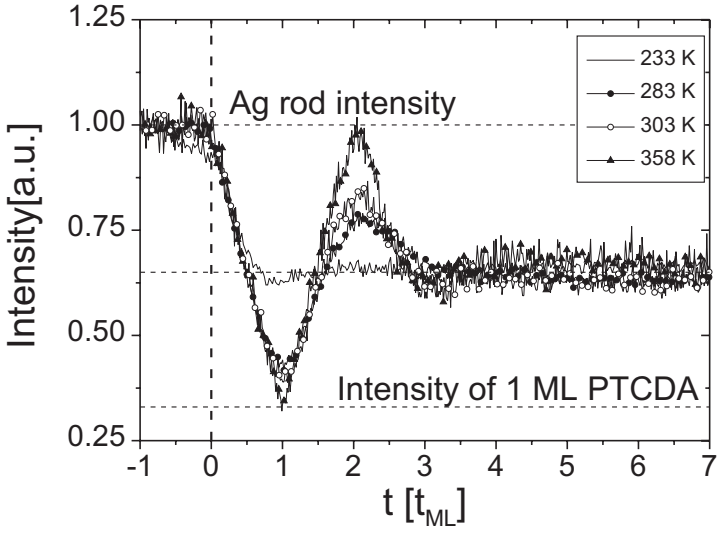

Figure 8.3: Intensity measurements as a function of T_g observed for low deposition rates (0.8–2 ML/s). The horizontal lines indicate the intensities characteristic for the growth of PTCDA on Ag(111). The vertical line signalizes the opening of the shutter.

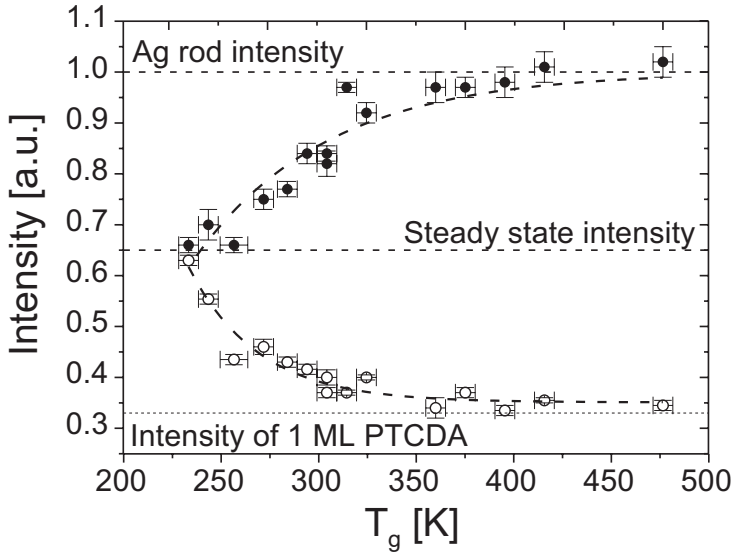

Figure 8.4: The intensity of the first intensity minimum, I_{Min} (open symbols), and the first intensity maximum, I_{Max} (filled symbols), as a function of the growth temperature. The measurements have been performed at low F. The dashed lines are a guide to the eye.

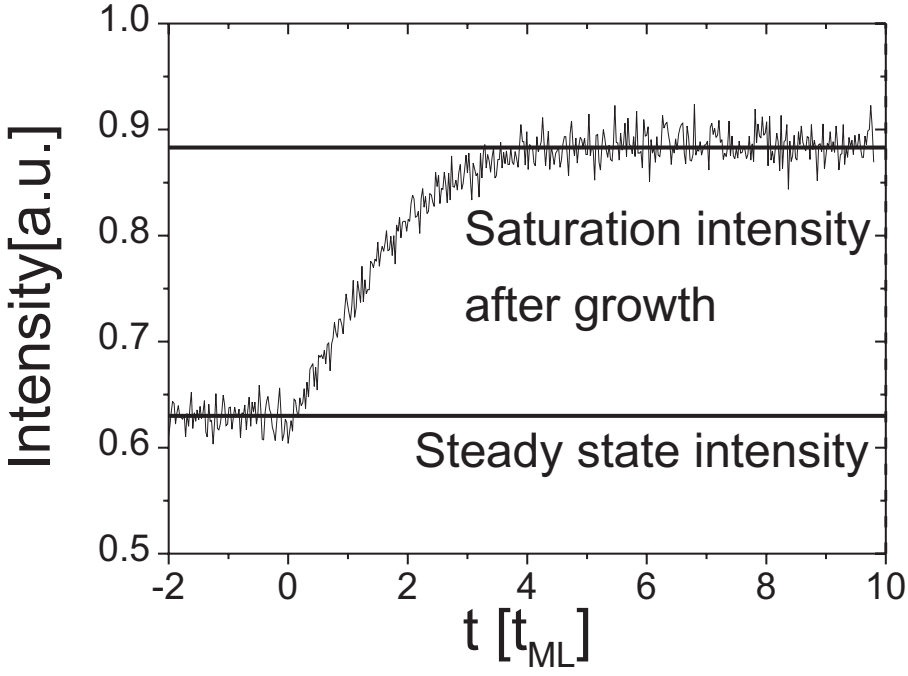

Figure 8.5: Post-growth recovery of the anti-Bragg point intensity as a function of time. The change of the signal after closing the shutter of the evaporation cell ($t = 0$) shows that significant changes of material distribution take place due to post-growth diffusion.

We now report the intensity measurements after the the deposition has been interrupted. Here, $t = 0$ is defined as the closing time of the shutter. By way of example, Fig. 8.5 shows a measurement at a sample with $F \approx 1$ Å/min and $T_g = 393$ K. At $t \leq 0\ t_{ML}$, we observe the steady state intensity. $\tilde{I}(t)$ increases for $t \geq 0\ t_{ML}$ up to a saturation intensity $I_{Sat} = 0.88$. We studied the intensity after growth in detail for the samples grown at low deposition rates. For $T_g \gtrsim 358$ K the intensity changes in the measured time interval of one hour after the deposition, for $T_g \lesssim 358$ K no intensity change has been observed. Fig. 8.6 shows that the saturation intensity observed for $T_g \gtrsim 358$ K increases with T_g. For $T_g = 473$ K, the intensity of the Ag rod prior to the growth process is recovered. While at $T_g = 393$ K the intensity is stable after 500 s, at $T_g = 473$ K this occurs after only 200 s. The rate of the intensity increase increases with T_g.

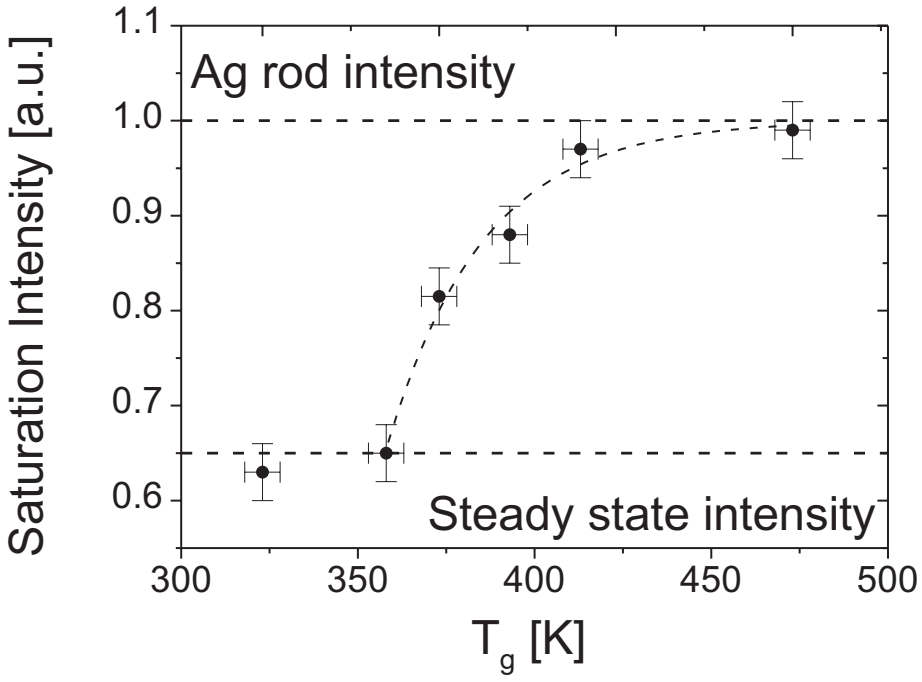

Figure 8.6: Intensity of the recovered signal (for large t) as a function of the substrate temperature.

8.1.3 High deposition rate

Fig 8.7 shows intensity measurements at q_z^{anti} during the deposition of samples at high deposition rates ($F = 12 - 14$ Å/min). At $t \approx 3\ t_{ML}$, $\tilde{I}(t)$ undergoes a transition from oscillatory behavior to the steady state intensity, as discussed in Sec. 8.1.1. I_{Max} and I_{Min} are shown in Fig. 8.8. I_{Max} varies between $I_{Max} = 0.69 \pm 0.02$ (near the steady state intensity) for $T_g \leq 358$ K and $I_{Max} = 1 \pm 0.02$ (the intensity of the substrate rod) for $T_g \geq 358$ K. I_{Min} varies between $I_{Min} = 0.60 \pm 0.02$ (approximately the steady state intensity) for $T_g \leq 358$ K and $I_{Min} = 0.36 \pm 0.02$ for $T_g \geq 358$ K. The observed damping of the oscillations is more irregular than observed for low F. The transition between damped and undamped oscillations takes place in a temperature range of $\lesssim 70$ K. For $T_g > 358$ K, an intensity increase up to a saturation intensity $I_{Sat} < 1$ has been observed after the deposition, but has not been systematically studied.

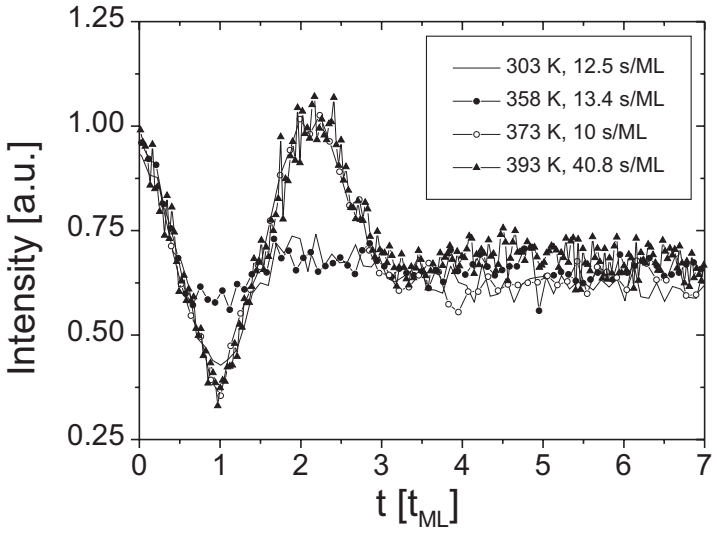

Figure 8.7: Intensity measurements as a function of the growth temperature, for high deposition rates. The dashed lines are a guide to the eye.

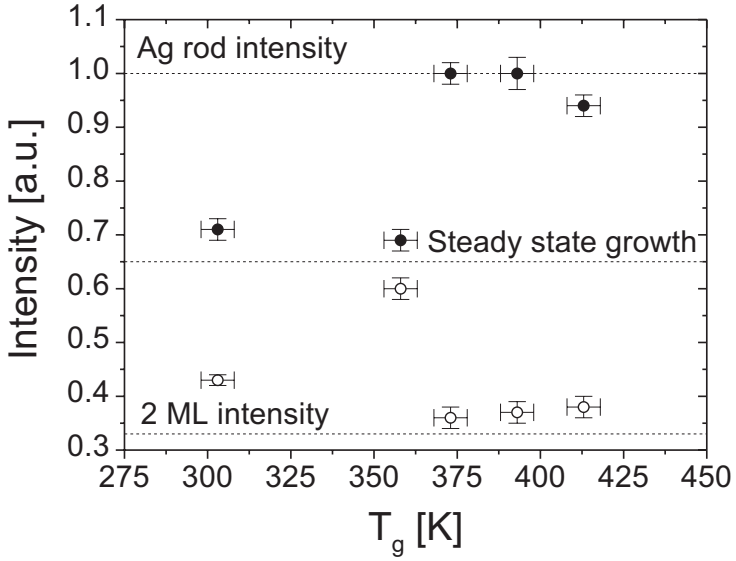

Figure 8.8: The intensity of the first intensity minimum, I_{Min} (open symbols), and the first intensity maximum, I_{Max} (filled symbols), as a function of the growth temperature. The measurements have been performed at high F. The dashed lines indicate the intensities characteristic for the growth of PTCDA/Ag.

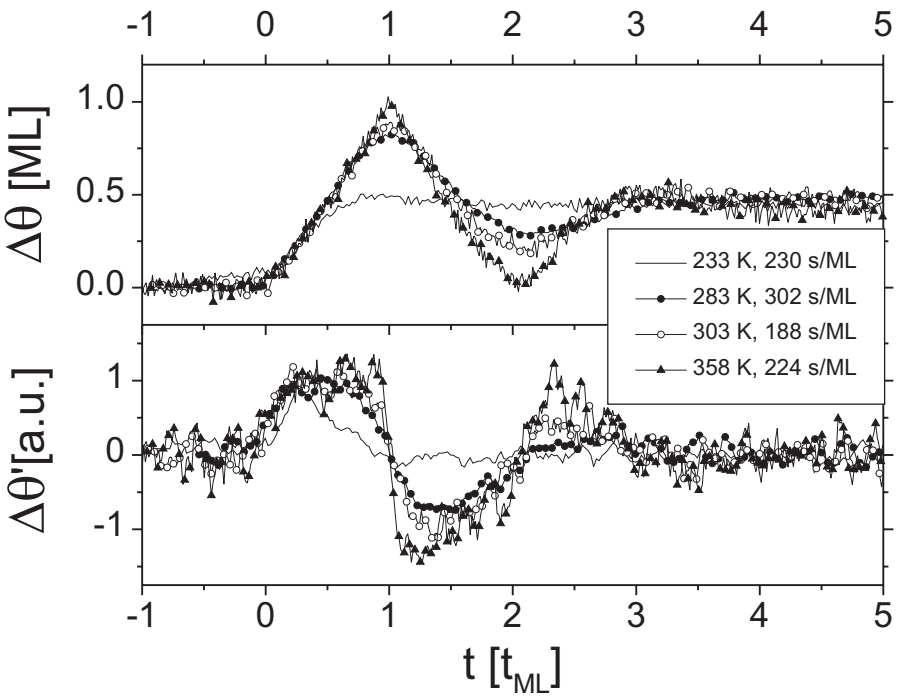

Figure 8.9: Examples of the coverage difference of odd and even monolayers and its derivative, calculated from intensity measurements at different T_g. Both T_g and F are indicated.

8.2 Discussion of the experimental results

The measurements for low and high deposition rates are qualitatively and quantitatively similar. In the following, we will discuss several aspects of the measurements and give a detailed analysis of the measured intensities for low F, since these data cover a larger temperature range and are measured with better statistics. In Sec. 8.2.1 we analyze the experimental data quantitatively in terms of a time-dependent coverage. This coverage is related to the growth mode as a function of the depositon time. A quantitative measure for the growth mode change as a function of the growth temperature is given in Sec. 8.2.2. In Sec. 8.2.3, we present a model for the steady state intensity, and in Sec. 8.2.4 a model for the post-growth intensity change.

8.2.1 Coverage as a function of time

In this section, the analytic method discussed in Sec. 3.6 will be applied on the intensity measurements at low deposition rate. In the experiment, we have observed no significant

diffuse background intensity during the deposition of PTCDA. This is consistent with the observation that even for low coverages, at room temperature the PTCDA islands much larger than the coherence area [15]. Therefore, we can analyze the measured specular intensity without any corrections in terms of the kinematic scattering theory.

In Sec. 3.6 it has been shown that the normalized intensity at the anti-Bragg point can be written as

$$\tilde{I}(t) = 1 + A[\Delta\theta(t)] + B[\Delta\theta(t)]^2. \tag{8.1}$$

The parameters A and B depend on the electron densities of the substrate and of the film, and on the lattice constants, which have been determined by modelling the specular rod of the samples after growth (Sec. 6.2.1). We assume that the lattice constants do not change significantly during deposition. This is supported by the fact that the absolute I_{Min} observed for the undamped oscillations corresponds to one completely closed monolayer PTCDA, calculated with the parameters derived from the rod measurements.

Fig. 8.9 shows $\Delta\theta$ and its partial derivative $\frac{\partial\Delta\theta}{\partial(Ft)} = \Delta\theta\,(t)'$ (Ft = total coverage) for selected data sets. $\Delta\theta(t)$ has been calculated for all samples with the same parameters. We find that $0 \leq \Delta\theta \leq 1$, and for $t \gtrsim 3\ t_{ML}$ we find $\Delta\theta = 0.5$ ML.

We now discuss four general cases of the derivative $\Delta\theta'(t)$ which corresponds to the slope of $\Delta\theta(t)$:

1. $\Delta\theta\,(t)' = 1 \Longleftrightarrow$ the material only grows in odd monolayers. It is unlikely that more than one odd monolayer participates in this, therefore we have layer-by-layer growth.

2. $\Delta\theta\,(t)' = -1 \Longleftrightarrow$ same case as above, but the material only grows in one even monolayer.

3. $\Delta\theta\,(t)' = 0 \Longleftrightarrow$ the same amount of material nucleates in even and odd monolayers. This leads to the assumption that several monolayers contribute to the growth process.

4. $-1 < \Delta\theta\,(t)' < 1 \Longleftrightarrow$ for a constant growth rate F, this indicates that several monolayers contribute to the growth. The curvature around $Ft =$ integer is a measure for how much the growth mode deviates from layer-by-layer growth:
   Strong curvature $\Longleftrightarrow$ near layer-by-layer growth.
   Weak curvature $\Longleftrightarrow$ transition to a 3D growth mode.

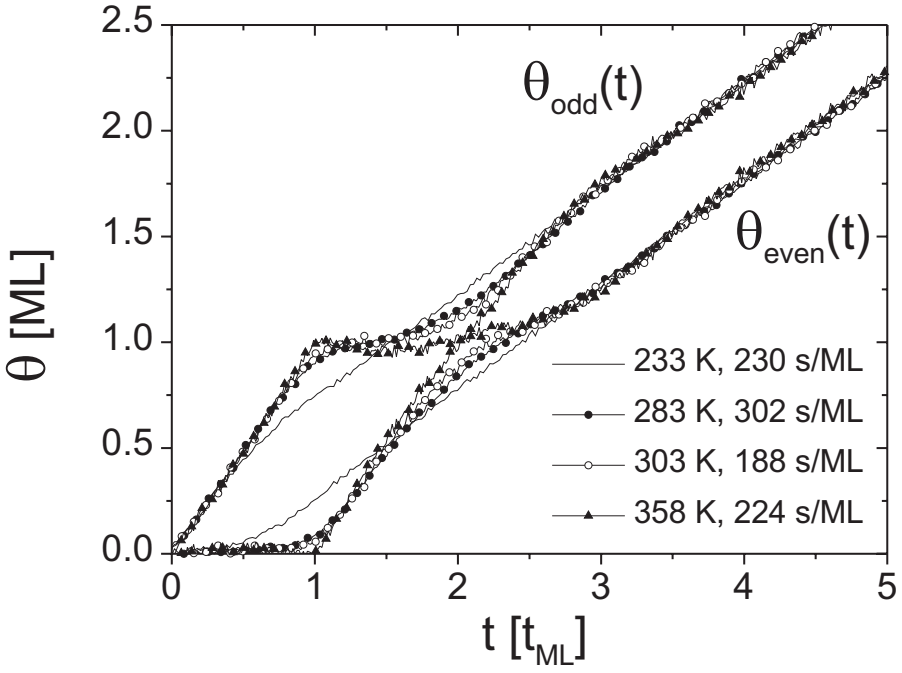

Figure 8.10: Separation of the coverages $\theta_{odd}(t)$ and $\theta_{even}(t)$.

These general cases of the derivative are found in the measurements of PTCDA on Ag, shown in the lower part of Fig. 8.9. Prior to the growth, i.e. for $t \leq 0$, $\Delta\theta\,(t)' = 0$ has been found. In this case, a constant intensity indicates a clean surface before growth. For $0 \leq t \lesssim 0.15 \pm 0.05\ t_{ML}$, $\Delta\theta'$ changes in a smooth, temperature independent, way from 0 to 1 corresponding to case (4). This might be an artifact of the numerical differentiation, but it might also indicate that the growth rate needs a short time to stabilize after opening of the shutter. The case of several monolayers contributing to the growth process can most probably be excluded because of the following value 1 for the derivative indicating ideal layer-by-layer growth. For $t \gtrsim 0.15 \pm 0.05\ t_{ML}$ the derivative becomes temperature-dependent. At $T_g \geq 358$ K, we find $\Delta\theta' = 1$ for $0.15 t_{ML} < t < t_{ML}$, and $\Delta\theta' = -1$ for $t_{ML} < t < 2t_{ML}$, i.e. layer-by-layer growth. With decreasing T_g, $\Delta\theta'$ deviates increasingly from these values. While for $T_g = 358$ K the transition from $\Delta\theta' = 1$ to $\Delta\theta' = -1$ takes place instantanously, for lower temperatures it becomes more and more smooth. For all T_g, $\Delta\theta' \to 0$ for $t \gg 3\ t_{ML}$, indicating 3D growth.

It is of great interest to separate the coverage of each monolayer as a function of the deposition time. Generally, this is not possible. A step in this direction is the analysis of

θ_{odd} and θ_{even} (see Sec. 3.6). In Fig. 8.10 the coverage difference $\Delta\theta$ is split in θ_{odd} and θ_{even}, using $Ft = \theta_{odd}(t) - \theta_{even}(t)$. At $T_g \geq 358$ K and for $t < t_{ML}$, the growth is mostly restricted to the first monolayer since all deposited material contributes to θ_{odd}. For $t_{ML} < t < 2t_{ML}$, the growth of the second monolayer takes place (all deposited material contributes to θ_{odd}). For $t > 2t_{ML}$, both $\theta_{odd}(t)$ and $\theta_{even}(t)$ increase, and 3D growth occurs. The lower T_g, the more deviates the growth of the first and the second monolayer from ideal layer-by-layer growth.

8.2.2 Deviation from ideal layer-by-layer growth

The intensity values for the first maximum and the first minimum of the oscillations are a measure for the degree of layer-by-layer growth during the deposition of the first monolayers. The growth process itself is characterized by the coverage distribution between the layers as a function of the deposition time. To quantify the deviation from ideal layer-by-layer growth, the intensities have to be transformed into the coverages of the monolayers. In this context, ideal layer-by-layer growth is defined as the filling of one layer after the other without any deviations from this behavior.

In Sec. 3.6 it has been shown that only the total coverages θ_{even} of all even and θ_{odd} of all odd layers can be calculated from the intensity measurements. For the first monolayers, the situation is simpler as long as only a small number of layers contributes to the growth. Neglecting a slight shift from the maximum position, I_{Max} corresponds to the total coverage $Ft = 2$ ML and I_{Min} to $Ft = 1$ ML. For perfect layer-by-layer growth, at the minimum position only the first monolayer, i.e. one odd ML and no even ML, is deposited. If the growth mode deviates from ideal layer-by-layer growth, the fraction δ_1 of the total coverage is deposited in the second (even) ML, while the first (odd) ML is missing this coverage. With this, the coverage difference $\Delta\theta^{Min} = \theta_{odd}^{Min} - \theta_{even}^{Min}$ is

$$\Delta\theta^{Min} = (1 - \delta_1) - (0 + \delta_1)\,. \tag{8.2}$$

In analogy to this, for the intensity maximum applies

$$\Delta\theta^{Max} = (1 + \delta_2) - (1 - \delta_2)\,. \tag{8.3}$$

I_{Min} and I_{Max} are directly related to the coverage differences δ_1 respectively δ_2. Inserting Eq. 8.2 respectively 8.3 in Eq. 3.35, δ_1 and δ_2 can be directly calculated from

$$\begin{aligned} \delta_1 &= \frac{1}{2}\left(1 - \frac{|R_{Ag}|}{|R_{PTCDA}|}\left[-\sqrt{\tilde{I}\,(t) - (1 - \cos^2\phi)} - \cos\phi\right]\right) \\ \text{and} \quad \delta_2 &= \frac{1}{2}\left(\frac{|R_{Ag}|}{|R_{PTCDA}|}\left[-\sqrt{\tilde{I}\,(t) - (1 - \cos^2\phi)} - \cos\phi\right]\right). \end{aligned} \tag{8.4}$$

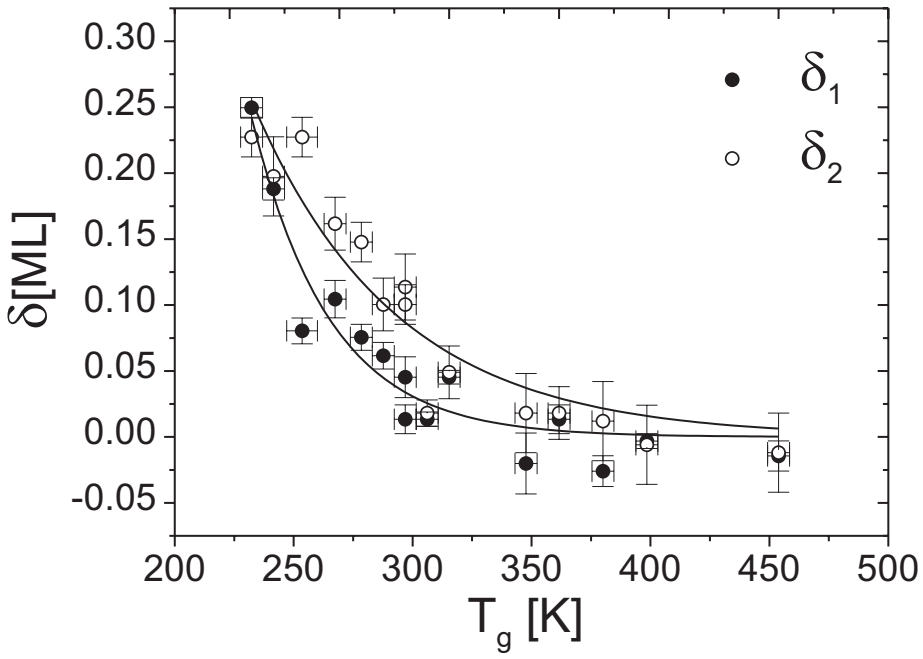

Figure 8.11: The coverage differences δ_1 and δ_2 as a function of the deposition temperature. The solid lines are a guide to the eye.

Fig. 8.11 shows δ_1 and δ_2 as a function of T_g. For all T_g, $\delta_2 \lesssim \delta_1$ since the intensity maximum at $2t_{ML}$ is always more damped than the intensity minimum at t_{ML}. For $T_g = 235$ K, $\delta_1 \approx \delta_2 \approx 0.25$, and for $T_g \gtrsim 358$ K, $\delta_1 \approx \delta_2 \approx 0$, as expected for ideal layer-by-layer growth. Inbetween these values, a monotonical transition as a function of T_g occurs.

Without further information from real-space measurements, it can only be estimated up to which temperature the δ-values really represent the misplaced material. Most probably this assumption is valid for $T_g \gtrsim 293$ K since in this temperature range only slight damping occurs. For lower temperatures more layers are expected to contribute to the growth process.

8.2.3 Model of the steady state behavior

In Sec. 8.2.1 it has been shown that the steady state intensity observed for large t corresponds to $\Delta\theta(t) = 0.5$. In this section we will present a model to explain this observation.

For $T < 385$ K, the coherence length of the PTCDA(102) Bragg reflection corresponds to the average sample thickness d, and the surface roughness can be simulated with a Gaussian

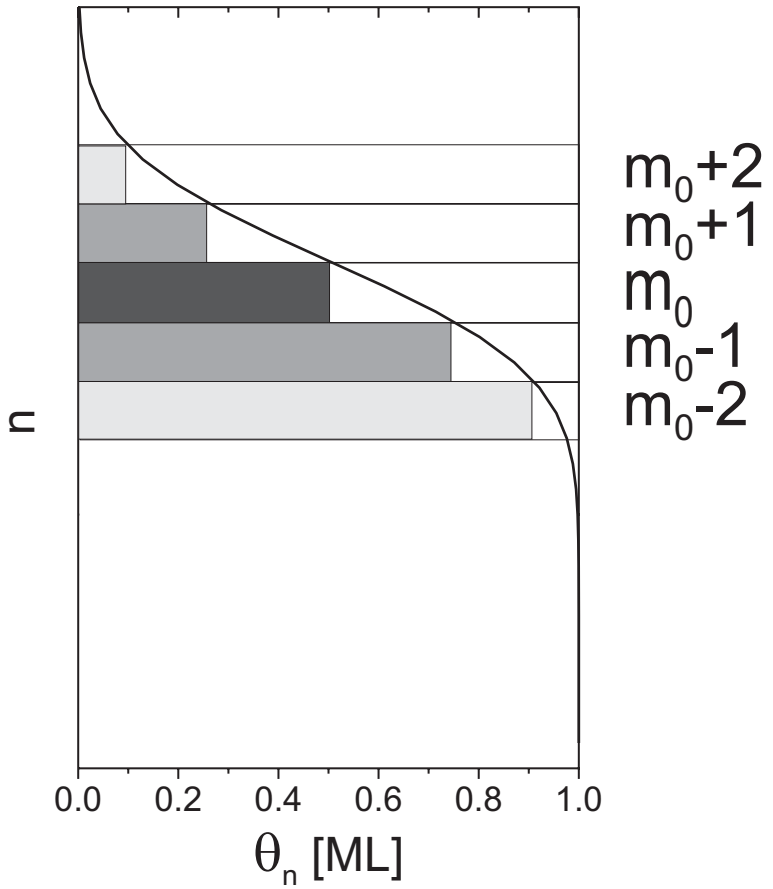

Figure 8.12: Schematic explaining the steady state intensity (see text). The roughness of the sample is assumed to be Gaussian. The layer m_0 correspond to the average sample surface.

height distribution (see Chap. 6). For a Gaussian height distribution, the coverages θ_n of a film with an average layer number m_0 are determined by

$$\theta_n = \frac{1}{2}\left(1 - erf\left(\frac{n - m_0}{\sigma_{PTCDA}}\right)\right) \tag{8.5}$$

where σ_{PTCDA} is the roughness of the PTCDA film. This is shown in Fig. 8.12. The function belongs to the group of functions with point symmetry around x_0, i.e.

$$\begin{aligned} f(x_0 + \Delta) &= 1 - f(x_0 - \Delta) \\ \text{and} \qquad f(x_0) &= 0.5. \end{aligned} \tag{8.6}$$

For θ_n, x_0 is replaced by m_0. In the following we show that for θ_n described by a function

of this type $\Delta\theta \approx 0.5$ is fulfilled. $\Delta\theta$ can be written as

$$\begin{aligned}\Delta\theta &= \sum_{n=1}^{\infty} \theta_n (-1)^{n-1} \\ &= \sum_{n=1}^{m_0-1} \theta_n (-1)^{n-1} + \sum_{n=m_0+1}^{\infty} \theta_n (-1)^{n-1} + \theta_{m_0} (-1)^{m_0-1} \end{aligned} \tag{8.7}$$

if we separate $\Delta\theta$ into the contribution of the layers with $n < m_0$, the layers with $n > m_0$, and the contribution of the layer m_0. The layer number n equals $m_0 - \Delta$

$$\Delta\theta = \sum_{\Delta=1}^{m_0-1} \theta_{m_0-\Delta} (-1)^{m_0-\Delta-1} + \sum_{\Delta=1}^{\infty} \theta_{m_0+\Delta} (-1)^{m_0+\Delta-1} + \theta_{m_0} (-1)^{m_0-1}. \tag{8.8}$$

The last expression allows to use Eq. 8.6, i.e. $\theta_{m_0-\Delta} = 1 - \theta_{m_0+\Delta}$, and since $(-1)^{m_0-\Delta} = (-1)^{m_0+\Delta}$, we get

$$\Delta\theta = \sum_{\Delta=1}^{m_0-1} (1 - \theta_{m_0+\Delta}) (-1)^{m_0+\Delta-1} + \sum_{\Delta=1}^{\infty} \theta_{m_0+\Delta} (-1)^{m_0+\Delta-1} + \theta_{m_0} (-1)^{m_0-1}. \tag{8.9}$$

Every term Δ of the first sum can be added to the corresponding term Δ of the second sum to

$$(1 - \theta_{m_0+\Delta}) (-1)^{m_0+\Delta-1} + \theta_{m_0+\Delta} (-1)^{m_0+\Delta-1} = 1, \tag{8.10}$$

and $\Delta\theta$ reduces to

$$\Delta\theta = \sum_{\Delta=1}^{m_0-1} (-1)^{m_0+\Delta-1} + \sum_{\Delta=m_0+1}^{\infty} \theta_{m_0+\Delta} (-1)^{m_0+\Delta-1} + \theta_{m_0} (-1)^{m_0-1}. \tag{8.11}$$

If $m_0 \gg \sigma_{PTCDA}$, the second sum negligible, and with $\theta_{m_0} = 0.5$ we get the final expression

$$\Delta\theta = (-1)^{m_0-1} \left(\sum_{\Delta=1}^{m_0-1} (-1)^{\Delta} + 0.5 \right). \tag{8.12}$$

Now we have to discuss the cases of m_0 being an even or an odd integer. For an even m_0, the sum equals -1, the factor $(-1)^{m_0-1} = -1$, and $\Delta\theta = 0.5$. For an odd integer m_0, the sum equals 0, the factor $(-1)^{m_0-1} = 1$, and $\Delta\theta = 0.5$ as for the other case.

The physical arguments for the results derived above are as follows. If enough layers contribute to the Gaussian surface roughness, a layer m_0 can always be chosen with $\theta_{m_0} \approx 0.5$, as indicated in Fig. 8.12. The X-rays scattered by the layer $m + 1$ interfere constructively with the X-rays scattered by the layer $m_0 - 1$. If we shift the coverage of the layer $m_0 + 1$ to the layer $m_0 - 1$, the specularly scattered intensity will not change. Because of the symmetry of the Gaussian lineshape, the coverage of the layer $m_0 + 1$ fills exactly the holes of the layer

$m_0 - 1$, and all layers $n < m_0$ can be filled with the coverage of a corresponding layer with $m_0 < n < 2m_0$. If m_0 is large enough compared to the roughness of the film, the layers with $n \geq 2m_0$ have the coverage 0. The total specular intensity scattered by the rough film is equivalent to the intensity scattered by $m_0 - 1$ layers with the coverage 1 (corresponding to Eq. 8.12), and by the layer m_0 with the coverage 0.5. Therefore, $\Delta\theta$ always equals 0.5.

The important result of this calculation is that the observation of a constant intensity is generally not equivalent to the step flow growth mode. A symmetric height distribution of the film as observed for the Gaussian roughness is sufficient to explain the time-independent intensity. In order to interpret the intensity measurements unequivocally in terms of the growth mode, further information about the system is needed.

8.2.4 Signal recovery after growth

Each change of $\tilde{I}(t)$, including the observed post-growth intensity changes, is related to a change in the coverages $\theta_n(t)$ of the layers n. The temperature range for which the intensity recovers after deposition coincides with the temperature range for which large separate crystallites have been observed. The growth in this temperature range has been interpreted as island growth on top of two wetting monolayers (Chapter 6). This leads to the assumption that the intensity change is related to the morphology.

The different areas (2 ML coverage and high islands) scatter incoherently (Sec. 6.2.1). The total intensity of the illuminated area is

$$I = A_{ML} I_{ML} + \frac{1}{2}\left(1 - A_{ML}\right) I_{island}^{even} + \frac{1}{2}\left(1 - A_{ML}\right) I_{island}^{odd}. \tag{8.13}$$

I_{ML} is the intensity of mosaic blocks covered by a wetting layer of two monolayers, I_{island}^{odd} is the intensity of mosaic blocks covered by islands with an odd layer number, I_{island}^{even} is the intensity of mosaic blocks covered by islands with an even layer number, and A_{ML} is the fraction of the substrate surface covered by the wetting layer. It has been assumed that the islands with even and odd layer numbers are equally distributed.

$\Delta\theta = 0$ for the wetting layers and the islands with an even layer number, $\Delta\theta = 1$ for the islands with an odd layer number. With $I(\Delta\theta) = 1 + A[\Delta\theta] + B[\Delta\theta]^2$, Eq. 8.13 reduces to

$$I = 1 + \frac{1}{2}\left(1 - A_{wett}\right)(A + B) \tag{8.14}$$

The deviation of the normalized intensity I from $I = 1$ is related to the area covered by islands. Since this area decreases with increasing T_g, as shown in Sec. 6.1.1, and since

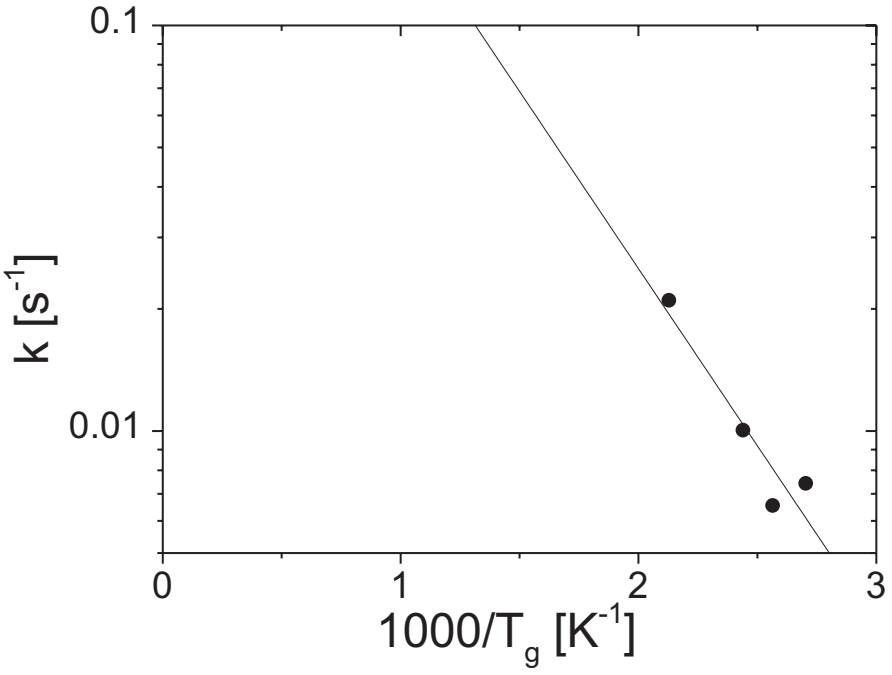

Figure 8.13: Arrhenius plot of the characteristic parameter k describing the post-growth recovery vs. the inverse temperature.

$A + B < 0$ for PTCDA on Ag(111), the correction term decreases with increasing T_g. This corresponds to the experimental observation that the intensity saturates at the value 1 as the growth temperature approaches 500 K. The model based on the Stransky-Krastanov morphology and the island height distribution is sufficient to explain the saturation intensity.

Now we discuss the recovery process which ends up in the saturation intensity. We attribute the time-dependent intensity change observed after the deposition to a complex surface diffusion process. For $T > 358$ K the intensity $I(t)$ measured during the recovery can be described by a step-function

$$I(t) = (I_{eq} - I_{sat}(T)) + \frac{2I_{sat}(T)}{1 + e^{-kt}}. \tag{8.15}$$

The equilibrium intensity I_{eq} and the temperature-dependent saturation intensity I_{sat} are given by the experimental data. The fitting parameter k is a measure for the rate of the diffusion process on the film surface. It is important to note that k does not equal a diffusion constant but rather an effective rate for the entire reordering process. The model describes the data in a phenomenological way and is not based on the theoretical description of

atomistic processes. The constant k can be related to an effective energy barrier E by the Arrhenius equation

$$k\left(\frac{1}{T_g}\right) = k\left(\frac{1}{T_g} \longrightarrow 0\right) e^{-\frac{E}{k_B T_g}}. \tag{8.16}$$

From Fig. 8.13 we find $k = 0.011 \pm 0.007$ s^{-1} and $E = 0.17 \pm 0.04$ eV.

8.2.5 Model for the growth process

From the analysis of the intensity measurements during the deposition, we have derived the following growth model.

For $T_g < 358$ K, the growth mode of the initial 2–3 layers is similar to a layer-by-layer growth, but deviates from it with decreasing T_g. For higher coverages we observe 3D growth, and a Gaussian height distribution is approached. This Gaussian height distribution also shows in the final morphology of the film after the growth (i.e. a relatively smooth film with a Gaussian roughness).

For $T_g \gtrsim 358$ K, the growth mode for $t \lesssim 2t_{ML}$ is ideal layer-by-layer growth. Since the wetting layer is 2 ML thick, we interpret this as the layer-by-layer growth of the wetting layer. On top of these two monolayers, islands nucleate. The stable clusters have a large separation, which shows in the separation of the crystallites observed after the film growth. During the growth of stable clusters, unstable clusters permanently grow and decay. Therefore, the Gaussian roughness model applies locally for the wetting layer during deposition. This explains the steady state intensity observed for $T_g \gtrsim 358$ K. After the growth, the unstable clusters and the diffusing monomers are captured by large islands, and the saturation intensity is reached.

The two scenarios for different growth temperatures are different modifications of the Stransky-Krastanov growth mode. This observation contradicts the conclusion of Taborski et al. [16] from near-edge X-ray absorption spectroscopy (NEXAFS) data that PTCDA grows in perfect layer-by-layer growth up to 1000 ML. The layer-by-layer growth of the first and the second ML is consistent with the observation of large 2D PTCDA islands on Ag at submonolayer coverages and room temperature [15]. Interestingly, the here observed intensity change during the deposition is similar to the one observed for the deposition of PTCDA/Au(111) at $F = 4.7$ Å/min and $T_g = 348$ K. We assume that the similarity of the

growth process on Ag(111) and Au(111) is related to the layer-dependent binding energy of PTCDA wich has been observed on both substrates.

For this system, also a layer-dependent binding energy has been observed. A similar intensity change from oscillatory behavior to a constant intensity during the deposition process has been observed for Sm/Mo(110) [118] and GaN/Al_2O_3(0001) [95]. In both cases it has been interpreted as a transition from 2D to 3D growth.

To understand the growth mode change as a function of T_g observed in this work, two approaches to model the experimental data have been used which will be discussed in the following sections.

8.3 Analytical description

In Sec. 4.2.2, we introduced a simple rate equation model [88] to calculate the X-ray intensity at the anti-Bragg point during growth. In this section, we introduce an expression for the effective diffusion constant k_n similar to the model of van der Vegt et al. [94] and apply the model to our data.

8.3.1 Model

Our model is based on the expression

$$k_n = 1 - \exp\left(\frac{-\alpha\beta(n)d\left(\theta_n\right)}{\theta_n}\right) \approx \frac{\alpha\beta(n)d\left(\theta_n\right)}{\theta_n} \tag{8.17}$$

for the effective diffusion rate constant k_n. The main feature of this model is that the effective interlayer diffusion constant k_n depends the layer number n and on the ratio $d(\theta_n)/\theta_n$ of the island (hole) perimeter, $d(\theta_n)$, and the layer coverage, θ_n. d_n is defined as

$$d(\theta_n) = \frac{1}{2} - \left|\theta_n - \frac{1}{2}\right|^{\frac{1}{2}}. \tag{8.18}$$

The ratio $d(\theta_n)/\theta_n$ contains the influence of the morphology on the effective diffusion rate. It is assumed that the probability for a diffusion downwards is small for atoms on top of compact islands but large for less compact ones. k_n is proportional to α and to the layer-dependent parameter $\beta(n)$. $\beta(n)$ contains the intrinsic properties of the material system, such as a layer-dependent surface diffusion constant. The proportionality factor α is independent of the intrinsic properties and acts as an effective temperature, i.e. the interlayer diffusion increases with an increasing α.

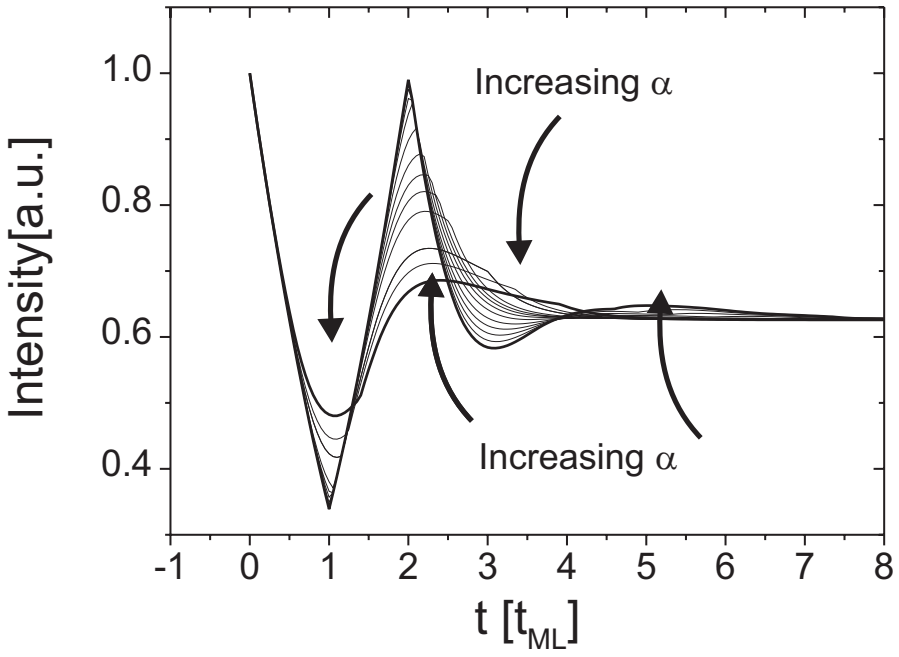

Figure 8.14: Calculation of the X-ray intensity during growth, based on rate equation theory. The arrows indicate the direction of the intensity changes for increasing α in the range of $1.5 \leq \alpha \leq 30$.

8.3.2 Simulation of the experimental data

Fig. 8.14 shows the results of the model of the X-ray intensity during the deposition. The coverages $\theta_n(t)$ have been calculated from the numeric solution of the rate equation system Eq. 4.2 using the expression of k_n given in Eq. 8.17. The intensity has been calculated from the coverages according to Eq. 3.33 using the lattice constants $d_0 = 2.82$ Å, $d_F = 3.25$ Å and the Ag parameters given in Tab. 6.5. These values have been derived experimentally from specular rod measurements.

For the calculation of the growth oscillations as a function of the deposition time, the variation of only one parameter was necessary. The parameters $\beta(1) = 1$, $\beta(2) = 0.3$, $\beta(3) = 0.02$, $\beta(4) = 0.01$, and $\beta(n > 4) = 0.001$ have been fixed for all simulations, while the parameter α has been varied between 1.5 for the most strongly damped, and 30 for the undamped oscillation (both indicated by thicker lines in Fig. 8.14). The variation of α in Fig. 8.14 is not linear (presented values: 1.5, 3, 3.5, 4, 5, 6, 7.5, 10, 18, 26, 30) since the influence of this parameter on the oscillation amplitude is much larger for low values than

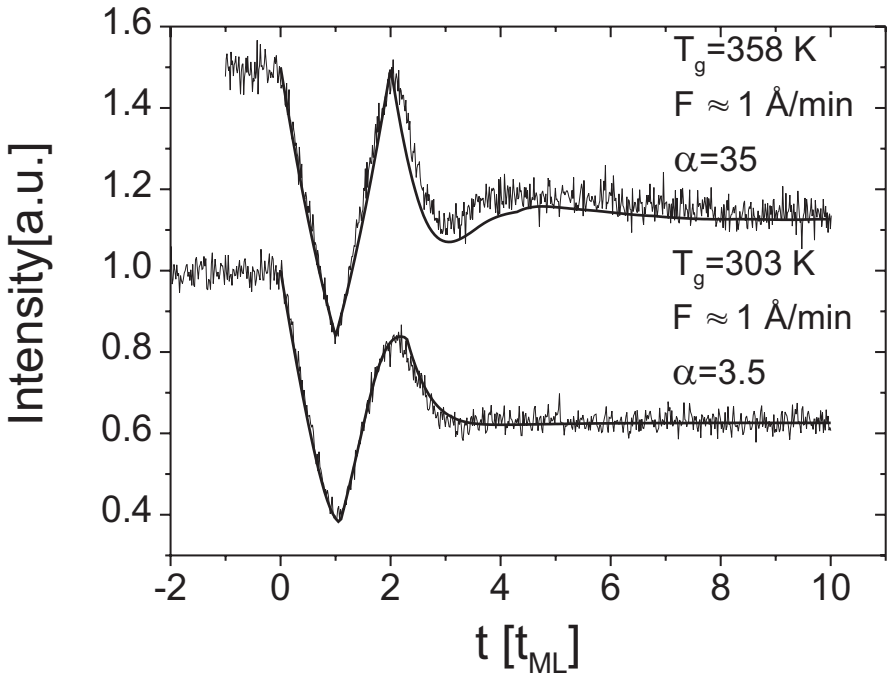

Figure 8.15: Comparison of the experimental and calculated intensities during deposition at different substrate temperatures.

for high values.

The result of the model reproduces several important features of the experiment: (1) Only one intensity maximum and minimum are clearly visible, followed at large α (large T_g in the experiment) by a weak second minimum and maximum, (2) the steady state intensity, and (3) the damping as a function of the deposition temperature which is associated with a shift of the first maximum. The rate equation model has been fitted to the experimental data by variation of α. In Fig. 8.15, the experiment and the model results are compared directly. The upper curve has been measured at $T_g = 343$ K and has been simulated with $\alpha = 35$. The lower curve has been measured at $T_g = 303$ K and modelled with $\alpha = 3.5$.

8.3.3 Discussion

The factors $\alpha\beta(n)$ contain the part of the interlayer diffusion rate k_n which is independent of the surface geometry. They have been determined by the comparison of the calculation with the experimental data. $\alpha\beta(1)$ is of the same order as $\alpha\beta(2)$, but by at least a factor 10

larger than $\alpha\beta(3)$ and $\alpha\beta(4)$, and by at least a factor 100 larger than $\alpha\beta(n > 4)$.

The parameters $\beta(n)$ do not follow the model introduced by van der Vegt et al. [94] with $\beta(n) = \beta_0^n$, where β_0 is a constant. They vary much stronger with the layer number. The model of Van der Vegt et al. leads to a continuous damping of the oscillation amplitude with the deposition time. This differs from our experimental observation of one oscillation period, which can also be undamped, followed by a constant intensity or a very weak second oscillation.

The simulations indicate that the interlayer diffusion rate varies as a function of the layer number, n. From desorption experiments and spectroscopic measurements we know that the binding energies of the first, the second and the subsequent monolayers behave like $E_{ML1} \gg E_{ML2} > E_{ML>2}$. This corresponds to an additional energy barrier for upward diffusion in contrast to downward diffusion for the diffusion between the first and the second monolayer, and a smaller additional energy barrier for the diffusion from the second to the third monolayer. Effectively, this increases the interlayer diffusion from the second to the first monolayer, and from the third to the second monolayer compared to the interlayer diffusion between the subsequent layers. This explains the large values for $\beta(1)$ and $\beta(2)$ in contrast to the subsequent $\beta(n > 2)$, but it does not explain the intermediate values $\beta(3)$ and $\beta(4)$, i.e. the existence of a second weak oscillation period. This may reflect the influence of the strain on the surface diffusion, but also geometric aspects, or a rearrangement of material already incorporated in islands.

The layer-dependent interlayer diffusion rate leads to a preferred layer-by-layer growth in the first and second monolayer. The strong decrease of the interlayer diffusion rate for higher n corresponds to a 3D growth mode at higher coverages. With decreasing T_g, the growth mode of the initial layers tends to a 3D growth mode. The simple model does not justify any detailed assumption about the progression of the 3D growth.

The rate equation model explains sufficiently the data for $T_g \lesssim 358$ K, i.e. the damping of the oscillations as a function of T_g and the transition to a constant intensity for $t \gtrsim 3t_{ML}$. It cannot be applied to $T_g > 358$ K. In this region, the experimentally observed X-ray intensity is independent of T_g, while the second oscillation period of the simulated intensity increases with increasing α.

The rate equation model takes into account an average island size, but ignores the lateral distribution of the deposited material. Therefore, it can reproduce the developement of the

local roughness of a relatively smooth film as a function of the deposition time, but it is not able to reproduce complex geometric arrangements such as facets or crystallites which have been observed for PTCDA at $T_g > 343$ K.

A similar rate equation approach as used here has been applied to the Stransky-Krastanov growth of GaN/Al_2O_3 [95]. For this system, only the first bilayer grows in layer-by-layer growth mode. The model assumes a layer-dependent effective interlayer diffusion rate with $k_n \neq 0$ for $n = 1$ and $k_n = 0$ for $n > 1$. In contrast to this model, our model allows a limited effective interlayer diffusion for all n and has an additional parameter taking to include the variation of the growth temperature.

8.4 Monte Carlo simulation of Stransky-Krastanov growth

8.4.1 Model

We have performed kinetic Monte Carlo (kMC) simulations of the growth process as a function of T_g in order to understand the 2D-3D transition observed for PTCDA/Ag(111) as a function of T_g. The molecular nature of the adsorbate has been neglected, and the growth process has been modelled independently of the characteristics of a specific model system. This approach is consistent with the observation of Weckesser et al. [29] that the surface diffusion of the molecule PVBA on Pd(110) follows an Arrhenius-like behavior, similar to the diffusion of n-alkanes on Ru(001) [119]. The Arrhenius-like behavior ensures that the diffusion process can be described by one effective energy barrier without referring to the geometrical aspects of the diffusing molecule. In the following we will refer to adsorbate *atoms*, which will include any type of adsorbate. The model is based on a refined bond-counting model with an additional interlayer diffusion barrier, E_{inter}, and a barrier for the detachment from step edges, E_{step}. The energy barrier $E_{ij}(n)$ for the diffusion process of an atom from the initial site i in the layer n to the final site j in an arbitrary layer n' is

$$E_{ij}(n) = E_D + n_i E_B + \delta_{inter} E_{inter}(n) + \delta_{step} E_{step}, \tag{8.19}$$

where E_D is the surface diffusion barrier of a monomer, n_i the number of the nearest neighbors of the initial site, and E_B the binding energy to a nearest neighbor. The interlayer

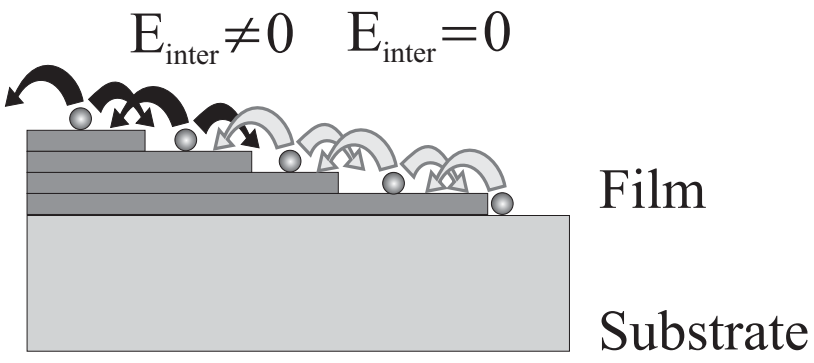

Figure 8.16: Schematic of the layer-dependent interlayer diffusion barrier $E_{inter}(n)$. A finite barrier $E_{inter}(n)$ is taken into account for the diffusion of atoms situated in layers with $n > 3$ (black arrows), for $n \leq 3$ the interlayer diffusion barrier $E_{inter}(n) = 0$ has been assumed (grey arrows).

diffusion barrier is taken into account if $n \neq n'$. Therefore we have

$$\delta_{inter} = \begin{cases} 1 & \text{for} \quad n \neq n' \\ 0 & \text{for} \quad n = n' \end{cases} . \tag{8.20}$$

It adds to the barrier $E_D + n_i E_B$ of the Bond counting model introduced in Sec. 4.3.2 if the diffusing atom changes the layer. In analogy to this, $\delta_{step} = 1$ if the initial site is at a step edge, and the final site is not at a step edge, otherwise it is 0. To allow for the transition between 2D and 3D growth characterizing the Stransky-Krastanov growth mode the destabilizing interlayer diffusion barrier $E_{inter}(n)$ is asumed to be a function of the layer number n of the initial lattice site of the diffusing atom. For $n \leq 3$, E_{inter} equals 0, and for $n > 3$, E_{inter} is larger than 0, as schematically shown in Fig. 8.16. The barrier E_{step} for the detachment favors diffusion of atoms along the step edges and is independent of n.

The atomic processes included in the model are (I) deposition, (II) diffusion of monomers, and (III) diffusion and detachment of atoms already bound to an island. To prevent overhangs and holes in the deposited film, and to minimize the computation time, the system obeys the following rules: (1) A newly deposited atom can occupy any lattice site on top of a surface atom of the initial atomic configuration (prior to the deposition); (2) only surface atoms with less than three in-plane nearest neighbors are treated as mobile; (3) the final site of a diffusing atom has to be on top of a surface atom of the initial configuration.

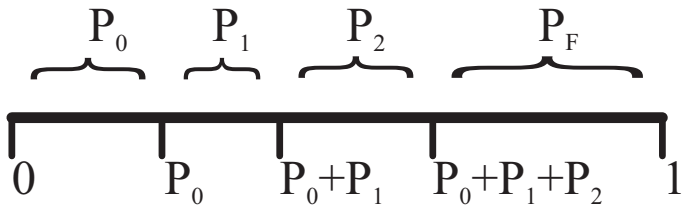

Figure 8.17: Table of probabilities for the choice of an diffusion event respectively the deposition of an atom.

8.4.2 Implementation of the model

The kinetic Monte Carlo simulations have been performed on a square lattice with $N = 200 \times 200$ sites, the lattice constant a, and periodic boundary conditions. The substrate has been assumed to be atomically flat, and for reasons of simplification the film lattice and the substrate lattice are identical. The surface is described by a height matrix $z(\mathbf{r}, t)$, where $\mathbf{r} = (i, j)$ are the lattice sites and t is the deposition time. For a given configuration $z(\mathbf{r}, t)$, a number N_0 of monomers, N_1 of atoms bound to one nearest neighbor, and N_2 of atoms bound to two nearest neighbors exists on the surface and may diffuse.

Each step of the Monte Carlo simulation consists of two parts. (1) A specific process (deposition, diffusion of a monomer, and diffusion of an atom with one or two nearest neighbors) is chosen arbitrarily. (2) If the chosen process is deposition, the deposition site is chosen; if the process is diffusion, a specific atom and the diffusion direction are chosen. The correct probabilities of the different options are contained in a table of probabilities as shown schematically for the choice of the diffusion or deposition process in Fig. 8.17. P_0, P_1, and P_2 are the probabilities of the monomer diffusion, the diffusion of an atom bound to one in-plane nearest neighbor, and an atom with two in-plane nearest neighbors, and P_F is the probability for a deposition process. The table of probabilities divides the range between 0 and 1 into sections corresponding to the probabilities. Each process (diffusion or deposition) is determined by the choice of an arbitrary number between 0 and 1 belonging to one of these sections. After the chosen process has been performed, the height matrix $z(\mathbf{r}, t)$, the numbers N_0, N_1, and N_2, and the table of probabilities have to be modified. For each set of model parameters this Monte Carlo step has been repeated up to a coverage of 4 monolayers. The height matrix of the calculated surface has been saved in steps of $0.1 t_{ML}$ where t_{ML} is the time for the deposition of one monolayer.

8.4.3 Analysis methods

For the quantitative analysis of the height matrices we introduce an autocorrelation function,

$$C(R) = \langle z(r)z(r+R)\rangle = z_0^2 + \langle \Delta z(R)\Delta z(r+R)\rangle, \tag{8.21}$$

which contains information about the lateral material distribution. Here, we have split the local surface height, $z(r) = z_0 + \Delta z(r)$, in the laterally averaged surface height, z_0,and the deviation from this, $\Delta z(r)$. For better comparison of the autocorrelation functions calculated from height matrices at different stages of the deposition, we will calculate the function $\tilde{C}(R) = C(R) - z_0^2$ with

$$\tilde{C}(0) = \langle z(r)z(r)\rangle = \sigma^2 \tag{8.22}$$

where σ is the surface roughness. The autocorrelation function has proven to be an appropriate method for the interpretation of similar morphologies as the ones modelled here, see, e.g., the references [120, 121].

8.4.4 Results

Model results at 300 K

Fig. 8.18 shows the results of a kinetic Monte Carlo simulation with the parameters $T = 300$ K, $F = 1$ ML/s, $E_D = 0.5$ eV, $E_B = 0.2$ eV, $E_{inter} = 0.5$ eV and $E_{step} = 0.2$ eV. Every matrix corresponds to a different deposition time, t. The height $z(\mathbf{r}, t)$ of the columns at every lattice site is symbolized by the grey scale. We observe a transition of layer-by-layer growth for $t \leq 2t_{ML}$ to 3D growth for $t > 2t_{ML}$. This qualitative analysis is restricted to simple growth situations, and it is difficult to distinguish between similar growth scenarios. For a quantitative understanding of the growth process, we will analyze the roughness and the autocorrelation function as a function of the deposition time and the deposition temperature.

Fig. 8.19 shows the roughness $\sigma(t)$ as a function of the deposition time, calculated for the height matrices $z(\mathbf{r}, t)$ at $T = 300$ K, in comparison to the roughness calculated for non-diffusive growth, $\sigma_{nd}(t)$. For $t \leq 2t_{ML}$, the roughness oscillates with the period t_{ML}. For $t > 2t_{ML}$, $\sigma(t)$ increases monotously. After the initial increase, the slope of $\sigma(t)$ approximates the slope of $\sigma_{nd}(t)$ with $\sigma(t) < \sigma_{nd}(t)$. This corresponds to layer-by-layer growth for $t < 2t_{ML}$, followed by 3D growth for $t > 2t_{ML}$.

Fig. 8.20 shows $\tilde{C}(R)$ calculated from the height matrix at $t = 4t_{ML}$ and averaged over L^2 lattice sites and the equivalent (01) and (10) directions (circles), together with $\tilde{C}(R)$

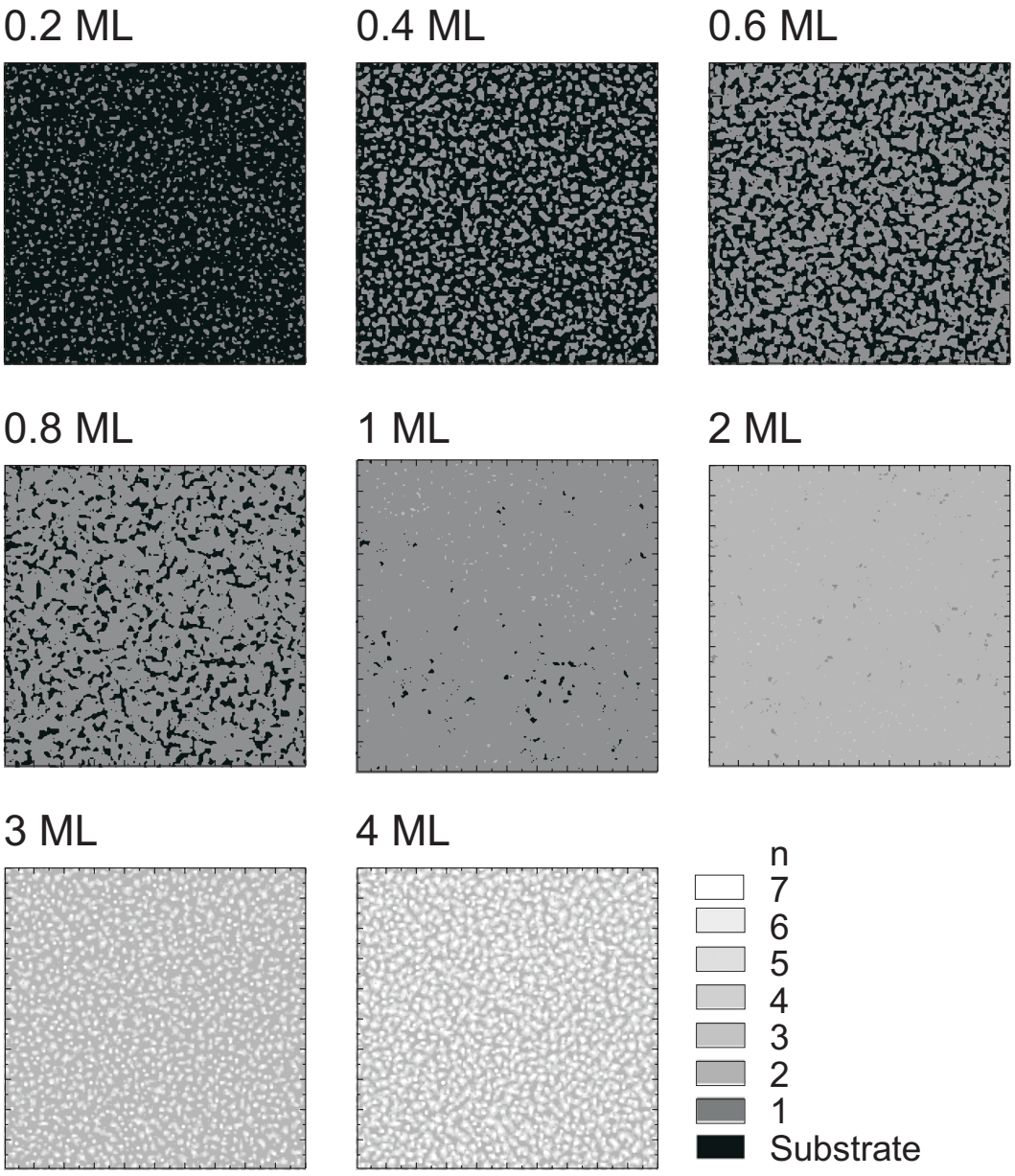

Figure 8.18: Different stages of the height matrix calculated for the parameters $T = 300$ K, $F = 1$ ML/s, $E_D = 0.5$ eV, $E_B = 0.2$ eV, $E_{inter} = 0.5$ eV and $E_{step} = 0.2$ eV.

averaged over only one of the two equivalent directions. $\tilde{C}(R)$ has a minimum at $R = 3.5a$, and a maximum at $R = 7a$, followed by less regular oscillations with approximately the same periodicity $\zeta \approx 7a$ which is the correlation length of the system. ζ corresponds to the distance of nearest neighbor islands and is approximately two times the position of the oscillation minimum. The statistical uncertainties have been calculated for the average over both direction according to the law of large numbers for a correlated system as $\sqrt{\zeta^2/2L^2}$ [120]. This lay says that the reliability of the correlation function increases with the sample area, but decreases with increasing correlation length. The comparison between the differently

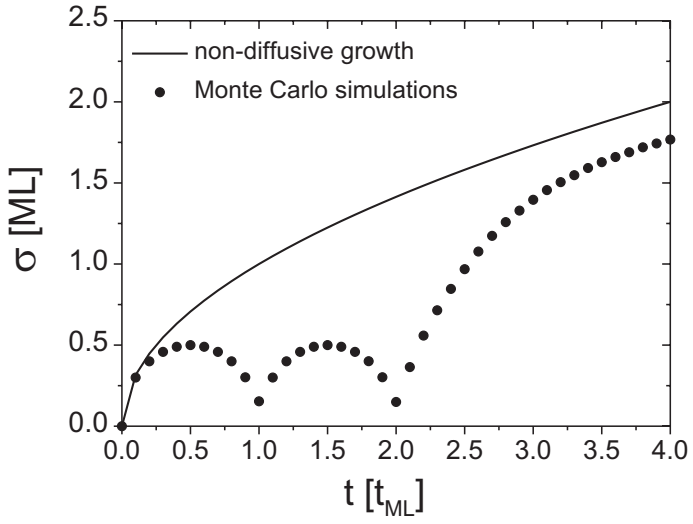

Figure 8.19: Roughness as a function of the deposition time, calculated from $z(\mathbf{r}, t)$ for the parameters $T = 300$ K, $F = 1$ ML/s, $E_D = 0.5$ eV, $E_B = 0.2$ eV, $E_{inter} = 0.5$ eV and $E_{step} = 0.2$ eV (filled circles). For comparison, the roughness calculated for non-diffusive growth is plotted as a solid line.

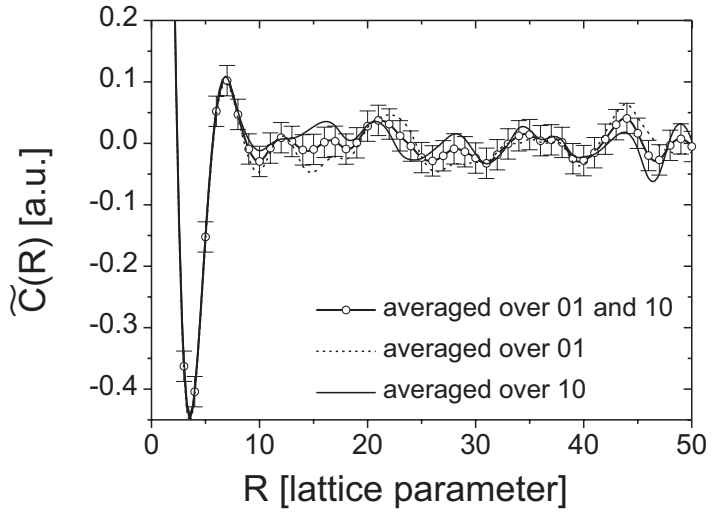

Figure 8.20: Normalized autocorrelation function $\tilde{C}(R) = C(R) - z_0^2$. The circles symbolize $\tilde{C}(R)$ calculated for all $N = L^2$ lattice sites and averaged over the equivalent directions (01) and (10), while each line is averaged over only one lattice direction.

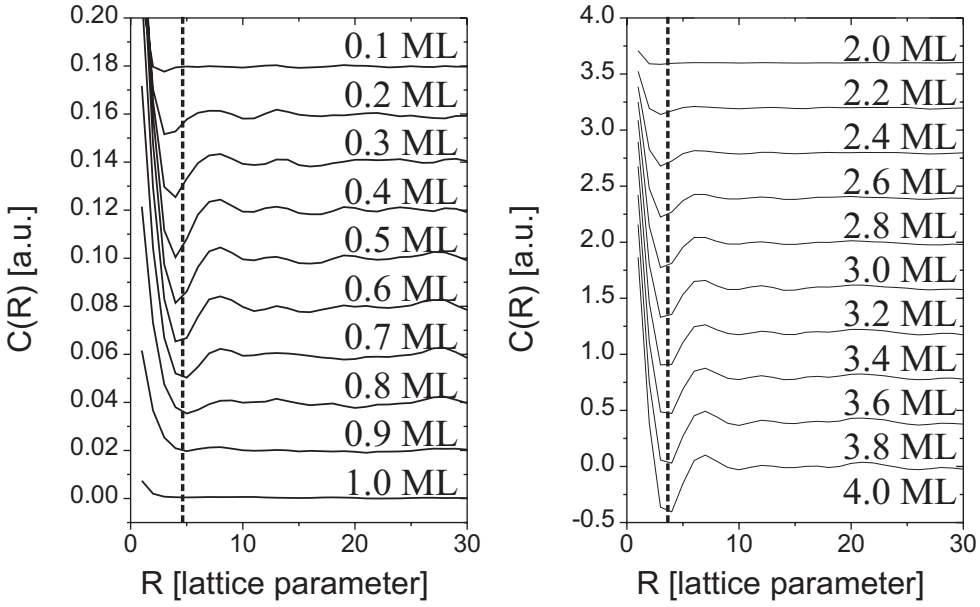

Figure 8.21: Normalized autocorrelation function, as a function of the deposition time. On the left, $\tilde{C}(R)$ for $t \leq t_{ML}$is shown, on the right for $t \leq 2t_{ML}$.

averaged $\tilde{C}(R)$ shows that the first oscillation period contains the most reliable information. We will focus on this feature during the further discussion.

Fig. 8.21 shows the normalized autocorrelation function as a function of the deposition time. For all t except $t = t_{ML}$ and $t = 2t_{ML}$, where $\tilde{C}(R)$ is almost constant, $\tilde{C}(R)$ has one pronounced damped oscillation. This oscillation indicates a correlation between nearest neighbor islands while islands with larger distances are less correlated. The amplitude and the period of the oscillations change as a function of the deposition time as shown in Fig. 8.21. This can be related to the growth process. The layer-by-layer growth observed for $t < 2t_{ML}$ is characterized by the nucleation, growth and coalescence of 2D islands. At $t \approx 2t_{ML}$, islands nucleate and grow continuously with increasing deposition time.

Variation of the deposition temperature

Several Monte Carlo simulations have been performed with the growth rate $F = 1$ ML/s and the energy barriers $E_D = 0.5$ eV, $E_B = 0.2$ eV, $E_{inter} = 0.5$ eV and $E_{step} = 0.2$ eV. The substrate temperature has been varied in 25 K steps between 200 K and 300 K. Fig. 8.22 shows the roughness, $\sigma(t)$, as a function of the deposition time, plotted for different deposition temperatures. At 200 K, $\sigma(t)$ increases monotonically with the deposition time. The

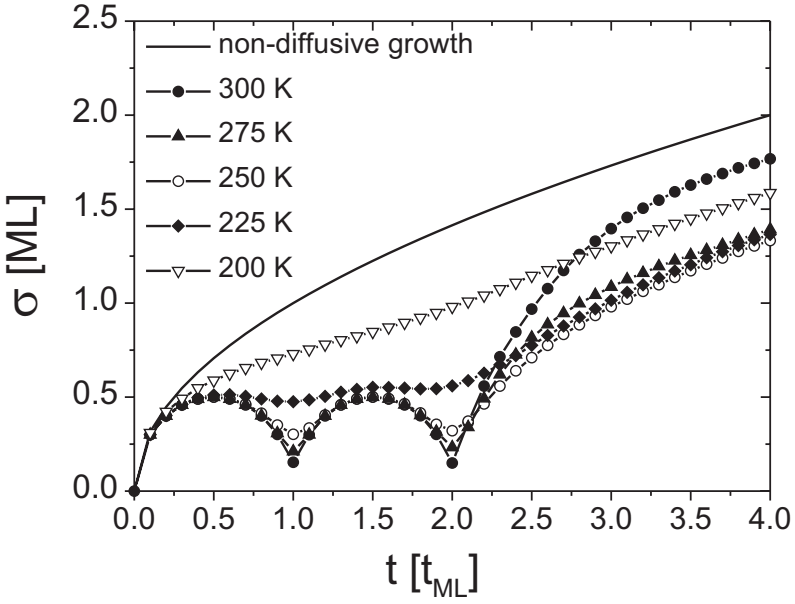

Figure 8.22: Comparison of the time-dependent roughness for different temperatures.

oscillations for $t \leq 2t_{ML}$ show for $T_g > 200$ K. For all temperatures, the roughness increases monotonically for $t \geq 2t_{ML}$, but stays lower than the roughness expected for non-diffusive growth. These observations show that the degree of the layer-by-layer growth for $t < 2t_{ML}$ increases with increasing T_g.

Fig. 8.23 shows the normalized autocorrelation function for $t = 4t_{ML}$, plotted for different T_g. The amplitude of the oscillations observed for low R increases with T_g, and the position of the minimum shifts to higher R. This corresponds to an increase of the island correlation and the island size at $t = 4t_{ML}$ as a function of the deposition temperature. The temperature dependence of $\tilde{C}(R)$ becomes apparent also for $t < 4t_{ML}$. It shows that for $t > 2t_{ML}$ the island size increases with the deposition time and the deposition temperature.

8.4.5 X-ray intensity at the anti-Bragg point

Fig. 8.24 shows the coverages $\theta_n(t)$ of the single layers as a function of the deposition time. The thick solid lines represent the results of the simulation at $T_g = 300\ K$, the thin dashed lines the expected values for non-diffusive growth. The coverages have been calculated from $z(\mathbf{r}, t)$ as the ratio of the occupied lattice sites of a layer n and the number N of all lattice sites of the layer. A constant slope of 1 nearly up to $\theta_n(t) = 1$ has been observed for the

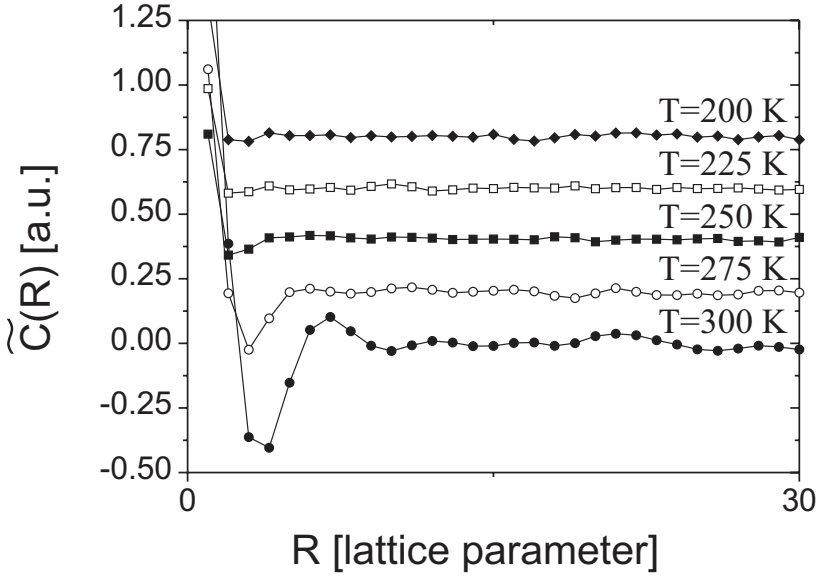

Figure 8.23: Comparison of the autocorrelation function at $t = 4t_{ML}$ for different temperatures.

first and second monolayer. This corresponds to ideal layer-by-layer growth. For $t \gtrsim 2t_{ML}$, several layers contribute to the growth process. The slope of $\theta_n(t)$ for $n > 2$ deviates clearly from 1.

The time-dependent coverage has been calculated for all simulated temperatures. With decreasing temperature, the slope of the first and second monolayer decreases, and an increasing number of layers contributes to the growth. At low temperatures, the coverages approach the time variation expected for non-diffusive growth.

Fig. 8.25 shows the X-ray intensity as a function of the deposition temperature and the deposition time, calculated with the parameters of the system PTCDA/Ag(111) used in Sec. 8.3.2. The undamped first minimum at $t = t_{ML}$ and the maximum at $t = 2t_{ML}$ for $T_g = 300$ K correspond to ideal layer-by-layer growth. Both minimum and maximum amplitude decrease with decreasing temperature. The minimum is slightly more damped than the maximum. With increasing damping, the position of the maximum shifts to larger t. After the maximum, the oscillatory behavior is replaced by a monotonically decreasing intensity. The higher the temperature, the slower this decrease takes place. After $t = 4t_{ML}$, all curves except the one for $T_g = 300$ K have approached the same value of ≈ 0.63.

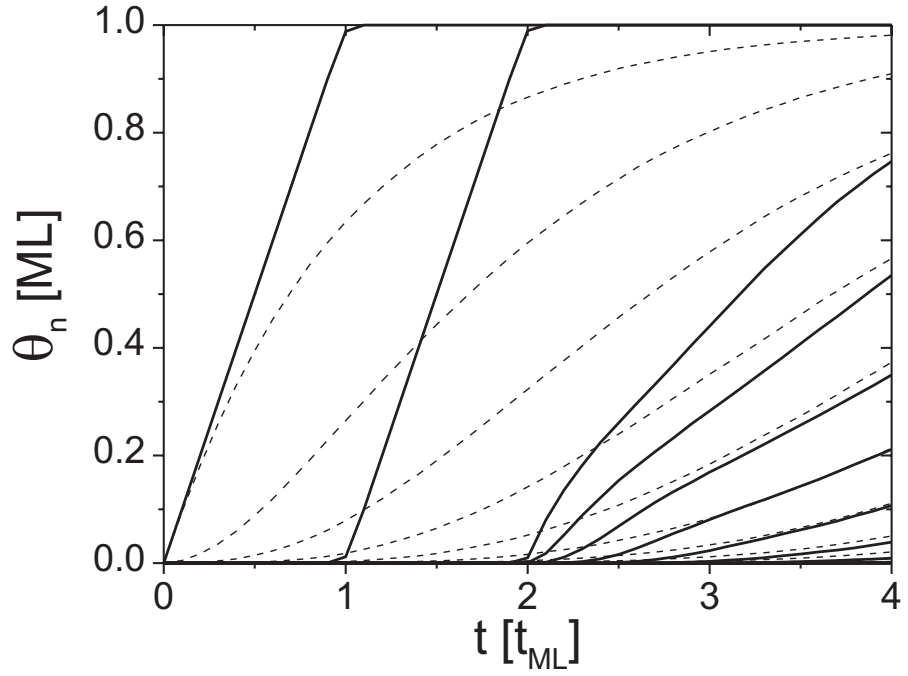

Figure 8.24: Coverage of the layers participating in the growth, as a function of the deposition time. The solid lines correspond to the Monte Carlo simulation with the parameters T_g = 300 K, F = 1 ML/s, E_D = 0.5 eV, E_B = 0.2 eV, E_{inter} = 0.5 eV and E_{step} = 0.2 eV, the dashed lines are calculated for non-diffusive growth.

8.4.6 Discussion

From the analysis of the kinetic Monte Carlo simulations, we deduce the following information on the growth mode of our model system. The autocorrelation function and the roughness as a function of the deposition time indicate correlated 2D growth for $t < 2t_{ML}$, and correlated 3D island growth for $t > 2t_{ML}$. The correlation is restricted to the nearest-neighbor distance. The damping of the roughness oscillations for $t < 2t_{ML}$ with decreasing temperature, accompanied by the decreasing amplitude of the oscillations of $\tilde{C}(R)$, shows that the degree of the layer-by-layer growth for $t < 2t_{ML}$ decreases with decreasing temperature. The transition between the initial 2D growth and the 3D growth smears out, and for T = 200 K, only 3D growth can be observed.

These observations correspond to an intrinsic Stransky-Krastanov growth mode of the system which can be observed at T = 300 K but which is kinetically suppressed for decreasing temperatures. The transition between the 2D and 3D growth mode is induced by the

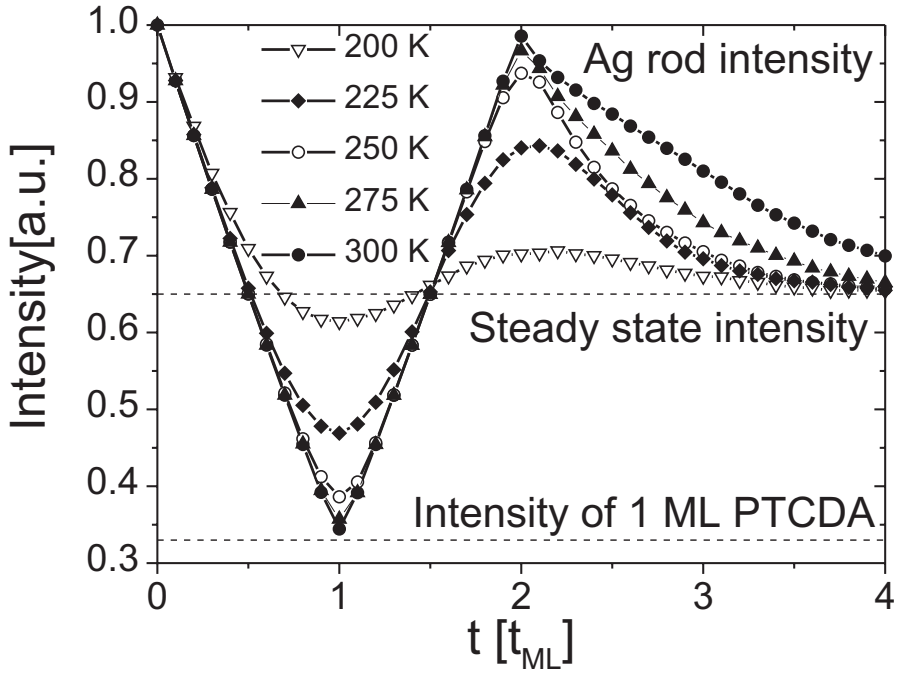

Figure 8.25: X-ray intensity as a function of the deposition time calculated from the Monte Carlo simulations with the parameters $F = 1$ ML/s, $E_D = 0.5$ eV, $E_B = 0.2$ eV, $E_{inter} = 0.5$ eV and $E_{step} = 0.2$ eV. Every line represents a different temperature.

layer-dependent interlayer diffusion barrier. Without this barrier, the growth would continue as layer-by-layer growth, while a barrier from the first monolayer on would directly induce island growth, without previous layer-by-layer growth.

In Sec. 8.1 we have reported the observation of intensity oscillations at the anti-Bragg point for the system PTCDA/Ag(111). These oscillations have been interpreted as Stransky-Krastanov growth. Fig. 8.26 compares the experimental X-ray data, measured at low deposition rates of $F \approx 0.05$ ML/s (Fig. 8.3) at $T_g = 233$, 303, and 358 K, with the result of the kinetic Monte Carlo simulations (Fig. 8.25) for $T_g = 200$, 225, and 250 K. Both experiment and model system agree in certain features including the intensity oscillations for $t < 2t_{ML}$, their damping with decreasing temperature, the shift of the maximum position, and the steady-state intensity observed for $t \gg 2t_{ML}$. The temperatures used for the calculations and the experiment are of the same order indicating that the magnitude of the energy barriers used for the simulations are reasonable.

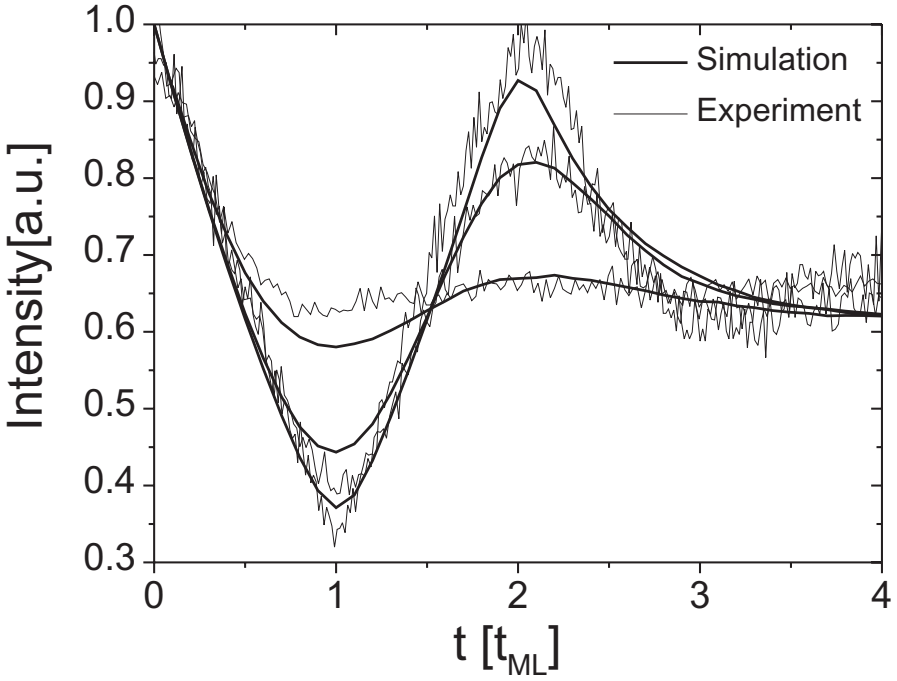

Figure 8.26: Comparison between the experimental and the calculated X-ray intensity (see text).

However, some qualitative differences between simulation and experiment are visible. The damping of the maximum compared to the minimum of the experimentally observed oscillations is much stronger than in the simulations. After the maximum, the measured intensity drops down very fast while the predicted intensity decrease is much slower. The second minimum sometimes observed experimentally is not reproduced in the simulations. The differences between the model system and the experiment show also in the behavior of the system after the deposition. In the experiment, a recovery of the intensity after growth has been found for $T_g \gtrsim 358$ K. This recovery has been interpreted as post-growth diffusion of many molecules to the islands. It is not reproduced by the chosen model parameters since the number of free atoms after the growth is negligible.

Now we analyze the growth morphology. The experimentally observed films are relatively smooth for $T_g \lesssim 343$ K, with a negligible increase of the roughness with increasing T_g, similar to the simulations for $225 \leq T_g \leq 275$ K and $4t = 4t_{ML}$. The distance between the islands increases with T_g, as observed experimentally for $T_g \gtrsim 343$ K. However, the islands are quite small, and it seems that the model system corresponds to the experimentally ob-

served morphology for $T_g \lesssim 343$ K. The model system does not reproduce experimentally observed details such as the facetted transition region between relatively smooth films and separate islands.

Several aspects contribute to the differences between the experiment and the Monte Carlo simulations. The model includes a small number of effective parameters which are not related to any specific material system. The energy barriers used are nearest-neighbor binding energy, the diffusion barrier, the barrier for detachment from steps, and the interlayer diffusion barrier. Long-range interactions are effectively contained in the interlayer diffusion barrier.

In the complex system PTCDA/Ag, however, several other energy barriers play a major part, such as the binding energy to the substrate in contrast to the binding energy between subsequent layers, the strain induced by the substrate, the crystallographic symmetry of the substrate and the film, and the grain boundaries between different domains. We cannot expect that such a oversimplified system reproduces all features of the experiment exactly, but the most significant aspect, the transition between 2D and 3D growth as a function of the growth temperature, is well-reproduced.

Now we compare the rate equation model with the kMC simulations. The rate equations are an effective description of the growth process, while the kMC simulations are based on atomistic model. Both simulations are independent of the intrinsic properties of the material. The results of both simulations correspond well to the X-ray measurements during growth for $T_g < 358$ K, the rate equations even better than the kMC simulations. The basic result of the rate equations is that the effective flux downwards between subsequent layers is larger between the first and the second monolayer compared to the subsequent layers. The kMC simulations attribute the effective flux to an effective interlayer diffusion barrier which depends on the layer number. This effective barrier might be related to strain or a Ehrlich-Schwoebel barrier. Both assumptions are supported by the experimental observations of a strained, partially relaxed film in the relatively smooth growth region, and the growth of separate islands at higher temperatures.

Chapter 9

Summary

Thin PTCDA films with the average thickness d between 50 and 200 Å, and the deposition rate F between 1 and 10 Å, have been deposited by molecular beam epitaxy on Ag(111). The films have been studied by non-contact AFM and X-ray diffraction. In the following, we summarize the main results of this study.

- The structural and morphological properties of the films vary significantly with the growth temperature. At $T_g \lesssim 350$ K, relatively smooth respectively faceted films have been observed, and for $T_g = 318$ K, two strained crystalline structures similar to the bulk polymorphs are observed. At $T_g \gtrsim 350$ K, separate crystallites on a wetting layer with two ML thickness have been found, and for $T_g = 448$ K, two relaxed crystalline structures similar to the bulk polymorphs have been observed. All crystalline structures measured at $T_g = 318$ K and $T_g = 448$ K are incommensurate to the substrate and have been observed for $d = 50$ Å and $d = 200$ Å.

- We assume that for both measured structures, an incommensurate PTCDA film grows on top of the commensurate monolayer structure [15]. At $T_g = 318$ K, the (01) and the (10) planes of both polymorphs are parallel to the respective planes of the ML structure. At $T_g = 448$ K, each polymorph has two epitaxial orientations to the ML structure, either aligned with (12) or with $(1\bar{2})$. Between these two orientations a continuous distribution of rotational domains has been observed.

- The crystallite density at a constant F and a constant d observed for $T_g \gtrsim 350$ K decreases with increasing T_g. The crystallite distribution has been analyzed in terms of the nucleation theory developed for inorganic systems, and the effective surface diffusion energy of the molecules on top of the wetting layer has been estimated as $pE_{eff} = 0.6 \pm 0.2$ eV.

- The relatively smooth PTCDA films with $T_g \lesssim 350$ K are metastable. They partially dewet with a wetting layer of approximately 2 ML for $T > 350$ K. The films with crystallite morphology grown at $T_g \gtrsim 350$ K have a stable morphology even if the island distribution might change during long-time annealing.

- The linear thermal expansion coefficient in the temperature range between room temperature and approximately 490 K is anisotrope. In the stacking direction of the molecules we find $\alpha_\perp = 1.05 \pm 0.06 \times 10^{-4}$ K^{-1}, perpendicular to the stacking direction we estimate $\alpha_\parallel = 5 \pm 2 \times 10^{-5}$ K^{-1}. The lattice parameter between the first ML and the substrate seems to be temperature independent. This anisotropy is characteristic for planar molecules forming stacks [20, 21].

- The specular scattering as a function of the deposition time depends on the coverage of the PTCDA film. In the scattering geometry we use for our experiments all layers n with $n = 2m$ contribute in the same way to the scattering intensity, as well as all layers with $n = 2m+1$. The scattered intensity gives information on the total coverage of all layers with even and odd n, respectively. If only few layers contribute to the growth, as in the case of the initial growth of PTCDA on Ag(111), it is possible to estimate the coverage of individual layers. This coverage is directly related to the growth mode of PTCDA/Ag(111).

- PTCDA on Ag(111) grows in the Stransky-Krastanov growth mode. The first and the second monolayer grow in the layer-by-layer growth mode, followed by the nucleation of islands on top of the second monolayer. For $T_g \gtrsim 350$ K perfect layer-by-layer growth of the wetting layer has been found, for $T_g \lesssim 350$ K the growth mode deviates from the perfect layer-by-layer growth mode. This deviation could be quantified. The intensity recovery after deposition observed for $T_g \gtrsim 350$ K has been interpreted as a post-growth diffusion process of molecules on top of the wetting layer. These molecules diffuse to the crystallites and are incorporated there.

- We modelled the *in situ* X-ray measurements as a function of T_g with two methods: (1) a rate-equation model, and (2) kinetic Monte Carlo simulations. Both models reproduce the main experimental features observed for $T_g \lesssim 350$ K. The rate equations show the influence of the effective interlayer diffusion on the growth mode. This interlayer diffusion is layer-dependent. The kinetic Monte Carlo simulations attribute the layer-dependence of the interlayer diffusion to an effective interlayer diffusion barrier which varies with the layer number. This barrier might be related to the observed strain of the PTCDA film, or to a Schwoebel barrier which is known to induce island growth.

Within this thesis, an extensive study of the growth of PTCDA/Ag(111) has been performed. The structural, morphological and kinetic aspects have been studied in detail. While many fundamental questions of the growth of organic thin films could be dicussed in this context, some disadvantages regarding the technical application of PTCDA have become obvious. Homogenous layers with $T_g \lesssim 350$ K are thermally unstable even for temperatures only slightly higher than room temperature. Films grown at $T_g \gtrsim 350$ K have a larger structural order of the crystallites, but have also an inhomogenous layer thickness. For all growth conditions, a large number of domains and the coexistence of two polymorphs have been observed.

The results of this theses are important for the understanding of the growth of organic thin films. Not only the here reported observations for the system PTCDA/Ag(111), but also the studies of several organic / inorganic thin film systems performed by other groups (e.g. see Ref. [28–30]) imply that many of the fundamental concepts of the inorganic MBE can be transferred on the growth of small organic molecules. This allows to take the theoretical and experimental results of several decades of research, and to extend these concepts to the growth of the complex molecular thin films.

Appendix A

Thermal expansion of a molecular crystal

In Sec. 7.2, we have discussed the anisotrope thermal expansion of PTCDA. In the following, we estimate the anisotropic thermal expansion of a molecular crystal consisting of planar molecules. We follow an approach similar to the one proposed by van Smaalen et al. [21]. The structure of this section is as follows. In Sec. A.1 we will introduce the basic assumptions of the model. Then we will calculate the relative displacement of the lattice planes parallel (Sec. A.2) and perpendicular (Sec. A.3) to the stacking direction. In the last section we will calculate the anisotropic thermal expansion, and finally we will discuss the model in Sec. A.5.

A.1 Basic assumptions of the model

Our model is based on several assumptions. The molecules placed on these planes are assumed to be rigid and rectangular, with the dimensions $m \times n \times 1$, as shown in Fig. A.1 (a). The stacking of the molecules in the crystal is shown in Fig. A.2 (a). The atoms (j,k) are assumed to be point-like and identical. Only corresponding atoms (j,k) on molecules of neighboring lattice planes i and $i-1$ interact, as shown in Fig. A.2 (b). They are coupled by springs with an anharmonic potential $V_{jk}^{i,(i-1)}$ depending on the relative displacement $\tilde{\mathbf{r}}_{ijk} = \mathbf{r}_{ijk} - \mathbf{r}_{(i-1)jk}$ of the atoms on neighboring lattice planes i and $i-1$. The absolute displacement $\mathbf{r}_{ijk}$ of an arbitrary atom (j,k) belonging to the lattice plane i, as observed in the laboratory system, is

$$\mathbf{r}_{ijk} = \begin{pmatrix} u_{xi} + x_j\,(1-\cos\chi_i) + x_j\,(1-\cos\psi_i) + & 0 \\ u_{yi} + y_k\,(1-\cos\chi_i) + & 0 & + y_k\,(1-\cos\phi_i) \\ u_{zi} + & 0 & + \; x_j \sin\psi_i \; + & y_k \sin\phi_i \end{pmatrix}, \tag{A.1}$$

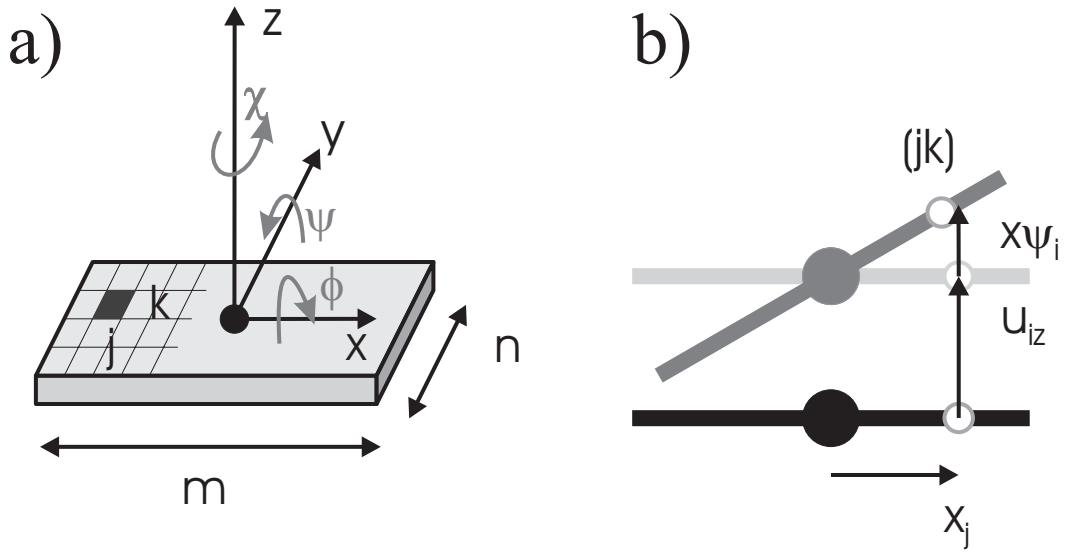

Figure A.1: (a) Coordinate system fixed to the molecule. (b) Total displacement of the atom (jk) for a translation along the z axis of the laboraty system and a rotation around the y axis of the coordinate system fixed to the molecule.

where u_{ix}, u_{iy} and u_{iz} are the translations of the center of mass of the molecule in the plane i, and ϕ_i, ψ_i and χ_i are the rotations around the x, y, and z axes fixed to the molecule itself, as indicated in Fig. A.1 (a). For small rotation amplitudes this expression simplifies to

$$\mathbf{r}_{ijk} = \begin{pmatrix} u_{xi} \\ u_{yi} \\ u_{zi} + x_j\psi_i + y_k\phi_i \end{pmatrix}. \tag{A.2}$$

The interaction potential $V_{jk}^{t,i,(i-1)}$ of two atoms situated in the planes i and $i-1$ depends on the orientation of the plane. If the lattice vector is parallel to the axis t with $t = x$, y, or z, then the anharmonic potential, expanded up to the third order, is

$$\begin{aligned} V_{jk}^{t,i,(i-1)} &= \frac{1}{2}a\left(r_{ijk}^t - r_{(i-1)jk}^t\right)^2 + \frac{1}{6}b\left(r_{ijk}^t - r_{(i-1)jk}^t\right)^3 \\ &= \frac{1}{2}a\left(\tilde{r}_{ijk}^t\right)^2 + \frac{1}{6}b\left(\tilde{r}_{ijk}^t\right)^3. \end{aligned} \tag{A.3}$$

A.2 Average displacement parallel to the stacking direction

We now discuss the thermal expansion parallel to the stacking direction of the molecules, i.e. for $t = z$. The interaction potential $V^{z,i,i-1}$ between neighboring molecules, normalized

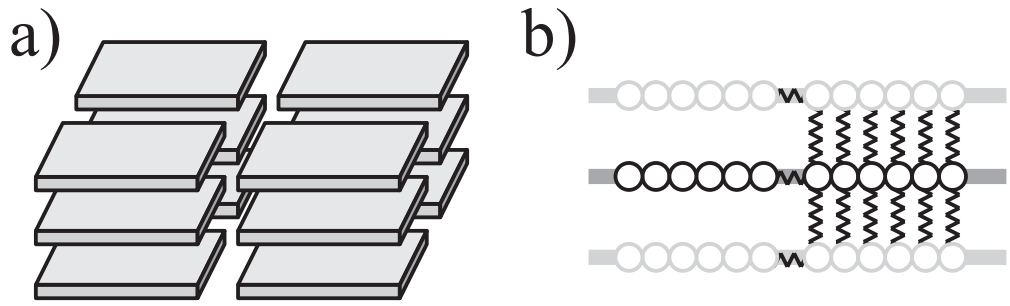

Figure A.2: (a) Model for the stacking of planar molecules in a crystal, (b) model for the interaction between adjacent molecules.

to the molecular area mn, is

$$V^{z,i,(i-1)} = \frac{1}{mn}\sum_{j=1}^{m}\sum_{k=1}^{n}\left(\frac{1}{2}a\left(\tilde{u}_{zi}+x_j\tilde{\psi}_i+y_k\tilde{\phi}_i\right)^2+\frac{1}{6}b\left(\tilde{u}_{zi}+x_j\tilde{\psi}_i+y_k\tilde{\phi}_i\right)^3\right) \tag{A.4}$$

where the variables $\tilde{q}_i$ are the relative displacements of the rotations and translations, $\tilde{q}_i = q_i - q_{i-1}$. This normalization, and the discussion of a molecular lattice in contrast to the interaction of two separate molecules, are the main differences between our model and the model of Smaalen et al. If we perform the summation, we finally get

$$V^{z,i,(i-1)} = a\frac{1}{2}\left(\tilde{u}_{iz}^2+\frac{1}{3}\tilde{\psi}_i^2l_x^2+\frac{1}{3}\tilde{\phi}_i^2l_y^2\right)+b\frac{1}{6}\left(\tilde{u}_{iz}^3+\tilde{u}_{iz}\tilde{\psi}_i^2l_x^2+\tilde{u}_{iz}\tilde{\phi}_i^2l_y^2\right). \tag{A.5}$$

Here we have used the approximation

$$\sum_{j=1}^{m}x_j^2\psi_i^2 = \psi_i^2\sum_{x=-m/2}^{m/2}x^2 \approx \psi_i^2\int_{-l_x}^{l_x}x^2dx \tag{A.6}$$

which is valid for large m. $2l_x$ is the length of the molecule in x direction. Since every lattice plane has two neighbors, the integrated potential V_i^z of the lattice plane i is

$$\begin{aligned}V_i^z &= V^{z,i,(i-1)}+V^{z,(i+1),i}\\ &= a\frac{1}{2}\left(\tilde{u}_{iz}^2+\frac{1}{3}\tilde{\psi}_i^2l_x^2+\frac{1}{3}\tilde{\phi}_i^2l_y^2+\tilde{u}_{(i+1)z}^2+\frac{1}{3}\tilde{\psi}_{(i+1)}^2l_x^2+\frac{1}{3}\tilde{\phi}_{(i+1)}^2l_y^2\right)\\ &+ b\frac{1}{6}\left(\tilde{u}_{iz}^3+\tilde{u}_{iz}\tilde{\psi}_i^2l_x^2+\tilde{u}_{iz}\tilde{\phi}_i^2l_y^2+\tilde{u}_{(i+1)z}^3+\tilde{u}_{(i+1)z}\tilde{\psi}_{(i+1)}^2l_x^2+\tilde{u}_{(i+1)z}\tilde{\phi}_{(i+1)}^2l_y^2\right)\end{aligned} \tag{A.7}$$

The equilibrium condition for the displacement $\tilde{u}_{iz}$ is

$$\frac{\partial V_i^z}{\partial\tilde{u}_{iz}} = a\tilde{u}_{iz}+\frac{b}{2}\tilde{u}_{iz}^2+\frac{b}{6}\left(\tilde{\psi}_i^2l_x^2+\tilde{\phi}_i^2l_y^2\right)=0 \tag{A.8}$$

which is equivalent to

$$\tilde{u}_{iz} = -\frac{b}{2a}\tilde{u}_{iz}^2-\frac{b}{6a}\left(\tilde{\psi}_i^2l_x^2+\tilde{\phi}_i^2l_y^2\right). \tag{A.9}$$

Since at $T \gg 0$ not only one phonon but a spectrum of phonons is excited, the measured displacement is the statistical average $\langle \tilde{u}_{iz} \rangle$ of all possible displacements with

$$\langle \tilde{u}_{iz} \rangle = -\frac{b}{2a} \langle \tilde{u}_{iz}^2 \rangle - \frac{b}{6a} \left(\langle \tilde{\psi}_i^2 \rangle l_x^2 + \langle \tilde{\phi}_i^2 \rangle l_y^2 \right). \tag{A.10}$$

The canonical distribution can be applied to phonons at high temperatures. We calculate $\langle \tilde{u}_{iz}^2 \rangle$ with

$$\langle \tilde{u}_{iz}^2 \rangle = \frac{\int \tilde{u}_{iz}^2 e^{-\beta V_i^z} d\tilde{u}_{iz}}{\int e^{-\beta V_i^z} d\tilde{u}_{iz}} = \frac{k_B T}{a}. \tag{A.11}$$

Similar to this, we get

$$l_x^2 \langle \psi_i \rangle = l_y^2 \langle \phi_i \rangle = \frac{3 k_B T}{a}. \tag{A.12}$$

k_B is the Boltzmann constant, and $\beta = k_B T$. With this, the average displacement $\langle \tilde{u}_{iz} \rangle$ in Eq. A.10 is

$$\langle \tilde{u}_{iz} \rangle = -\frac{3}{2} \frac{b k_B T}{a^2}. \tag{A.13}$$

A.3 Average displacement perpendicular to the stacking direction

In analogy to the displacement parallel to the stacking direction, we now discuss the average displacement perpendicular to the stacking direction. Since $t = x$ and $t = y$ are equivalent, we will restrict the calculations to $t = x$. Only the atoms at the end of the molecule with $j = 1$ interact with the adjacent lattice plane, and the interaction potential per unit area is

$$\begin{aligned} V^{x,i,(i-1)} &= \sum_{k=1}^{n} \frac{1}{n} \left(\frac{1}{2} a \tilde{u}_{xi}^2 + \frac{1}{6} b \tilde{u}_{xi}^3 \right) \\ &= a \frac{1}{2} \tilde{u}_{xi}^2 + \frac{1}{6} b \tilde{u}_{xi}^3. \end{aligned} \tag{A.14}$$

The total interaction potential of the lattice plane i is

$$V_i^x = V^{x,i,(i-1)} + V^{x,(i+1),i}. \tag{A.15}$$

The equilibrium condition for the displacement $\tilde{u}_{ix}$ is

$$\frac{\partial V_i^x}{\partial \tilde{u}_{ix}} = a \tilde{u}_{ix} + \frac{b}{2} \tilde{u}_{ix}^2 = 0 \tag{A.16}$$

which leads to the average displacement

$$\langle \tilde{u}_{ix} \rangle = -\frac{b}{2a} \langle \tilde{u}_{ix}^2 \rangle = -\frac{1}{2} \frac{k_B T}{a^2}. \tag{A.17}$$

Here we have used the Boltzmann distribution of the phonons at high temperatures.

A.4 Anisotropic thermal expansion

The ratio of the relative thermal expansion is

$$\frac{\tilde{u}_{iz}}{\tilde{u}_{ix}} = \frac{3}{1}. \tag{A.18}$$

The linear thermal expansion coefficient is defined as

$$\alpha = \frac{l(T) - l_0}{l_0}. \tag{A.19}$$

On the atomic scale, $l(T)$ is the temperature dependent lattice constant and l_0 is a reference value of the lattice constant chosen here as the minimum lattice constant at $T = 0$. In our model, the molecular size $l_0^x = m$, $l_0^y = n$, and $l_0^z = 1$, is a measure for the minimum lattice constant. The temperature dependent lattice constant is

$$\begin{aligned} l^x(T) &= l_0^x + \tilde{u}_{ix} = m - \frac{1}{2}\frac{k_B T}{a^2}, \\ l^y(T) &= l_0^y + \tilde{u}_{ix} = n - \frac{1}{2}\frac{k_B T}{a^2}, \quad \text{and} \\ l^z(T) &= l_0^x + \tilde{u}_{ix} = 1 - \frac{3}{2}\frac{k_B T}{a^2}. \end{aligned} \tag{A.20}$$

Inserting this in Eq. A.19, we receive

$$\begin{aligned} \alpha_x &= -\frac{1}{2}\frac{k_B T}{a^2 m}, \\ \alpha_x &= -\frac{1}{2}\frac{k_B T}{a^2 n} \quad \text{and} \\ \alpha_z &= -\frac{3}{2}\frac{k_B T}{a^2}. \end{aligned} \tag{A.21}$$

If $m \approx n$, α_x and α_y are of the same order and can be summarized by $\alpha_\perp$, and with $\alpha_z = \alpha_\parallel$, anisotropy of the absolute thermal expansion is

$$\frac{\alpha_\parallel}{\alpha_\perp} = 3m \tag{A.22}$$

A.5 Discussion of the model

The atom-atom potential approach has been successfully used to explain the packing of organic crystals [33]. It is based on the additivity of the interatomic interactions of neighboring molecules, and a commonly applied interaction potential is the Lennard-Jones potential

$$E_{pot} = \frac{A}{r^6} - \frac{B}{r^{12}}. \tag{A.23}$$

The anharmonic potential used in our approach corresponds to the development of E_{pot} around the equilibrium distance of the atoms r_0 as a function of the displacement $\Delta r = r - r_0$.

In contrast to a more sophisticated model, our model neglects the different types of atoms in the molecule, assumes a simple molecular packing, and neglects permanent dipole or quadrupole moments. The latter occurs for example in the system PTCDA. It is expected that the anisotropy of the nearest-neighbor interactions due to these contributions might lead to an anisotropic thermal expansion.

The model predicts that the largest thermal anisotropy is found perpendicular to the molecular plane, as observed experimentally for planar molecules. It also predicts that the anisotropy of the thermal expansion depends on the molecular size in the direction of the thermal expansion. Due to the lack of systematic data, we cannot compare this dependence with systematic experimental observations on van der Waals crystals. For a number of TNCQ salts, the ratio $\alpha_x/\alpha_\perp$ raries between 1 and 5 in one in-plane direction, and $\alpha_y/\alpha_\perp$ varies between -10 and 70 [21]. Our model predicts that $|\alpha_x| > |\alpha_y|$ which corresponds to the experimental observations for most of the salts. Since the TNCQ salts are more complex than simple van der Waals crystals the in-plane anisotropy of the interaction needs further discussion.

Appendix B

List of acronyms

AES	Auger electron spectroscopy
AFM	atomic force microscopy
CTR	crystal truncation rod
ESRF	European Synchrotron Radiation Facility
FWHM	full-width at half maximum
GIXD	grazing incidence X-ray diffraction
HASYLAB	Hamburger Synchrotronstrahlungslabor
HOPG	highly-oriented pyrolytic graphite
KS	Kurdjumov-Sachs
LEED	low-energy electron diffraction
MBE	molecular beam epitaxy
MC	Monte Carlo
MD	molecular dynamics
MEIS	medium-energy ion scattering
ML	monolayer
NC-AFM	non-contact atomic force microscopy
NW	Nishiyama-Wassermann
OMBE	organic molecular beam epitaxy
PSD	position sensitive detector
PTCDA	3,4,9,10-perylenetetracarboxylic dianhydride ($C_{24}O_6H_8$)
QCM	quartz crystal microbalance
QMS	quadrupole mass spectrometer
RHEED	reflection high-energy electron diffraction
STM	scanning tunneling microscopy
TEAS	thermal-energy atom scattering
UHV	ultra-high vacuum

Appendix C

List of symbols

A	rea covered by an island
A_{coh}	coherently illuminated area
A_{illum}	total illuminated area
A_{thick}, A_{thin}, A_{res}	sample surface areas (Sec. 7.1.3)
A_{ML}	sample surface area (Sec. 6.2.1 and Sec. 8.2.4)
a, b, c, β	parameters of the monoclinic unit cell
$\mathbf{a}_1$, $\mathbf{a}_2$	lattice vectors of the 2D substrate surface
$\mathbf{b}_1$, $\mathbf{b}_2$, γ	lattice vectors of the 2D film structure, and the angle they include
C	autocorrelation function
$\tilde{C}$	normalized autocorrelation function
$[C]$	transformation matrix from the 2D lattice vectors of the film to the 2D lattice vectors of substrate
C^{area}	area correction
$C^{Lorentz}$	Lorentz factor
C^{pol}	polarization factor
C^{rod}	rod correction
d	average film thickness
d_{102}, d_S, d_F	lattice parameters
d_0	lattice spacing between the substrate surface and the film
$d(\theta)$	island / hole perimeter
D, D_{eff}	(effective) surface diffusion constant
E	energy
E_a, E_b, E^+	energy of the states a, b, and a transition state
E_{ab}	energy barrier between the states a and b
E_B	binding energy
E_D, E_{eff}	(effective) energy barrier for surface diffusion

E_{ex}	exciton binding energy
E_i	nucleation energy of the critical cluster
E_{inter}	effective interlayer diffusion barrier
E_{opt}	optical gap
E_{step}	energy barrier for the detachment from a step edge
E_t	transport gap
f	observable
f_e	scattering factor of the electron
f_0	atomic scattering factor without corrections
f_m	corrected atomic scattering factor
f', f''	real and imaginary part of the dispersion corrections of the atomic scattering factor
F	deposition rate
F	structure factor
h	island height
i	critical cluster size
I	scattered intensity
$\tilde{I}$	normalized scattered intensity
I_{exp}	measured intensity
I_{Sat}	saturation intensity
I_{Min}, I_{Max}	intensity of the first oscillation minimum (maximum)
k	reaction constant
k_B	Boltzmann constant
k_n	effective diffusion constant
$\mathbf{k}_i$, $\mathbf{k}_f$	wave vectors of the incident and the diffracted wave
L	length
l_l, l_{t1}, l_{t2}	longitudinal and transverse coherence lengths
l_x, l_y	dimensions of a planar, rectangular molecule
n, n_F	monolayer number
$\mathbf{n}$	surface normal
$n_\parallel$, $n_\perp$	refraction indices
n_1	number of monomers
n_j	number of the clusters with the size j
n_x	number of the stable clusters
N_0	number of nucleation sites
P, p, p_{ij}, p_F	probabilities
$\mathbf{q}$	momentum transfer of the scattering process

$q_\parallel$, q_z	component of $\mathbf{q}$ parallel (perpendicular) to the surface
q_z^{anti}	momentum transfer at the anti-Bragg point
$\mathbf{r}$, $\mathbf{r}_m$	position vectors
r, r'	states of an n-particle system (Sec. 4.3)
r_{ij}	diffusion rate from the lattice site i to the site j
R_{sub}, ϕ_{sub}	amplitude and phase of the wave scattered by the substrate
R_{film}, ϕ_{film}	amplitude and phase of the wave scattered by one monolayer of the film (layer-independent part)
r_0	classical electron radius
$\mathbf{r}_{ijk}$	absolute molecular displacement of the molecule (jk) in the layer i
$\tilde{\mathbf{r}}_{ijk}$	relative molecular displacement
s	strain
S	scattering function
t	time
t_{ML}	deposition time for one monolayer at a constant deposition rate
T	temperature
T_a	annealing temperature
T_g	substrate temperature during the deposition
u_{xi}, u_{yi}, u_{zi}	displacement of the center or mass of the molecule in the laboratory system
$\tilde{u}_{xi}$, $\tilde{u}_{yi}$, $\tilde{u}_{zi}$	relative molecular displacement in x, y, and z direction
$U(r)$	potential energy
$U(\phi)$	azimuthal potential energy
U_i	nucleaton rate of stable clusters
V_{coh}	coherence volume
$V_{jk}^{t,i,(i-1)}$	pair interaction potential
$V^{z,i,(i-1)}$	interaction potential of two separate ML's
V_i^z	interaction potential of one ML in a crystal
w_x	average number of atoms in a stable cluster
$z(x,z)$	surface height
z_0	average surface height
α, β	bulk polymorphs of PTCDA
α, β	proportionality constants (Sec. 8.3)
$\alpha_\parallel$, $\alpha_\perp$	linear thermal expansion coefficients
α_c	critical angle
$\Delta\alpha$	divergence of the beam
δ_1, δ_2	coverage deviations from a filled ML

γ	interfacial energy
λ	wavelength
$\Delta\lambda$	width of the wavelength distribution
μ	charge carrier mobility
ν	attempt frequency
$\phi(r)$, ϕ_{ij}	potentials
ϕ	azimuthal in-plane direction relative to Ag[22$\bar{4}$]
ϕ_i, χ_i, ξ_i	rotations of a molecule in the layer i
ρ	density of stable islands
ρ_e, ρ_F, ρ_S	electron densities
σ, σ_{sub}, σ_{film}	roughnesses
σ_i	capture number
2θ	angle between the incident and the diffracted beam
θ_n	coverage of the nth monolayer
θ_{even}, θ_{odd}	sum over the coverage of all monolayers with even (odd) layer number n
$\Delta\theta$	difference between θ_{even} and θ_{odd}
ξ	measure for the in-plane distortion of the unit cell

Appendix D

Samples

sample	T_{growth} [K]	T_{source} [K]	d [Å]	F [Å/min]	Experiment
pag1	405	551	≈ 90		BW6 (Stuttgart), PCH, structure, thermal expansion
film 1	402	290	≈ 60		ID10B, PCH, growth, structure, thermal expansion
film 2	401	546	≈ 30		ID10B, PCH, growth, structure, thermal expansion
film 3	400	548	13.0	2.0	ID10B, PCH, growth, structure, thermal expansion
film 4	400	546	10.6	1.7	ID10B, PCH, growth, structure, thermal expansion
pag2	384	573	256	6.3	BW6 (Stuttgart), PCH, structure, thermal expansion
pag3	385	573	189	6.3	BW6 (Stuttgart), PCH, structure, thermal expansion
pag4	381	573	63	6.3	BW6 (Stuttgart), PCH, structure, thermal expansion
pag6	408	573	126	6.3	BW6 (Stuttgart), PCH, structure, thermal expansion
pag7	444	573	126	6.3	BW6 (Stuttgart), PCH, structure, thermal expansion
pag8	464	573	126	6.3	BW6 (Stuttgart), PCH, structure, thermal expansion
pag9	484	573	126	6.3	BW6 (Stuttgart), PCH, structure, thermal expansion
pag10	365	573	126	6.3	BW6 (Stuttgart), PCH, structure, thermal expansion
pag11	346	573	126	6.3	BW6 (Stuttgart), PCH, structure, thermal expansion
pag12	478	573	126	6.3	BW6 (Stuttgart), PCH, structure, thermal expansion
pag13	383	573	126	6.3	BW6 (Stuttgart), PCH, structure, thermal expansion
pag14	388	573	180	6.3	ID10B, PCH, growth structure, thermal expansion
pag15	400	571	31	6.3	ID10B, PCH, growth, structure, thermal expansion
pag16	423	546	16	0.8	ID10B, PCH, growth, structure
pag17	473	577	32	6.3	ID10B, PCH, growth, structure
pag18	448	546	52	0.9	ID10B, PCH, growth, structure

Table D.1: Growth parameters of the PTCDA/Ag samples

Table D.2: Growth parameters of the PTCDA/Ag samples (continuation)

sample	T_{growth} [K]	T_{source} [K]	d [Å]	F [Å/min]	Experiment
pag19	318	543	54	0.9	ID10B, PCH, growth, structure, annealing
pag20	428	549			ID10B, PCH, growth
pag21	428	548			ID10B, PCH, growth
pag22	428	549			ID10B, PCH, growth
pag23	428	548	47	0.8	ID10B, PCH, growth
pag24	336	558	202	3.5	BW6 (Stuttgart), PCH, structure
pag25	453	558	202	3.5	BW6 (Stuttgart), PCH, structure
pag27	$\approx$ 432 (3A)	563	624	4.2	W1, PCH, structure, desorption
pag28	$\approx$ 323 (0A)	516	51	2.4	W1, PCH, growth, structure, annealing, desorption
pag29	$\approx$ 373 (2.35A)	563	51	2.0	W1, PCH, growth, structure, desorption
pag30	$\approx$ 393 (2.7A)	550	51	1.2	W1, PCH, growth, structure, desorption
pag31	$\approx$ 413 (2.9A)	552	51	1.2	W1, PCH, growth, structure, desorption
pag32	$\approx$ 303 (0A)	550	51	1.4	W1, PCH, growth, structure, annealing, desorption
pag33	$\approx$ 473 (3.67A)	550	51	0.9	W1, PCH, growth, structure, cooling, desorption
pag34	$\approx$ 373 (2.7A)	569	51	4.1	W1, PCH, growth, structure
pag35	$\approx$ 358 (2.1A)	551	51	0.8	W1, PCH, growth, structure, desorption
pag36	$\approx$ 358 (2.1A)	603	51	13.4	W1, PCH, growth, structure, desorption
pag37	$\approx$ 473 (3.66A)	603	51	13.6	W1, PCH, growth, structure, cooling, desorption
pag38	$\approx$ 413 (2.95A)	602	51.38	11.7	W1, PCH, growth, structure, desorption
pag39	$\approx$ 303 (0A)	605	51	13.2	W1, PCH, growth, structure, annealing
pag41	197	560	51	0.8	W1, PCH, growth, structure, annealing, desorption
pag42	235	569	51	0.8	W1, PCH, growth, structure, annealing, desorption
pag43	271	569	51	0.8	W1, PCH, growth, structure, annealing, desorption

sample	T_{growth} [K]	T_{source} [K]	d [Å]	F [Å/min]	Experiment
pag44	283	569			W1, PCH, growth, structure, desorption
pag45	293	571			W1, PCH, growth, structure, annealing, desorption
pag46	258 ± 5	560			W1, PCH, growth, structure, desorption
pag47	243	571			W1, PCH, growth, structure
pag48	303	573			W1, PCH, growth, structure
pag49	313	573			W1, PCH, growth, structure
pag50	213	568	50	1.9	OMBE (Stuttgart), AFM, desorption
pag51	135	573	50	0.8	OMBE (Stuttgart), AFM, morphology, annealing
pag52	413	583	50	0.7	OMBE (Stuttgart), AFM, morphology, optical microscopy
pag53	298	583	52	1.4	OMBE (Stuttgart), AFM, morphology, optical microscopy
pag54	319	593	50	1.7	OMBE (Stuttgart), AFM, morphology, optical microscopy
pag55	328	583	50	1.1	OMBE (Stuttgart), AFM, morphology, optical microscopy
pag56	333	583	50	1.5	OMBE (Stuttgart), AFM, morphology, optical microscopy
pag57	353	583	50	1.3	OMBE (Stuttgart), AFM, morphology, optical microscopy
pag58	373	578	50	1.6	OMBE (Stuttgart), AFM, morphology, optical microscopy
pag59	343	583	53	1.2	OMBE (Stuttgart), AFM, morphology, optical microscopy
pag60	473	593	50	1.8	OMBE (Stuttgart), AFM, morphology, optical microscopy
pag61	433	593	50	1.1	OMBE (Stuttgart), AFM, morphology, optical microscopy
pag62	423		440	3.1	OMBE (Stuttgart), AFM, morphology, optical microscopy

Table D.3: Growth parameters of the PTCDA/Ag samples (continuation)

List of Figures

List of Tables

Bibliography

[1] G. Horowitz, *Organic field-effect transistors*, Adv. Mater. **10**, 365–377 (2001).

[2] C. D. Dimitrakopoulos and D. J. Mascaro, *Organic thin-film transistors: A review of recent advances*, IBM J. Res. & Dev. **45**, 11–27 (2001).

[3] C. Rompf, B. Hilmer, and W. Kowalsky, *Heterostructures of crystalline organic and inorganic semiconductors for applications in optoelectronic integrated circuits*, Jpn. J. Appl. Phys. **33**, 832–835 (1994).

[4] D. A. Pardo, G. E. Jabbor, and N. Peyghambarian, *Application of screen printing in the fabrication of organic light-emitting devices*, Adv. Mater. **12**, 1249–1252 (2000).

[5] P. Peumans, V. Bulović, and S. R. Forrest, *Efficient, high-bandwidth organic multilayer photodetectors*, Appl. Phys. Lett. **76**, 3855–3857 (1997).

[6] Y. G. Kozlov, G. Parthasarathy, P. E. Burrows, S. R. Forrest, Y. You, and M. E. Thompson, *Optically pumped blue organic semiconductor lasers*, Appl. Phys. Lett. **72**, 144–147 (1997).

[7] N. Tessler, *Laser based on semiconducting organic materials*, Adv. Mater. **11**, 363–370 (1999).

[8] C. D. Dimitrakopoulos, A. R. Brown, and A. Pomp, *Molecular beam deposited thin films of pentacene for organic field effect transistor applications*, J. Appl. Phys. **80**, 2501–2508 (1996).

[9] N. Karl and J. Marktanner, *Structural order and photoelectric properties of organic thin films*, Mol. Cryst. Liq. Cryst. **315**, 163–168 (1998).

[10] Y. Hirose, A. Kahn, V. Aristov, P. Soukiassian, V. Bulovic, and S. R. Forrest, *Chemistry and electronic properties of metal-organic semiconductor interfaces: Al, Ti, In, Sn, Ag, and Au on PTCDA*, Phys. Rev. B **54**, 13748–13758 (1996).

[11] H. Fuchigami, S. Tanimura, Y. Uehara, T. Kurata, and S. Tsunoda, *Preparation and characterization of 3,4,9,10-perylenetetracarboxylic dianhydride (PTCDA) films deposited by organic molecular beam deposition method*, Jpn. J. Appl. Phys. **34**, 3852–3857 (1995).

[12] S. R. Forrest, *Ultrathin organic films grown by organic molecular beam deposition and related techniques*, Chem. Rev. **97**, 1793–1896 (1997).

[13] I. G. Hill, A. Kahn, Z. G. Soos, and R. A. Pascal, Jr., *Charge-separation energy in films of π-conjugated organic molecules*, Chem. Phys. Lett. **327**, 181–188 (2000).

[14] M. I. Alonso, M. Garriga, N. Karl, J. O. Ossó, and F. Schreiber, *Anisotropic optical properties of singly crystalline PTCDA studied by spectroscopic ellipsometry*, Organic Electronics , (2002), accepted.

[15] K. Glöckler, C. Seidel, A. Soukopp, M. Sokolowski, E. Umbach, M. Böhringer, R. Berndt, and W.-D. Schneider, *Highly ordered structures and submolecular scanning tunneling microscopy contrast of PTCDA and DM-PBDCI monolayers on Ag(111) and Ag(110)*, Surf. Sci. **405**, 1–20 (1998).

[16] J. Taborski, P. Väterlein, H. Dietz, U. Zimmermann, and E. Umbach, *NEXAFS investigations on ordered adsorbate layers of large aromatic molecules*, J. Electron Spectrosc. Relat. Phenom. **75**, 129–147 (1995).

[17] K. Ritley, B. Krause, F. Schreiber, and H. Dosch, *A portable UHV organic molecular beam deposition system for in situ X-Ray diffraction measurements*, Rev. Sci. Instr. **72**, 1453–1457 (2001).

[18] http://www-hasylab.desy.de/.

[19] http://www.esrf.fr/.

[20] K. Lonsdale, *Experimental studies of atomic vibrations in crystals and of their relationship to thermal expansion*, Z. Kristallogr. **112**, 188–212 (1959).

[21] S. van Smaalen, J. de Boer, C. Haas, and J. Kommandeur, *Anisotropic thermal expansion in crystals with stacks of planar molecules, such as tetracyanoquinodimethanide (TCNQ) salts*, Phys. Rev. B **31**, 3496–3503 (1985).

[22] E. Bauer and J. H. van der Merwe, *Structure and growth of crystalline superlattices: from monolayer to superlattice*, Phys. Rev. B **33**, 3657–3671 (1986).

[23] O. Hellwig, K. Theis-Bröhl, G. Wilhelmi, A. Stierle, and H. Zabel, *Growth of fcc(111) on bcc(110): new type of epitaxial transition observed for Pd on Cr*, Surf. Sci. **398**, 379–385 (1998).

[24] R. Pfandzelter, T. Igel, and H. Winter, *Growth and structure of ultrathin Mn films on Fe(001)*, Surf. Sci. **389**, 317–328 (1997).

[25] J. A. Venables, *Rate equation approaches to thin film nucleation kinetics*, Phil. Mag. **27**, 697–737 (1973).

[26] J. A. Venables, G. D. T. Spiller, and M. Hanbücken, *Nucleation and growth of thin films*, Rep. Prog. Phys. **47**, 399–459 (1984).

[27] J. A. Venables, *Atomic processes in crystal growth*, Surf. Sci. **299/300**, 798–817 (1994).

[28] F.-J. Meyer zu Heringsdorf, M. C. Reuter, and R. M. Tromp, *Growth dynamics of pentacene thin films*, Nature **412**, 517–520 (2001).

[29] J. Weckesser, J. V. Barth, and K. Kern, *Direct observation of surface diffusion of large organic molecules at metal surfaces: PVBA on Pd(110)*, J. Chem. Phys. **110**, 5351–5354 (1999).

[30] E. Umbach, S. Sokolowski, and R. Fink, *Substrate-interaction, long-range order, and epitaxy of large organic adsorbates*, Appl. Phys. A **63**, 565–576 (1996).

[31] J. H. Schön, Ch. Kloc, and B. Batlogg, *Fractional quantum hall effect in organic molecular semiconductors*, Science **288**, 2338–2340 (2000).

[32] P. Peumans and S. R. Forrest, *Very-high-efficiency double-heterostructure copper phthalocyanine/C_{60} photovoltaic cells*, Appl. Phys. Lett. **79**, 126–128 (2001).

[33] E. A. Silinsh and V. Čápek, *Organic Molecular Crystals: Interaction, Localization and Transport Phenomena*, AIP Press (1994).

[34] A. I. Kitaigorodsky, *Physical Chemistry: Molecular Crystals and Molecules*, Academic Press (1973).

[35] M. Pope and Ch. E. Swenberg, *Electronic Processes in Organic Crystals and Polymers*, Oxford University Press (1999).

[36] G. de la Torre, P. Vázques, F. Agulló-Lópes, and T. Torres, *Phthalocyanines and related compounds: organic targets for nonlinear optical applications*, J. Mat. Chem. **8**, 1671–1683 (1998).

[37] G. Klebe, F. Graser, E. Hädicke, and J. Berendt, *Crystallochromy as a solide-state effect: correlation of molecular conformation, crystal packing and colour in perylene-3,4:9,10-bis(dicarbocimide) pigments*, Acta Cryst. **B45**, 69–77 (1988).

[38] N. Karl and Ch. Günther, *Structure and ordering principles of ultrathin organic molecular films on surfaces of layered semiconductors: organic-on-inorganic MBE*, Cryst. Res. Technol. **34**, 243–254 (1999).

[39] C. C. Leznoff and A. B. P. Lever, *Phthalocyanines: Properties and Applications*, VCH Publishers, Inc. (1989).

[40] A. Koma, *Molecular beam epitaxial growth of organic thin films*, Prog. Crystal Growth and Charact. **30**, 129–152 (1995).

[41] D. E. Hooks, T. Fritz, and M. D. Ward, *Epitaxy and molecular organization on solid substrates*, Adv. Mater. **13**, 227–241 (2001).

[42] C. Ludwig, R. Gompf, W. Glatz, J. Petersen, W. Eisenmenger, M. Möbus, U. Zimmermann, and N. Karl, *Video-STM, LEED and X-ray investigations of PTCDA on graphite*, Z. Phys. B **86**, 397–404 (1992).

[43] T. Schmitz-Hübsch, F. Sellam, R. Staub, M. Törker, R. Fritz, Ch. Kübel, K. Müller, and K. Leo, *Direct observation of organic-inorganic heteroepitaxy: perylene-tetracarboxylic-dianhydride on hexa-peri-benzocoronene on highly ordered pyrolytic graphite*, Surf. Sci. **445**, 358–367 (2000).

[44] R. Fink, D. Gador, U. Stahl, Y. Zou, and E. Umbach, *Substrate-dependent lateral order in naphtalene-tetracarboxylic-dianhydride monolayers*, Phys. Rev. B **60**, 2818–2826 (1999).

[45] C. Kendrick, A. Kahn, and S. R. Forrest, *STM study of the organic semiconductor PTCDA on highly-oriented pyrolytic graphite*, Appl. Surf. Sci. **104/105**, 586–594 (1996).

[46] C. Kendrick and A. Kahn, *Epitaxial growth and phase transition in multilayers of the organic semiconductor PTCDA on InAs(001)*, J. Cryst. Growth **181**, 181–192 (1997).

[47] C. Seidel, J. Poppensieker, and H. Fuchs, *Real-time monitoring of phase transitions of vacuum deposited organic films by molecular beam deposition*, Surf. Sci. **408**, 223–231 (1998).

[48] P. Fenter, P. E. Burrows, P. Eisenberger, and S. R. Forrest, *Layer-by-layer quasi-epitaxial growth of a crystalline organic thin film*, J. Cryst. Growth **152**, 65–72 (1995).

[49] U. Sondermann, A. Kutoglu, and H. Bässler, *X-ray diffraction study of the phase transition in crystalline tetracene*, J. Phys. Chem. **89**, 1735–1741 (1985).

[50] M. Möbus, N. Karl, and T. Kobayashi, *Structure of perylene-tetracarboxylic-dianhydride thin films on alcali halide crystal substrates*, J. Cryst. Growth **116**, 495–504 (1992).

[51] A. J. Lovinger, S. R. Forrest, M. L. Kaplan, P. H. Schmidt, and T. Venkatesan, *Structural and morphological investigation of the development of electrical conductivity in ion-irradiated thin films of an organic material*, J. Appl. Phys. **55**, 476–482 (1984).

[52] M. L. Kaplan, C. S. Day, A. J. Lovinger, P. H. Schmidt, and S. R. Forrest, privat communication.

[53] T. Ogawa, K. Kuwamoto, S. Isoda, T. Kobayashi, and N. Karl, *3,4:9,10-Perylenetetracarboxylic dianhydride (PTCDA) by electron crystallography*, Acta cryst. B **55**, 123–130 (1999).

[54] C. Seidel, C. Awater, X. D. Liu, R. Ellerbrake, and H. Fuchs, *A combined STM, LEED and molecular modelling study of PTCDA grown on Ag(110)*, Surf. Sci. **371**, 123–130 (1997).

[55] J. J. Cox and T. S. Jones, *The structure of copper phthalocyanine and perylene-3,4,9,10-tetracarboxylic dianhydride overlayers on the (111)A surfaces of InAs and InSb*, Surf. Sci. **457**, 311–318 (2000).

[56] S. Mannsfeld, M. Toerker, T. Schmitz-Hübsch, F. Sellam, T. Fritz, and K. Leo, *Combined LEED and STM study of PTCDA growth on reconstructed Au(111) and Au(100) single crystals*, Organic Electronics **2**, 121–134 (2001).

[57] M. Jung, U. Baston, G. Schnitzler, M. Kaiser, J. Papst, T. Porwol, H. J. Freund, and E. Umbach, *The electronic structure of adsorbed aromatic molecules: perylene and PTCDA on Si(111) and Ag(111)*, J. of Molecular Structure **293**, 239–244 (1993).

[58] T. Schmitz-Hübsch, T. Fritz, R. Staub, A. Back, N. R. Armstrong, and K. Leo, *Structure of 3,4,9,10-perylene-tetracarboxylic-dianhydride grown on reconstructed and unreconstructed Au(100)*, Surf. Sci. **437**, 163–172 (1999).

[59] P. Fenter, F. Schreiber, L. Zhou, P. Eisenberger, and S. R. Forrest, *In situ studies of morphology, strain, and growth modes of a molecular organic thin film*, Phys. Rev. B **56**, 3046–3053 (1997).

[60] D. Schlettwein, A. Back, B. Schilling, T. Friz, and N. R. Armstrong, *Ultrathin films of perylenedianhydride and perylenebis(dicarboximide) dyes on (001) alkali halide surfaces*, Chem. Mater. **10**, 601–612 (1998).

[61] S. R. Forrest, P. E. Burrows, E. I. Haskal, and F. F. So, *Ultrahigh-vacuum quasiepitaxial growth of model van der Waals thin films. II. Experiment*, Phys. Rev. B. **49**, 11309–11321 (1994).

[62] P. Fenter, P. Eisenberger, P. Burrows, S. R. Forrest, and K. S. Liang, *Epitaxy at the organic-inorganic interface*, Physica B **221**, 145–151 (1996).

[63] M. Leonhardt, O. Mager, and H. Port, *Two-component optical spectra in thin PTCDA films due to the coexistence of alpha- and beta-phase*, Chem. Phys. Lett. **313**, 24–30 (1999).

[64] B. Krause, A. C. Dürr, K. A. Ritley, F. Schreiber, H. Dosch, and D. Smilgies, *On the coexistence of different polymorphs in organic epitaxy: α and β phase of PTCDA on Ag(111)*, Appl. Surf. Sci. **175–176**, 332–336 (2001).

[65] B. E. Warren, *X-ray Diffraction*, Dover Publications, inc. (1990).

[66] J. Als-Nielsen and D. McMorrow, *Elements of Modern X-ray Physics*, John Wiley & Sons, ldt. (2001).

[67] A. Guinier, *X-ray Diffraction in Crystals, Imperfect Crystals and Amorphous Bodies*, Dover Publications, Inc. (1994).

[68] V. Holý, W. Pietsch, and T. Baumbach, *High-Resolution X-ray Scattering from Thin Films and Multilayers*, Springer-Verlag (1999).

[69] A. J. C. Wilson and E. Prince, editors, *International Tables for X-ray Crystallography* volume C, Kluwer Academic Publisher (1999).

[70] H. Dosch, *Springer Tracts in Modern Physics, Critical Phenomena at Surfaces and Interfaces* volume 126, Springer-Verlag (1992).

[71] R. Feidenhans'l, *Surface structure determination by X-ray diffraction*, Surf. Sci. Rep. **10**, 105–188 (1989).

[72] P. Guenard, *Surface d'oxyde et interface metal/oxyde etudiées par diffraction X en incidence rasante: structure de la surface (0001) de l'alumine α et étapes de la croissance de Ag sur MgO(001)*, PhD thesis Université Joseph Fourier - Grenoble I (1992).

[73] E. Vlieg, *Integrated intensities using a six-circle surface X-ray diffractometer*, J. Appl. Cryst. **30**, 532–534 (1997).

[74] A. Pimpinelli and J. Villain, *Physics of Crystal Growth*, Cambridge University Press (1999).

[75] M. A. Herman and H. Sitter, *Molecular Beam Epitaxy*, Springer-Verlag (1996).

[76] H. Lüth, *Surfaces and Interfaces of Solid Materials*, Springer-Verlag (1995).

[77] *Dynamik und Strukturbildung in kondensierter Materie, 28. IFF-Ferienkurs* (1997).

[78] A. Zangwill, *Physics at Surfaces*, Cambridge University Press (1988).

[79] M. Siegert and M. Plieschke, *Formation of pyramids and mounds in molecular beam epitaxy*, Phys. Rev. E **53**, 307 (1996).

[80] J. A. Meyer, J. Vrijmoeth, H. A. van der Vegt, E. Vlieg, and R. J. Behm, *Importance of the additional step-edge barrier in determining film morphology during epitaxial growth*, Phys. Rev. B **20**, 14790–14793 (1995).

[81] S. Tan and P.-M. Lam, *Monte Carlo simulation of three-dimensional islands*, Phys. Rev. B **60**, 997–1000 (1999).

[82] K. A. Fichthorn and M. Scheffler, *Island nucleation in thin-film epitaxy: a first-principle investigation*, Phys. Rev. Lett. **84**, 5371–5374 (2000).

[83] R. Stumpf and M. Scheffler, *Ab initio calculations of energies and self-diffusion on flat and stepped surfaces of Al and their implications on crystal growth.*, Phys. Rev. B **53**, 4958–4973 (1996).

[84] K. Mae, K. Kyuno, and R. Yamamoto, *The microscopic mechanism of surfactant epitaxy by molecular dynamics*, Modelling Simul. Mater. Sci. Eng. **4**, 73–85 (1996).

[85] J. G. Amar and F. Family, *Kinetics of submonolayer and multilayer epitaxial growth*, Thin Solid Films **272**, 208–222 (1996).

[86] H. T. Dobbs, D. D. Vvedensky, and A. Zangwill, *Theory of quantum dot formation in Stranski-Kranstanov systems*, Appl. Surf. Sci. **123/124**, 646–652 (1998).

[87] *Computersimulation in der Physik, 20. IFF-Ferienkurs* (1989).

[88] P. I. Cohen, G. S. Petrich, P. R. Pucite, G. J. Whaley, and A.S. Arrott, *Birth-death models of epitaxy*, Surf. Sci. **216**, 222–247 (1988).

[89] F. Family and P. Meakin, *Kinetics of droplet growth process: simulations, theory, and experiment*, Phys. Rev. A **40**, 3836–3854 (1989).

[90] C. D. Pownall and P. A. Mulheran, *Simulation and theory of island nucleation, growth, and coalescence on stepped substrates*, Phy. Rev. B **60**, 9037–9045 (1999).

[91] M. N. Popescu, J. G. Amar, and F. Family, *Self-consistent rate-equation approach to transitions in critical island size in metal (100) and metal (111) homoepitaxy*, Phy. Rev. B **58**, 1613–1619 (1997).

[92] G. S. Bales and A. Zangwill, *Self-consistens rate theory of submonolayer homoepitaxy with attachment/detachment kinetics*, Phys. Rev. B **55**, R1973–R1976 (1997).

[93] J. Johansson and W. Seifert, *Size control of self-assembled quantum dots*, J. Cryst. Growth **221**, 566–570 (2000).

[94] H. A. van der Vegt, H. M. van Pinxteren, M. Lohmeier, E. Vlieg, and J. M. Thornton, *Surfactant-induced layer-by-layer growth of Ag on Ag(111)*, Phys. Rev. B **68**, 3335–3338 (1992).

[95] A. R. Woll, R. L. Headrick, S. Kycia, and J. D. Brock, *GaN nucleation and growth on sapphire (0001): incorporation and interlayer transport*, Phys. Rev. Lett. **83**, 4349–4352 (1999).

[96] J. Alvarez, E. Lundgren, X. Torrelles, and S. Ferrer, *Determination of scaling exponents in Ag(100) homoepitaxy with X-ray diffraction profiles*, Phys. Rev. B **57**, 6325–6328 (1998).

[97] J. Johansson, N. Carlsson, and W. Seifert, *Manipulations of size and density of self-assembled quantum dots grown by MOVPE*, Physica E **2**, 667–671 (1998).

[98] H. A. van der Vegt, J. Vrijmoeth, R. J. Behm, and E. Vlieg, *Sb-enhanced nucleation in the homoepitaxial growth of Ag(111)*, Phys. Rev. B **57**, 4127–4131 (1998).

[99] M. E. J. Newman and G. T. Barkema, *Monte Carlo Methods in Statistical Physics*, Clarendon Press (1999).

[100] *Synchrotronstrahlung zur Erforschung kondensierter Materie, 23. IFF-Ferienkurs* (1992).

[101] S. N. Magonov and M.-H. Whangbo, *Surface Analysis with STM and AFM: Experimental and Theoretical Aspects of Image Analysis*, VCH (1996).

[102] M. Lohmeier and E. Vlieg, *Angle calculations for a six-circle diffractometer*, J. Appl. Cryst. **26**, 706–716 (1993).

[103] E. Umbach, K. Glöckler, and M. Sokolowski, *Surface "architecture" with large organic molecules: interface order and epitaxy*, Surf. Sci. **402–404**, 20–31 (1998).

[104] G. Salvan, D. A. Tenne, A. Das, T. U. Kampen, and D. R. T. Zahn, *Influence of deposition temperature on the structure of 3,4,9,10-perylene tetracarboxylic dianhydride thin films on H-passivated silicon probed by Raman spectroscopy*, Organic Electronics **1**, 49–56 (2000).

[105] E. A. Soares, G. S. Leatherman, R. D. Diehl, and M. A. Van Hove, *Low-energy electron diffraction study of the thermal expansion of Ag(111)*, Surf. Sci. **468**, 129–136 (2000).

[106] P. Statiris, H. C. Lu, and T. Gustafsson, *Temperature dependent sign reversal of the surface contraction of Ag(111)*, Phys. Rev. Lett. **72**, 3574–3577 (1994).

[107] V. A. Shchukin and D. Bimberg, *Spontanous ordering of nanostructures on crystal surfaces*, Rev. Mod. Phys. **71**, 1125–1171 (1999).

[108] S. Liu and H. Metiu, *A kinetic model for island shape variations under epitaxial growth conditions*, Surf. Sci. **405**, L497–L502 (1998).

[109] T. Schmitz-Hübsch, T. Fritz, F. Sellam, R. Staub, and K. Leo, *Epitaxial growth of 3,4,9,10-perylene-tetracarboxylic-dianhydride on Au(111): a AFM and RHEED study*, Phys. Rev. B **55**, 7072–7976 (1997).

[110] J. H. van der Merwe, *Interplay between misfit strain relief and Stranski-Krastanov growth in fcc(111)/bcc(110) ultrathin epitaxy. Part I. Analytical approach*, Surf. Sci. **449**, 151–166 (2000).

[111] J. H. van der Merwe and D. L. Tönsing, *Interplay between misfit strain relief and Stranski-Krastanov growth in fcc(111)/bcc(110) ultrathin epitaxy. Part I. Quantification using embedded atom method potentials*, Surf. Sci. **449**, 167–179 (2000).

[112] G. Salvan, , C. Himcinschi, A. Yu. Kobitski, M. Friedrich, H. P. Wagner, T. U. Kampen, and D. R. T. Zahn, *Crystallinity of PTCDA films on silicon derived via optical spectroscopic measurements*, Appl. Surf. Sci. **175–176**, 363–368 (2001).

[113] M. C. Desjonquères and D. Spanjaard, *Concepts in Surface Physics*, Springer-Verlag (1998).

[114] J. Y. Grand, T. Kunstmann, D. Hoffmann, A. Haas, M. Dietsche, J. Seifritz, and R. Möller, *Epitaxial growth of copper phthalocyanine monolayers on Ag(111)*, Surf. Sci. **366**, 403–414 (1996).

[115] F. J. Ramírez, M. A. G. Aranda, V. Hernández, J. Casado, S. Hotta, and J. T. López Navarrete, *Temperature-dependent infrared spectroscopic and crystallographic study of α,α'-dimethyl oligothiophenes in neutral form*, J. Chem. Phys. **109**, 1920–1929 (1998).

[116] S. T. Bramwell and J. H. Williams, *Thermal expansion of the lowest-temperature phase of benzene:hexafluorobenzene*, J. Chem. Soc. Faraday Trans. **88**, 2721–2724 (1992).

[117] Y. S. Touloukian, R. K. Kirby, R. E. Taylor, and P. D. Desai, *Thermophysical Properties of Matter. Vol. 12: Thermal Expansion - Metallic Elements and Alloys, vol. 13: Thermal Expansion - Nonmetallic Solids*, IFI/Plenum (1975).

[118] C. L. Nicklin, C. Norris, P. Steadman, J. S. G. Taylor, and P. B. Howes, *The growth of Sm on Mo(110) studied by surface X-ray diffraction*, Physica B **221**, 86–89 (1996).

[119] J. L. Brand, M. V. Arena, A. A. Deckert, and S. M. George, *Diffusion mechamisms of short-chain alkanes on metal substrates: unique molecular features*, J. Chem. Phys. **92**, 5136–5143 (1989).

[120] H.-N. Yang, Y.-R. Zhao, A. Chan, T.-M. Lu, and G.-C. Wang, *Sampling-induced hidden cycles in correlated random rough surfaces*, Phy. Rev. B **56**, 4224–4232 (1997).

[121] J. A. Stroscio, D. T. Pierce, M. D. Stiles, A. Zangwill, and L. M. Sander, *Coarsening of unstable surface features during Fe(001) homoepitaxy*, Phys. Rev. Lett. **75**, 4246–4249 (1995).

Dank

Zum Gelingen dieser Arbeit haben viele Leute beigetragen. Insbesondere möchte ich den folgenden Personen danken:

- Herrn Professor Dr. Helmut Dosch für die Ermöglichung dieser Arbeit, und für viele fruchtbare Diskussionen.
- Herrn Dr. Frank Schreiber für die gute Betreuung der Arbeit, die Initiierung der Kooperation mit Alberto Pimpinelli und die Hilfe bei den Synchrotronstrahlzeiten.
- Allen Mitarbeitern der Gruppe "organische dünne Schichten" für die angenehme Zusammenarbeit. Mein besonderer Dank gilt Herrn Dr. Ken Ritley für die Weitergabe seines Wissens über UHV-Anlagen und die vielen nützliche Ratschläge, und Herrn Arndt C. Dürr für die Unterstützung bei den Experimenten am Synchrotron.
- Frau Annette Weißhardt für die Unterstützung bei der Probenpräparation, die hervorragende Zusammenarbeit, und die freundschaftliche Arbeitsatmosphäre.
- Herrn Professor Norbert Karl, Herrn Dr. Jens Pflaum und Herrn Stefan Hirschmann für hilfreiche Diskussionen und die Bereitstellung des purifizierten PTCDA.
- Professor Alberto Pimpinelli und Arnaud Videcoq für die Hilfe bei den Monte Carlo Simulationen.
- Herrn Oliver H. Seeck für die Betreuung an der Beamline W1 des HASYLAB, und Herrn Detlef Smilgies für die Unterstützung an der Beamline ID10B der ESRF.
- Den Mitarbeitern der Werkstätten des MPI für Metallforschung und des Instituts für theoretische und angewandte Physik der Universität Stuttgart. Besonders hervorzuheben ist die Hilfe von Herrn Plenert und den Mitarbeitern der Feinmechanikwerkstatt, die immer bereit waren, "erste Hilfe" an den experimentellen Apparaturen zu leisten.
- Den Mitgliedern der Abteilung Dosch und aller anderen Abteilungen des MPIs für Metallforschung und des MPIs für Festkörperforschung für ihre Hilfsbereitschaft, viele interessante und hilfreiche Diskussionen und die freundliche Atmosphäre, die sich nicht nur auf den Arbeitsalltag beschränkte.